Terahertz Photonics Utilising Photonic Crystals Exhibiting Fano Resonances and Photonic Band Gaps

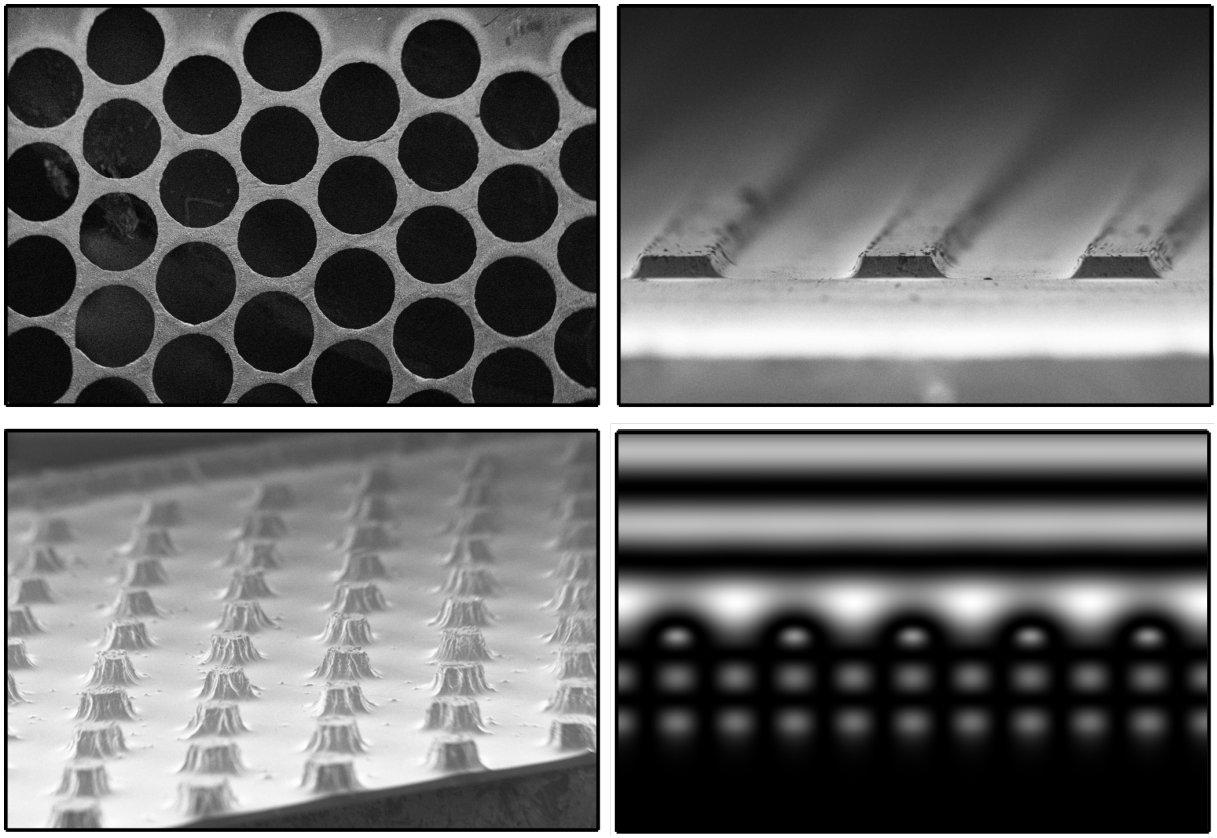

Master's Thesis

Group 5.340

Aalborg University
Department of Materials and Production

Department of Materials and Production
Aalborg University
http://www.mp.aau.dk/

AALBORG UNIVERSITY
DENMARK

Title:
Terahertz Photonics Utilising Photonic Crystals Exhibiting Fano Resonances and Photonic Band Gaps

Theme:
Master's thesis

Project Period:
September 2021 - June 2022

Project Group:
Group 5.340 - MNNF3/4

Participants:
Karl Grundahl Danielsen
Jesper Lauritz Winkel Sonne
Anders Malthe Westerkam

Supervisors:
Thomas Møller Søndergaard
Esben Skovsen

ECTS Points: 60

Number of Pages: 145

Appendices: 5

Date of Completion:
1st June, 2022

Abstract:

This project sets out to fabricate and characterise terahertz photonic components, namely spectral-specific reflectors based on Fano resonances and waveguides utilising photonic crystals. To this end, three theoretical models are implemented to design the structures that exhibit the desired response in the lower end of the terahertz region. These methods are the plane wave expansion, Fourier modal method, and an iterative method based on the fast Fourier transform. The fabrication methods reactive ion etching and laser ablation, which are both readily available in most research and industrial environments, are used to produce the samples. The spectral response of the produced samples is measured using terahertz time-domain spectroscopy.
The measured spectra of the structures exhibiting Fano resonances are shown to be in great agreement with the Fourier modal method. An additional model to predict the resonances is developed, and it too proved to be in great agreement with the Fourier modal method.
Photonic crystals are fabricated by ablating holes or etching silicon rods in high-resistivity silicon wafers. The photonic crystals are made in both hexagonal and square arrays, and band gaps are shown in the lower end of the terahertz region for both configurations. Solid-core waveguide, and cavity, modes are detected for a hexagonal array of air holes and a hexagonal array of silicon rods, respectively.

Resumé

Frekvensområdet for mikrobølger og synligt lys har længe været veludviklet, mest affødt af de relativt let tilgængelige metoder til at både danne, detektere, og manipulere stråling i disse områder. Imellem disse to områder finder man en tidligere noget uudforsket del af det elektromagnetiske spektrum, nemlig området for terahertz stråling. Dette område var op til 80'erne forbeholdt hvad bedst kan beskrives som nicheforskning eftersom ingen af komponenterne påkrævet for at udforske dette område var lettilgængelige.
I 80'erne skete der et gennembrud, da forskellige forskergrupper viste, at man ved hjælp af femtosekund lasere kan danne og detektere terahertz stråling. To af disse grupper, som er specielt nævneværdige, er Grischkowskys gruppe der var tilknyttet IBM og Austons gruppe der var tilknyttet Bell Labs. Disse grupper udgiver i årene 1988 til 1990 nogle af de artikler der lagde grundstenene for terahertz tidsdomæne spektroskopi.
Brugen af femtosekund lasere til både at excitere og detektere terahertz stråling blev et vendepunkt for forskningen indenfor terahertz området da det betragteligt sænkede adgangsbarrieren til feltet, og dermed gjorde det mere tilgængeligt.
Selvom området har oplevet en stor udvikling over de seneste 30 år, er det stadigvæk et område af interesse. Dette skyldes at mange af komponenterne i dette område ikke er lige så veludviklede som de tilsvarende komponenter i de omgivende frekvensområder, som for eksempel mikrobølger og synligt lys.

Formålet med dette kandidatspeciale var at designe og lave forskellige passive komponenter til manipulation af terahertz stråling, hvorfor sådanne både er blevet modelleret, fremstillet, og karakteriseret. Mere specifikt er der fokus på to slags komponenter, en der udviser Fano resonanser samt en anden der udviser fotoniske båndgab. Disse er henholdsvis baseret på en- og to-dimensionelle fotoniske krystaller i høj resistivitet silicium. Komponenterne der udviser Fano resonancer er fremstillet ved at ætse et en-dimensionelt gitter ned i overfladen af 100μm tynde wafere, og disse kan for eksempel benyttes som spektral specifikke reflektorer. Komponenterne der udviser fotoniske båndgab er fremstillet ved enten at ætse i 100 og 200μm tynde wafere således at et firkantet eller hexagonalt gitter af stave står tilbage, eller ved at brænde huller i et hexagonal mønster ved at benytte en høj energi pulset laser. Disse komponenter kan bruges til at reflektere områder af frekvenser, men kan også bruges til at lave bølgeledere og kaviteter.
Efter fremstillingen blev de forskellige komponenter også karakteriseret ved hjælp af flere forskellige metoder såsom skannende elektron mikroskopi, lys mikroskopi, og profilometri. Derudover er de også blevet optisk karakteriseret ved transmissionsmålinger, og efterfølgende er de blevet sammenholdt med tilhørende teoretiske modeller.

Målingerne på de fremstillede komponenter der udviser Fano resonanser er i fremragende ov-

erensstemmelse med de spektrummer beregnet med den teoretiske Fourier modal metode, både under normalt og vinklet lysindfald. Samtidigt blev der også fundet en tilfredsstillende overensstemmelse mellem målingerne på de fremstillede komponenter der udviser båndgab, og de båndstrukturer der blev beregnet med en iterativ tre-dimensionel Fast Fourier Transform metode. Selvom det ikke var muligt at detektere bølgeledertilstande i en luftbølgeleder, så blev der med succes fundet bølgeledertilstande i en siliciumbølgeleder i en prøve med et hexagonalt gitter af lufthuller i silicium, samt kavitetstilstande for en kavitet i en prøve med et hexagonalt gitter af silicium stænger i luft.

De resultater og overvejelser som er præsenteret i dette kandidatspeciale kan bruges som inspiration til videre undersøgelse af: Samling af signal ved hjælp af bøjede bølgeledere, nedskalering af de producerede komponenter, og fremstilling af fungerende luftbølgeledere.

Contents

Preface

This project is written by group 5.340, as a Master's thesis at Aalborg University. The project was supervised by associate professors Esben Skovsen and Thomas Møller Søndergaard. The project lasted from the 2nd of September 2021 to the 2nd of June 2022.

The purpose of this project was to model and fabricate passive optical components in the frequency region 0.1-3.0 THz based on photonic crystals. This project has been sectioned into three parts. The first part includes an introduction to the field of terahertz radiation, followed by the theory used to establish the models that determined the ideal dimensions of the fabricated structures. Finally, the methods used to fabricate the two types of structures are introduced. In the second part, the results and discussion of the samples exhibiting Fano resonances are presented together with a partial conclusion. In the third and final part, the results of the samples based on two-dimensional photonic crystals are presented and discussed, along with a partial conclusion. Finally, a joint conclusion to the whole project is presented. The software MATLAB was used for all the presented models, while Python and Arduino were used to automate one of the fabrication methods.

All sections, tables, and significant equations are numbered for reference. This report uses a numerical reference system and a reference is represented as [*number*]. Referenced sources are in the bibliography. References before periods only refer to the associated sentence. References after periods are associated with the entire paragraph. The project is written with Oxford comma.

Aalborg University, 1st June, 2022

Karl Grundahl Danielsen
kdanie17@student.aau.dk

Jesper Lauritz Winkel Sonne
jsonne17@student.aau.dk

Anders Malthe Westerkam
aweste17@student.aau.dk

Part I

Background, Theory and Method

1 Introduction

The terahertz region is of increasing interest and spans the frequency interval from 0.1 to 10 terahertz, corresponding to wavelengths between 3.0 mm and 30 μm [1–6]. This region lies between microwaves and infrared, and was before the late 1980s referred to as the "terahertz gap" due to the lack of efficient emitters and detectors in this frequency region compared to the adjacent regions [3, 7, 8]. The terahertz frequency range has been actively researched in the last 30 years following the introduction of using femtosecond lasers to both excite and detect freely propagating terahertz radiation in the late 1980s [3, 8, 9]. Although the selection of both emitters and detectors has improved since then [10, 11] it is still an area actively being researched [12, 13], wherein particular the realisation of quantum cascade lasers operational at room temperature is of great interest but has yet to be achieved [14, 15]. The reason for this interest is grounded on the expectation that it will reduce the complexity, cost, and improve the portability of terahertz laser systems which would help the commercialisation of the field [14], which has only experienced an increasing interest over the years, due to the multiple areas in which it has usages. [2, 3, 8, 15]

In the defence and public security sector terahertz imaging can be used to detect hidden metallic objects, given that many materials such as clothing and many common types of packaging are transparent in this spectral region. In addition, terahertz spectroscopy may be used to detect many illicit drugs and explosives since they have material-specific spectra. [16, 17]
Since terahertz radiation is strongly absorbed by water it may also be used for medical diagnostics of phenomena where the water content of the tissue, and in the future potentially cells, under investigation changes [18, 19]. Terahertz imaging has also been proved able to identify cartilage deterioration in a rabbit knee [20]. An overarching benefit of using terahertz in medical diagnostics is the inherently lower energy of terahertz radiation compared to visible light and X-rays, and consequently, the ionisation potential of terahertz is nearly non-existent, and it therefore poses a significantly lower risk for unwanted side effects [20]. Another area where terahertz radiation can be exploited is in non-destructive quality control of, e.g., plastics and different foods. For plastics, it can be used to determine water content, the presence of contaminants, and the quality of plastic welds [21, 22]. For foods, it can be used to determine moisture content and the presence of pesticides, antibiotics, as well as foreign bodies [23]. Furthermore, an almost certain future exploitation of terahertz radiation is found in telecommunications, since following the current trend of the technology the bands of the next generation, 6G, will extend into the terahertz region [24–26].

Besides the need for better emitters and detectors, all these applications also require components that enable the possibility to manipulate the radiation, components that are not as readily

available in the terahertz region [27–29]. Examples of the components are filters, waveguides, and reflectors. Furthermore, phased arrays could be a possible way to collect and steer the output from multiple sources in an attempt to circumvent the rather low output power from terahertz sources [3, 13, 30].

A mechanism that can be exploited to create components such as spectral-specific reflectors is Fano resonances [31–34]. These are well established in the literature [5, 31, 35–40], and as the name suggests, they are resonances of some system. They materialise when a continuous and a discrete set of states coexist, with the interference between these states resulting in the asymmetric spectral line shape that characterises Fano resonances. The formulation of the Fano resonance theory was developed by Ugo Fano in 1935 [32], when some of the Rydberg spectral lines were observed to be anomalous, and could not be understood using the theory at the time. Fano showed that these lines can be understood as interference between superimposed wave functions corresponding to a discrete transition as well as a continuous transition. Fano gained this insight by considering the photo-ionisation of an atom, which may occur several ways, the most straightforward being the case in which the photon simply has enough energy to ionise the electron, resulting in the process $A + \hbar\omega \rightarrow A^+ + e^-$. Another process that may occur is that the photon excites two electrons into some quasi discrete level, from which one of the electrons may fall back down into its initial energy state providing the energy needed for the other electron to be ejected into the vacuum continuum. This last process is also known as an Auger process and can be expressed as $\hbar\omega + A \rightarrow A^* \rightarrow A^+ + e^-$. These autoionising levels are discrete, and due to the nature of quantum mechanics, the real process can be described as the superposition of these two cases. With this description, Fano used perturbation theory to arrive at the following expression for the scattering cross-section, σ, which could then explain the asymmetric absorption peaks

$$\sigma = \frac{(\epsilon + q)^2}{\epsilon^2 + 1}, \qquad \epsilon = \frac{2(E - E_F)}{\Gamma}, \tag{1.1}$$

with E_F being the resonance frequency, Γ the width of the resonance, E a continuous frequency variable, and q being a phenomenological shape parameter. This shape parameter can be further understood if eq. (1.1) is rewritten to be the superposition of a Lorentzian peak, expected for absorption of a discrete set of modes, as well as a continuous level, i.e.,

$$\sigma = \frac{q^2 - 1}{\epsilon^2 + 1} + 1 + \frac{2q\epsilon}{\epsilon^2 + 1}. \tag{1.2}$$

Here the last term can be understood as a mixing term, which strongly depends on the value of q. Thus the parameter q governs to which degree the two ionisation methods are probable in relation to one another, which is what Fano proposed in his original paper. This means that in the limit $q \rightarrow \infty$ the absorption process by the continuum of states is very weak, and the Fano resonance simply looks like the standard Lorentzian peak, whereas if q is on the order of unity, both transitions are equally probable resulting in an asymmetric dip. In the case where $q = 0$ a symmetric dip appears, sometimes called an antiresonance, and is unique to the Fano resonance. These profiles are illustrated in fig. 1.1. This interference between discrete and continuous states is then the physical interpretation of the Fano resonance, and also explains why this phenomenon is present in the field of photonics. If a structure supports coupling into and out of discrete and continuous modes, Fano resonances may appear, a mechanism that can then be used for, e.g., spectral-specific reflectors.

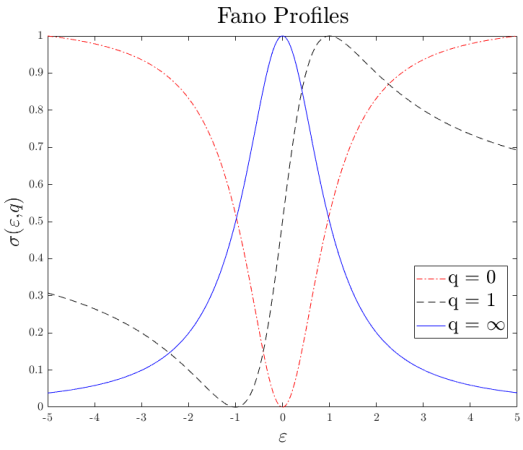

Figure 1.1: Plots the peaks of different absorption processes discussed in this section. In the limit where $q \longrightarrow \infty$ the absorption process is dominated by discrete transitions, whereas when $q = 0$ the absorption is facilitated by a continuum of states. When $q \approx 1$ both absorption processes are equally likely, and it is by this mechanism Fano resonances occur.

A class of materials that can be used to create optical devices for the terahertz spectrum are photonic crystals. These have been studied since the late 19th century, when Lord Rayleigh showed that multilayered dielectric stacks, i.e., the Bragg Mirror, had a spectral region of high reflectivity dubbed the stop band [41]. Such a structure, where the dielectric function is varied periodically along one or more axes, is today commonly thought of as a photonic crystal, though it is contended by one of the progenitors of the name, Eli Yablonovitch, that the name *photonic crystal* should be reserved for materials that are both periodical in either two or three dimensions, to distinguish them from the materials studied by Rayleigh, and have large modulations of the refractive indexes, separating the field from X-ray crystallography [42]. Nevertheless, a commonly accepted definition of the word *photonic crystal* is simply that of a material in which the dielectric function varies periodically in one or more dimensions [43–45].

The name photonic crystal was first brought into existence in 1987 when Sajeev John and Eli Yablonovitch published two pioneering papers [46, 47]. S. John showed that light could be confined by introducing defects into a photonic crystal, in a similar way that an electron can be confined by introducing a potential trap in the form of impurity atoms in a semiconductor. The defects could be any disruption to the otherwise periodic dielectric function such as point defects, line defects, or grain boundaries [46]. The paper written by E. Yablonovitch investigated the possibility of inhibiting the spontaneous emissions of systems at specific frequencies by using two- and three-dimensional photonic crystals with band gaps at these frequencies, concluding that the effect could play a significant role in solid-state physics, specifically in the study of semiconductor lasers [46]. That the spontaneous emission rates of systems could be altered had been known since the 1940s, when Edward Purcell published a paper regarding the enhancement of nuclear magnetic moment transitions by coupling with a resonant electrical circuit [48], where he showed that the spontaneous emission of a system at a given frequency can be changed by a factor proportional to the ratio between the systems density of states and the free space density of states. Thus, creating a material with a true band gap would inhibit the system from spontaneously emitting light with frequencies inside the gap. [48]

Since the pioneering work of S. John and E. Yablonovitch, the number of publications regarding photonic crystals have exploded [45], with the first three-dimensional photonic crystal being fabricated in 1991 by Eli Yablonovitch. The crystal used a pseudo-FCC lattice that was dubbed *Yablonovite*. The fabricated structure had a photonic band gab in the microwave regime and was fabricated by drilling holes at three different angles into a suitable transparent material. Yablonovitch further commented that his structure could readily be scaled down by using state-of-the-art reactive ion etching, resulting in a band gap near-visible frequencies [49]. The first photonic crystal exhibiting a band gap in the near visible spectrum was, however, based on a two-dimensional crystal, due to the difficulties of scaling down three-dimensional structures to the nanoscale. The crystal was based on a hexagonal array of air holes etched into SiO_2 using electron-beam lithography and reactive ion etching [50]. Although three-dimensional photonic crystals have since been fabricated in a variety of lattices [51], it is the two-dimensional versions or varieties thereof that see the most success [43, 45]. In fact, the first three-dimensional photonic crystal fabricated on the micrometer scale was the woodpile crystal, which is essentially fabricated one two-dimensional layer at a time, by iteratively depositing and etching silicon, lending from the decades worth of expertise with top down methods acquired in the research and fabrication of electronic chips [43, 45, 52, 53].

Today, photonic crystals are still the subject of major research, yet they have also become the major component in a variety of industries, perhaps the most prominent example being the photonic crystal fibre (PCF), the first of which was fabricated by Phillip Russel and his team in the 1990s [45, 54]. These structures, capable of acting as waveguides, can be created by melting thin glass capillaries together, leaving air gaps in between resulting in a two-dimensional photonic crystal in the plane perpendicular to the length of the fibre. By introducing a defect in the center, either air or just a massive rod of glass, the periodicity of the photonic crystal plane is interrupted, allowing light of specific frequencies to be trapped [54]. The fabrication procedure also allows for one or more of the constituent capillaries to be doped, making it possible to have gain or even creating laser fibers [44, 54]. Two types of PCF, referred to as solid-core and hollow-core fibers, see a wide variety of purposes, with the most mature product being the solid-core [44]. An example are telecommunications, where solid-core PCF has two distinct advantages over the traditional waveguide using a high-index core surrounded by a low index cladding where the light is trapped using total internal reflection [44]. First, the freedom to engineer the zero point for chromatic dispersion is better, making it possible to tailor the PCF for the specific need, and secondly because the structure is single mode for a larger span of frequencies, removing modal dispersion. [54]

The hollow-core PCF has the advantage that large intensities of light can be confined in the fibre without damaging the guiding core, allowing products such as high effect fibre lasers. Furthermore, if the interface between the hollow-core and surrounding glass can be made smooth enough, the hollow-core PCF promises outstandingly low attenuation lengths, again an interesting parameter for telecommunications as it would allow for an increased distance between repeaters. [44, 54, 55]

1.1 The Aim of the Project

The focus of this project is to develop passive optical components based on photonic crystals that can be used to manipulate terahertz radiation. Specifically, one- and two-dimensional photonic crystals will be modelled, fabricated and characterised. The one-dimensional photonic crystals will be all-silicon, sub-wavelength gratings that exploit Fano resonances to create low-loss spectral-specific reflectors. Using the models established in the later sections, the dimensions of the structures will be optimised for resonances in the frequency range 0.1-3.0 terahertz.

The two-dimensional photonic crystals will be based on both hexagonal and quadratic arrays of circular shapes. Specifically, structures consisting of silicon rods standing on a thin silicon substrate as well as air holes in a silicon wafer will be fabricated. The structures will be tailored, within the limitations set by the available equipment, such that their primary band gap lies in the lower end of the terahertz spectrum. Line defects will be introduced to the various two-dimensional photonic crystals, investigating the possibility of using the design to guide frequencies inside the band gap. Furthermore, point defects will be introduced to samples based on silicon rods, such that the associated cavity modes can be explored.

2 | Theory

This chapter will cover some of the fundamental equations in electromagnetism, laying the foundation for the models that will be derived in the following sections. Using assumptions suitable for the topics covered in this project, the general Maxwell equations will be simplified and rewritten to their frequency-dependent form. From these, the wave equations will be derived and the nature and general features explored. Building upon these equations, the expected solutions in a periodic dielectric medium will be investigated, laying the foundation for the following sections where models for periodic materials in one and two dimensions are established. Specifically, the plane wave expansions (PWE) method is introduced and used to calculate the band structures of infinitely extending one- and two-dimensional photonic crystals. Thereafter, the Fourier Modal Method (FMM) is presented, which will be used to model the transmittance spectra of two-dimensional, but layer-wise one-dimensional periodic structures. Finally, the method of Fast Fourier Transform (FFT) is introduced, and used to calculate the band structure of photonic crystals with defects.

2.1 Maxwell's Equations

The macroscopic Maxwell equations account for all free charges and currents. On differential form they are given as

$$\nabla \cdot \mathbf{B}(\mathbf{r}, t) = 0, \tag{2.1}$$

$$\nabla \cdot \mathbf{D}(\mathbf{r}, t) = \rho_F(\mathbf{r}, t), \tag{2.2}$$

$$\nabla \times \mathbf{H}(\mathbf{r}, t) = \mathbf{J}_F(\mathbf{r}, t) + \frac{\partial}{\partial t}\mathbf{D}(\mathbf{r}, t), \tag{2.3}$$

$$\nabla \times \mathbf{E}(\mathbf{r}, t) = -\frac{\partial}{\partial t}\mathbf{B}(\mathbf{r}, t). \tag{2.4}$$

These equations relate the four fields, the displacement field $\mathbf{D}(\mathbf{r}, t)$, electric field $\mathbf{E}(\mathbf{r}, t)$, magnetic field $\mathbf{H}(\mathbf{r}, t)$, and the magnetic induction field $\mathbf{B}(\mathbf{r}, t)$, to the sources, being the free charge and current density, $\rho_F(\mathbf{r}, t)$ and $\mathbf{J}_F(\mathbf{r}, t)$, and the changes in the fields. [43, 56] The magnetic field is defined from the magnetic induction field and the response from the medium in the form of the magnetisation,

$$\mathbf{H}(\mathbf{r}, t) = \frac{\mathbf{B}(\mathbf{r}, t)}{\mu_0} - \mathbf{M}(\mathbf{r}, t). \tag{2.5}$$

For the problems considered in this project, it is reasonable to ignore this medium response as they are non-magnetic, such that eq. (2.5) simplifies to $\mathbf{B}(\mathbf{r}, t) = \mu_0 \mathbf{H}(\mathbf{r}, t)$ [43]. The displacement field $\mathbf{D}(\mathbf{r}, t)$ is defined by the electric field and the material response in the form of the

polarisation as

$$\mathbf{D}(\mathbf{r},t) = \varepsilon_0 \mathbf{E}(\mathbf{r},t) + \mathbf{P}(\mathbf{r},t). \tag{2.6}$$

Generally speaking, the displacement field and the electric field do not need to be parallel, which can be seen from the definition of $\mathbf{P}(\mathbf{r},t)$ [57]

$$\frac{P_i(\mathbf{r},t)}{\varepsilon_0} = \sum_j \chi^{(1)}_{i,j}(\mathbf{r},t) E_j(\mathbf{r},t) + \sum_{j,n} \chi^{(2)}_{i,j,n}(\mathbf{r},t) E_j(\mathbf{r},t) E_n(\mathbf{r},t) + ..., \tag{2.7}$$

where P_i is a given component of $\mathbf{P}$ and $\chi^{(n)}$ is the n'th order electric susceptibility. Assuming isotropic, linear media, all but the first term on the right-hand side of eq. (2.7) disappear and $\chi^{(1)}$ becomes a diagonal matrix with one unique entry and the equation therefore simplifies to

$$\mathbf{P}(\mathbf{r},t) = \varepsilon_0 \chi^{(1)}(\mathbf{r}) \mathbf{E}(\mathbf{r},t), \tag{2.8}$$

where the time dependence of $\chi^{(1)}$ has been dropped, corresponding to the material polarising instantaneously. Inserting eq. (2.8) in eq. (2.6) results in the following relation

$$\mathbf{D}(\mathbf{r},t) = \varepsilon_0 \left[1 + \chi^{(1)}(\mathbf{r})\right] \mathbf{E}(\mathbf{r},t) = \varepsilon_0 \varepsilon(\mathbf{r}) \mathbf{E}(\mathbf{r},t), \tag{2.9}$$

where ε is the relative permittivity of the material, which is used to form the material permittivity $\epsilon(\mathbf{r}) = \varepsilon(\mathbf{r})\varepsilon_0$ [56]. Finally, the fact that Maxwell's equations are separable allows the spatial and temporal parts for each plane wave of the field to be separated, as shown in [43],

$$\mathbf{H}(\mathbf{r},t) = \mathrm{Re}\{\mathbf{H}(\mathbf{r}) e^{-i\omega t}\}, \tag{2.10}$$

$$\mathbf{E}(\mathbf{r},t) = \mathrm{Re}\{\mathbf{E}(\mathbf{r}) e^{-i\omega t}\}, \tag{2.11}$$

known as a harmonic mode. This is allowed because Fourier analysis shows that any time dependence can be formed by a suitable sum over harmonic modes with varying frequency dependence [43]. With these assumptions and modifications, the Maxwell equations in frequency domain take the form

$$\nabla \times \mathbf{E}(\mathbf{r},\omega) = i\omega\mu_0 \mathbf{H}(\mathbf{r},\omega), \tag{2.12}$$

$$\nabla \times \mathbf{H}(\mathbf{r},\omega) = \mathbf{J}_F(\mathbf{r},\omega) - i\omega\varepsilon_0 \varepsilon(\mathbf{r},\omega) \mathbf{E}(\mathbf{r},\omega), \tag{2.13}$$

$$\nabla \cdot [\varepsilon_0 \varepsilon(\mathbf{r},\omega) \mathbf{E}(\mathbf{r},\omega)] = \rho_F(\mathbf{r},\omega), \tag{2.14}$$

$$\nabla \cdot \mu_0 \mathbf{H}(\mathbf{r},\omega) = 0. \tag{2.15}$$

2.1.1 Wave Equations

From the Maxwell equations in frequency domain, it is straightforward to formulate wave equations for both the electric and magnetic fields. Taking the curl of eq. (2.12) and inserting eq. (2.13)

$$\nabla \times \nabla \times \mathbf{E}(\mathbf{r},\omega) = i\omega\mu_0 \left[\mathbf{J}_F(\mathbf{r},\omega) - i\omega\varepsilon_0 \varepsilon(\mathbf{r},\omega) \mathbf{E}(\mathbf{r},\omega)\right]. \tag{2.16}$$

Utilizing that $\nabla \times \nabla \times = -\nabla^2 + \nabla\nabla\cdot$, and setting the free current density to zero results in

$$\left(-\nabla^2 + \nabla\nabla\cdot\right) \mathbf{E}(\mathbf{r},\omega) = \omega^2 \mu_0 \varepsilon_0 \varepsilon(\mathbf{r},\omega) \mathbf{E}(\mathbf{r},\omega). \tag{2.17}$$

Equation (2.17) will be used to tackle problems where $\mathbf{E}(\mathbf{r}) = \hat{\mathbf{z}}E(x,y)$, which is a divergence less field, and therefore the equation reduces to

$$\left(\nabla^2 + k_0^2\varepsilon(\mathbf{r},\omega)\right)\mathbf{E}(\mathbf{r},\omega) = 0, \tag{2.18}$$

with $k_0^2 = \omega^2\mu_0\varepsilon_0$. To get a wave equation for the magnetic field, eq. (2.13) is divided by $\varepsilon(\mathbf{r},\omega)$, $\mathbf{J}_F$ is set to zero and the curl is taken, after which eq. (2.12) is inserted on the right-hand side resulting in

$$\nabla \times \frac{1}{\varepsilon(\mathbf{r},\omega)}\nabla \times \mathbf{H}(\mathbf{r},\omega) = k_0^2\mathbf{H}(\mathbf{r},\omega). \tag{2.19}$$

Moving forward, the frequency dependence of $\varepsilon(\mathbf{r})$ and $\mathbf{H}(\mathbf{r})$ is implicit. In fact, for all of the structures modelled in this project, ε will be treated independently of ω. If the dielectric function is independent of position eq. (2.19) becomes

$$\left(\nabla^2 + k_0^2\varepsilon\right)\mathbf{H}(\mathbf{r},\omega) = 0. \tag{2.20}$$

Equation (2.19) is an eigenvalue problem, with the linear operator $\hat{\Theta} = \nabla \times \frac{1}{\varepsilon(\mathbf{r})}\nabla\times$, which means that linear combinations of eigenvectors, with the same frequency, are also solutions to eq. (2.19), e.g., given the eigenvectors $\mathbf{H}_1(\mathbf{r})$ and $\mathbf{H}_2(\mathbf{r})$ the linear combination

$$\hat{\Theta}\left(\alpha\mathbf{H}_1(\mathbf{r}) + \beta\mathbf{H}_2(\mathbf{r})\right) = k_0^2\left(\alpha\mathbf{H}_1(\mathbf{r}) + \beta\mathbf{H}_2(\mathbf{r})\right), \tag{2.21}$$

where α and β are some arbitrary coefficients, is also a solution. This has the direct consequence that a given eigenvector can be scaled by any constant, and still have the same eigenvalue which gives the freedom to normalise obtained solutions, i.e., requiring that the inner product equals unity,

$$\langle\mathbf{H}(\mathbf{r})|\mathbf{H}(\mathbf{r})\rangle = \int \mathbf{H}(\mathbf{r})^*\mathbf{H}(\mathbf{r})d^3r = 1. \tag{2.22}$$

This is convenient in some cases, however, if the physical energy of the field is of interest and not just its spatial profile, the overall multiplier is important. [43] The fact that the operator, $\hat{\Theta}$, in eq. (2.19) is a Hermitian operator also means that the eigenvalues are real and the eigenvectors of non-degenerate frequencies are orthogonal. A Hermitian operator, $\hat{\Xi}$, satisfies

$$\langle\mathbf{F}|\hat{\Xi}|\mathbf{G}\rangle = \langle\hat{\Xi}\mathbf{F}|\mathbf{G}\rangle. \tag{2.23}$$

Note that for any operator it applies that $\langle\mathbf{F}|\hat{\mathbf{O}}|\mathbf{G}\rangle = \langle\hat{\mathbf{O}}\mathbf{G}|\mathbf{F}\rangle^*$. To show that $\hat{\Theta}$ is a Hermitian operator, the following vector identity is applied, $\mathbf{B}\cdot(\nabla\times\mathbf{A}) = \nabla\cdot(\mathbf{A}\times\mathbf{B}) + \mathbf{A}\cdot(\nabla\times\mathbf{B})$,

$$\begin{aligned}\int \mathbf{F}^*\cdot\nabla\times\left(\frac{1}{\varepsilon(\mathbf{r})}\nabla\times\mathbf{G}\right)d^3r \\ = \int\left\{\nabla\cdot\left[\left(\frac{1}{\varepsilon(\mathbf{r})}\nabla\times\mathbf{G}\right)\times\mathbf{F}^*\right] + (\nabla\times\mathbf{F}^*)\cdot\left(\frac{1}{\varepsilon(\mathbf{r})}\nabla\times\mathbf{G}\right)\right\}d^3r.\end{aligned} \tag{2.24}$$

Applying the divergence theorem, $\int_V(\nabla\cdot\mathbf{F})\,dV = \oint_S(\mathbf{F}\cdot\hat{\mathbf{n}})\,dS$, to the first term on the right-hand side it disappears in the cases where the field goes to zero at infinity, or when the fields are periodic in the region of integration, which are the only scenarios of interest [43,56]. Because the dot product commutes, the order of the last term on the right hand side can be interchanged, and by reapplying the vector identity and the divergence theorem the result is

$$\int(\nabla\times\mathbf{G})\cdot\left(\frac{1}{\varepsilon(\mathbf{r})}\nabla\times\mathbf{F}^*\right)d^3r = \int\mathbf{G}\cdot\nabla\times\frac{1}{\varepsilon(\mathbf{r})}\nabla\times\mathbf{F}^*d^3r = \langle\hat{\Theta}\mathbf{F}|\mathbf{G}\rangle, \tag{2.25}$$

and as such $\hat{\Theta}$ is a Hermitian operator. To show that the hermicity of $\hat{\Theta}$ entails real eigenvalues is straightforward, simply take the inner product of $\mathbf{H}(\mathbf{r})$ with eq. (2.19)

$$\langle \mathbf{H}(\mathbf{r})|\hat{\Theta}|\mathbf{H}(\mathbf{r})\rangle = k_0^2\langle \mathbf{H}(\mathbf{r})|\mathbf{H}(\mathbf{r})\rangle, \tag{2.26}$$

after which both sides of the equation are conjugated

$$\langle \mathbf{H}(\mathbf{r})|\hat{\Theta}|\mathbf{H}(\mathbf{r})\rangle^* = \langle \hat{\Theta}\mathbf{H}(\mathbf{r})||\mathbf{H}(\mathbf{r})\rangle \Rightarrow ({k_0}^2)^* = k_0^2, \tag{2.27}$$

where it is used that the inner product is always real and positive. However, what is usually of interest is k_0, and not k_0^2. The condition above only requires k_0 to be completely real or completely imaginary. Provided that $\varepsilon(\mathbf{r}) > 0$, it is easy to show that k_0 is in fact real, and thus that k_0^2 is positive. To do this, the same procedure used to show that $\hat{\Theta}$ is Hermitian, eq. (2.24), is repeated with $\mathbf{F}, \mathbf{G} = \mathbf{H}(\mathbf{r})$, resulting in

$$\langle \mathbf{H}(\mathbf{r})|\hat{\Theta}|\mathbf{H}(\mathbf{r})\rangle = k_0^2\langle \mathbf{H}(\mathbf{r})|\mathbf{H}(\mathbf{r})\rangle = \int \frac{1}{\varepsilon(\mathbf{r})}|\nabla \times \mathbf{H}(\mathbf{r})|^2 d^3r. \tag{2.28}$$

If k_0 is imaginary while $\varepsilon(\mathbf{r})$ is positive, then eq. (2.28) is a contradiction, thus k_0 is real and positive. That the hermicity of $\hat{\Theta}$ causes the harmonic modes of differing frequency, $\mathbf{H}(\mathbf{r}, \omega_1)$ and $\mathbf{H}(\mathbf{r}, \omega_2)$, to be orthogonal follows straight from the property that $\langle \mathbf{H}_1(\mathbf{r}, \omega_1)|\hat{\Theta}|\mathbf{H}_2(\mathbf{r}, \omega_2)\rangle = \langle \hat{\Theta}\mathbf{H}_1(\mathbf{r}, \omega)|\mathbf{H}_2(\mathbf{r}, \omega_2)\rangle$ which implies that

$$\left(k_{0,1}^2 - k_{0,2}^2\right)\langle \mathbf{H}_1(\mathbf{r}, \omega_1)|\mathbf{H}_2(\mathbf{r}, \omega_2)\rangle = 0, \tag{2.29}$$

which is only true if the two eigenmodes are orthogonal. These properties of the operator will be used repeatedly in the coming section.

2.2 Solutions in Photonic Crystals

The following section draws inspiration from *Photonic Crystals Molding the Flow of Light* by *John D.* [43].

Before proceeding with the derivation of the various methods used to model photonic crystals, it is advantageous to discuss the attributes of such structures. As mentioned in the introduction, photonic crystals are structures where the dielectric function is periodic in one, two, or three dimensions. This periodicity results in band structures and band gaps for electromagnetic radiation in the same way that the periodic potential of a regular crystal results in electronic band structures. Inside of these band gaps, there is no combination of frequency and wave vector that can support a propagating mode, and incident radiation with these combinations is therefore reflected. The immediate difference between the two crystal types is the distance between their unit cells. The periodicity of regular crystals comes from the ordered crystal lattice where the magnitude of their translational vectors, vectors that move the observer to an indistinguishable position in the lattice, are on the order of a couple of angstroms, which is on the same order of magnitude as the wavelength of electrons in crystals [58, 59]. On the other hand, the length of the translational vectors for photonic crystals is comparable to the wavelength of the light for which there should be a band gap. [43, 58]
A one-dimensional photonic crystal is a multilayered stack, where two or more dielectric materials are repeated. Two- and three-dimensional photonic crystals can be made by introducing structures such as rods or holes repeated periodically, with the periodicity spanning the nanometer to millimeter scale, with the larger scale exhibiting control of the microwave spectrum, and the smaller scale controlling the visible spectrum [44]. By breaking the periodicity of the photonic crystal, which is done by introducing defects in the crystal, localised states are supported. These defects come in two forms, point defects, and line defects. For point defects the ordered crystal is changed at a single point, resulting in a cavity, in which localised modes with frequencies inside the band gap are supported, with their field decaying exponentially away from the defect. For line defects, the crystal order is perturbed along a line through the crystal. Similar results occur, where light with frequencies inside the gap is supported inside the defect, with their field strength decaying exponentially away from the defect. It is therefore possible to create waveguides by introducing line defects into a photonic crystal and spectral-specific transmitters based on point defects. [43]

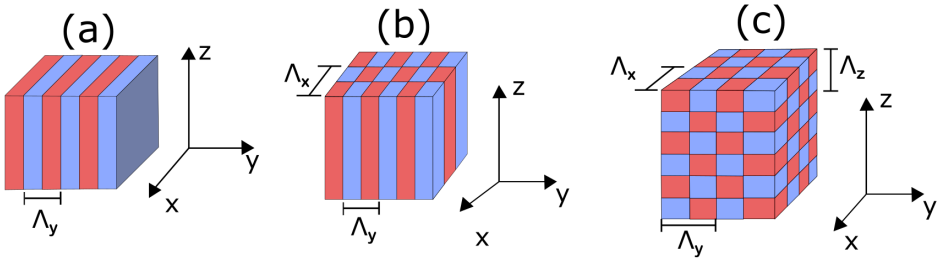

Figure 2.1: Sketches one-, two-, and three-dimensional photonic crystals.

To determine what sort of solutions are expected for eq. (2.19) in a region where the dielectric function is periodic a one- or two-dimensional photonic crystal can be considered. Here, at least one direction is completely translational invariant, e.g., the z-direction, such that any shift of

the structure in this direction leaves the system unchanged, as is the case for fig. 2.1(**a**) and fig. 2.1(**b**). This can be described by introducing a translational operator, $\hat{T}_{\mathbf{z},d}$, such that

$$\hat{T}_{\mathbf{z},d}\varepsilon(\mathbf{r}) = \varepsilon(\mathbf{r} + \hat{\mathbf{z}}d) = \varepsilon(\mathbf{r}), \qquad d \in \mathbb{R}. \tag{2.30}$$

Because the two positions in the system are identical, it should not matter if the system is shifted by $\hat{T}_{\mathbf{z},d}$ first, and then $\hat{\Theta}$ is applied or the other way around. This means that the two operators must commute,

$$\left[\hat{T}_{\mathbf{z},d}, \hat{\Theta}\right]\mathbf{H}(\mathbf{r}) = \left(\hat{T}_{\mathbf{z},d}\hat{\Theta} - \hat{\Theta}\hat{T}_{\mathbf{z},d}\right)\mathbf{H}(\mathbf{r}) = 0. \tag{2.31}$$

There is more than one way for this to be true. When $\hat{\Theta}$ acts on $\mathbf{H}(\mathbf{r})$ it returns the eigenvalue $\left(\frac{\omega}{c}\right)^2$. If the field $\mathbf{H}(\mathbf{r})$ does not depend on z, the operator $\hat{T}_{\mathbf{z},d}$ does nothing, and the operators therefore obviously commute. A more interesting possibility is that $\mathbf{H}(\mathbf{r})$ does depend on z, and is a simultaneous eigenfunction of $\hat{\Theta}$ and $\hat{T}_{\mathbf{z},d}$.
Let the field be polarised along $\hat{\mathbf{x}}$ and propagating in the zy-plane of the one-dimensional photonic crystal depicted in fig. 2.1 (**a**). A z-dependence that is an eigenfuntion of all $\hat{T}_{\mathbf{z},d}$ is $e^{ik_z z}$, with the limitation that because the system extends infinitely in all directions, k_z must be a real number such that the field is finite. Hence $\mathbf{H}(\mathbf{r})$ will be an eigenfunction to $\hat{T}_{\mathbf{z},d}$ with the eigenvalue $e^{ik_z d}$ which would make eq. (2.31) straightforward. In the y-direction the photonic crystal has discrete translational symmetry, such that

$$\hat{T}_{\mathbf{R}_y}\varepsilon(\mathbf{r}) = \varepsilon(\mathbf{r} + \mathbf{R}_y) = \varepsilon(\mathbf{r}), \tag{2.32}$$

with $\mathbf{R}_y = \hat{\mathbf{y}}\Lambda_y h$, where Λ_y is a primitive lattice vector and h is an integer. Following the same line of thought as previously, it is required that $\hat{T}_{\mathbf{R}_y}$ commutes with $\hat{\Theta}$, which can again be solved by the eigenfunctions being on the form $e^{ik_y y}$, such that

$$\hat{T}_{\mathbf{R}_y}e^{ik_y y} = e^{ik_y \Lambda_y h}e^{ik_y y}. \tag{2.33}$$

Unlike the directions with continuous translational symmetry, not all values of k_y lead to different eigenvalues. It is easily determined that $k_y + \frac{2\pi}{\Lambda_y}m, \quad m \in \mathbb{Z}$, form a degenerate set. This value that can be added freely to k_y is called the reciprocal lattice vector, $|\mathbf{b}_y| = \frac{2\pi}{\Lambda_y}$. In the same way that the lattice vectors move the observer to an equivalent point in the lattice, so does the reciprocal lattice vector b_y move the wave vector k_y to an equivalent point in reciprocal space. Thus, when determining the supported eigenvalues in the structure, there is no reason to investigate wave vectors outside the span $-\frac{\pi}{\Lambda_y} < k_y \leq \frac{\pi}{\Lambda_y}$.

Using that the operator $\hat{\Theta}$ is linear and commutes with $\hat{T}_{\mathbf{z},d}$ and $\hat{T}_{\mathbf{R}_y}$, $\mathbf{H}(\mathbf{r})$ can be constructed as a linear combination over the wave vectors

$$\mathbf{H}_{k_z,k_y}(\mathbf{r}) = \hat{\mathbf{x}}e^{ik_z z}\sum_m c_{k_y,m}e^{i(k_y+b_y m)y} = \hat{\mathbf{x}}e^{ik_z z}e^{ik_y y}\sum_m c_{k_y,m}e^{ib_y m y} = \hat{\mathbf{x}}e^{ik_z z}e^{ik_y y}u_{k_y}(y), \tag{2.34}$$

where u_{k_y} is a periodic function with the same periodicity as the photonic crystal, and the wave vectors have been used to index the given eigenvector. Thus, the dependence in the periodic direction has the form of a plane wave multiplied by a periodic function. This result extends to two- and three-dimensional crystals and is known as Bloch's theorem, which states that the solution to the wave equation in a periodic medium will be on the form of a plane wave multiplied by a periodic function [58, 60]

$$\mathbf{H}_{\mathbf{k}}(\mathbf{r}) = e^{i\mathbf{k}\cdot\mathbf{r}}\mathbf{u}_{\mathbf{k}}(\mathbf{r}). \tag{2.35}$$

This theorem will be used to find the band structures of one and two-dimensional photonic crystals.

2.3 Plane Wave Expansion

In this section, the band structure for various photonic crystals is calculated based on the PWE method in one and two dimensions. In one dimension, on- and off-axis propagation is considered, while only in-plane propagation is used in the two-dimensional case. The goal is to determine photonic crystals which exhibit band gaps that can be used for practical applications in the terahertz regime, such as spectral-specific reflectors or waveguides, and can be fabricated by this project group. The following subsection derives the PWE method for one-dimensional photonic crystals.

2.3.1 One-Dimensional Photonic Crystals

Given a one-dimensional photonic crystal that is periodic in the y-direction, fig. 2.1, the field can in accordance with Bloch's theorem be given as

$$\mathbf{H}_{\mathbf{k}}(\mathbf{r}) = \mathbf{H}_{k_x,k_y}(x,y) = \hat{\mathbf{z}} e^{i(k_x x + k_y y)} \sum_n C_n e^{iG_n y}, \qquad G_n = \frac{2\pi}{\Lambda_y} n, \tag{2.36}$$

with Λ_y being the period along y. Inserting this field into eq. (2.19) results in

$$\hat{\Theta}\mathbf{H}_{k_x,k_y}(x,y) = \nabla \times \frac{1}{\varepsilon(y)} \nabla \times \mathbf{H}_{k_x,k_y}(x,y) = k_0^2 \mathbf{H}_{k_x,k_y}(x,y). \tag{2.37}$$

The dielectric function is periodic with the lattice, which can be described by a Fourier series. However, because it is the reciprocal of the dielectric function that enters in eq. (2.37) it is convenient to instead define

$$\frac{1}{\varepsilon(y)} = \eta(y) = \sum_m \eta_m e^{iG_m y}, \qquad G_m = \frac{2\pi}{\Lambda_y} m. \tag{2.38}$$

The coefficients $\eta_{m'}$ are determined by

$$\eta_{m'} = \frac{1}{\Lambda_y} \int_0^{\Lambda_y} \eta(y) e^{-iG_{m'} y} dy = \frac{1}{\Lambda_y} \int_0^{\Lambda_y} \frac{1}{\varepsilon(y)} e^{-iG_{m'} y} dy. \tag{2.39}$$

Inserting eq. (2.38) and eq. (2.36) in eq. (2.37) gives

$$\nabla \times \left[\sum_m \eta_m e^{iG_m y} \nabla \times \left(\hat{\mathbf{z}} e^{i(k_x x + k_y y)} \sum_n C_n e^{iG_n y} \right) \right] = \hat{\mathbf{z}} k_0^2 e^{i(k_x x + k_y y)} \sum_{n'} C_{n'} e^{iG_{n'} y} \tag{2.40}$$

Taking the first curl

$$\nabla \times \left[\sum_m \eta_m e^{iG_m y} e^{(ik_x x + k_y y)} \sum_n C_n e^{iG_n y} i \left(\hat{\mathbf{x}}(k_y + G_n) - \hat{\mathbf{y}} k_x \right) \right] = \hat{\mathbf{z}} k_0^2 e^{i(k_x x + k_y y)} \sum_{n'} C_{n'} e^{iG_{n'} y}. \tag{2.41}$$

Proceeding and taking the second curl results in

$$\hat{\mathbf{z}} e^{i(k_x x + k_y y)} \sum_m \sum_n \eta_m C_n e^{i(G_n + G_m) y} \left(k_x^2 + (k_y + G_n)(k_y + G_n + G_m) \right) = \hat{\mathbf{z}} k_0^2 e^{i(k_x x + k_y y)} \sum_{n'} C_{n'} e^{iG_{n'} y}. \tag{2.42}$$

It can be seen that $\hat{\mathbf{z}}e^{i(k_x x+k_y y)}$ can be divided out of the equation. Additionally, introducing $n' = m + n$, eq. (2.42) becomes

$$\sum_{n'} e^{iG_{n'}y}\left[\sum_{n}\eta_{n'-n}C_n\left(k_x^2+(k_y+G_n)(k_y+G_{n'})\right)-k_0^2C_{n'}\right]=0. \tag{2.43}$$

This equation must be satisfied for all values of y, which means that everything inside the square brackets must equal 0,

$$\sum_{n}\eta_{n'-n}C_n\left(k_x^2+(k_y+G_n)(k_y+G_{n'})\right)-k_0^2C_{n'}=0. \tag{2.44}$$

Equation (2.44) contains an infinite sum, and is itself one of an infinite amount of equations, corresponding to all the possible n'. To handle these equations numerically it is necessary to truncate these summations, such that $-N \leq n \leq N$. By doing this, eq. (2.44) can be written as a matrix equation

$$\begin{bmatrix}\eta_0 & \eta_{-1} & \cdots & \eta_{-2N}\\ \eta_1 & \eta_0 & \cdots & \eta_{-2N+1}\\ \vdots & \vdots & \ddots & \vdots\\ \eta_{2N} & \eta_{2N-1} & \cdots & \eta_0\end{bmatrix}\odot\left(k_x^2\bar{\bar{\mathbf{J}}}_{2N+1}+\begin{bmatrix}(k_y-NG)\\(k_y-(N-1)G)\\\vdots\\(k_y+NG)\end{bmatrix}\otimes\begin{bmatrix}(k_y-NG)\\(k_y-(N-1)G)\\\vdots\\(k_y+NG)\end{bmatrix}\right)\begin{bmatrix}C_{-N}\\C_{-N+1}\\\vdots\\C_N\end{bmatrix}=k_0^2\begin{bmatrix}C_{-N}\\C_{-N+1}\\\vdots\\C_N\end{bmatrix}, \tag{2.45}$$

where $\odot$ refers to a Hadamard product and $\otimes$ refers to a tensor product, and $\mathbf{J}_{2N+1}$ refers to a matrix of all ones with size $[2N+1 \times 2N+1]$. This matrix equation can be solved by an eigensolver such as `eigs` in MATLAB, which returns the eigenvalues k_0^2 and the coefficients of the eigenmodes, C_i.

In fig. 2.2 the square root of the eigenvalues, k_0, is plotted against k_y for three different structures, determined by $\varepsilon(y)$, and with $k_x = 0$, meaning that the mode is only propagating in the y-direction. The plots are in dimensionless units of $k_0\Lambda/(2\pi)$, because the solutions are scalable [43, 44]. The solutions being scalable means that for a given set of materials, determining the values of $\varepsilon(\mathbf{r})$, it is possible to design general photonic crystals in terms of the periodicity Λ, and then choose Λ so that the band gaps lie in the frequency range of interest. For the same reason, the size of the band gap is not given by an absolute value, but rather as the gap-midgap (GMG) ratio in percent defined as

$$\text{GMG} = \frac{\Delta\omega}{\omega_m}, \tag{2.46}$$

where ω_m is the frequency in the middle of the gap, and $\Delta\omega$ is the width of the gap.
In fig. 2.2a, $\varepsilon(x) = 4$, meaning that there is no periodic structure. The result is therefore simply a light line given by the dispersion relation of light in a homogeneous medium, $\omega(k_y) = \frac{ck_y}{\sqrt{\varepsilon}}$, which is linear [43]. The *zig-zac* behaviour of the dispersion relation is a result of the periodicity enforced on the modes. When reaching the edge of the Brillouin zone, the line gets shifted by $\pm G_y$.
Figure 2.2b is the band structure of a dielectric slab, where each layer has the same physical

thickness, with $\varepsilon_1 = 1$ and $\varepsilon_2 = 1.3$. Again, it can be seen that when the lines reach the edges of the Brillouin zone, they are shifted by $\pm G_y$. However, now there are gaps apparent, as indicated by the red bars. Within these frequency ranges, there is no combination of k_y and k_0 which gives rise to a propagating mode. There can exist solutions in these regions, but their wave vector is complex, so they decrease exponentially inside the structure and are known as evanescent waves. [43]. The GMG ratio of the two band gaps is 8.3% and 0.85%. Increasing the difference between the dielectric constants by choosing $\varepsilon_2 = 4$, the GMG ratio changes to 37.7% and 18.4% for first and second band gap, respectively, shown in fig. 2.2c. Furthermore, the location of the band gap moves to lower frequencies. As is apparent in fig. 2.2, a given set of k_y and k_x can have more than one eigenvalue, and therefore eigenmode. Therefore, the band number, n, is used along with the wave vector to index a given solution.
Illuminating the same structure as fig. 2.2c with a plane wave propagating in the y-direction, total reflectance is expected for frequencies inside the band gap. This is confirmed by fig. 2.2d, where the transmittance as a function of frequency calculated using the one-dimensional Finite Element Method (FEM) for a 40-layer dielectric slab with the same parameters as fig. 2.2c is plotted. The red regions are given by the values determined in fig. 2.2c, and it can be seen that they correspond with the region where $T = 0$.

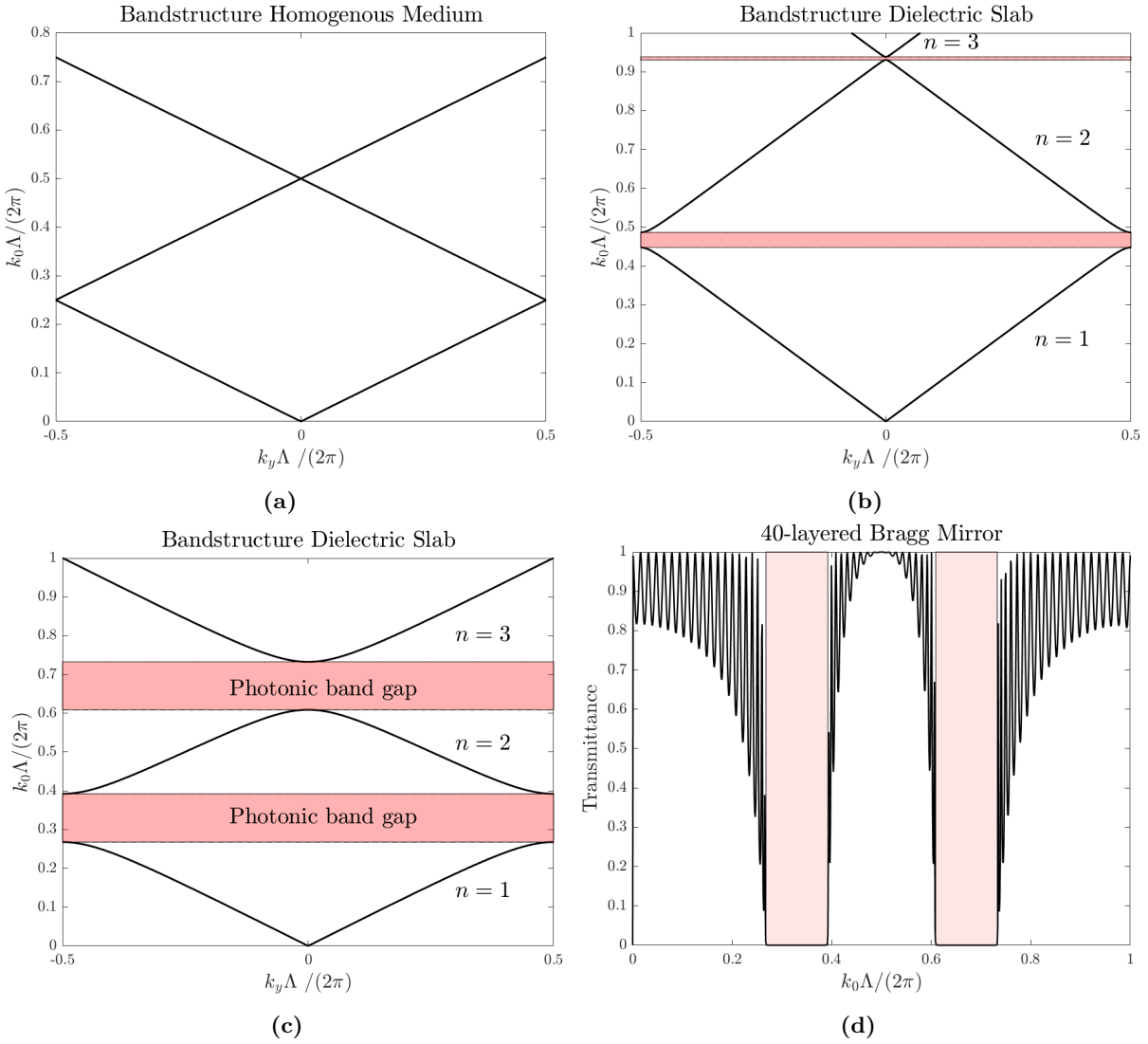

Figure 2.2: **(a)** - **(c)** Band structures, and **(d)** transmittance graph, of one-dimensional photonic crystals with layer thickness of $d_1 = d_2 = \frac{\Lambda_y}{2}$. **(a)** $\varepsilon_1 = \varepsilon_2 = 4$. **(b)** $\varepsilon_1 = 1$, $\varepsilon_2 = 1.3$. **(c)** $\varepsilon_1 = 1$, $\varepsilon_2 = 4$. **(d)** $\varepsilon_1 = 1$, $\varepsilon_2 = 4$ and 40 layers, 20 of each dielectric material.

The graphs in fig. 2.2 had $k_x = 0$, corresponding to on-axis propagation. By changing k_x the allowed modes in the structure change as well. This can be seen in fig. 2.3a, where the band structure of the dielectric slab from fig. 2.2c has been plotted with varying k_x and $k_y = \{0, \pi/2\}$. Between two corresponding black and red lines there is a region in which an allowed mode (combination of k_x, k_0) exists, with a given k_y in the range $0 \leq k_y \leq \pi/2$. These bands of allowed modes have been labeled with n's. The opposite is also true; in the region between these allowed bands, there are no propagating modes in the crystal. By stepping between the values $k_y = 0, \pi/2$, and calculating the band structure for each k_y, the allowed bands can easily be visualised. This is done in fig. 2.3b, where the allowed bands are blue, and bounded by red and black curves. It can be seen that the band diagram contains no actual band gaps; there are always combinations of k_y and k_x that lead to an allowed mode, for a given frequency k_0. In fig. 2.3b the dashed black line is the dispersion relation of a plane wave in a medium with a

refractive index of 1, such as air. Only modes at or above the light line can characterise plane waves propagating in air. Therefore, all the white regions above the light line correspond to incoming plane waves which would be completely reflected from the structure.

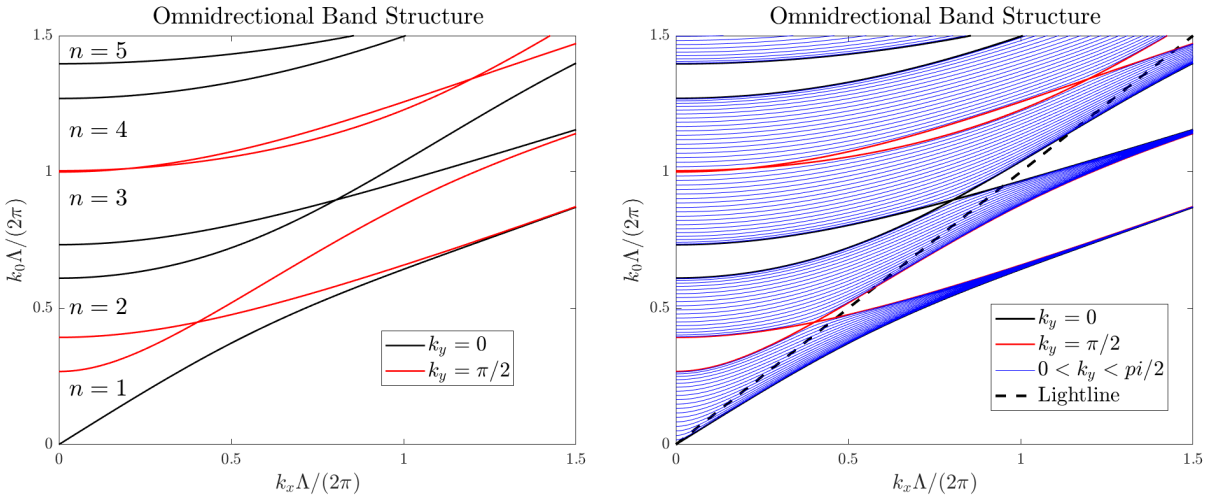

(a) **(b)**

Figure 2.3: Band structure of a photonic crystal, $d_a = d_b = \Lambda/2$ and $\varepsilon_1 = 1$, $\varepsilon_1 = 4$. **(a)** Plots the square root of the eigenvalues as a function of the off-axis wavenumber k_x for both $k_y = \{0, \pi/2\}$. **(b)** Plots the square root of the eigenvalues as a function of the off-axis wavenumber k_x with $k_y = (0, \pi/2)$.

2.3.2 Two-Dimensional Photonic Crystals

Given a two-dimensional photonic crystal where the dielectric function is periodic in two linearly independent directions in the xy plane but constant in the z-direction, the field can be categorised into two different polarisations, S and P, if it is only propagating in the periodic plane, that is $k_z = 0$. The P (S) polarisation has the magnetic field (electric field) perpendicular to the plane of propagation. Thus, for the P-polarisation the field can in accordance with Bloch's theorem be given as

$$\mathbf{H}(\mathbf{r}) = \hat{\mathbf{z}} e^{i(\mathbf{k}_\perp \cdot \mathbf{r}_\perp)} u(\mathbf{r}_\perp) = \hat{\mathbf{z}} e^{i(\mathbf{k}_\perp \cdot \mathbf{r}_\perp)} \sum_n C_n e^{i(\mathbf{G}_{\perp,n} \cdot \mathbf{r}_\perp)}, \tag{2.47}$$

where the $\perp$ symbol refers to (x,y)-coordinates and $\mathbf{G}_{\perp,n} = \mathbf{b}_1 n_1 + \mathbf{b}_2 n_2$. The summation over n is taken to mean all the sets of $\{n_1, n_2\}$, e.g., if the summation is truncated at $-N \leq n_i \leq N$ the amount of $\mathbf{G}_{\perp,n}$ vectors is $(2N+1)^2$. The reciprocal lattice vectors, $\mathbf{b}_1$, $\mathbf{b}_2$, are defined from the lattice vectors as,

$$\mathbf{b}_1 = \frac{2\pi}{\mathbf{a}_1 \cdot \bar{\bar{Q}}(\pi/2)\mathbf{a}_2} \bar{\bar{Q}}(\pi/2)\mathbf{a}_2, \tag{2.48}$$

$$\mathbf{b}_2 = \frac{2\pi}{\mathbf{a}_2 \cdot \bar{\bar{Q}}(\pi/2)\mathbf{a}_1} \bar{\bar{Q}}(\pi/2)\mathbf{a}_1, \tag{2.49}$$

which follows directly from the condition $\mathbf{b}_i \cdot \mathbf{a}_j = 2\pi\delta_{i,j}$ [58]. The matrix $\bar{\bar{Q}}(\theta)$ is the rotation matrix defined as

$$\bar{\bar{Q}}(\theta) = \begin{bmatrix} \cos(\theta) & -\sin(\theta) \\ \sin(\theta) & \cos(\theta). \end{bmatrix} \tag{2.50}$$

The reciprocal dielectric function is expanded as a Fourier series

$$\eta(\mathbf{r}_\perp) = \sum_m \eta_m e^{i(\mathbf{G}_{\perp,m}\cdot\mathbf{r}_\perp)}, \tag{2.51}$$

with

$$\eta_m = \frac{1}{\Lambda_x\Lambda_y}\int_0^{\Lambda_x}\int_0^{\Lambda_y}\frac{1}{\varepsilon(\mathbf{r}_\perp)}e^{i(\mathbf{G}_{\perp,m}\cdot\mathbf{r}_\perp)}dydx. \tag{2.52}$$

To ease the notation, the dot product is defined as $\mathbf{G}_{\perp,n}\cdot\mathbf{r}_\perp = G_{x,n}x + G_{y,n}y$, as opposed to the formally correct form of $\mathbf{G}_{\perp,n}\cdot\mathbf{r}_\perp = x(b_{1,x}n_1 + b_{2,x}n_2) + y(b_{1,y}n_1 + b_{2,y}n_2)$. In section 2.4 the effect of using the reciprocal dielectric function, $\eta(\mathbf{r}_\perp)$, instead of $\frac{1}{\varepsilon(\mathbf{r}_\perp)}$ will be discussed, based on the works of Lifeng Li [61]. For this chapter, it will suffice to test the convergence when using the two functions. Inserting eq. (2.47) and eq. (2.51) in eq. (2.19) and performing the first rotation results in

$$\begin{aligned}\nabla\times\left[\sum_m\sum_n \eta_m e^{i(\mathbf{G}_{\perp,m}\cdot\mathbf{r}_\perp)} i\left(\hat{\mathbf{x}}(k_y+G_{y,n}) - \hat{\mathbf{y}}(k_x+G_{x,n})\right) C_n e^{i(\mathbf{G}_{\perp,n}\cdot\mathbf{r}_\perp)} e^{i(\mathbf{k}_\perp\cdot\mathbf{r}_\perp)}\right] \\ = \hat{\mathbf{z}}k_0^2 e^{i(\mathbf{k}_\perp\cdot\mathbf{r}_\perp)}\sum_{n'} C_{n'}e^{i(\mathbf{G}_{\perp,n'}\cdot\mathbf{r}_\perp)}.\end{aligned} \tag{2.53}$$

Introducing $m+n=n'$, this expression simplifies to

$$\begin{aligned}\sum_{n'}\sum_n \eta_{n'-n}C_n\nabla\times\left[e^{(i\mathbf{G}_{\perp,n'}\cdot\mathbf{r}_\perp)} i\left(\hat{\mathbf{x}}(k_y+G_{y,n}) - \hat{\mathbf{y}}(k_x+G_{x,n})\right) e^{i(\mathbf{k}_\perp\cdot\mathbf{r}_\perp)}\right] \\ = \hat{\mathbf{z}}k_0^2 e^{i(\mathbf{k}_\perp\cdot\mathbf{r}_\perp)}\sum_{n'} C_{n'}e^{i(\mathbf{G}_{\perp,n'}\cdot\mathbf{r}_\perp)},\end{aligned} \tag{2.54}$$

which becomes

$$\begin{aligned}&\sum_{n'} e^{i(\mathbf{G}_{\perp,n'}\cdot\mathbf{r}_\perp)}e^{i(\mathbf{k}_\perp\cdot\mathbf{r}_\perp)} \\ &\quad\left[\sum_n \eta_{n'-n}C_n\left\{(k_x+G_{x,n})(k_x+G_{x,n'}) + (k_y+G_{y,n})(k_y+G_{y,n'})\right\} - C_{n'}k_0^2\right] = 0.\end{aligned} \tag{2.55}$$

This equation must hold for all values of $\mathbf{r}_\perp$, meaning that the terms in the square brackets must give 0,

$$\sum_n \eta_{n'-n}C_n\left\{(k_x+G_{x,n})(k_x+G_{x,n'}) + (k_y+G_{y,n})(k_y+G_{y,n'})\right\} = C_{n'}k_0^2. \tag{2.56}$$

On matrix form eq. (2.56) becomes

$$\begin{bmatrix} \eta_{0,0} & \eta_{-1,0} & \cdots & \eta_{-2N,-1} & \cdots & \eta_{-2N,-2N} \\ \eta_{1,0} & \eta_{0,0} & \cdots & \eta_{-2N+1,-1} & \cdots & \eta_{-2N+1,-2N} \\ \vdots & \vdots & \ddots & \vdots & \cdots & \vdots \\ \eta_{2N,1} & \eta_{2N-1,1} & \cdots & \eta_{0,0} & \cdots & \eta_{0,-2N+1} \\ \vdots & \vdots & \cdots & \vdots & \ddots & \vdots \\ \eta_{2N,2N} & \eta_{2N-1,2N} & \cdots & \eta_{0,2N-1} & \cdots & \eta_{0,0} \end{bmatrix}$$

$$\odot \left(\begin{bmatrix} k_x + G_{x,\{-N,-N\}} & k_y + G_{y,\{-N,-N\}} \\ k_x + G_{x,\{-N+1,-N\}} & k_y + G_{y,\{-N+1,-N\}} \\ \vdots & \vdots \\ k_x + G_{x,\{N,-N\}} & k_y + G_{y,\{N,-N\}} \\ k_x + G_{x,\{-N,-N+1\}} & k_y + G_{y,\{-N,-N+1\}} \\ \vdots & \vdots \\ k_x + G_{x,\{N,N\}} & k_y + G_{x,\{N,N\}} \end{bmatrix} \begin{bmatrix} k_x + G_{x,\{-N,-N\}} & k_y + G_{y,\{-N,-N\}} \\ k_x + G_{x,\{-N+1,-N\}} & k_y + G_{y,\{-N+1,-N\}} \\ \vdots & \vdots \\ k_x + G_{x,\{N,-N\}} & k_y + G_{y,\{N,-N\}} \\ k_x + G_{x,\{-N,-N+1\}} & k_y + G_{y,\{-N,-N+1\}} \\ \vdots & \vdots \\ k_x + G_{x,\{N,N\}} & k_y + G_{x,\{N,N\}} \end{bmatrix}^{\mathbf{T}} \right)$$

$$\begin{bmatrix} C_{\{-N,-N\}} \\ C_{\{-N+1,-N\}} \\ \vdots \\ C_{\{N,-N+1\}} \\ \vdots \\ C_{\{N,N\}} \end{bmatrix} = k_0^2 \begin{bmatrix} C_{\{-N,-N\}} \\ C_{\{-N+1,-N\}} \\ \vdots \\ C_{\{N,-N+1\}} \\ \vdots \\ C_{\{N,N\}} \end{bmatrix}, \quad (2.57)$$

where the specific set of n for a given η, G, and C has been explicitly stated. Similar calculations can be made for the S-polarisation using the wave equation from eq. (2.18), which results in

$$C_n \left[(k_x + G_{x,n})^2 + (k_y + G_{x,n})^2 \right] = C_{n'} k_0^2 \sum_n \varepsilon_{n'-n}. \quad (2.58)$$

2.3.3 Convergence

In this subsection, the convergence of the band structure based on the number of Fourier coefficients and choice of using η or ε will be tested. For all the following calculations in this subsection, the photonic crystal is a square lattice of air holes, with $n_{medium} = 3.4^2$, $n_{air} = 1$ and $r = 0.4\Lambda$. The solutions will be referred to as S_ε and S_η and likewise for the P-polarisation, with the understanding that in the case of S_η the used matrix is $\bar{\bar{\eta}}^{-1}$, and in the case of P_ε the used matrix is $\bar{\bar{\varepsilon}}^{-1}$. The convergence of S-polarised modes is seen in fig. 2.4, using N = 3, 6 and 9, corresponding to 49, 169, and 361 plane waves. It is seen that S_ε converges much faster than S_η. The same convergence test is performed for the P-polarisation, shown in fig. 2.5, and the result is the same. When using the η matrix, the convergence is significantly slower, while 361 plane waves are sufficient when using the ε matrix.

However, as S_ε (P_ε) and S_η (P_η) in principle should be identical, the number of plane waves used to calculate S_η (P_η) is increased, to test if it converges towards S_ε (P_ε). This is shown in fig. 2.6, where S_η and P_η are calculated with up to 2401 plane waves. While an increasing number

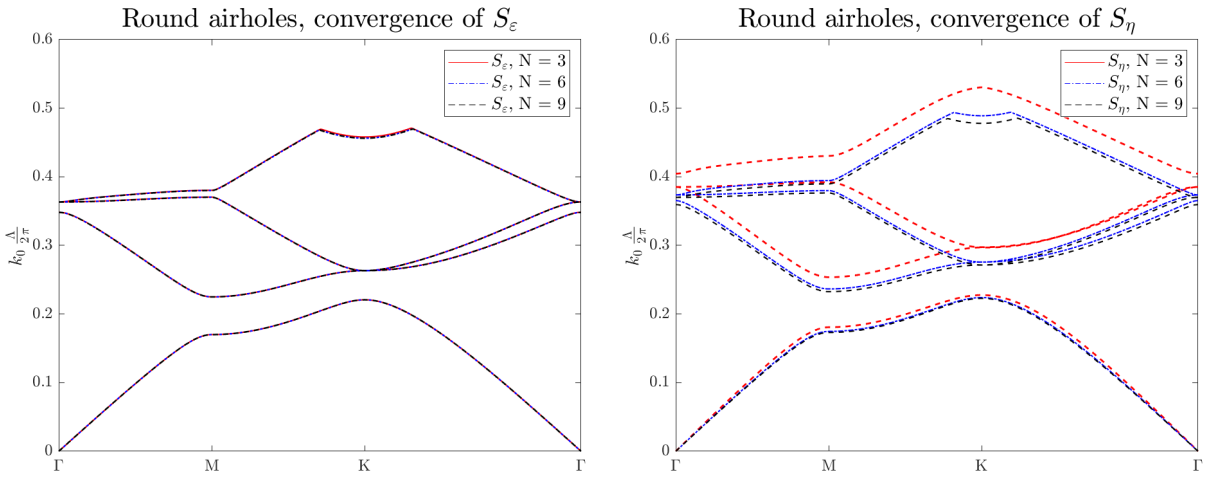

(a) **(b)**

Figure 2.4: Band diagram for S-polarised modes in a rectangular grid of air holes with $r = 0.4\Lambda$, $n_{medium} = 3.4^2$, $n_{air} = 1$. **(a)** Uses the $\bar{\bar{\varepsilon}}$ matrix. **(b)** Uses the $\bar{\bar{\eta}}^{-1}$ matrix.

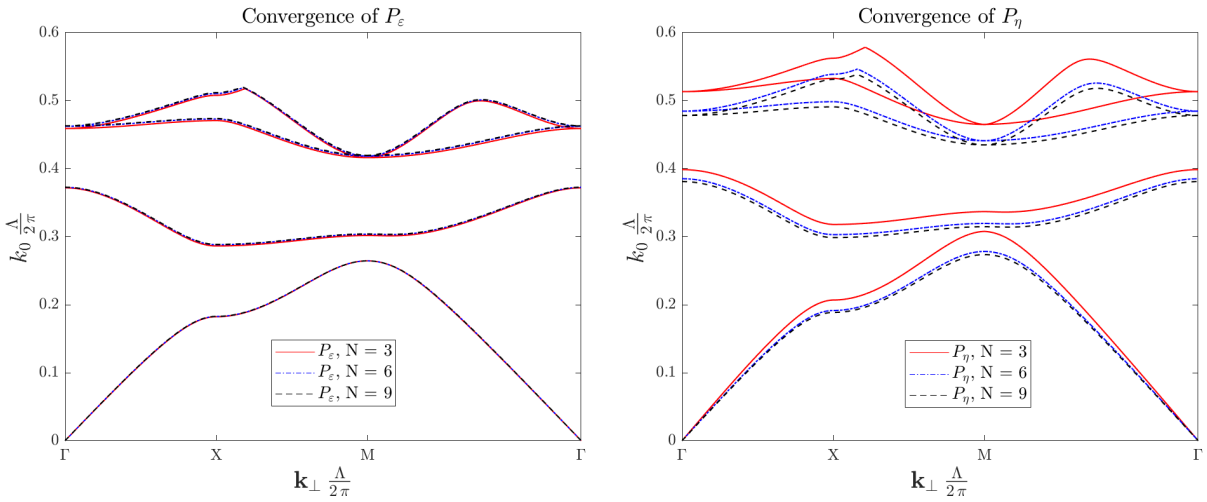

(a) **(b)**

Figure 2.5: Band diagram for P-polarised modes in a rectangular grid of air holes with $r = 0.4\Lambda$, $n_{medium} = 3.4^2$, $n_{air} = 1$. **(a)** Uses the $\bar{\bar{\varepsilon}}^{-1}$ matrix. **(b)** Uses the $\bar{\bar{\eta}}$ matrix.

of plane waves do make S_η (P_η) approach the result of S_ε (P_ε), it does so incredibly slowly. The cause of the slow convergence has been tackled by Lifeng Li [61], and will be discussed in greater depth in subsection 2.4.1. For now, the η matrix will be discarded, and all following band diagrams will only use the $\bar{\bar{\varepsilon}}$ matrix.

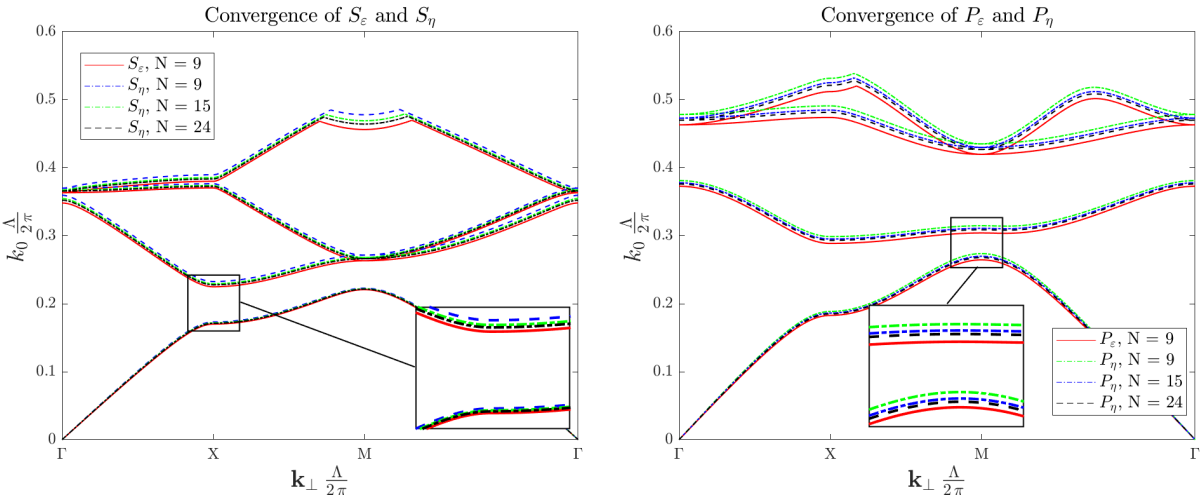

Figure 2.6: Band diagram for modes in a rectangular grid of air holes with $r = 0.4\Lambda$, $n_{medium} = 3.4^2$, $n_{air} = 1$, calculated using either the $\bar{\bar{\varepsilon}}$ or $\bar{\bar{\eta}}$ matrices. **(a)** S-polarised modes. **(b)** P-polarised modes.

2.3.4 Band Structures

In this subsection, different photonic crystals are explored in an attempt to find a suitable candidate that exhibits a band gap, and can be fabricated in the laboratory using tools available to this project group. As was demonstrated in the one-dimensional case, a high index contrast leads to wider band gaps. The search is therefore based on silicon-air structures, in part due to the high refractive index of silicon which is ~ 3.4 in the THz regime, and because many decades of it being the workhorse of microelectronics has led to a tremendous amount of experience with micro structuring the material [45]. Additionally, high resistivity silicon exhibits low attenuation for radiation in the giga- and terahertz region [62]. The search takes inspiration from the work done in *Photonic Crystals: Molding the flow of light* by *John D.* [43]. The structures that will be investigated can be seen in fig. 2.7, with their unit cells outlined by the dashed black lines. All patterns have lattice vectors of equal size, $|\mathbf{a}_i| = \Lambda$. With material and pattern chosen, the ratio between radius and period can now be varied in order to determine a suitable photonic crystal. Specifically, the ratio is varied in 60 steps within $0.05 \leq r/\Lambda \leq 0.5$. For each radius, the band structure for the first eight bands is calculated, and the maximum and minimum value of adjacent bands for each polarisation is subtracted from each other, to see if there is a gap between the bands. If there is a band gap, the midgap frequency, GMG ratio, upper and lower band gap frequency are stored and plotted. This way, the optimal radii and pattern can be found. The calculations are performed using $N = 9$, based on the findings in subsection 2.3.3.

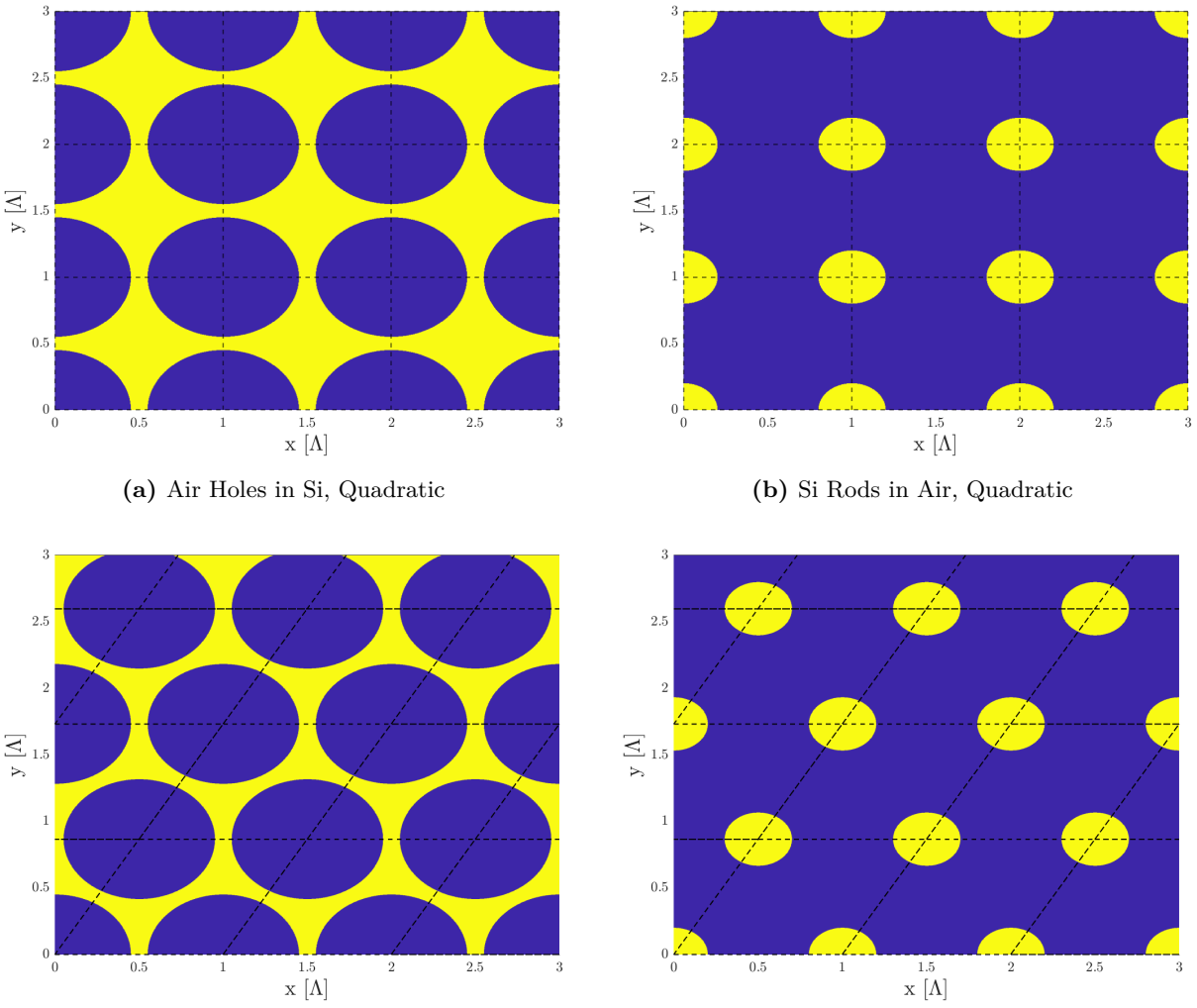

(a) Air Holes in Si, Quadratic

(b) Si Rods in Air, Quadratic

(c) Air Holes in Si, Hexagonal

(d) Si Rods in Air, Hexagonal

Figure 2.7: Plots the dielectric profile of the photonic crystals that are investigated in the coming sections. Unit cells are outlined by the dashed black lines.

2.3.4.1 Quadratic Array of Air Holes in Silicon

In fig. 2.8 the band structure of a square array of air holes in silicon is plotted against a path going between high symmetry points in the first Brillouin zone for the first four bands of both S- and P-polarised modes. The high symmetry points all lie at the edge of the Brillouin zone, except Γ, and are of special interest because the bands are continuous, resulting in most maxima and minima of the bands, which determines the band gaps, being found at these points. In two dimensions, the area bounded by the high symmetry points for a given reciprocal lattice is known as the irreducible Brillouin zone and can be seen as the shaded blue area in the insert of fig. 2.8(a). All **k**-vectors in the entire first Brillouin zone can be obtained by rotating and reflecting the irreducible Brillouin zone. In this case, the ratio between the first Brillouin zone and the irreducible Brillouin zone is eight.
All band structures in this project are based on the Fourier expansions of dielectric functions, such as the one seen in Figure 2.8b, where the dielectric function and the Fourier expanded dielectric function, using $N = 9$ corresponding to 361 plane waves, is plotted. The band structure in fig. 2.8 has band gaps for both polarisations, indicated by the blue and red horizontal bars with gap mid-gap ratios of $\text{GMG}_{1,S} = 1.9\%$, $\text{GMG}_{1,P} = 8.7\%$ and $\text{GMG}_{2,P} = 11.8\%$. However, because the band gaps do not lie on top of each other there are no frequencies where both polarisations are reflected from the structure. The photonic crystal is said to not feature a simultaneous band gap.
The effect of changing the radii of the air holes can be seen in fig. 2.9. When the radii of the

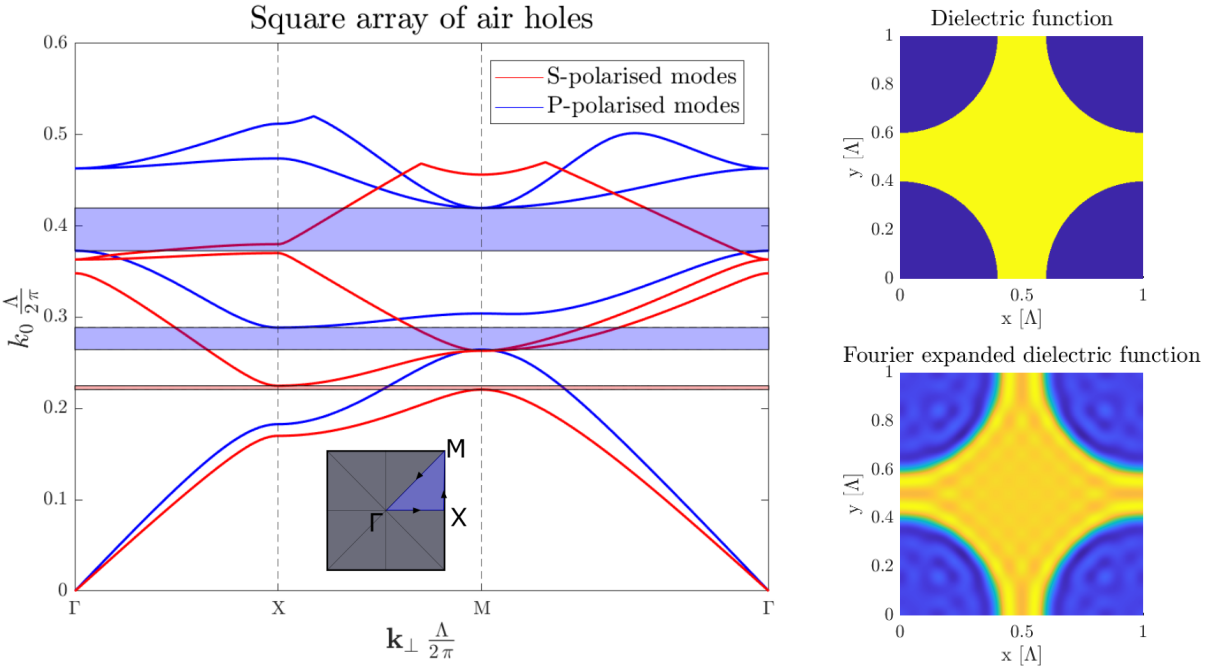

(a) **(b)**

Figure 2.8: Depicts the band structure and dielectric function using $\varepsilon_{holes} = 1$, $\varepsilon_{medium} = 3.4^2$, $\Lambda_x = \Lambda_y$, $N = 9$ and $r = 0.4\Lambda$. **(a)** Band structure of a photonic crystal consisting of a square lattice of circular air holes for both P- and S-polarised light. The path through the first Brillouin zone is shown along with the irreducible Brillouin zone as the shaded blue area in the mini-figure. **(b)** Dielectric function and the Fourier expanded dielectric function used to calculate the band structure.

holes are reduced to $r = 0.38\Lambda$ the band gap for S-polarised modes vanishes, and the GMG ratios of the band gap for P-polarised modes are reduced to $\text{GMG}_{1,P} = 7.4\%$, and $\text{GMG}_{2,P} = 9.3\%$. Increasing the radii of the holes to $r = 0.44\Lambda$ the GMG ratios are changed to $\text{GMG}_{1,P} = 8.6\%$, $\text{GMG}_{2,P} = 14\%$ and $\text{GMG}_{1,S} = 10.2\%$. Another effect is the change of the position of ω_m. When the r/Λ ratio is increased, all band gaps, and therefore ω_m, is moved to higher frequencies. This may be useful if for example only holes of a fixed radius can be produced, in which case the only way to manipulate the position of the band gap is to change the ratio r/Λ.

In fig. 2.10 the midgap frequency, frequency of the top and bottom of the band gap, and the gap mid-gap ratio is plotted for varying ratios between the radius and period. Gathering the plots of the frequency of the top and bottom of the band gap, fig. 2.10e, it is revealed that this photonic crystal supports a simultaneous band gap when $r > 0.46\Lambda$ with eigenvalues around $0.46\Lambda/2\pi$, because, for the same radius, the upper-frequency boundary of the second S-band gap is between the frequency boundaries of the second P-band gap. This happens because a band gap between the third and fourth S-band opens up around $r = 0.45\Lambda$, which can be seen in fig. 2.10d. Although this means that a square array of air holes is a possible candidate, this structure corresponds to the dielectric profile plotted in fig. 2.7a which may prove fragile. Additionally, it sets high requirements for the precision of the fabrication. If the radius becomes smaller than 0.46Λ the band gap closes, and if it becomes larger the structure falls apart.

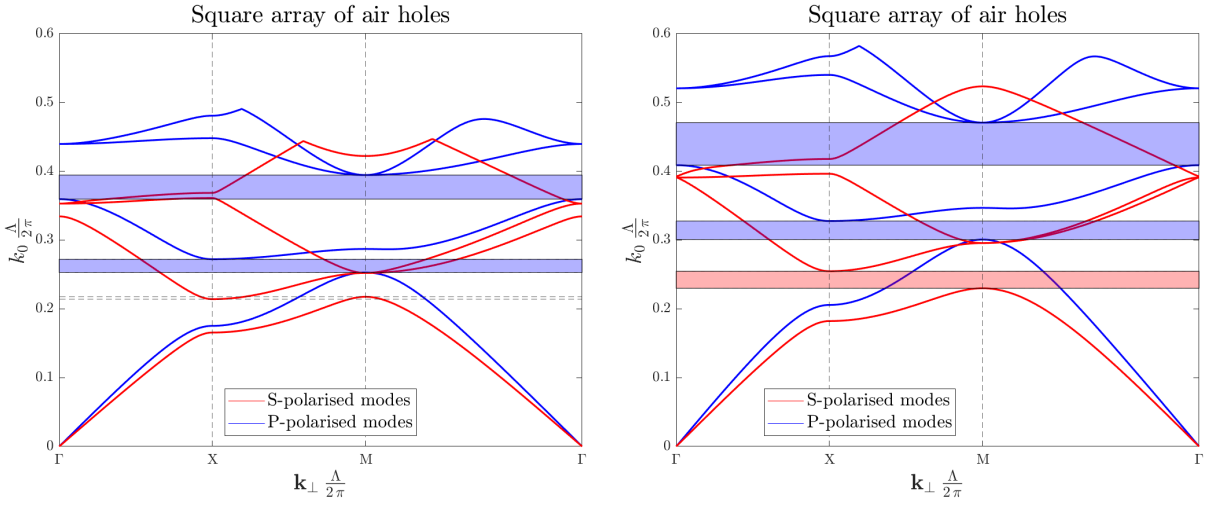

(a) **(b)**

Figure 2.9: Depicts the band structure using $\varepsilon_{holes} = 1$, $\varepsilon_{medium} = 3.4^2$, $\Lambda_x = \Lambda_y$, $N = 9$ and **(a)** $r = 0.38\Lambda$, **(b)** $r = 0.44\Lambda$, of a square array of air holes in Si.

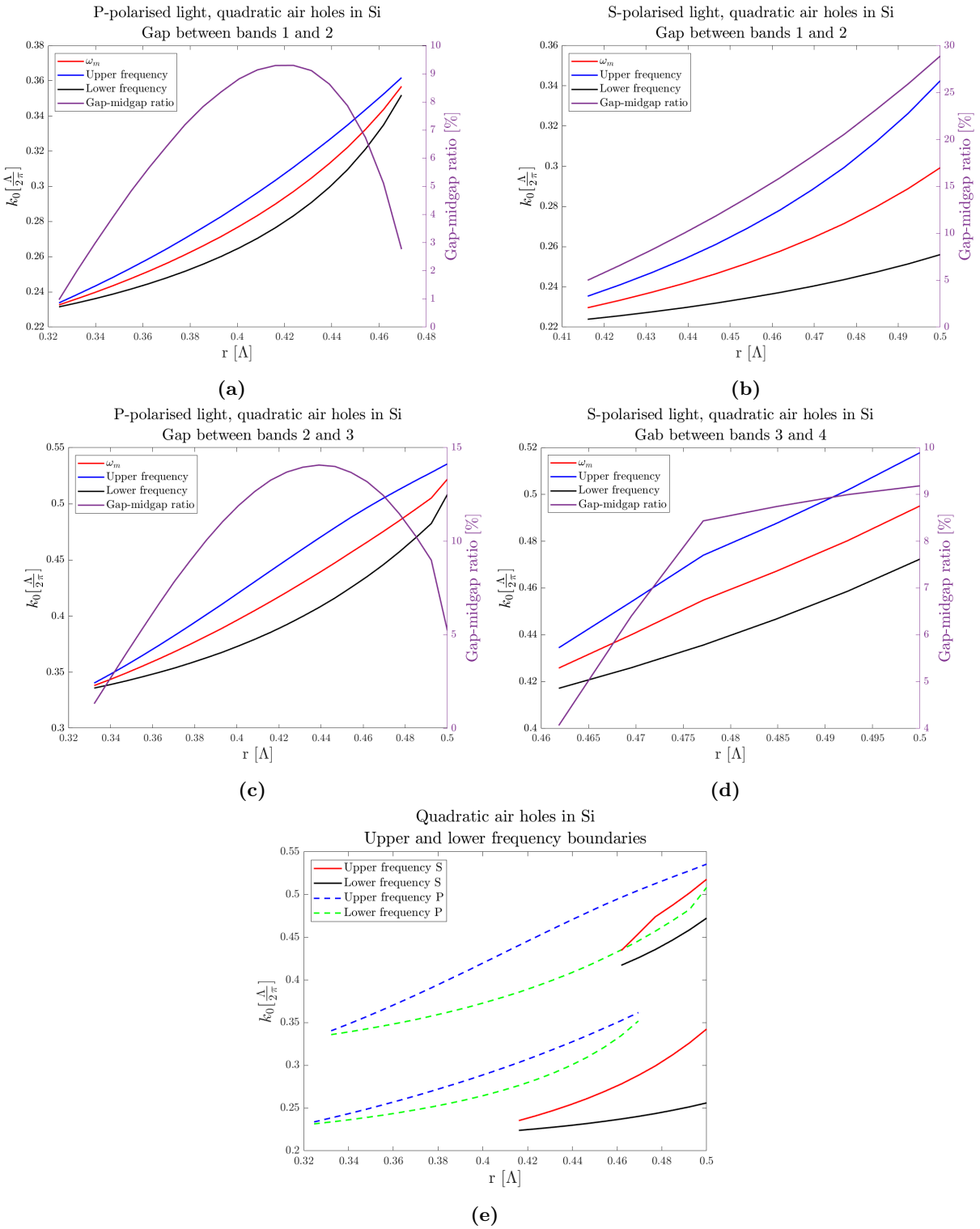

Figure 2.10: **(a)** - **(d)** Plots the midgap frequency, frequency of the top and bottom of the band gap, and the gap mid-gap ratio of two band gaps for varying radii-period ratios in a photonic crystal consisting of a square array of air holes in Si. **(e)** Collects the upper and lower frequencies of the band gaps in a single plot.

2.3.4.2 Square Array of Si Rods in Air

In fig. 2.11 the same graphs are plotted for the case of a square array of Si rods in air. At $r = 0.19\Lambda$ the first band gap of the S-polarisation is widest, with a 38% GMG ratio while the largest GMG ratio for the P-polarisation is 1%. The band structure for $r = 0.19\Lambda$ is plotted in fig. 2.11f. In fig. 2.11e it can be seen that the band gaps for the S- and P-polarisation never overlap and that there are thus no simultaneous band gaps. However, this photonic crystal may still be of interest. If the P-polarisation can be removed, the structure can still exhibit band gaps, as well as the various modes associated with defects in photonic crystals. This can be achieved by sandwiching the structure between metal plates. Assuming that the metal is a perfect conductor, the tangential part of the electric field must be zero inside the metal, and hence also at the interface between the photonic crystal and metal, removing the P-polarisation [63]. Therefore, structures that have a large band gap for S-polarised light are still of interest.

2.3.4.3 Hexagonal Array of Si Rods in Air

In fig. 2.12 the same graphs are plotted for the case of a hexagonal array of Si rods in air. As was the case for the quadratic array, Si rods favour large band gaps for the S-polarisation with the highest occurring between bands 1 and 2 with a peak GMG ratio of 46% at the ratio $r/\Lambda = 0.175$. The GMG ratios for the P-polarisation are much larger than the quadratic case, with the highest being above 9%. As was the case for the quadratic array, no simultaneous band gaps exist, see fig. 2.12(f). To create photonic crystals with measurable band gaps based on dielectric rods, it is therefore necessary, regardless of pattern, to remove the P-polarisation.

2.3.4.4 Hexagonal Array of Air Holes in Si

The last photonic crystal investigated is the hexagonal array of air holes in Si. The relevant graphs are plotted in fig. 2.13. This photonic crystal exhibits the largest band gaps observed for the P-polarisation, up to GMG ratios of 49%, and respectable band gaps for the S-polarisation, GMG ratios of 19%. Crucially, some of these band gaps have the same r/Λ ratio and frequencies. No less than three simultaneous band gaps can be found, with overlap between the first band gap occurring for S- and P-polarised modes being seen in fig. 2.13f. This gap opens at $r/\Lambda > 0.42$ whereafter it remains open for increasing ratios.

2.3.5 Summary

The most important findings of the previous subsections are gathered in table 2.1. In terms of GMG ratios, it is clear that the hexagonal patterns are superior both in the case of rods and air holes. The value of the midgap frequency differs for the two patterns, but the midgap frequency, ω_m, of any band gap can always be tuned to some desired frequency by scaling the value of Λ. Therefore, the only reason that the square patterns may be relevant is if there are limitations to the dimensions of the structures that can be fabricated. In that case, the square array may be of interest over the hexagonal, simply by virtue of midgap frequency being placed at different values. For the air holes in silicon, the hexagonal patterns holds additional

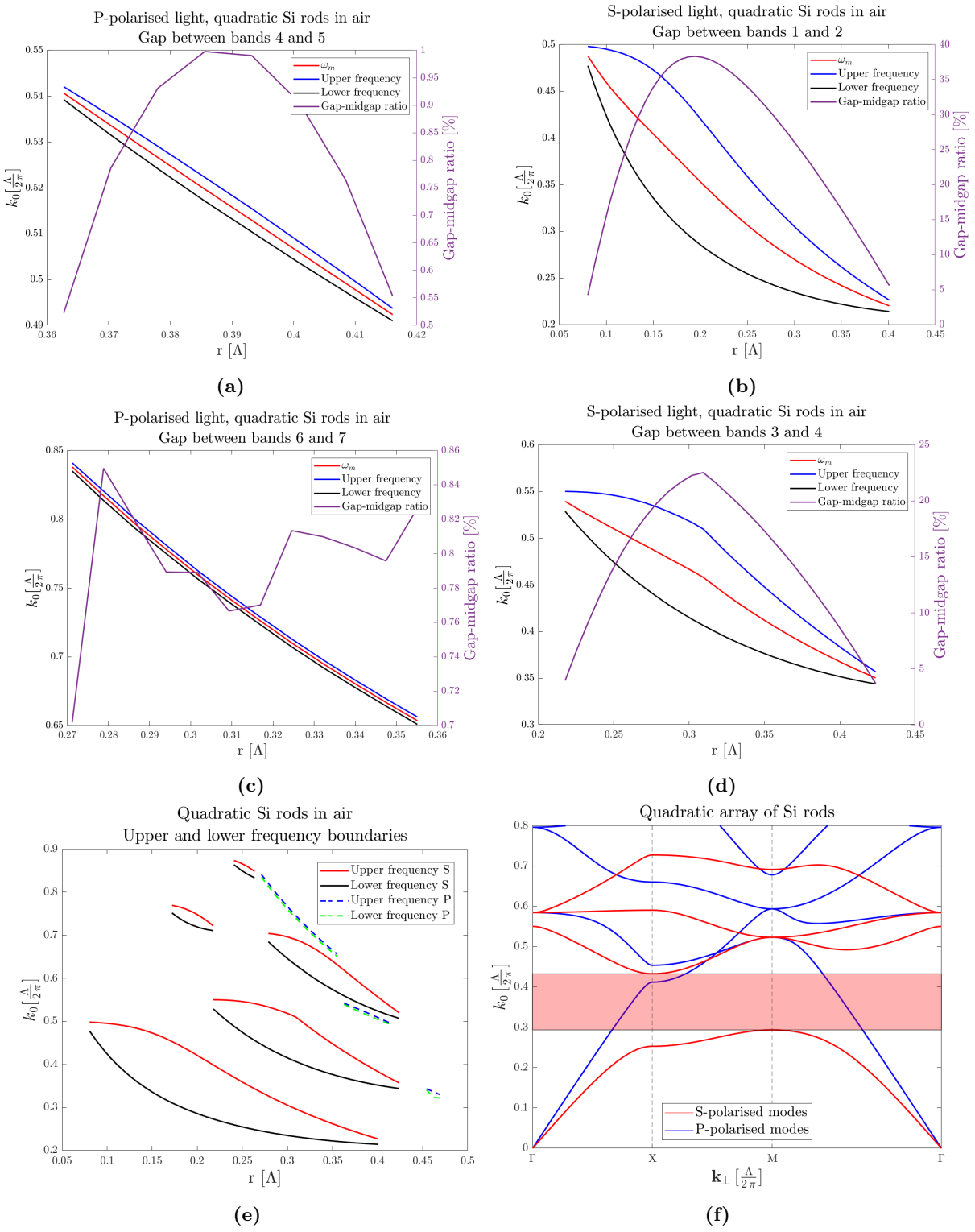

Figure 2.11: **(a)** - **(d)** Plots the midgap frequency, frequency of the top and bottom of the band gap, and the gap mid-gap ratio of two band gaps for varying radii-period ratios in a photonic crystal consisting of a square array of Si rods in air. **(e)** Collects the upper and lower frequencies of the band gaps in a single plot. **(f)** Band structure with $r = 0.19\Lambda$.

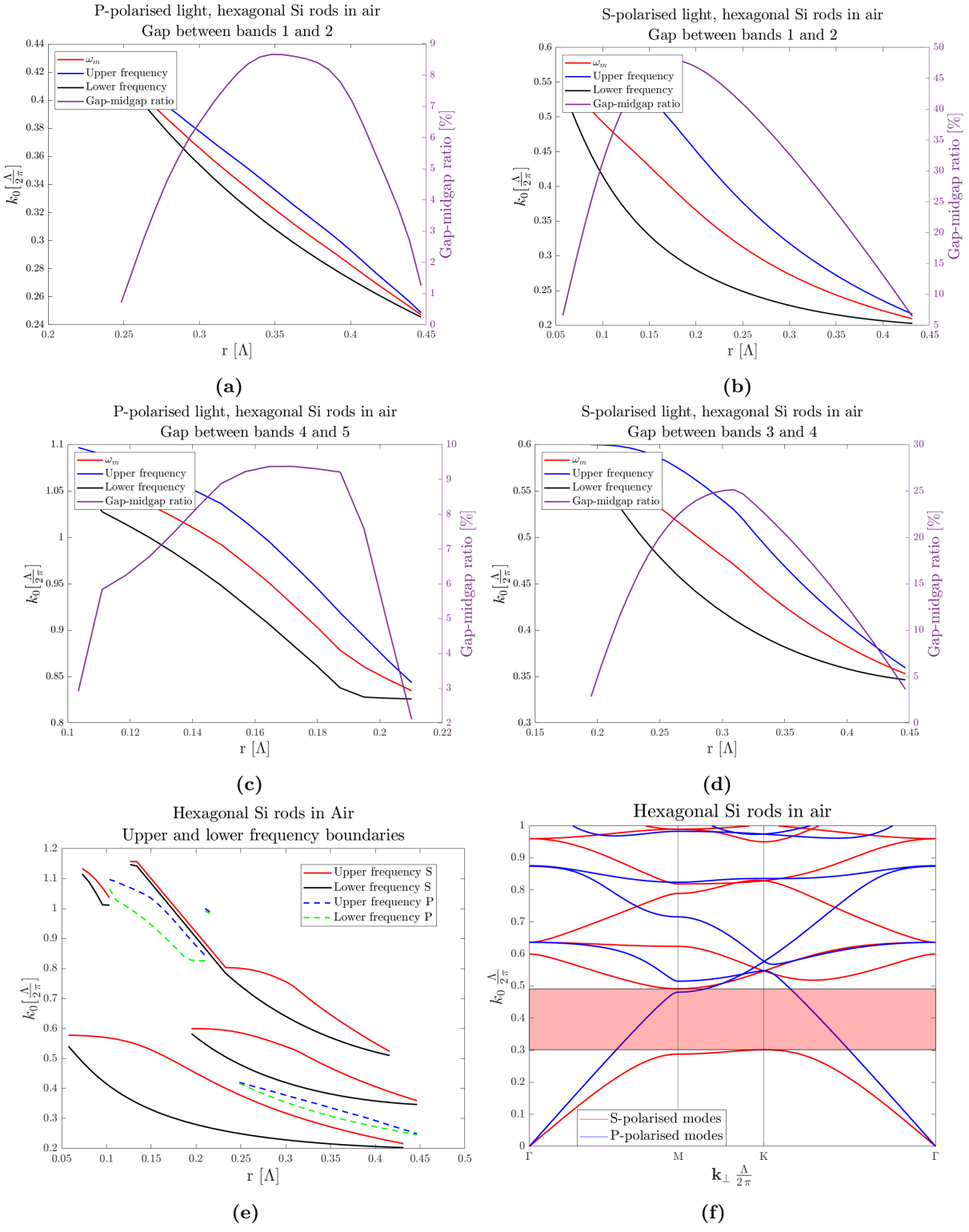

Figure 2.12: **(a)** - **(d)** Plots the midgap frequency, frequency of the top and bottom of the band gap, and the gap mid-gap ratio for varying radii in a photonic crystal consisting of a hexagonal array of Si rods in air. **(e)** Collects the upper and lower frequencies of the band gaps in a single plot. **(f)** Band structure with $r/\Lambda = 0.175$.

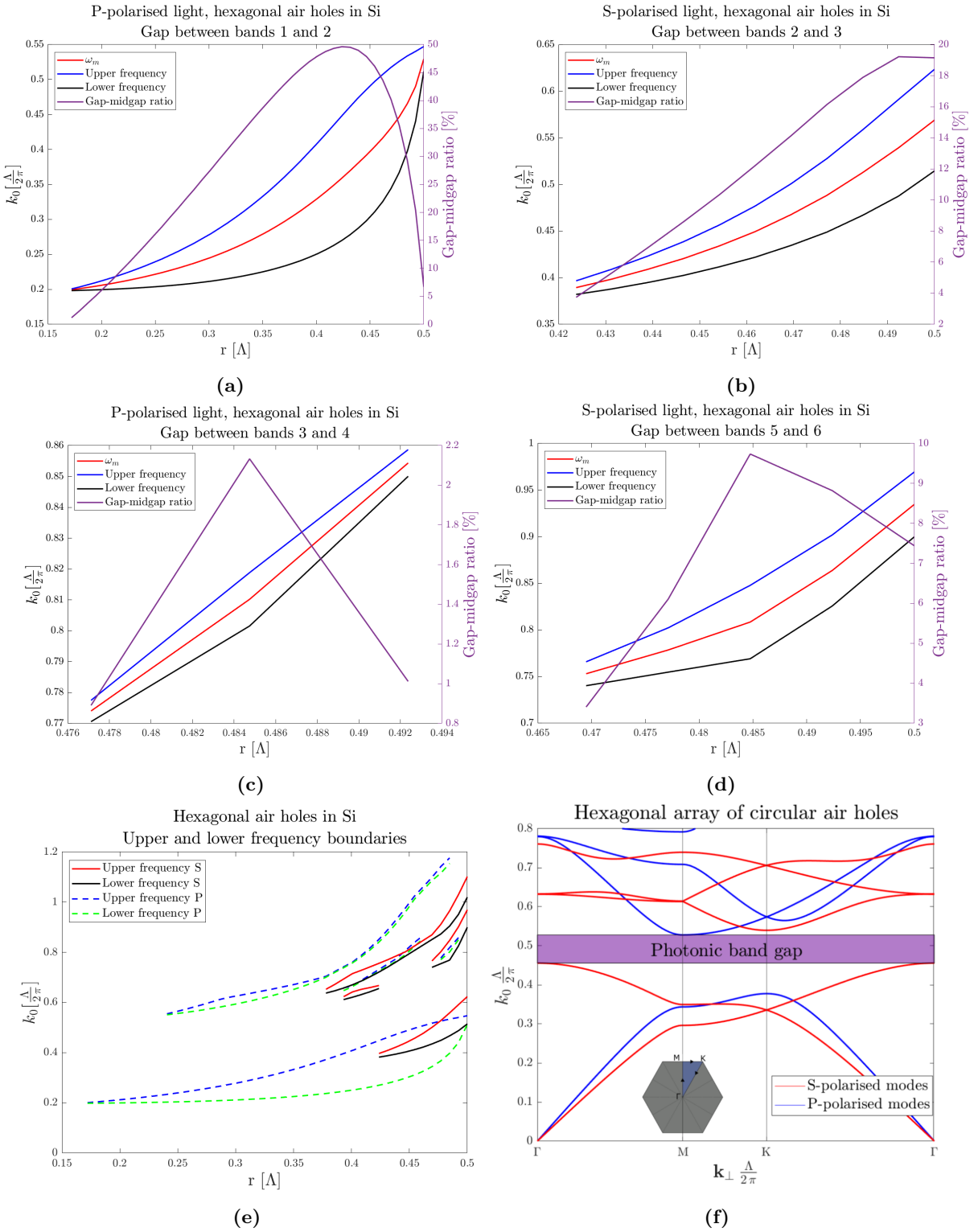

Figure 2.13: **(a)** - **(d)** Plots the midgap frequency, frequency of the top and bottom of the band gap, and the gap mid-gap ratio for varying radii in a photonic crystal consisting of a hexagonal array of air holes in Si. **(e)** Collects the upper and lower frequencies of the band gaps in a single plot. **(f)** Band structure with $r/\Lambda = 0.48$.

advantages. While both patterns support simultaneous band gaps, the GMG ratio is larger in the hexagonal case, with the largest gap opening up around $r \sim 0.42\Lambda$, while the gap in the quadratic case opens up around $r \sim 0.46\Lambda$. It is therefore likely that the hexagonal array is structurally more stable, which may or may not be a concern during production. Attempts at fabricating both hexagonal and square arrays of silicon rods using RIE, while laser ablation will be used to fabricate hexagonal arrays of air holes in silicon. A sample holder made of aluminium will be fabricated, which hopefully will suppress the P-polarisation.

Table 2.1: Collects the most important findings from the previous subsections.

Photonic crystal	ω_m $[\frac{\Lambda}{2\pi}]$ S/P	GMG [%] S/P	$r[\Lambda]$ S/P	Sim. BG
Quad Si rods	0.36 / 0.52	38.3 / 1.0	0.19 / 0.39	No
Hex Si rods	0.40 / 0.93	47.9 / 9.4	0.17 / 0.17	No
Quad air holes	0.30 / 0.44	19.2 / 14.1	0.49 / 0.44	Yes
Hex air holes	0.54/0.36	19.2 / 49.6	0.49 / 0.42	Yes

2.4 Fourier Modal Method

This section covers the Fourier Modal Method (FMM), which will be used to model the transmittance spectra of the photonic crystals investigated in this project. The coming sections are written with the focus on the one-dimensional photonic crystal, also referred to as the sub-wavelength grating, used to excite Fano resonances. However, it will be shown in subsection 2.4.5.3 how the model can be implemented for two-dimensional photonic crystals.
The aim is to identify the dimensions of the structure seen in fig. 2.14 that exhibits Fano resonances in the frequency interval of interest. The FMM is suitable to handle structures that are layer-wise homogeneous or periodic as the method employs Fourier expansions of the fields and the relative permittivity profiles. To apply the method, the structure of interest is divided into layers, as the one presented in fig. 2.15, each of which is homogeneous in the z-direction, and periodic in the x-direction. It is in each of these layers that the Fourier expansions of the fields and the relative permittivity are carried out. Using these Fourier expansions when solving the eigenvalue problem the result is eigenvectors that hold the coefficients of each allowed mode. The FMM then employs a recursive matrix formalism, in order to obtain matrices describing the transmission and reflection for the whole structure.

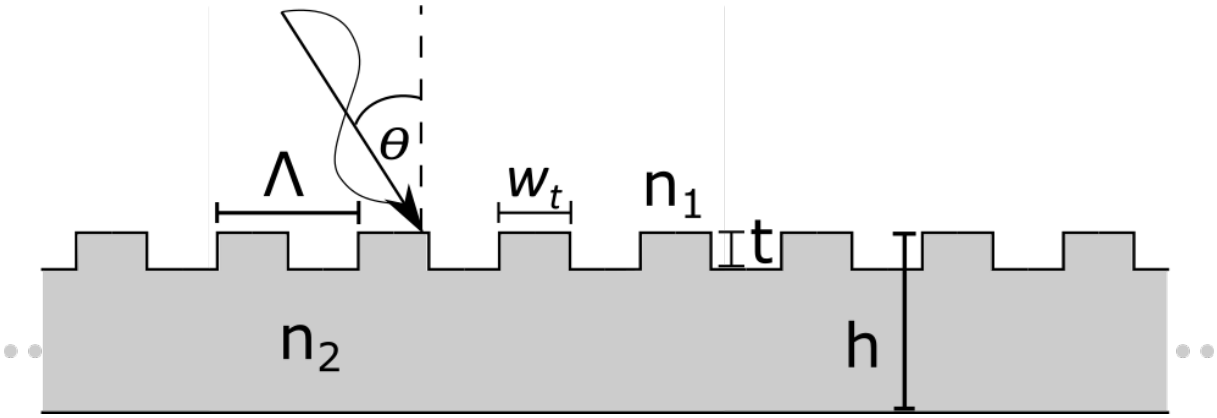

Figure 2.14: Sketch of the structure of interest with regards to Fano resonances in this project.

2.4.1 Eigenvalue Problem

The first step in formulating the problem with FMM is to find the eigenvectors and -values in the different layers separately. This is done by Fourier expanding the periodic parts of the functions which enter in the wave equation, e.g., that presented in eq. (2.63), and then expressing the resulting system of equations on a matrix form. For a structure with a period Λ in the x-direction, the relative permittivity profile can be given as

$$\varepsilon(x, z) = \varepsilon(x + \Lambda, z). \tag{2.59}$$

As discussed previously, see subsection 2.3.1, the field related to a plane wave in two-dimensional structures that are periodic in one direction and homogeneous in the other will be on the following form,

$$\mathbf{A}(x, z) = \hat{\mathbf{y}} A(x) e^{\pm i\beta z}, \tag{2.60}$$

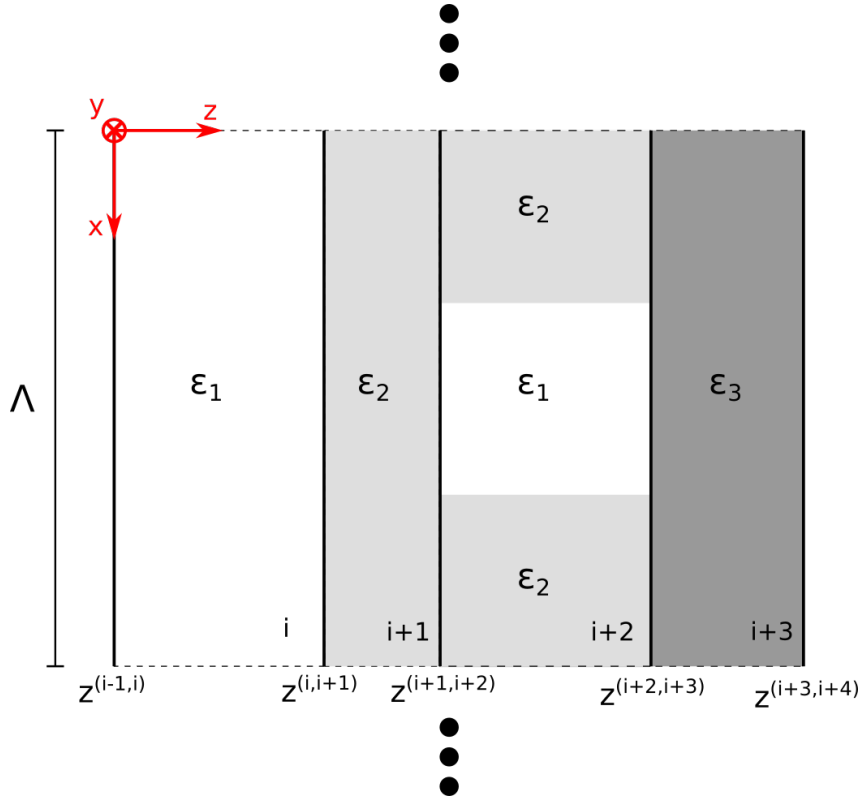

Figure 2.15: A sketch resembling the structure investigated with the FMM, having four layers along the z-direction, where the layer $i+2$ is seen to have a homogeneous permittivity profile along the z-axis, but having a periodic inhomogeneous permittivity profile along the x-axis.

where $\mathbf{A}$ represents either the electric or magnetic field. $A(x)$ is a Bloch wave that has the form

$$A(x) = u(x)e^{ik_x x}, \tag{2.61}$$

and $u(x)$ has the same periodicity as the structure, meaning that

$$A(x+\Lambda) = u(x+\Lambda)e^{ik_x(x+\Lambda)} = A(x)e^{ik_x\Lambda}. \tag{2.62}$$

The wavenumber in the homogeneous direction is dubbed $\beta = k_z$. Considering P-polarised modes, using the wave equation seen in eq. (2.19), which is written here for the benefit of the reader

$$\nabla \times \left(\frac{1}{\varepsilon(\mathbf{r})}\nabla \times \mathbf{H}(\mathbf{r})\right) = k_0^2 \mathbf{H}(\mathbf{r}), \tag{2.63}$$

the left-hand side (LHS) of eq. (2.63) can be rewritten using the identities

$$\nabla \times (B\mathbf{A}) = B\nabla \times \mathbf{A} + (\nabla B) \times \mathbf{A}, \tag{2.64}$$

$$\nabla \times \nabla \times \mathbf{A} = \nabla(\nabla \cdot \mathbf{A}) - \nabla^2 \mathbf{A}, \tag{2.65}$$

where $B = B(\mathbf{r})$ is some scalar dependent on $\mathbf{r}$ and $\mathbf{A} = \mathbf{A}(\mathbf{r})$ is some vector dependent on $\mathbf{r}$. Using the identity eq. (2.64), with $\mathbf{A} = \nabla \times \mathbf{H}(\mathbf{r})$ and $B = \frac{1}{\varepsilon(\mathbf{r})}$, the LHS of eq. (2.63) becomes

$$\nabla \times \left(\frac{1}{\varepsilon(\mathbf{r})}\nabla \times \mathbf{H}(\mathbf{r})\right) = \frac{1}{\varepsilon(\mathbf{r})}\nabla \times \nabla \times \mathbf{H}(\mathbf{r}) + \left(\nabla \frac{1}{\varepsilon(\mathbf{r})}\right) \times (\nabla \times \mathbf{H}(\mathbf{r})). \tag{2.66}$$

Applying the identity eq. (2.65), with $\mathbf{A} = \mathbf{H}(\mathbf{r})$, and recalling that $\nabla \cdot \mathbf{H}(\mathbf{r}) = 0$, it becomes possible to recast eq. (2.63) as

$$\left(\nabla \frac{1}{\varepsilon(\mathbf{r})}\right) \times (\nabla \times \mathbf{H}(\mathbf{r})) - \frac{1}{\varepsilon(\mathbf{r})} \nabla^2 \mathbf{H}(\mathbf{r}) = k_0^2 \mathbf{H}(\mathbf{r}). \tag{2.67}$$

The expression presented in eq. (2.67) is the general form of the problem, and using the expressions for the relative permittivity and magnetic field as presented in eq. (2.59) and eq. (2.60), the result, after a little rearranging, becomes

$$\begin{aligned} -\partial_z^2 \mathbf{H}(x,z) = \varepsilon(x,z) k_0^2 \mathbf{H}(x,z) + \partial_x^2 \mathbf{H}(x,z) \\ + \varepsilon(x,z) \Big(\Big[\partial_x \eta(x,z)\Big] \Big[\partial_x \mathbf{H}(x,z)\Big] + \Big[\partial_z \eta(x,z)\Big] \Big[\partial_z \mathbf{H}(x,z)\Big] \Big), \end{aligned} \tag{2.68}$$

with $\partial_u = \frac{\partial}{\partial u}$ being a shorthand notation for the derivative, $\partial_u^2 = \frac{\partial^2}{\partial u^2}$ being a shorthand notation for the double derivative, and $\eta(x,z) = [\varepsilon(x,z)]^{-1}$. It is possible to further simplify this expression. As a first step, it is advantageous to look at the different derivatives with respect to x, and realise the sum of these can be given as

$$\partial_x^2 \mathbf{H}(x,z) + \varepsilon(x,z) \Big[\partial_x \eta(x,z)\Big] \Big[\partial_x \mathbf{H}(x,z)\Big] = \varepsilon(x,z) \partial_x \Big[\eta(x,z) \partial_x \mathbf{H}(x,z)\Big]. \tag{2.69}$$

The reasoning behind the second step of the simplification is found in the considered problem. As the eigenvalues are found in each layer, and each layer is homogeneous in the z-direction, the derivative of $\eta(x,z)$ with respect to z is zero. Due to the homogeneous nature along this direction, the z-dependence will be omitted for the relative permittivity profiles and the inverse relative permittivity profile from now on. Lastly, the double derivative of the magnetic field with respect to z simply corresponds to a factor of $-\beta^2$. All these considerations therefore lead to the simplified, problem-specific version of eq. (2.63), which is eq. (2.70)

$$\varepsilon(x) \partial_x \Big[\eta(x) \partial_x \mathbf{H}(x,z)\Big] + \varepsilon(x) k_0^2 \mathbf{H}(x,z) = \beta^2 \mathbf{H}(x,z). \tag{2.70}$$

For a more general field than that presented in eq. (2.60), it is possible to solve eq. (2.70) for each eigenmode, thus finding all those allowed in the layer. The eigenmodes are given similar to eq. (2.60),

$$\mathbf{H}_m(x,z) = \hat{\mathbf{y}} H_m(x) e^{\pm i \beta_m z}, \tag{2.71}$$

with the only difference being the subscript, m, which refers to the given eigenmode. The part of the eigenmode related to the periodic direction of the layer, the Bloch wave in the x-direction, can be Fourier expanded as

$$H_m(x) = \sum_{n=-\infty}^{\infty} H_{m,\{n\}} e^{i(k_x + nG)x}, \tag{2.72}$$

where $H_{m,\{n\}}$ are Fourier coefficients of the eigenmode and $G = \frac{2\pi}{\Lambda}$. The relative permittivity profile and its inverse, η, along x can be expressed by similar expansions

$$\varepsilon(x) = \sum_{n=-\infty}^{\infty} \varepsilon_{\{n\}} e^{inGx}, \tag{2.73}$$

$$\eta(x) = \sum_{n=-\infty}^{\infty} \eta_{\{n\}} e^{inGx}, \tag{2.74}$$

with the Fourier coefficients given as

$$\varepsilon_{\{n\}} = \frac{1}{\Lambda} \int_0^{\Lambda} \varepsilon(x) e^{-inGx} dx, \tag{2.75}$$

$$\eta_{\{n\}} = \frac{1}{\Lambda} \int_0^{\Lambda} \eta(x) e^{-inGx} dx. \tag{2.76}$$

Substituting the expressions from eqs. (2.72) to (2.74) into eq. (2.70) leads to the following expression

$$\begin{aligned} \sum_{n=-\infty}^{\infty} \varepsilon_{\{n\}} e^{inGx} \partial_x \left\{ \sum_{l=-\infty}^{\infty} \eta_{\{l\}} e^{ilGx} \partial_x \left[\sum_{q=-\infty}^{\infty} H_{m,\{q\}} e^{i(k_x+qG)x} e^{\pm i\beta_m z} \right] \right\} \\ + k_0^2 \sum_{n=-\infty}^{\infty} \varepsilon_{\{n\}} e^{inGx} \sum_{j=-\infty}^{\infty} H_{m,\{j\}} e^{i(k_x+jG)x} e^{\pm i\beta_m z} \\ = \beta_m^2 \sum_{p=-\infty}^{\infty} H_{m,\{p\}} e^{i(k_x+pG)x} e^{\pm i\beta_m z}. \end{aligned} \tag{2.77}$$

where the vector notation has been omitted as it is redundant at this point. Taking the missing derivatives and afterwards removing the common factor of $e^{ik_x x} e^{\pm i\beta_m z}$ the expression becomes

$$\begin{aligned} \sum_{n=-\infty}^{\infty} \varepsilon_{\{n\}} e^{inGx} \left\{ \sum_{l=-\infty}^{\infty} e^{ilGx} \sum_{q=-\infty}^{\infty} \left(i\left[k_x + (l+q)G\right]\right) \eta_{\{l\}} \left(i\left[k_x + qG\right]\right) H_{m,\{q\}} e^{iqGx} \right\} \\ + k_0^2 \sum_{n=-\infty}^{\infty} \varepsilon_{\{n\}} e^{inGx} \sum_{j=-\infty}^{\infty} H_{m,\{j\}} e^{ijGx} = \beta_m^2 \sum_{p=-\infty}^{\infty} H_{m,\{p\}} e^{ipGx} . \end{aligned} \tag{2.78}$$

The first term on the LHS can then be further manipulated. The first step is to define $j = l + q$ meaning that $l = j - q$, leading to

$$\begin{aligned} \sum_{n=-\infty}^{\infty} \varepsilon_{\{n\}} e^{inGx} \left\{ \sum_{l=-\infty}^{\infty} e^{ilGx} \sum_{q=-\infty}^{\infty} \left(i\left[k_x + (l+q)G\right]\right) \eta_{\{l\}} \left(i\left[k_x + qG\right]\right) H_{m,\{q\}} e^{iqGx} \right\} \\ = - \sum_{n=-\infty}^{\infty} \varepsilon_{\{n\}} e^{inGx} \left\{ \sum_{j=-\infty}^{\infty} e^{ijGx} \sum_{q=-\infty}^{\infty} \left[k_x + jG\right] \eta_{\{j-q\}} \left[k_x + qG\right] H_{m,\{q\}} \right\}, \end{aligned} \tag{2.79}$$

where the reason for keeping the same summation limits can be found in Appendix A. The substitution can be carried out yet another time, by defining $p = n + j$,

$$\begin{aligned} - \sum_{n=-\infty}^{\infty} \varepsilon_{\{n\}} e^{inGx} \left\{ \sum_{j=-\infty}^{\infty} e^{ijGx} \sum_{q=-\infty}^{\infty} \left[k_x + jG\right] \eta_{\{j-q\}} \left[k_x + qG\right] H_{m,\{q\}} \right\} \\ = - \sum_{p=-\infty}^{\infty} e^{ipGx} \sum_{j=-\infty}^{\infty} \varepsilon_{\{p-j\}} \sum_{q=-\infty}^{\infty} \left[k_x + jG\right] \eta_{\{j-q\}} \left[k_x + qG\right] H_{m,\{q\}}. \end{aligned} \tag{2.80}$$

For the second term on the LHS using the same substitution, namely $p = n + j$, the term can be given as

$$k_0^2 \sum_{n=-\infty}^{\infty} \varepsilon_{\{n\}} e^{inGx} \sum_{j=-\infty}^{\infty} H_{m,\{j\}} e^{ijGx} = k_0^2 \sum_{p=-\infty}^{\infty} e^{ipGx} \sum_{j=-\infty}^{\infty} \varepsilon_{\{p-j\}} H_{m,\{j\}}, \tag{2.81}$$

and then collecting all the terms leads to eq. (2.78) being recast as

$$\sum_{p=-\infty}^{\infty} e^{ipGx} \Bigg\{ - \sum_{j=-\infty}^{\infty} \varepsilon_{\{p-j\}} \sum_{q=-\infty}^{\infty} [k_x + jG]\, \eta_{\{j-q\}}\, [k_x + qG]\, H_{m,\{q\}} \\ - \beta_m^2 H_{m,\{p\}} + k_0^2 \sum_{j=-\infty}^{\infty} \varepsilon_{\{p-j\}} H_{m,\{j\}} \Bigg\} = 0, \tag{2.82}$$

from which it is possible to eliminate the front factor, as it has to hold for all x. Hence for each p, the following equation should be obeyed

$$- \sum_{j=-\infty}^{\infty} \varepsilon_{\{p-j\}} \sum_{q=-\infty}^{\infty} [k_x + jG]\, \eta_{\{j-q\}}\, [k_x + qG] H_{m,\{q\}} \\ + k_0^2 \sum_{j=-\infty}^{\infty} \varepsilon_{\{p-j\}} H_{m,\{j\}} = \beta_m^2 H_{m,\{p\}}. \tag{2.83}$$

This could then be converted to a matrix equation from which the eigenvalues and eigenvectors could be found, by truncating the sums and introducing the Toeplitz matrices $\overline{\overline{\boldsymbol{\varepsilon}}}$ and $\overline{\overline{\boldsymbol{\eta}}}$. However, based on the article by Lifeng Li in [61], the convergence for P-polarised modes using the Laurent rule, eq. (2.86) [64], is slow. As a matter of fact, it is not precise everywhere, as oscillations will occur for concurrent complementary jump continuities, e.g., those found between the inverse of the relative permittivity profile along x and $\partial_x H(x, z)$ [61]. But there is a solution to this problem which is to apply the so-called inverse rule [61]. The application of this rule can be presented by first looking at the product between two periodic functions

$$s(x) = f(x)g(x), \tag{2.84}$$

where the normal Fourier expansion of this product is given in a simple manner as

$$\sum_{n=-\infty}^{\infty} s_{\{n\}} e^{inGx} = \sum_{p=-\infty}^{\infty} f_{\{p\}} e^{ipGx} \sum_{m=-\infty}^{\infty} g_{\{m\}} e^{imGx} = \sum_{n=-\infty}^{\infty} \sum_{m=-\infty}^{\infty} f_{\{n-m\}} g_{\{m\}} e^{inGx}, \tag{2.85}$$

$$s_{\{n\}} = \sum_{m=-\infty}^{\infty} f_{\{n-m\}} g_{\{m\}}. \tag{2.86}$$

In the case $s(x)$ is continuous but $f(x)$ and $g(x)$ have concurrent complementary jump discontinuities, Laurent's rule, presented in eq. (2.86), should be exchanged with the inverse rule. The effect of this is the introduction of a subtle and seemingly redundant substitution, namely interchanging the Fourier coefficients related to $f(x)$ with some related to

$$u(x) = \frac{1}{f(x)} = \frac{g(x)}{s(x)}, \tag{2.87}$$

where it should be clear from the above that $s(x)$ can be found as

$$s(x) = [u(x)]^{-1} g(x). \tag{2.88}$$

The inverse rule is essentially based on what seems to be empirical results [61, 65] obtained by Philippe Lalanne and G. Micheal Morris [66], and G. Granet and B. Guizal [67] independent of each other in 1996. The basis for the reformulation of the eigenvalue problem is according to Li a result of the wrong assumption [61]

$$\bar{\bar{\mathbf{f}}}^{-1} = \bar{\bar{\mathbf{u}}}, \tag{2.89}$$

with this assumption explicitly being stated by both P. Lalanne et al. and G. Granet et al. [66, 67]. However, their proposed rewriting proved very efficient, and is the essential part of the inverse rule, as implementing the inverse rule in eq. (2.85) is simply making the rewriting

$$\sum_{n=-\infty}^{\infty} s_{\{n\}} e^{inGx} = \sum_{n=-\infty}^{\infty} \left(\sum_{m=-\infty}^{\infty} \left[u_{\{n-m\}} \right]^{-1} g_{\{m\}} \right) e^{inGx}, \tag{2.90}$$

where the parenthesis is equal to $s_{\{n\}}$ on the LHS [61]. So the inverse rule should be implemented when the product of two functions is continuous, but the two functions have concurrent complementary jump discontinuities. As mentioned earlier, such concurrent complementary jump discontinuities are found for the product between the inverse of the relative permittivity profile along x and $\partial_x H(x,z)$, which is related to the z-component of the electric field.
Both components of the electric field can be found from eq. (2.13), assuming no free current density, and are given by

$$\mathbf{E}_{m,x}(x,z) = -\hat{\mathbf{x}} \frac{(\pm\beta_m)}{\omega\varepsilon_0} \eta(x) H_m(x,z), \tag{2.91}$$

$$\mathbf{E}_{m,z}(x,z) = \hat{\mathbf{z}} \frac{-1}{i\omega\varepsilon_0} \eta(x) \partial_x H_m(x,z). \tag{2.92}$$

Due to $\mathbf{E}_{m,z}(x,z)$ being perpendicular to the x-axis and thus tangential to the periodic direction of the relative permittivity profile, the boundary conditions require that this component of the field is conserved when traversing an interface in the x-direction, meaning that the product $\eta(x)\partial_x \mathbf{H}(x,z)$ needs to be continuous and thus the inverse rule should be applied on $\eta(x)$. Furthermore, the boundary conditions also require the tangential part of the magnetic field to be conserved when traversing an interface in the x-direction, leading to the magnetic field being continuous, which means that the product of $\varepsilon(x)$ and the factor on the LHS of

$$\varepsilon(x) \left(\partial_x \left[\eta(x) \partial_x \right] + k_0^2 \right) H_m(x,z) = \beta_m^2 H_m(x,z), \tag{2.93}$$

should be continuous since β_m is merely a constant for the given mode, meaning that the right-hand side (RHS) is continuous, leading to the inverse rule also should be applied on $\varepsilon(x)$. Thus the final result is obtained by truncating the sums and recasting eq. (2.83) as

$$\begin{aligned} -\sum_{j=-N}^{N} \left[\eta_{\{p-j\}} \right]^{-1} \sum_{q=-N}^{N} \left[k_x + jG \right] \left[\varepsilon_{\{j-q\}} \right]^{-1} \left[k_x + qG \right] H_{m,\{q\}} \\ + k_0^2 \sum_{j=-N}^{N} \left[\eta_{\{p-j\}} \right]^{-1} H_{m,\{j\}} = \beta_m^2 H_{m,\{p\}}. \end{aligned} \tag{2.94}$$

Thus, to ensure convergence, the expression in eq. (2.94) has been used instead of eq. (2.83) [61] when constructing the matrix equation which is on the form

$$\left[\bar{\bar{\boldsymbol{\eta}}}\right]^{-1}\left(k_0^2\bar{\bar{\mathbf{I}}}-\bar{\bar{\mathbf{K}}}\left[\bar{\bar{\boldsymbol{\varepsilon}}}\right]^{-1}\bar{\bar{\mathbf{K}}}\right)\bar{\mathbf{H}}_m=\beta_m^2\bar{\mathbf{H}}_m, \tag{2.95}$$

where $\bar{\bar{\mathbf{I}}}$ is an appropriate identity matrix, $\bar{\bar{\boldsymbol{\eta}}}$ and $\bar{\bar{\boldsymbol{\varepsilon}}}$ are Toeplitz matrices, and $\bar{\mathbf{H}}_m$ is a column vector with the Fourier coefficients of the m'th mode. Furthermore, $\bar{\bar{\mathbf{K}}}$ is a diagonal matrix with entries $diag\left(k_x+\left[-N,-N+1,\ldots,N-1,N\right]G\right)$ where no distinction has been made between the two matrices arising from the factors (k_x+jG) and (k_x+qG), as they are identical. From the matrix equation in eq. (2.95) it is then possible to find a maximum of $2N+1$ different modes and associated eigenvalues. As the operator in question, eq. (2.19), is Hermitian, the eigenmodes will form a complete set, and hence the total field may be expressed as a superposition of these modes. Furthermore, it is required that β_m is purely positive, meant as

$$\mathrm{Re}\left\{\beta_m\right\}\wedge\mathrm{Im}\left\{\beta_m\right\}\geq 0. \tag{2.96}$$

The requirement on the real part facilitates the possibility to introducing weighting coefficients a_m and b_m which handle waves propagating to the right and left, respectively, and the requirement on the imaginary part ensures that the coefficients are related to an exponential decrease in the same directions. Thus the field can be expressed as [68]

$$H(x,z)=\sum_{m=-N}^{N}H_m(x)\left(a_me^{i\beta_mz}+b_me^{-i\beta_mz}\right). \tag{2.97}$$

Inserting a truncated version of the Fourier expansion of $H_m(x)$ in eq. (2.72) and rewriting a bit, the expression becomes

$$H(x,z)=\sum_n e^{i(k_x+nG)x}\sum_m H_{m,\{n\}}\left(a_me^{i\beta_mz}+b_me^{-i\beta_mz}\right), \tag{2.98}$$

where the limits on the summation have been omitted and will likewise be in the following sections, as it should implicitly be understood that the summation is from $-N$ to N unless explicitly stated otherwise. As such, the layer-wise eigenvalue problem for the magnetic field has been determined, where the inverse rule has been applied in order to ensure convergence [61]. Furthermore, the total magnetic field for a structure periodic in the x-direction and homogeneous in z has been found as a superposition of eigenmodes in the given layer.

2.4.2 Considerations for an Interface between Layers

In the former section, an expression for the field together with the eigenvalue problem for a single layer was found. This section will deal with the transmission and reflection from the interfaces when two layers are put into contact. As the expression for the field, expressed with respect to the position of the interface between the two layers, forms the basis of the derivation of the reflection and transmission it is advantageous to start with that. The field on the RHS of the interface between layer $i-1$ and i, see fig. 2.16 for clarification of the notation, can be expressed as

$$H^{(i)}(x,z)=\sum_n e^{i(k_x+nG)x}\sum_m H^{(i)}_{m,\{n\}}\left[a_m^{(i)}e^{i\beta_m^{(i)}\left(z-z^{(i-1,i)}\right)}+b_m^{(i)}e^{-i\beta_m^{(i)}\left(z-z^{(i-1,i)}\right)}\right], \tag{2.99}$$

where the introduction of the difference $z - z^{(i-1,i)}$ ensures that $a_m^{(i)}$ and $b_m^{(i)}$ refer to the coefficients related to the interface on the LHS of a layer i, with $z^{(i-1,i)}$ being the z-coordinate for the interface between layer $i-1$ and i. In the case of a current free material, the magnetic field is conserved across an interface. Based on this it is then in the interface, $z = z^{(1,2)}$, required that

$$\begin{aligned}&\sum_n e^{i(k_x+nG)x} \sum_m H^{(1)}_{m,\{n\}} \left[a'^{(1)}_m e^{i\beta^{(1)}_m \left(z - z^{(1,2)}\right)} + b'^{(1)}_m e^{-i\beta^{(1)}_m \left(z - z^{(1,2)}\right)} \right] \\ &= \sum_n e^{i(k_x+nG)x} \sum_m H^{(2)}_{m,\{n\}} \left[a^{(2)}_m e^{i\beta^{(2)}_m \left(z - z^{(1,2)}\right)} + b^{(2)}_m e^{-i\beta^{(2)}_m \left(z - z^{(1,2)}\right)} \right],\end{aligned} \tag{2.100}$$

where the primed coefficients, a' and b', refer to coefficients related to the interface on the RHS of a layer, whereas the unprimed case refers to the coefficients related to the interface on the LHS of a layer as mentioned earlier. The annotation has been illustrated in fig. 2.16. The

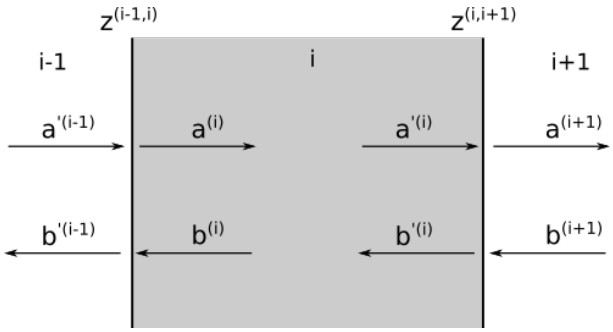

Figure 2.16: Illustration showing which interface the primed and unprimed coefficients refer to.

superscripts on $H_{m,\{n\}}$, a, b, and β_m denote what layer they are associated with. Thus at the interface when $z = z^{(1,2)}$, eq. (2.100) reads

$$\sum_n e^{i(k_x+nG)x} \sum_m H^{(1)}_{m,\{n\}} \left[a'^{(1)}_m + b'^{(1)}_m \right] = \sum_n e^{i(k_x+nG)x} \sum_m H^{(2)}_{m,\{n\}} \left[a^{(2)}_m + b^{(2)}_m \right]. \tag{2.101}$$

Using an argument from earlier, namely that this equality should hold for all x, the front exponential dependent on x can be omitted, and the equality can be reformulated on a matrix form as

$$\bar{\bar{\mathbf{M}}}^{(1)}_H \left(\bar{\mathbf{a}}'^{(1)} + \bar{\mathbf{b}}'^{(1)} \right) = \bar{\bar{\mathbf{M}}}^{(2)}_H \left(\bar{\mathbf{a}}^{(2)} + \bar{\mathbf{b}}^{(2)} \right), \tag{2.102}$$

where $\bar{\bar{\mathbf{M}}}^{(i)}_H$ is a matrix consisting of column vectors with the Fourier coefficients of the different modes in layer i. The different $\bar{\mathbf{a}}$ and $\bar{\mathbf{b}}$ column vectors contain the weighting coefficients for the different modes in regard to their respective layer and interface. In source-free material it is also required that the tangential part of the electric field is conserved across an interface. This means that $E_x = \frac{-1}{i\omega\varepsilon_0}\eta(x)\partial_z H(x,z)$ should be conserved. Thus using eq. (2.91), with $+\beta_m$ following from eq. (2.96), the result of eq. (2.100) at the interface becomes

$$\begin{aligned}&\sum_n \sum_p e^{i(k_x+[n+p]G)x} \sum_m \eta^{(1)}_{\{p\}} H^{(1)}_{m,\{n\}} \beta^{(1)}_m \left[a'^{(1)}_m - b'^{(1)}_m \right] \\ &\qquad = \sum_n \sum_p e^{i(k_x+[n+p]G)x} \sum_m \eta^{(2)}_{\{p\}} H^{(2)}_{m,\{n\}} \beta^{(2)}_m \left[a^{(2)}_m - b^{(2)}_m \right],\end{aligned} \tag{2.103}$$

where making the substitution $j = n + p$ facilitates that the equation can be rewritten as

$$\begin{aligned}\sum_n \sum_j e^{i(k_x+jG)x} \sum_m \eta^{(1)}_{\{j-n\}} H^{(1)}_{m,\{n\}} \beta^{(1)}_m \left[a'^{(1)}_m - b'^{(1)}_m\right] \\ = \sum_n \sum_j e^{i(k_x+jG)x} \sum_m \eta^{(2)}_{\{j-n\}} H^{(2)}_{m,\{n\}} \beta^{(2)}_m \left[a^{(2)}_m - b^{(2)}_m\right].\end{aligned} \tag{2.104}$$

Conservation of the magnetic field should not be dependent on x, and neither should conservation of the electric field, facilitating the reformulation of the equation into a matrix form as

$$\bar{\bar{\mathbf{M}}}^{(1)}_E \left(\bar{\mathbf{a}}'^{(1)} - \bar{\mathbf{b}}'^{(1)}\right) = \bar{\bar{\mathbf{M}}}^{(2)}_E \left(\bar{\mathbf{a}}^{(2)} - \bar{\mathbf{b}}^{(2)}\right), \tag{2.105}$$

where the matrix $\bar{\bar{\mathbf{M}}}^{(i)}_E$ is given on the form

$$\bar{\bar{\mathbf{M}}}^{(i)}_E = \bar{\bar{\boldsymbol{\eta}}}^{(i)} \bar{\bar{\mathbf{M}}}^{(i)}_H \bar{\bar{\boldsymbol{\beta}}}^{(i)}, \tag{2.106}$$

and $\bar{\bar{\boldsymbol{\beta}}}^{(i)}$ is a diagonal matrix containing the different $\beta^{(i)}_m$ as $diag\left(\left[\beta^{(i)}_{-N}, \beta^{(i)}_{-N+1}, \ldots, \beta^{(i)}_N\right]\right)$. From eqs. (2.102) and (2.105) it is possible to obtain reflection and transmission matrices for the interface using the relations

$$\bar{\mathbf{a}}^{(2)} = \bar{\bar{\mathbf{T}}}_{1,2} \bar{\mathbf{a}}'^{(1)}, \tag{2.107}$$

$$\bar{\mathbf{b}}'^{(1)} = \bar{\bar{\mathbf{R}}}_{1,2} \bar{\mathbf{a}}'^{(1)}, \tag{2.108}$$

$$\bar{\mathbf{b}}'^{(1)} = \bar{\bar{\mathbf{T}}}_{2,1} \bar{\mathbf{b}}^{(2)}, \tag{2.109}$$

$$\bar{\mathbf{a}}^{(2)} = \bar{\bar{\mathbf{R}}}_{2,1} \bar{\mathbf{b}}^{(2)}, \tag{2.110}$$

where eqs. (2.107) and (2.108) is found based on the assumption $\bar{\mathbf{b}}^{(2)} = \bar{\mathbf{0}}$, and eqs. (2.109) and (2.110) is found based on the assumption $\bar{\mathbf{a}}'^{(1)} = \bar{\mathbf{0}}$. Thus as an example assuming $\bar{\mathbf{b}}^{(2)} = \bar{\mathbf{0}}$, $\bar{\bar{\mathbf{R}}}_{1,2}$ and $\bar{\bar{\mathbf{T}}}_{1,2}$ can be found as

$$\begin{aligned}\bar{\bar{\mathbf{R}}}_{1,2} = \left(\left[\bar{\bar{\mathbf{M}}}^{(2)}_E\right]^{-1} \bar{\bar{\mathbf{M}}}^{(1)}_E + \left[\bar{\bar{\mathbf{M}}}^{(2)}_H\right]^{-1} \bar{\bar{\mathbf{M}}}^{(1)}_H\right)^{-1} \\ \left(\left[\bar{\bar{\mathbf{M}}}^{(2)}_E\right]^{-1} \bar{\bar{\mathbf{M}}}^{(1)}_E - \left[\bar{\bar{\mathbf{M}}}^{(2)}_H\right]^{-1} \bar{\bar{\mathbf{M}}}^{(1)}_H\right),\end{aligned} \tag{2.111}$$

$$\bar{\bar{\mathbf{T}}}_{1,2} = \left[\bar{\bar{\mathbf{M}}}^{(2)}_E\right]^{-1} \bar{\bar{\mathbf{M}}}^{(1)}_E \left(\bar{\bar{\mathbf{I}}} - \bar{\bar{\mathbf{R}}}_{1,2}\right). \tag{2.112}$$

In this subsection, the expressions for the transmission and reflection matrices for a single interface have been derived.

2.4.3 A Three Layer Structure

Adding another layer to the structure considered in the former section results in a structure with three layers. The second layer is confined by the first and third layers, meaning the second

layer has a finite thickness of $L_2 = z^{(2,3)} - z^{(1,2)}$. In this case the modes that are transmitted, or partially transmitted, at the first interface, will travel across the second layer and reach the second interface. At this interface the modes in the layer will either be transmitted, reflected, or a combination of both. The reflected part then travels across the layer again reaching the first interface, where the same occurs, which in theory repeats infinitely, except for the case $\bar{\bar{\mathbf{T}}}_{1,2} = \bar{\bar{\mathbf{T}}}_{2,3} = \bar{\bar{\mathbf{I}}}$. However, this case equates to having three identical layers and is essentially a single layer, which has unnecessarily been divided into three. The same considerations done here for modes incident on the three-layer structure from the first layer can be made for modes incident on the structure from the third layer.
To determine the reflection and transmission of this structure, a way to propagate the modes across the second layer is needed. This is done by introducing a propagation matrix

$$\bar{\bar{\mathbf{P}}}_{2,\pm} = \begin{bmatrix} e^{\pm i\beta^{(2)}_{-N} L_2} & 0 & \cdots & 0 \\ 0 & e^{\pm i\beta^{(2)}_{-N+1} L_2} & \cdots & 0 \\ \vdots & \vdots & \ddots & \vdots \\ 0 & 0 & \cdots & e^{\pm i\beta^{(2)}_{N} L_2} \end{bmatrix}, \tag{2.113}$$

which handles the phase introduced for the different modes when traversing the second layer once, with $\bar{\bar{\mathbf{P}}}_{2,+}$ $\left(\bar{\bar{\mathbf{P}}}_{2,-}\right)$ being once from left (right) to right (left) [68]. The transmission and reflection matrices for the structure for light incident from the left can then be found as [68]

$$\bar{\bar{\mathbf{T}}}_{1,3} = \bar{\bar{\mathbf{T}}}_{2,3} \sum_{n=0}^{\infty} \left(\bar{\bar{\mathbf{P}}}_{2,+}\bar{\bar{\mathbf{R}}}_{2,1}\bar{\bar{\mathbf{P}}}_{2,-}\bar{\bar{\mathbf{R}}}_{2,3}\right)^n \bar{\bar{\mathbf{P}}}_{2,+}\bar{\bar{\mathbf{T}}}_{1,2}, \tag{2.114}$$

$$\bar{\bar{\mathbf{R}}}_{1,3} = \bar{\bar{\mathbf{R}}}_{1,2} + \bar{\bar{\mathbf{T}}}_{2,1} \sum_{n=0}^{\infty} \left(\bar{\bar{\mathbf{P}}}_{2,-}\bar{\bar{\mathbf{R}}}_{2,3}\bar{\bar{\mathbf{P}}}_{2,+}\bar{\bar{\mathbf{R}}}_{2,1}\right)^n \bar{\bar{\mathbf{P}}}_{2,-}\bar{\bar{\mathbf{R}}}_{2,3}\bar{\bar{\mathbf{P}}}_{2,+}\bar{\bar{\mathbf{T}}}_{1,2}. \tag{2.115}$$

The infinite series of the summands in both expressions are geometric series since both summands obey the requirement that the absolute eigenvalue of the summand is below unity [68], or at least all cases where this treatment makes sense as the only case where it is possible to disobey the requirement is $\left|\bar{\bar{\mathbf{R}}}_{1,2}\right| = \bar{\bar{\mathbf{I}}}$. However, in that case eqs. (2.114) and (2.115) both become obsolete since no part of any of the modes gets over the first interface, and thus the modes effectively only see a single interface. Thus for all other cases than the special one mentioned here the expressions for the transmission and reflection can be expressed using geometric series as [68]

$$\bar{\bar{\mathbf{T}}}_{1,3} = \bar{\bar{\mathbf{T}}}_{2,3} \left(\bar{\bar{\mathbf{I}}} - \bar{\bar{\mathbf{P}}}_{2,+}\bar{\bar{\mathbf{R}}}_{2,1}\bar{\bar{\mathbf{P}}}_{2,-}\bar{\bar{\mathbf{R}}}_{2,3}\right)^{-1} \bar{\bar{\mathbf{P}}}_{2,+}\bar{\bar{\mathbf{T}}}_{1,2}, \tag{2.116}$$

$$\bar{\bar{\mathbf{R}}}_{1,3} = \bar{\bar{\mathbf{R}}}_{1,2} + \bar{\bar{\mathbf{T}}}_{2,1} \left(\bar{\bar{\mathbf{I}}} - \bar{\bar{\mathbf{P}}}_{2,-}\bar{\bar{\mathbf{R}}}_{2,3}\bar{\bar{\mathbf{P}}}_{2,+}\bar{\bar{\mathbf{R}}}_{2,1}\right)^{-1} \bar{\bar{\mathbf{P}}}_{2,-}\bar{\bar{\mathbf{R}}}_{2,3}\bar{\bar{\mathbf{P}}}_{2,+}\bar{\bar{\mathbf{T}}}_{1,2}. \tag{2.117}$$

The geometric series thus involves the need to invert a matrix. Since this is a rather computationally expensive operation it is preferred to reduce the number of times this is necessary, which is achieved by rewriting either eq. (2.114) or eq. (2.115) a bit, so the factor that is inverted is identical in the two expressions. The interested reader is referred to chapter 6 in *Numerical Methods in Photonics* [68]. However, the equations presented in these sections will be on a form that, according to the authors of this project, emerge more naturally when trying to derive the expressions compared to those found in [68]. Expressions similar to eqs. (2.114) and (2.115) can

be found for the case of light incident from the right, after which the geometric series again can be implemented leading to

$$\bar{\bar{\mathbf{T}}}_{3,1} = \bar{\bar{\mathbf{T}}}_{2,1}\left(\bar{\bar{\mathbf{I}}} - \bar{\bar{\mathbf{P}}}_{2,-}\bar{\bar{\mathbf{R}}}_{2,3}\bar{\bar{\mathbf{P}}}_{2,+}\bar{\bar{\mathbf{R}}}_{2,1}\right)^{-1}\bar{\bar{\mathbf{P}}}_{2,-}\bar{\bar{\mathbf{T}}}_{3,2}, \tag{2.118}$$

$$\bar{\bar{\mathbf{R}}}_{3,1} = \bar{\bar{\mathbf{R}}}_{3,2} + \bar{\bar{\mathbf{T}}}_{2,3}\left(\bar{\bar{\mathbf{I}}} - \bar{\bar{\mathbf{P}}}_{2,+}\bar{\bar{\mathbf{R}}}_{2,1}\bar{\bar{\mathbf{P}}}_{2,-}\bar{\bar{\mathbf{R}}}_{2,3}\right)^{-1}\bar{\bar{\mathbf{P}}}_{2,+}\bar{\bar{\mathbf{R}}}_{2,1}\bar{\bar{\mathbf{P}}}_{2,-}\bar{\bar{\mathbf{T}}}_{3,2}, \tag{2.119}$$

and thus the reflection and transmission matrices, for modes incident from both the left and right, for a three-layer structure have been determined. The reflection and transmission matrices for a three-layer structure, as will be shown in the next section, are the basis for the reflection and transmission matrices for structures with many layers.

2.4.4 Structure with More than Three Layers

This section will handle the construction of the reflection and transmission matrices for structures consisting of four or more layers, together with how the mode weighting coefficients in a layer inside the structure are found. The idea behind the construction of the reflection and transmission matrices for a many-layered structure is simple. Take the three-layer structure from the former section and recursively condense the two interfaces in this structure down to one effective interface, and then add another layer to the left of this structure and calculate the reflection and transmission matrices for this structure. When this is done, the next iteration can be started and this process can be repeated until the desired structure is constructed. Using this recursive formalism, the reflection and transmission matrices for a structure with $\gamma + 1$ layers can be found as

$$\bar{\bar{\mathbf{T}}}_{1,\gamma+1} = \bar{\bar{\mathbf{T}}}_{\gamma,\gamma+1}\left(\bar{\bar{\mathbf{I}}} - \bar{\bar{\mathbf{P}}}_{\gamma,+}\bar{\bar{\mathbf{R}}}_{\gamma,1}\bar{\bar{\mathbf{P}}}_{\gamma,-}\bar{\bar{\mathbf{R}}}_{\gamma,\gamma+1}\right)^{-1}\bar{\bar{\mathbf{P}}}_{\gamma,+}\bar{\bar{\mathbf{T}}}_{1,\gamma}, \tag{2.120}$$

$$\bar{\bar{\mathbf{R}}}_{1,\gamma+1} = \bar{\bar{\mathbf{R}}}_{1,\gamma} + \bar{\bar{\mathbf{T}}}_{\gamma,1}\left(\bar{\bar{\mathbf{I}}} - \bar{\bar{\mathbf{P}}}_{\gamma,-}\bar{\bar{\mathbf{R}}}_{\gamma,\gamma+1}\bar{\bar{\mathbf{P}}}_{\gamma,+}\bar{\bar{\mathbf{R}}}_{\gamma,1}\right)^{-1}\bar{\bar{\mathbf{P}}}_{\gamma,-}\bar{\bar{\mathbf{R}}}_{\gamma,\gamma+1}\bar{\bar{\mathbf{P}}}_{\gamma,+}\bar{\bar{\mathbf{T}}}_{1,\gamma}, \tag{2.121}$$

$$\bar{\bar{\mathbf{T}}}_{\gamma+1,1} = \bar{\bar{\mathbf{T}}}_{\gamma,1}\left(\bar{\bar{\mathbf{I}}} - \bar{\bar{\mathbf{P}}}_{\gamma,-}\bar{\bar{\mathbf{R}}}_{\gamma,\gamma+1}\bar{\bar{\mathbf{P}}}_{\gamma,+}\bar{\bar{\mathbf{R}}}_{\gamma,1}\right)^{-1}\bar{\bar{\mathbf{P}}}_{\gamma,-}\bar{\bar{\mathbf{T}}}_{\gamma+1,\gamma}, \tag{2.122}$$

$$\bar{\bar{\mathbf{R}}}_{\gamma+1,1} = \bar{\bar{\mathbf{R}}}_{\gamma+1,\gamma} + \bar{\bar{\mathbf{T}}}_{\gamma,\gamma+1}\left(\bar{\bar{\mathbf{I}}} - \bar{\bar{\mathbf{P}}}_{\gamma,+}\bar{\bar{\mathbf{R}}}_{\gamma,1}\bar{\bar{\mathbf{P}}}_{\gamma,-}\bar{\bar{\mathbf{R}}}_{\gamma,\gamma+1}\right)^{-1}\bar{\bar{\mathbf{P}}}_{\gamma,+}\bar{\bar{\mathbf{R}}}_{\gamma,1}\bar{\bar{\mathbf{P}}}_{\gamma,-}\bar{\bar{\mathbf{T}}}_{\gamma+1,\gamma}. \tag{2.123}$$

To find the field inside a given layer, ζ, the mode weighting coefficients, a and b, for the layer has to be computed. Considering a complete structure with $\Gamma > \zeta$ layers, calculating a and b is a computationally expensive task, as the recursive construction of the structure has to be carried out from each side of the complete structure. When constructing the complete structure from the opposite direction, here meant as recursively adding layers, the added layers should be added to the right of the last layer of the complete structure. This means that in addition to eqs. (2.120) to (2.123) the following equations are needed for the recursive construction of the structure from the opposite side [68]

$$\bar{\bar{\mathbf{T}}}_{\Gamma,\gamma-1} = \bar{\bar{\mathbf{T}}}_{\gamma,\gamma-1}\left(\bar{\bar{\mathbf{I}}} - \bar{\bar{\mathbf{P}}}_{\gamma,-}\bar{\bar{\mathbf{R}}}_{\gamma,\Gamma}\bar{\bar{\mathbf{P}}}_{\gamma,+}\bar{\bar{\mathbf{R}}}_{\gamma,\gamma-1}\right)^{-1}\bar{\bar{\mathbf{P}}}_{\gamma,-}\bar{\bar{\mathbf{T}}}_{\Gamma,\gamma}, \tag{2.124}$$

$$\bar{\bar{\mathbf{R}}}_{\Gamma,\gamma-1} = \bar{\bar{\mathbf{R}}}_{\Gamma,\gamma} + \bar{\bar{\mathbf{T}}}_{\gamma,\Gamma}\left(\bar{\bar{\mathbf{I}}} - \bar{\bar{\mathbf{P}}}_{\gamma,+}\bar{\bar{\mathbf{R}}}_{\gamma,\gamma-1}\bar{\bar{\mathbf{P}}}_{\gamma,-}\bar{\bar{\mathbf{R}}}_{\gamma,\Gamma}\right)^{-1}\bar{\bar{\mathbf{P}}}_{\gamma,+}\bar{\bar{\mathbf{R}}}_{\gamma,\gamma-1}\bar{\bar{\mathbf{P}}}_{\gamma,-}\bar{\bar{\mathbf{T}}}_{\Gamma,\gamma}, \tag{2.125}$$

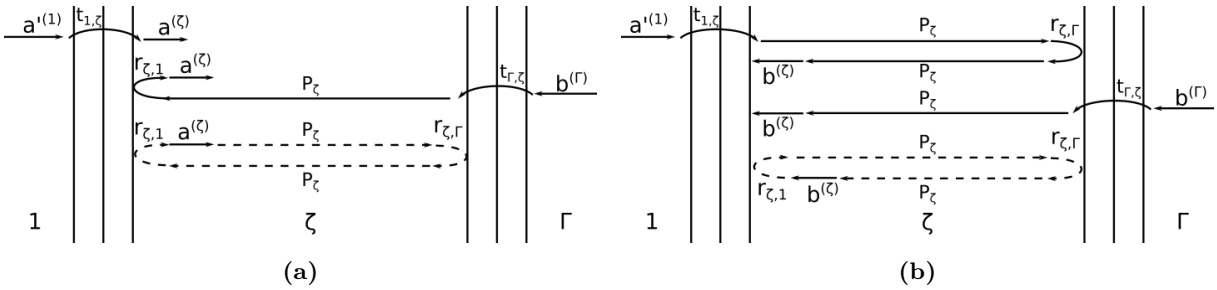

Figure 2.17: Shows the contributions to the different weighting coefficients **(a)** a and **(b)** b, in layer ζ. As can be seen, there is a possible contribution from the fields incident on each side for both coefficients. The dashed arrows indicate that additionally to the direct contribution from the outside fields, there is also a contribution from the outside field which has traversed the layer more than once.

$$\bar{\bar{\mathbf{T}}}_{\gamma-1,\Gamma} = \bar{\bar{\mathbf{T}}}_{\gamma,\Gamma}\left(\bar{\bar{\mathbf{I}}} - \bar{\bar{\mathbf{P}}}_{\gamma,+}\bar{\bar{\mathbf{R}}}_{\gamma,\gamma-1}\bar{\bar{\mathbf{P}}}_{\gamma,-}\bar{\bar{\mathbf{R}}}_{\gamma,\Gamma}\right)^{-1}\bar{\bar{\mathbf{P}}}_{\gamma,+}\bar{\bar{\mathbf{T}}}_{\gamma-1,\gamma}, \tag{2.126}$$

$$\bar{\bar{\mathbf{R}}}_{\gamma-1,\Gamma} = \bar{\bar{\mathbf{R}}}_{\gamma-1,\gamma} + \bar{\bar{\mathbf{T}}}_{\gamma,\gamma-1}\left(\bar{\bar{\mathbf{I}}} - \bar{\bar{\mathbf{P}}}_{\gamma,-}\bar{\bar{\mathbf{R}}}_{\gamma,\Gamma}\bar{\bar{\mathbf{P}}}_{\gamma,+}\bar{\bar{\mathbf{R}}}_{\gamma,\gamma-1}\right)^{-1}\bar{\bar{\mathbf{P}}}_{\gamma,-}\bar{\bar{\mathbf{R}}}_{\gamma,\Gamma}\bar{\bar{\mathbf{P}}}_{\gamma,+}\bar{\bar{\mathbf{T}}}_{\gamma-1,\gamma}. \tag{2.127}$$

Having determined the different reflection and transmission matrices associated with layer ζ it is possible to express the weighting coefficient vectors for the layer. This is done by adding the different contributions to the weighting coefficients. The coefficients can be thought to have direct contributions from the outside fields, but also an additional contribution from the direct contributions traversing the layer multiple times. The weighting coefficients can thus be given as

$$\bar{\mathbf{a}}^{(\zeta)} = \sum_{n=0}^{\infty}\left(\bar{\bar{\mathbf{R}}}_{\zeta,1}\bar{\bar{\mathbf{P}}}_{\zeta,-}\bar{\bar{\mathbf{R}}}_{\zeta,\Gamma}\bar{\bar{\mathbf{P}}}_{\zeta,+}\right)^{n}\left(\bar{\bar{\mathbf{T}}}_{1,\zeta}\bar{\mathbf{a}}'^{(1)} + \bar{\bar{\mathbf{R}}}_{\zeta,1}\bar{\bar{\mathbf{P}}}_{\zeta,-}\bar{\bar{\mathbf{T}}}_{\Gamma,\zeta}\bar{\mathbf{b}}^{(\Gamma)}\right), \tag{2.128}$$

$$\bar{\mathbf{b}}^{(\zeta)} = \sum_{n=0}^{\infty}\left(\bar{\bar{\mathbf{P}}}_{\zeta,-}\bar{\bar{\mathbf{R}}}_{\zeta,\Gamma}\bar{\bar{\mathbf{P}}}_{\zeta,+}\bar{\bar{\mathbf{R}}}_{\zeta,1}\right)^{n}\left(\bar{\bar{\mathbf{P}}}_{\zeta,-}\bar{\bar{\mathbf{R}}}_{\zeta,\Gamma}\bar{\bar{\mathbf{P}}}_{\zeta,+}\bar{\bar{\mathbf{T}}}_{1,\zeta}\bar{\mathbf{a}}'^{(1)} + \bar{\bar{\mathbf{P}}}_{\zeta,-}\bar{\bar{\mathbf{T}}}_{\Gamma,\zeta}\bar{\mathbf{b}}^{(\Gamma)}\right), \tag{2.129}$$

where the summations in both expressions can be replaced by geometric series, and as such they can instead be given as

$$\bar{\mathbf{a}}^{(\zeta)} = \left(\bar{\bar{\mathbf{I}}} - \bar{\bar{\mathbf{R}}}_{\zeta,1}\bar{\bar{\mathbf{P}}}_{\zeta,-}\bar{\bar{\mathbf{R}}}_{\zeta,\Gamma}\bar{\bar{\mathbf{P}}}_{\zeta,+}\right)^{-1}\left(\bar{\bar{\mathbf{T}}}_{1,\zeta}\bar{\mathbf{a}}'^{(1)} + \bar{\bar{\mathbf{R}}}_{\zeta,1}\bar{\bar{\mathbf{P}}}_{\zeta,-}\bar{\bar{\mathbf{T}}}_{\Gamma,\zeta}\bar{\mathbf{b}}^{(\Gamma)}\right), \tag{2.130}$$

$$\bar{\mathbf{b}}^{(\zeta)} = \left(\bar{\bar{\mathbf{I}}} - \bar{\bar{\mathbf{P}}}_{\zeta,-}\bar{\bar{\mathbf{R}}}_{\zeta,\Gamma}\bar{\bar{\mathbf{P}}}_{\zeta,+}\bar{\bar{\mathbf{R}}}_{\zeta,1}\right)^{-1}\left(\bar{\bar{\mathbf{P}}}_{\zeta,-}\bar{\bar{\mathbf{R}}}_{\zeta,\Gamma}\bar{\bar{\mathbf{P}}}_{\zeta,+}\bar{\bar{\mathbf{T}}}_{1,\zeta}\bar{\mathbf{a}}'^{(1)} + \bar{\bar{\mathbf{P}}}_{\zeta,-}\bar{\bar{\mathbf{T}}}_{\Gamma,\zeta}\bar{\mathbf{b}}^{(\Gamma)}\right), \tag{2.131}$$

and from these, it should be possible to find the field inside layer ζ using eq. (2.99). Thus the considerations needed to find the transmission and reflection through a given structure, together with how the field inside a layer can be found, have been accounted for.

2.4.5 Supplementary Considerations and Derivations

This subsection is divided into three parts, deriving the eigenvalue problem for S-polarised light, numerical considerations when calculating the transmittance, and how FMM may be used to calculate the transmittance of photonic crystals. These may be read in any order or skipped without loss of continuity.

2.4.5.1 Electric Field and Noteworthy Differences

The eigenvalue problem for the electric field is rather simple compared to the one for the magnetic field. This can mainly be attributed to the assumption that the permeability is constant, namely $\mu = 1$. With this assumption, and current free media, the double rotation of the electric field results in

$$\nabla \times \nabla \times \mathbf{E}(\mathbf{r}) = k_0^2 \varepsilon(x,z)\mathbf{E}(\mathbf{r}). \tag{2.132}$$

Furthermore, assuming source-free media and a field on the form of eq. (2.60) the result simplifies to

$$\partial_x^2 \mathbf{E}(x,z) + k_0^2 \varepsilon(x,z)\mathbf{E}(x,z) = \beta^2 \mathbf{E}(x,z). \tag{2.133}$$

It is less involved to construct the eigenvalue problem for this equation, compared to the magnetic field. Thus the following derivation will be rather limited, and the interested reader is instead referred to chapter 6 in *Numerical Methods in Photonics* for a more elaborate derivation [68]. Moving forward, the z-dependence of the relative permittivity profile will be omitted as the layer is taken to be homogeneous along z. Inserting the expressions for $\varepsilon(x)$ and the eigenmodes, $\mathbf{E}_m(x,z)$, using the truncated Fourier expansions for the x-dependent parts eq. (2.133) becomes

$$-\sum_n e^{inGx}\left(k_x + nG\right)^2 E_{m,\{n\}} + k_0^2 \sum_n e^{inGx} \sum_p \varepsilon_{\{n-p\}} E_{m,\{p\}} = \sum_n e^{inGx} \beta_m^2 E_{m,\{n\}}, \tag{2.134}$$

where the factor $e^{\pm i\beta_m z}$ has been removed, and likewise was $e^{ik_x x}$ after the differentiation. The above equality should hold for all values of x and hence

$$-\left(k_x + nG\right)^2 E_{m,\{n\}} + k_0^2 \sum_p \varepsilon_{\{n-p\}} E_{m,\{p\}} = \beta_m^2 E_{m,\{n\}}. \tag{2.135}$$

Given that none of these terms contain factors that are able to make concurrent jumps, the implementation of the inverse rule becomes obsolete and the matrix equation of eq. (2.135) is thus straightforwardly given as

$$\left(-\bar{\bar{\mathbf{K}}}^2 + k_0^2 \bar{\bar{\boldsymbol{\varepsilon}}}\right) \bar{\mathbf{E}}_m = \beta_m^2 \bar{\mathbf{E}}_m. \tag{2.136}$$

Besides the difference in the eigenvalue problem, another difference is found in the expressions for the reflection and transmission matrices for a single interface. The basis for deriving the transmission and reflection matrices for a single interface will again be based on eqs. (2.107) to (2.110) and the continuity of the tangential parts of the fields. The continuity of the tangential part of the magnetic field in relation to the interface thus requires that $\frac{-1}{i\omega\mu\mu_0}\partial_z E(x,z)$ is continuous. Hence the following two equalities emerge at the interface

$$\sum_n e^{i(k_x+nG)x} \sum_m E^{(1)}_{m,\{n\}} \left(a'^{(1)}_m + b'^{(1)}_m\right) = \sum_n e^{i(k_x+nG)x} \sum_m E^{(2)}_{m,\{n\}} \left(a^{(2)}_m + b^{(2)}_m\right), \tag{2.137}$$

$$\sum_n e^{i(k_x+nG)x} \sum_m \beta^{(1)}_m E^{(1)}_{m,\{n\}} \left(a'^{(1)}_m - b'^{(1)}_m\right) = \sum_n e^{i(k_x+nG)x} \sum_m \beta^{(2)}_m E^{(2)}_{m,\{n\}} \left(a^{(2)}_m - b^{(2)}_m\right). \tag{2.138}$$

Equations (2.137) and (2.138) can be reformulated as a matrix equations,

$$\bar{\bar{\mathbf{M}}}^{(1)}_E \left(\bar{\mathbf{a}}'^{(1)} + \bar{\mathbf{b}}'^{(1)}\right) = \bar{\bar{\mathbf{M}}}^{(2)}_E \left(\bar{\mathbf{a}}^{(2)} + \bar{\mathbf{b}}^{(2)}\right), \tag{2.139}$$

$$\bar{\bar{\mathbf{M}}}_H^{(1)}\left(\bar{\mathbf{a}}'^{(1)}-\bar{\mathbf{b}}'^{(1)}\right)=\bar{\bar{\mathbf{M}}}_H^{(2)}\left(\bar{\mathbf{a}}^{(2)}-\bar{\mathbf{b}}^{(2)}\right), \tag{2.140}$$

where $\bar{\bar{\mathbf{M}}}_H^{(i)}$ is on the form

$$\bar{\bar{\mathbf{M}}}_H^{(i)}=\bar{\bar{\mathbf{M}}}_E^{(i)}\bar{\bar{\boldsymbol{\beta}}}^{(i)}. \tag{2.141}$$

From these equations it is possible to determine the reflection and transmission matrices using the formerly mentioned equations, eqs. (2.107) to (2.110), which, for the case of $\bar{\mathbf{b}}^{(2)}=\bar{\mathbf{0}}$, results in

$$\begin{aligned}\bar{\bar{\mathbf{R}}}_{1,2}=&\left(\left[\bar{\bar{\mathbf{M}}}_H^{(2)}\right]^{-1}\bar{\bar{\mathbf{M}}}_H^{(1)}+\left[\bar{\bar{\mathbf{M}}}_E^{(2)}\right]^{-1}\bar{\bar{\mathbf{M}}}_E^{(1)}\right)^{-1}\\&\left(\left[\bar{\bar{\mathbf{M}}}_H^{(2)}\right]^{-1}\bar{\bar{\mathbf{M}}}_H^{(1)}-\left[\bar{\bar{\mathbf{M}}}_E^{(2)}\right]^{-1}\bar{\bar{\mathbf{M}}}_E^{(1)}\right),\end{aligned} \tag{2.142}$$

$$\bar{\bar{\mathbf{T}}}_{1,2}=\left[\bar{\bar{\mathbf{M}}}_H^{(2)}\right]^{-1}\bar{\bar{\mathbf{M}}}_H^{(1)}\left(\bar{\bar{\mathbf{I}}}-\bar{\bar{\mathbf{R}}}_{1,2}\right), \tag{2.143}$$

where those for the case $\bar{\mathbf{a}}^{(1)}=\bar{\mathbf{0}}$ can be found by interchanging the layers 1 and 2 in all sub- and superscripts.

2.4.5.2 Considerations for the Numerical Implementation of FMM

This section will consider how the transmittance for the structure is calculated when a plane wave polarised along y and propagating in the xz-plane is incident on the structure from one side, and how the right mode weighting coefficient is chosen in the first layer when the method is implemented numerically. Before handling the numerical implementation, it is advantageous recall that the transmittance is given as the fraction between the incident and transmitted power, and as will be shown at the end of this section, the expression for the transmittance can be used to determine a requirement that facilitates a way to choose the right weighting coefficient in the first layer for a plane wave.
The Poynting vector describes the instantaneous directional energy per unit area per unit time and is given as [69]

$$\mathbf{S}(\mathbf{r},t)=\mathbf{E}(\mathbf{r},t)\times\mathbf{H}(\mathbf{r},t). \tag{2.144}$$

For the case of a plane wave or at least in this limit, the expression has a rather neat solution. The solution follows from the relation between the fields and their respective Fourier transforms, together with the fact that the fields are real. In the case of a plane wave, the actual fields can be given on the form [69]

$$\mathbf{A}_{actual}(\mathbf{r},t)=\operatorname{Re}\left\{\mathbf{A}(\mathbf{r};\omega)e^{-i\omega t}\right\}=\frac{1}{2}\left(\mathbf{A}(\mathbf{r};\omega)e^{-i\omega t}+\mathbf{A}^*(\mathbf{r};\omega)e^{i\omega t}\right), \tag{2.145}$$

Using fields on this form in eq. (2.144) then leads to

$$\mathbf{S}(\mathbf{r},t)=\frac{1}{2}\operatorname{Re}\left\{\mathbf{E}(\mathbf{r};\omega)\times\mathbf{H}^*(\mathbf{r};\omega)\right\}+\frac{1}{2}\operatorname{Re}\left\{\mathbf{E}(\mathbf{r};\omega)\times\mathbf{H}(\mathbf{r};\omega)e^{-2i\omega t}\right\}. \tag{2.146}$$

However, a quantity of more interest is the time-averaged Poynting vector, which is given as

$$\langle\mathbf{S}(\mathbf{r};\omega)\rangle=\frac{1}{T}\int_0^T\mathbf{S}(\mathbf{r},t)dt, \tag{2.147}$$

where $T = \frac{2\pi}{\omega}$ is the period of an oscillation. Inserting eq. (2.146) in eq. (2.147), it is clear that the second term cancels following the integration, and the first term is independent on t, thus [69]

$$\langle \mathbf{S}(\mathbf{r};\omega)\rangle = \frac{1}{2}\,\mathrm{Re}\left\{\mathbf{E}(\mathbf{r};\omega)\times\mathbf{H}^{*}(\mathbf{r};\omega)\right\}, \tag{2.148}$$

from which the time-averaged power passing through an area is found by integrating the time-averaged Poynting vector over the normal to the area as [69]

$$\langle P\rangle = \int_A \langle \mathbf{S}(\mathbf{r};\omega)\rangle\cdot\hat{\mathbf{n}}dA, \tag{2.149}$$

which in the case of a periodic one-dimensional structure with the interface perpendicular to the z-direction becomes

$$\langle P\rangle = \int_{-\Lambda/2}^{\Lambda/2} \langle \mathbf{S}(\mathbf{r};\omega)\rangle\cdot\hat{\mathbf{z}}dx. \tag{2.150}$$

The transmittance of a plane wave through a structure like that shown in fig. 2.15, can for either a magnetic or electric field polarised along y and propagating in the xz-plane in the positive z-direction, be expressed as

$$\tau = \frac{\langle P_\tau\rangle}{\langle P_i\rangle} \tag{2.151}$$

where $\langle P_\tau\rangle$ is the transmitted power, and $\langle P_i\rangle$ is the incident power, expressed on the form in eq. (2.150). Here the expression for the transmittance will be found on the basis of a magnetic field polarised along y. Considering the incident field, it is clear that for a plane wave propagating towards the structure under a given angle with respect to the z-axis, θ, the field can be given as

$$\mathbf{H}_i(x,z;\omega) = \hat{\mathbf{y}}H_i e^{ik_x x}e^{ik_z z}, \tag{2.152}$$

where $k_x = k_0 n_i\sin(\theta)$, $k_z = k_0 n_i\cos(\theta)$, and n_i is the refractive index of the medium before the structure which is assumed real. This implies that

$$\mathbf{E}_i(x,z;\omega) = \frac{-1}{ik_0\varepsilon_i}\sqrt{\frac{\mu_0}{\varepsilon_0}}\nabla\times\mathbf{H}_i(x,z;\omega) = \frac{1}{k_0\varepsilon_i}\sqrt{\frac{\mu_0}{\varepsilon_0}}\left(\hat{\mathbf{x}}k_z - \hat{\mathbf{z}}k_x\right)H_i(x,z;\omega), \tag{2.153}$$

where all the dependencies on the frequency will be omitted when moving forward, as it should be implicitly understood what fields and quantities are frequency-dependent in this section. The time-averaged Poynting vector of the incident field becomes

$$\langle \mathbf{S}_0(x,z)\rangle = \frac{1}{2k_0\varepsilon_i}\sqrt{\frac{\mu_0}{\varepsilon_0}}\left|H_i(x,z)\right|^2\left(\hat{\mathbf{x}}k_x + \hat{\mathbf{z}}k_z\right) = \frac{1}{2k_0\varepsilon_i}\sqrt{\frac{\mu_0}{\varepsilon_0}}\left|H_i\right|^2\left(\hat{\mathbf{x}}k_x + \hat{\mathbf{z}}k_z\right), \tag{2.154}$$

where the real part has been omitted since k_x and k_z are assumed real. The incident power is for this case given as

$$\langle P_i\rangle = \Lambda\langle S_{0,z}(x,z)\rangle = \frac{\Lambda}{2k_0\varepsilon_i}\sqrt{\frac{\mu_0}{\varepsilon_0}}\left|H_i\right|^2 k_z. \tag{2.155}$$

The transmitted field consists of a superposition of the modes that can propagate through the structure,

$$\mathbf{H}_\tau(x,z) = \hat{\mathbf{y}}\sum_n H_{\tau,n}e^{i(k_x+nG)x}e^{i\beta_n z}. \tag{2.156}$$

where β_n is the wavenumber in the z-direction for a given mode n. The reason for this is that $k^2 = \beta_n^2 + (k_x + nG)^2$, which implies that $\beta_n^2 = k^2 - (k_x + nG)^2$, being the reason for the n subscript on β. The associated electric field is given as

$$\mathbf{E}_\tau(x,z) = \frac{1}{k_0\varepsilon_\tau}\sqrt{\frac{\mu_0}{\varepsilon_0}}\sum_n \left(\hat{\mathbf{x}}\beta_n - \hat{\mathbf{z}}(k_x + nG)\right) H_{\tau,n} e^{i(k_x+nG)x} e^{i\beta_n z}. \tag{2.157}$$

From which the cross product in eq. (2.148) becomes

$$\mathbf{E}_\tau(x,z)\times\mathbf{H}_\tau^*(x,z) = \frac{1}{k_0\varepsilon_\tau}\sqrt{\frac{\mu_0}{\varepsilon_0}}\sum_{n,n'} \left(\hat{\mathbf{x}}(k_x + nG) + \hat{\mathbf{z}}\beta_n\right) H_{\tau,n}H_{\tau,n'}^* e^{i(n-n')Gx} e^{i(\beta_n-\beta_{n'})z}. \tag{2.158}$$

Integrating the real part is equal to integrating and then taking the real part. Thus, the averaged transmitted power becomes

$$\langle P_\tau\rangle = \frac{1}{2}\frac{1}{k_0\varepsilon_\tau}\sqrt{\frac{\mu_0}{\varepsilon_0}}\sum_{n,n'} \mathrm{Re}\left\{\beta_n H_{\tau,n}H_{\tau,n'}^* e^{i(\beta_n-\beta_{n'})z}\int_{-\Lambda/2}^{\Lambda/2} e^{i(n-n')Gx}dx\right\}, \tag{2.159}$$

where the choice of integration limits ensures that the result is purely real, namely

$$\int_{-\Lambda/2}^{\Lambda/2} e^{i(n-n')Gx}dx = \Lambda\frac{\sin\left(\pi\left(n-n'\right)\right)}{\pi\left(n-n'\right)}, \tag{2.160}$$

which equals $\Lambda\delta_{n,n'}$, where $\delta_{n,n'}$ is the Kronecker delta. This simplifies the expression for the transmitted power significantly to

$$\langle P_\tau\rangle = \frac{1}{2}\frac{\Lambda}{k_0\varepsilon_\tau}\sqrt{\frac{\mu_0}{\varepsilon_0}}\sum_n |H_{\tau,n}|^2\ \mathrm{Re}\left\{\beta_n\right\}. \tag{2.161}$$

The transmittance through the structure from eq. (2.151) can then, by inserting eqs. (2.155) and (2.161), be given as

$$\tau = \frac{\varepsilon_i}{\varepsilon_\tau}\sum_n \frac{|H_{\tau,n}|^2}{|H_i|^2}\frac{\mathrm{Re}\left\{\beta_n\right\}}{k_z} = \frac{\varepsilon_i}{\varepsilon_\tau}\sum_n \frac{|H_{\tau,n}|^2}{|H_i|^2}\frac{\mathrm{Re}\left\{\beta_n\right\}}{k_0 n_i\cos(\theta)}. \tag{2.162}$$

For the case where the last and first layer consists of air the expression simplifies further into

$$\tau = \sum_n \frac{|H_{\tau,n}|^2}{|H_i|^2}\frac{\mathrm{Re}\left\{\beta_n\right\}}{k_0\cos(\theta)}. \tag{2.163}$$

The reasoning for this section given in the beginning was, besides showing how the transmittance through the structure was calculated, also related to how the correct mode weighting coefficient is chosen when implementing FMM numerically. The reason why it is worth dwelling on this is related to the fact that, when the command `eig` in MATLAB solves the eigenvalue problem, it orders the eigenvalues in ascending order. A way to find the right mode weighting coefficient in the first layer can be done by using the last factor in eq. (2.162), and then checking for the case where

$$\frac{\mathrm{Re}\left\{\beta_m^{(1)}\right\}}{k_0 n_i\cos(\theta)} = 1, \tag{2.164}$$

the mode, m', for which this equality is satisfied, the associated coefficient $a_{m'} = 1$, so that $\bar{\mathbf{a}} = \delta_{m'}$. Even though the unmodified version of the factor emerges in the expression for the transmittance originally, the modified fraction nonetheless still describes the relation between the numerically solved β's in the first layer and propagating wave-number of the chosen plane wave, and thus makes it possible to choose the right mode weighting coefficient for the incident field.

2.4.5.3 Calculating the Transmittance through a Photonic Crystal

This section will briefly outline how the FMM is used to model a photonic crystal with a finite extension in the z-direction and then compare how the transmittance spectra pair up with the band structures calculated for infinite photonic crystals. The structure modelled here should somewhat resemble a two-dimensional photonic crystal slab placed in a parallel plate metal waveguide. Furthermore, it is assumed that there is only in-plane propagation, which leads to the case that only the S-polarisation can exist within the waveguide, as mentioned earlier.

The photonic crystal in this case consists of free-standing high index circular rods in a hexagonal grid with a total of ten lines of rods in the z-direction. The radii of the rods are $r_{rods} = 168.6$ μm and the period between the rods along one of the crystal axes is $\Lambda = 687.6$ μm. Furthermore, $\varepsilon_{rods} = 3.4^2$ and $\varepsilon_{surroundings} = 1^2$. In order to model this photonic crystal with FMM, it is necessary to split it into layers homogeneous along z, and periodic along x. A division into layers along the z-direction has been sketched in fig. 2.18c. However, the homogeneity along z naturally results in what should be circles, instead appearing rugged, especially if too few layers are used to construct them, which in turn could lead to erroneous results. This can be seen when comparing the different spectra in fig. 2.19 as neither the placement nor the size of even the first band gap are the same between the two graphs. Furthermore, the graph in fig. 2.19a does not express the second and third band gap which is clearly found in the graph seen in fig. 2.19b. The graphs in figs. B.1 and 2.19 are all for in-plane propagation corresponding to the **K**-direction in the first Brillouin zone and the inserts show the relative permittivity profile. In the later sections, where the FMM is used as a way to evaluate measured spectra, a division equivalent to the one presented in fig. 2.19b is used, as a more crude division is not sufficient for a converged result, as noticeable differences are found when comparing with i.e. fig. B.1a, whereas a more refined division does not result in any significant changes, when compared with, i.e., fig. B.1b, especially not compared to the additional computational time.

The result of the FMM for the above settings is in fig. 2.20 compared with the band structure of S-polarised modes of a comparable infinite photonic crystal calculated with PWE, where similar figures can be found for the **M**-direction in fig. B.2. In fig. 2.20 the symmetry of the bands is denoted since only the even modes can be excited, as the odd modes do not match the symmetry of the input field [70,71]. Furthermore, the part of the bands that can not be reached given that the propagation is taken to be in the **K**-direction is also shown explicitly, where the high symmetry points in reciprocal space covered in the **K**-direction has been sketched in fig. 2.18a, and in fig. 2.18b for the **M**-direction. If the graphs are examined closely some minor discrepancies are found, e.g., that the precise placement and size of the gaps does not match exactly. However, it should be noted that both graphs are calculated numerically, and thus both are prone to numerical errors. Furthermore, the PWE assumes an infinite photonic crystal, whereas the FMM assumes that the photonic crystal only contains ten lines of rods. Numerical errors, the slightly different modelled structures, or a combination of both could potentially be enough to explain the minor discrepancies observed between the graphs. Hence all things considered a satisfactory agreement between the PWE band structure and the FMM transmittance spectrum is found given the overall fine overlap between the band gaps in the band structure and the reflectance bands of the transmittance spectrum, the FMM can therefore be directly compared to the later obtained transmittance spectra.

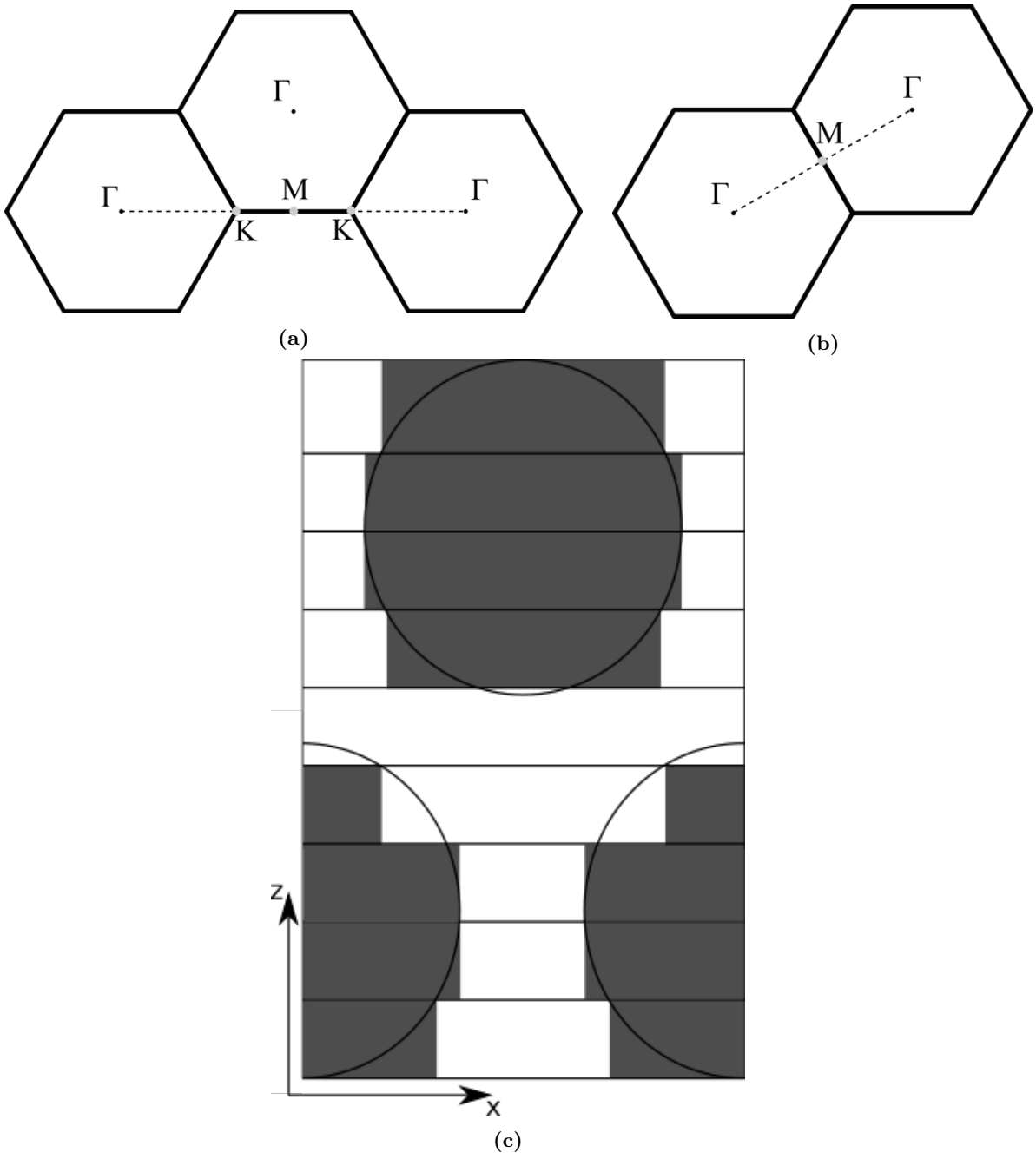

Figure 2.18: High symmetry points that are covered when going in the **(a)** **K**-direction, and **(b)** **M**-direction in reciprocal space. **(c)** A skecth showing how the photonic crystal is divided into homogeneous layers along z.

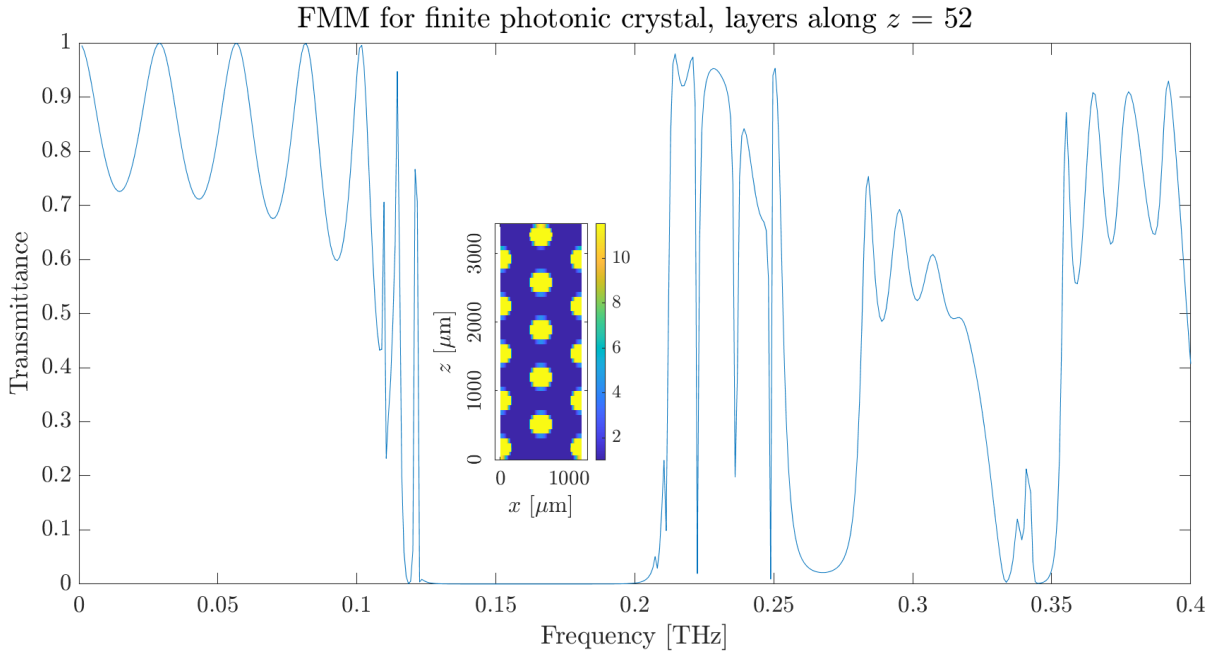

(a)

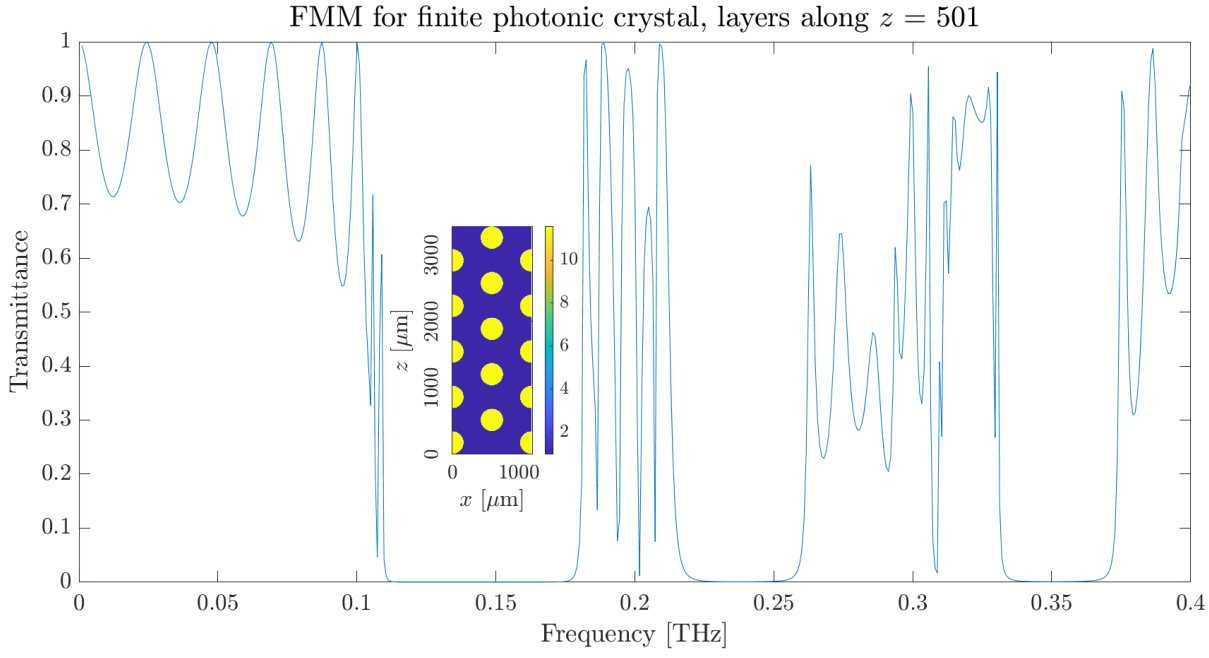

(b)

Figure 2.19: (a)-(b) Shows the transmittance of S-polarised radiation through a photonic crystal that is composed of 10 lines of rods along z, which is parallel with the **K**-direction in the first Brillouin zone. The insert in each figure shows the relative permittivity profile, where $\varepsilon_{rods} = 3.4^2$ and $\varepsilon_{surroundings} = 1^2$. The intermediate values arise from a geometric averaging of the relative permittivity for the points around the interface between the rods and the surrounding medium. The radii of the rods are $r_{rods} = 168.6$ μm and the period between the rods along one of the crystal axes is $\Lambda = 687.6$ μm. The spectra for other number of layers along z, can be found in fig. B.1.

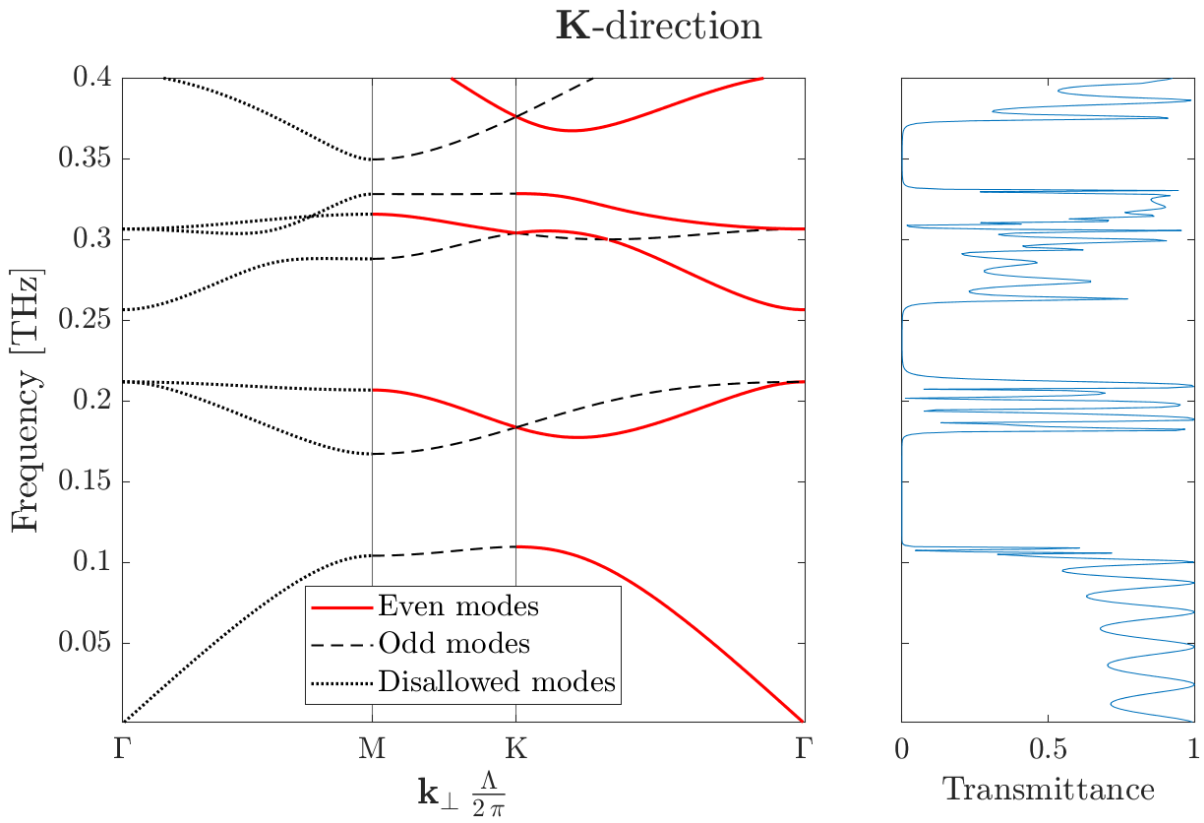

Figure 2.20: A comparison between the band diagram calculated with PWE for an infinite photonic crystal seen on the left and the transmittance calculated with FMM seen on the right, both only for S-polarisation. In the figure to the left, only the even modes can be excited, since the odd modes do not match the symmetry of the input field [70, 71] and the disallowed modes are not covered for the given propagation direction. The number of layers along z used for the FMM is identical to that of fig. 2.19b. Again the photonic crystal for the FMM is composed of 10 lines of rods along z, which is parallel with the **K**-direction in the first Brillouin zone, and $\varepsilon_{rods} = 3.4^2$, $\varepsilon_{surroundings} = 1^2$, $r_{rods} = 168.6$ μm, $\Lambda = 687.6$ μm. Similar figures for the **M**-direction can be found in fig. B.2.

2.5 Iterative Method for Solving Large Photonic Crystal Problems

For calculations of cavity or waveguide states, the method outlined in section 2.2 could be used, however, the cell under consideration would have to be extended to a supercell. This cell would consist of multiple unit cells in which a discontinuity could be introduced to represent the cavity or waveguide. However, getting a satisfying resolution of the supercell using the standard method of PWE for very large cells is difficult since the computation time scales poorly with the eigenvalue solver scaling as N^3. [72] Furthermore, the memory requirement also scales poorly, and hence extending this method into very large supercells or supercells in three dimensions becomes practically impossible. For these reasons, it is necessary to find another method to calculate the band structure of supercells.

To this end, an iterative method using the Fast Fourier Transform (FFT) can be employed. This method was first developed for tackling similar problems in quantum mechanics, however, as the operator in question, eq. (2.19), is also Hermitian the method can be extended into optics. The method uses the variational principle, which states that any trial function to the operator in question will always result in a higher expectation value than if the trial function had been an eigenvector [60]. An iterative approach may therefore be employed to continually improve the guess of the trial vector, apply the operator and evaluate if the expectation value of the trial vector is sufficiently converged. This is an advantage as the most computationally expensive step of taking the operator on some trial vector will amount to taking a Fourier transform which computationally goes as $N\log(N)$ and is hence much more feasible for large problems.

2.5.1 In-Plane Propagation in a Photonic Crystal

As was previously proposed, all two-dimensional photonic crystals will be measured using a parallel metal plate sample holder, and therefore, only the S-polarisation will be considered. In this case, the field can be expressed as a Fourier series on the form,

$$\mathbf{E}_{\mathbf{k},n}(\mathbf{r}) = \hat{\mathbf{z}} \sum_{\mathbf{G}} q_{\mathbf{G},\mathbf{k},n} e^{i(\mathbf{G}+\mathbf{k})\cdot\mathbf{r}}. \tag{2.165}$$

Here the sum over $\mathbf{G}$ amounts to summing over each component in the vector, i.e., $\mathbf{G} = m_x G_x \hat{\mathbf{x}} + m_y G_y \hat{\mathbf{y}}$. The corresponding $\mathbf{H}$ field can then be given as

$$\mathbf{H}_{\mathbf{k},n}(\mathbf{r}) = \sum_{\mathbf{G}} h_{\mathbf{G},\mathbf{k},n} \hat{\mathbf{z}} \times \frac{\mathbf{G}+\mathbf{k}}{|\mathbf{G}+\mathbf{k}|} e^{i(\mathbf{G}+\mathbf{k})\cdot\mathbf{r}}, \tag{2.166}$$

this field is constructed such that it naturally satisfies $\nabla \cdot \mathbf{H} = 0$. For the convenience of the reader, the Hermitian operator is rewritten here using bra-ket notation,

$$\hat{O}|\mathbf{H}\rangle = k_0^2 |\mathbf{H}\rangle, \qquad \hat{O} = \nabla \times \frac{1}{\varepsilon(\mathbf{r})} \nabla \times . \tag{2.167}$$

Due to the variational principle, it can then be said

$$1 - \frac{\langle \mathbf{H}|\hat{O}|\mathbf{H}\rangle}{\sqrt{\langle \mathbf{H}|\hat{O}|\mathbf{H}\rangle}\sqrt{\langle \hat{O}\mathbf{H}|\mathbf{H}\rangle}} \leq \delta, \tag{2.168}$$

with δ being an arbitrarily small constant. The idea is then to construct an algorithm that iteratively changes some trial vector until it conforms to eq. (2.168) within some chosen error δ. To begin, the effect of the operator $\hat{O}$ on a Fourier series is examined

$$\nabla \times |\mathbf{H}\rangle = \hat{\mathbf{z}} \sum_{\mathbf{G}} |\mathbf{h}\rangle i |\mathbf{G}+\mathbf{k}| e^{i(\mathbf{G}+\mathbf{k})\cdot\mathbf{r}} = \hat{\mathbf{z}} \sum_{\mathbf{G}} |\mathbf{f}\rangle e^{i(\mathbf{G}+\mathbf{k})\cdot\mathbf{r}}, \tag{2.169}$$

with $|\mathbf{f}\rangle$ being the vector containing the states $|\mathbf{f}\rangle = i|\mathbf{G}+\mathbf{k}||\mathbf{h}\rangle$, introduced to reduce clutter. This can then be Fourier transformed into real space where the reciprocal dielectric profile can be multiplied onto the resulting transform. The result may then be transformed back into reciprocal space as

$$\frac{1}{\varepsilon(\mathbf{r})} \nabla \times |\mathbf{H}\rangle = \hat{\mathbf{z}} \sum_{\mathbf{G}} |\mathbf{a}\rangle e^{i(\mathbf{G}+\mathbf{k})\cdot\mathbf{r}}, \tag{2.170}$$

after which the last curl can be applied as

$$\nabla \times \frac{1}{\varepsilon(\mathbf{r})} \nabla \times |\mathbf{H}\rangle = \sum_{\mathbf{G}} |\mathbf{a}\rangle i |\mathbf{G}+\mathbf{k}| \frac{\mathbf{G}+\mathbf{k}}{|\mathbf{G}+\mathbf{k}|} \times \hat{\mathbf{z}}\, e^{i(\mathbf{G}+\mathbf{k})\cdot\mathbf{r}} = \sum_{\mathbf{G}} \hat{\mathbf{z}} \times \frac{\mathbf{G}+\mathbf{k}}{|\mathbf{G}+\mathbf{k}|} |\mathbf{p}\rangle e^{i(\mathbf{G}+\mathbf{k})\cdot\mathbf{r}}, \tag{2.171}$$

with $|\mathbf{p}\rangle = -i|\mathbf{G}+\mathbf{k}||\mathbf{a}\rangle$. As can be seen eq. (2.171) is the same as eq. (2.166) except for the Fourier coefficients hence only the Fourier coefficients are needed to carry out the operator, and hence to test if the trial vector is indeed an eigenvector.

The method used in this project is a slightly modified version of the preconditioned conjugate-gradient method presented by M. P. Teter et al. in [73]. In this method, the gradient of a given function is computed, after which this gradient is used to create a so-called change vector. This change vector is then added to the existing parameters in such a way that it minimises the function. This is iteratively done while forcing each new change vector to be a conjugate of the previous with respect to the operator in question. The problem with this method is that for a problem with a broad interval of eigenvalues the method converges very slowly. This can be shown by considering a nearly converged state $|\mathbf{C}_m\rangle$, to the operator in question

$$|\mathbf{C}_m\rangle = |\mathbf{H}_m\rangle + \sum_{i \neq m} \epsilon_i |\mathbf{H}_i\rangle. \tag{2.172}$$

Here ϵ_i is some small parameter with $\epsilon_i^2 \sim 0$. The sum then represents the error of the state $|\mathbf{C}_m\rangle$ with respect to the converged state $|\mathbf{H}_m\rangle$, dubbed the error vector. Hence it is this error one wants to recover when proceeding with the algorithm. However, as the ϵ parameters are small when squared, it is not possible to recover this vector easily. Instead, the residual vector is calculated as

$$|\mathbf{R}\rangle = \lambda_m |\mathbf{C}_m\rangle - \hat{O}|\mathbf{C}_m\rangle, \tag{2.173}$$

here $\lambda_m = \langle \mathbf{C}_m | \hat{O} | \mathbf{C}_m \rangle$ which in the case of normalised states, $|\mathbf{C}_m\rangle$ and $|\mathbf{H}_m\rangle$, is also the eigenvalue to the state $|\mathbf{H}_m\rangle$. The goal is then to get the residual vector on a form resembling the error vector, which can then be used to get the actual eigenstate from the trial state. To proceed eq. (2.172) is inserted into eq. (2.173), which results in the following expression for the residual vector

$$|\mathbf{R}\rangle = \sum_{i \neq m} \epsilon_i (\lambda_m - \lambda_i) |\mathbf{H}_i\rangle. \tag{2.174}$$

As can be seen from eq. (2.174) if the difference between eigenvalues m and i are large. This may result in some of the eigenvectors in question being overrepresented, and hence no projection

of the residual vector will be a good approximation to the error vector which in turn would result in slow convergence. The problem is better behaved if the residual vector is multiplied by the inverse of the operator as this better reproduces the error vector [73]. This is then what constitutes the preconditioning in the name of the method, but inverting the operator matrix is quite expensive computationally and hence another approach is desirable. This is done by approximating the inverse of the operator and it turns out that the approximation does not need to be very good, though it is important that the operator is always positive and definite such that the residual vector is never zero. With the procedure used for the operator in this case the operator becomes almost diagonal as the high wavenumber plane waves end up dominating such that each of these would almost constitute an eigenvector themselves. Hence the procedure proposed in [73] is to precondition the residual vector by means of a diagonal matrix meant to equalise the contribution of each plane wave such that they converge at the same rate. However, before constructing this precondition matrix the residual vector has to be calculated.

The procedure is started by guessing a state $|\mathbf{C}^{(n)}\rangle$. Here the dependence on band and $\mathbf{k}$ is suppressed, and the superscript n denotes the iteration in question. This state is then made orthonormal to any previously found states for the $\mathbf{k}$-point in question, dubbed $|\mathbf{H}_j\rangle$,

$$|\mathbf{C}'^{(n)}\rangle = |\mathbf{C}^{(n)}\rangle - \sum_j \langle \mathbf{H}_j|\mathbf{C}^{(n)}\rangle |\mathbf{H}_j\rangle. \tag{2.175}$$

The resulting vector is then normalised as

$$|\mathbf{C}''^{(n)}\rangle = \frac{|\mathbf{C}'^{(n)}\rangle}{\sqrt{\langle \mathbf{C}'^{(n)}|\mathbf{C}'^{(n)}\rangle}}. \tag{2.176}$$

after which the residual vector can be calculated as

$$|\mathbf{R}^{(n)}\rangle = \langle \mathbf{C}''^{(n)}|\hat{O}|\mathbf{C}''^{(n)}\rangle |\mathbf{C}''^{(n)}\rangle - \hat{O}|\mathbf{C}''^{(n)}\rangle, \tag{2.177}$$

this amounts to taking the difference between the projection of the vector resulting from the operator onto the $|\mathbf{C}''\rangle$ state, and the resulting vector itself. Using this as a gradient would result in the problems outlined earlier and hence this is where the precondition comes in. The proposed procedure is to construct a diagonal matrix with entries [73],

$$K_{\mathbf{G}}^{(n)} = \frac{27 + 18x_{\mathbf{G}}^{(n)} + 12\left(x_{\mathbf{G}}^{(n)}\right)^2 + 8\left(x_{\mathbf{G}}^{(n)}\right)^3}{27 + 18x_{\mathbf{G}}^{(n)} + 12\left(x_{\mathbf{G}}^{(n)}\right)^2 + 8\left(x_{\mathbf{G}}^{(n)}\right)^3 + 16\left(x_{\mathbf{G}}^{(n)}\right)^4}. \tag{2.178}$$

with $x_{\mathbf{G}}$ being the ratio of the kinetic energy of a plane wave with the given wavenumber to the total kinetic energy of the trial vector. This has little meaning in the context of optics, however, if the method outlined in [73] is followed the operator from quantum mechanics, $-\frac{1}{2}\nabla^2$, should still be used to calculate the kinetic energy. Using this approach, the kinetic energy of a plane wave becomes,

$$E_{kin}(\mathbf{G}) = \langle Ae^{i(\mathbf{G}+\mathbf{k})\cdot\mathbf{r}}| - \frac{1}{2}\nabla^2 |Ae^{i(\mathbf{G}+\mathbf{k})\cdot\mathbf{r}}\rangle = \frac{1}{2}|\mathbf{G}+\mathbf{k}|^2, \tag{2.179}$$

while the total energy of the residual vector becomes

$$E_{kin,tot}^{(n)} = \langle \mathbf{R}^{(n)}| - \frac{1}{2}\nabla^2 |\mathbf{R}^{(n)}\rangle = \frac{1}{2}\sum_{\mathbf{G}} |r_{\mathbf{G}}^{(n)}|^2 \, |\mathbf{G}+\mathbf{k}|^2. \tag{2.180}$$

By these definitions the variable $x_{\mathbf{G}}$ is given as,

$$x_{\mathbf{G}}^{(n)} = \frac{E_{kin}(\mathbf{G})}{E_{kin,tot}^{(n)}} = \frac{|\mathbf{G}+\mathbf{k}|^2}{\sum_{\mathbf{G}'} |r_{\mathbf{G}'}^{(n)}|^2 \, |\mathbf{G}'+\mathbf{k}|^2}. \tag{2.181}$$

The precondition matrix, eq. (2.178), can be understood in the context of the convergence for each frequency. As mentioned, the goal is for each of the frequency components to converge at about the same rate as otherwise most of the iterations will be making small changes to the high frequency components. The precondition matrix was found by Teter et. al. [73] and it can be seen from eq. (2.178) that when $x_{\mathbf{G}}^{(n)} = 0 \Rightarrow K_{\mathbf{G}}^{(n)} = 1$, hence leaving the low-frequency components unchanged while when $x_{\mathbf{G}}^{(n)} \to \infty \Rightarrow K_{\mathbf{G}}^{(n)} \to \frac{1}{2\,(x_{\mathbf{G}}^{(n)}-1)}$, which was found to result in about the same convergence for each component. Thus, to calculate the error vector the residual vector is multiplied by the preconditioning matrix

$$|\mathbf{R}'^{(n)}\rangle = \bar{\bar{\mathbf{K}}}^{(n)} \, |\mathbf{R}^{(n)}\rangle. \tag{2.182}$$

If the preconditioned residual vector is then orthogonal to all bands and the current trial vector it would be the gradient, and this could then be used to calculate the state of the next iteration. However, this is not implicitly true, and hence the other eigenstates, along with the trial vector, have to be projected out of $|\mathbf{R}'\rangle$ as

$$|\mathbf{Y}^{(n)}\rangle = |\mathbf{R}'^{(n)}\rangle - \sum_j \langle \mathbf{H}_j | \mathbf{R}'^{(n)} \rangle |\mathbf{H}_j\rangle - \langle \mathbf{C}''^{(n)} | \mathbf{R}'^{(n)} \rangle |\mathbf{C}''^{(n)}\rangle. \tag{2.183}$$

From this, an error vector, $|\mathbf{F}^{(n)}\rangle$, can be constructed. However, conjugacy between the residual vector at the current iteration and all the previous error vectors $|\mathbf{F}^{(n-1)}\rangle, |\mathbf{F}^{(n-2)}\rangle, |\mathbf{F}^{(n-3)}\rangle, ...$, should be ensured, for which the following procedure can be used

$$|\mathbf{F}^{(n)}\rangle = |\mathbf{Y}^{(n)}\rangle + \gamma^{(n)} |\mathbf{F}^{(n-1)}\rangle, \qquad \gamma^{(n)} = \frac{\langle \mathbf{Y}^{(n)} | \mathbf{Y}^{(n)} \rangle}{\langle \mathbf{Y}^{(n-1)} | \mathbf{Y}^{(n-1)} \rangle}, \qquad \gamma^{(1)} = 0. \tag{2.184}$$

The final task is then to change the current trial vector by use of this gradient. However, the following calculations will be significantly simplified if the error vector in question $|\mathbf{F}^{(n)}\rangle$ is orthonormal to the trial vector in question and can be made so by

$$|\mathbf{D}'^{(n)}\rangle = |\mathbf{F}^{(n)}\rangle - \langle \mathbf{C}''^{(n)} | \mathbf{F}^{(n)} \rangle |\mathbf{C}''^{(n)}\rangle, \tag{2.185}$$

$$|\mathbf{D}^{(n)}\rangle = \frac{|\mathbf{D}'^{(n)}\rangle}{\sqrt{\langle \mathbf{D}'^{(n)} | \mathbf{D}'^{(n)} \rangle}}. \tag{2.186}$$

To construct the next trial vector $|\mathbf{C}^{(n+1)}\rangle$ the subspace spanned by $|\mathbf{C}''^{(n)}\rangle$ and $|\mathbf{D}^{(n)}\rangle$ is searched for the combination which minimises the energy, under the constraint that the resulting vector should also be normalised. This can be done as,

$$|\mathbf{C}^{(n+1)}\rangle = |\mathbf{C}''^{(n)}\rangle \cos(\phi) + |\mathbf{D}^{(n)}\rangle \sin(\phi), \tag{2.187}$$

due to the orthonormality of $|\mathbf{C}''^{(n)}\rangle$ and $|\mathbf{D}^{(n)}\rangle$, the new trial vector will also be of unit length independent of the angle ϕ. Then to determine the best combination, the "energy"-functional is minimised in the parameter ϕ, with the functional being given as

$$E^{(n)}[\phi] = \frac{\langle \mathbf{C}^{(n+1)} | \hat{O} | \mathbf{C}^{(n+1)} \rangle}{\langle \mathbf{C}^{(n+1)} | \mathbf{C}^{(n+1)} \rangle}, \tag{2.188}$$

which can be expanded as

$$E^{(n)}[\phi] = \langle \mathbf{C}''^{(n)}|\hat{O}|\mathbf{C}''^{(n)}\rangle \cos^2(\phi) + \langle \mathbf{D}^{(n)}|\hat{O}|\mathbf{D}^{(n)}\rangle \sin^2(\phi) + \mathrm{Re}\left\{\langle \mathbf{D}^{(n)}|\hat{O}|\mathbf{C}''^{(n)}\rangle\right\} \sin(2\,\phi) = A^{(n)}\,\cos^2(\phi) + B^{(n)}\,\sin^2(\phi) + C^{(n)}\,\sin(2\,\phi). \quad (2.189)$$

This functional may then be minimised in ϕ by taking the derivative with respect to ϕ and setting it equal to zero. This would then yield two possible minima at

$$\phi_{min}^{(n)} = \frac{1}{2}\,\tan^{-1}\left(\frac{2\,C^{(n)}}{A^{(n)} - B^{(n)}}\right) + p\frac{\pi}{2}, \qquad p = \{0, 1\}. \quad (2.190)$$

These two angles may then be tested to determine which of the two yields the lowest energy, and that one may then be used to construct the next state $|\mathbf{C}^{(n+1)}\rangle$. Thus by insertion of this state in eq. (2.168) the error can be determined and if it is below a predetermined threshold the vector is said to have converged and is kept as an eigenvector $|\mathbf{H}_j\rangle = |\mathbf{C}^{(n+1)}\rangle$. This process may then be started over until the desired amount of bands have converged. It is worth noting that both the band and **k**-dependence of the states were suppressed, hence each band has to be converged for each **k**-point of interest. Thus this method is not well suited for small problems, but it scales much better than the standard plane wave expansion otherwise used in this project and is capable of calculating the eigenstates of super cells containing defects, which allows for the calculation of guiding bands in, e.g., waveguides, or the bound modes in cavities.

2.5.2 Out-Of-Plane Propagation in a Photonic Crystal

The FFT method presented in the previous section can also be modified to account for out-of-plane propagation. The modification in relation to the iterative calculation is rather insignificant and mostly applies in regards to obtaining the expressions for the fields and establishing the boundary conditions. As a first step, the requirements for having out-of-plane propagation together with the complications that emerge will be considered. Afterwards the additional steps needed for handling photonic crystal slabs sandwiched by parallel metal plates are presented.

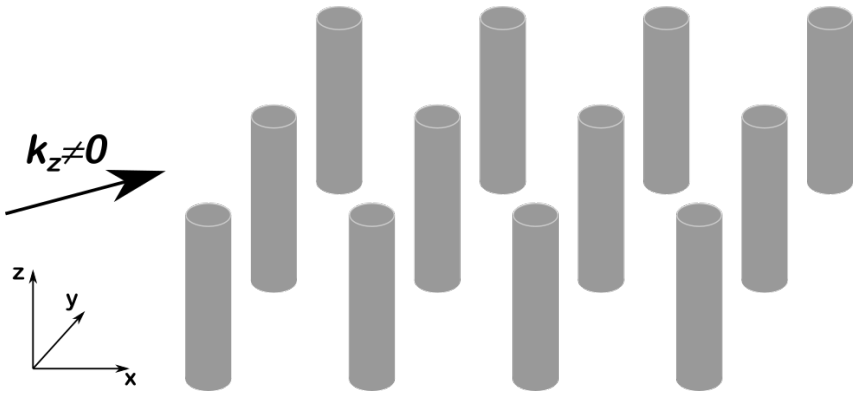

Figure 2.21: Sketch of a photonic crystal. Assume the rods extend infinitely in the z-direction, with out-of-plane propagation.

To have out-of-plane propagation, it is a requirement that $k_z \neq 0$, sketched in fig. 2.21. Hence the dielectricity profile in the plane of a mode with an out-of-plane component will not have mirror

symmetry, leading to no clear distinction between the two polarisations [43]. For out-of-plane propagation, the fields now naturally need to have components both in and out of the plane in order to satisfy the requirement that the magnetic field should be divergence-free. Given the ambiguity of the polarisation of out-of-plane modes, the choice of field does not simplify the problem. However, the rigid divergence requirement together with the associated hermitian operator, eq. (2.167), makes it easier to work with the magnetic field, and the field can thus be expressed similar to that in eq. (2.166) as

$$\mathbf{H}_{\mathbf{k},n}(\mathbf{r}) = \sum_{\mathbf{G},\zeta} \hat{\boldsymbol{\gamma}}_{\mathbf{G},\mathbf{k},n,\zeta}\, h_{\mathbf{G},\mathbf{k},n,\zeta}\, e^{i(\mathbf{G}+\mathbf{k})\cdot\mathbf{r}}, \tag{2.191}$$

where $\zeta = [1,2]$, is related to the polarisation of the field, with $\hat{\boldsymbol{\gamma}}_{\mathbf{G},\mathbf{k},n,1} \perp \hat{\boldsymbol{\gamma}}_{\mathbf{G},\mathbf{k},n,2} \perp (\mathbf{k}+\mathbf{G})$ meaning that the set $\{\hat{\boldsymbol{\gamma}}_{\mathbf{G},\mathbf{k},n,\zeta}\}$ spans all the possible polarisations the field of the given Fourier component could have. The field is thus composed of a superposition of two Fourier series, which in the end also gives the polarisation of the field. The unit vectors can quite easily be determined and ensured to be perpendicular to the direction of propagation by using

$$\hat{\boldsymbol{\gamma}}_{\mathbf{G},\mathbf{k},n,1} = \frac{\hat{\mathbf{z}} \times (\mathbf{G}+\mathbf{k})}{|\hat{\mathbf{z}} \times (\mathbf{G}+\mathbf{k})|}, \tag{2.192}$$

$$\hat{\boldsymbol{\gamma}}_{\mathbf{G},\mathbf{k},n,2} = \frac{\mathbf{G}+\mathbf{k}}{|\mathbf{G}+\mathbf{k}|} \times \hat{\boldsymbol{\gamma}}_{\mathbf{G},\mathbf{k},n,1}. \tag{2.193}$$

Here the first unit vector only has components in the plane and is perpendicular to the propagation direction, which follows naturally given it is found from the cross-product of the out-of-plane direction and the propagation direction. The second unit vector is then determined from the cross product between the propagation direction and the found unit vector, ensuring that both unit vectors are perpendicular to the direction of propagation. The special case $k_x = k_y = m_x = m_y = 0$ requires individual handling since both eqs. (2.192) and (2.193) would equate to $\mathbf{0}$. This is circumvented by choosing $\hat{\boldsymbol{\gamma}}_{\mathbf{G},\mathbf{k},n,1} = \hat{\mathbf{x}}$ and $\hat{\boldsymbol{\gamma}}_{\mathbf{G},\mathbf{k},n,2} = \text{sign}\{k_z\}\,\hat{\mathbf{y}}$.
Using the same procedure corresponding to those presented in eqs. (2.169) to (2.171) has the form

$$\begin{aligned} \nabla \times \mathbf{H}_{\mathbf{k},n}(\mathbf{r}) &= \sum_{\mathbf{G},\zeta} \left[i\,(\mathbf{G}+\mathbf{k}) \times \hat{\boldsymbol{\gamma}}_{\mathbf{G},\mathbf{k},n,\zeta} \right] h_{\mathbf{G},\mathbf{k},n,\zeta}\, e^{i(\mathbf{G}+\mathbf{k})\cdot\mathbf{r}} \\ &= i \sum_{\mathbf{G},\zeta} (-1)^{\zeta-1}\, \hat{\boldsymbol{\gamma}}_{\mathbf{G},\mathbf{k},n,(3-\zeta)}\, h_{\mathbf{G},\mathbf{k},n,\zeta}\, |\mathbf{G}+\mathbf{k}|\; e^{i(\mathbf{G}+\mathbf{k})\cdot\mathbf{r}}, \end{aligned} \tag{2.194}$$

with the reason for the change of ζ in the subscript of $\hat{\boldsymbol{\gamma}}$ and the introduction of the factor $(-1)^{\zeta-1}\,|\mathbf{G}+\mathbf{k}|$ being found from eqs. (2.192) and (2.193) together with the relation $\mathbf{A} \times (\mathbf{B} \times \mathbf{C}) = \mathbf{B}\,(\mathbf{A}\cdot\mathbf{C}) - \mathbf{C}\,(\mathbf{A}\cdot\mathbf{B})$. The next step is to find the equation similar to eq. (2.170) which is

$$\frac{1}{\varepsilon(\mathbf{r})} \nabla \times \mathbf{H}_{\mathbf{k},n}(\mathbf{r}) = i \sum_{\mathbf{G},\zeta} (-1)^{\zeta-1}\, \hat{\boldsymbol{\gamma}}_{\mathbf{G},\mathbf{k},n,(3-\zeta)}\, a_{\mathbf{G},\mathbf{k},n,\zeta}\, |\mathbf{G}+\mathbf{k}|\; e^{i(\mathbf{G}+\mathbf{k})\cdot\mathbf{r}}, \tag{2.195}$$

where $a_{\mathbf{k},\mathbf{G},n,\zeta}$ are the Fourier coefficients for the Fourier series associated to transforming the

left-hand side from real space to reciprocal space. The last rotation then results in

$$\begin{aligned}\nabla \times \left[\frac{1}{\varepsilon(\mathbf{r})}\nabla \times \mathbf{H}_{\mathbf{k},n}(\mathbf{r})\right] &= i\sum_{\mathbf{G},\zeta}(-1)^{\zeta-1}\left[i\left(\mathbf{G}+\mathbf{k}\right)\times\hat{\boldsymbol{\gamma}}_{\mathbf{G},\mathbf{k},n,(3-\zeta)}\right]a_{\mathbf{G},\mathbf{k},n,\zeta}\left|\mathbf{G}+\mathbf{k}\right|e^{i(\mathbf{G}+\mathbf{k})\cdot\mathbf{r}} \\ &= \sum_{\mathbf{G},\zeta}\hat{\boldsymbol{\gamma}}_{\mathbf{G},\mathbf{k},n,\zeta}\,a_{\mathbf{G},\mathbf{k},n,\zeta}\left|\mathbf{G}+\mathbf{k}\right|^2 e^{i(\mathbf{G}+\mathbf{k})\cdot\mathbf{r}} \\ &= \sum_{\mathbf{G},\zeta}\hat{\boldsymbol{\gamma}}_{\mathbf{G},\mathbf{k},n,\zeta}\,f_{\mathbf{G},\mathbf{k},n,\zeta}\,e^{i(\mathbf{G}+\mathbf{k})\cdot\mathbf{r}},\end{aligned} \tag{2.196}$$

with $f_{\mathbf{G},\mathbf{k},n,\zeta} = a_{\mathbf{G},\mathbf{k},n,\zeta}\left|\mathbf{G}+\mathbf{k}\right|^2$. As was shown in the former section it is evident that the first and last expressions are identical except for a difference in the Fourier coefficients, thus the iterative algorithm from the former section can also be applied for out-of-plane propagation.

2.5.3 Photonic Crystal Slabs

Having considered out-of-plane propagation in a two-dimensional photonic crystal, the next thing worth considering is out-of-plane propagation in a two-dimensional photonic crystal slab, which is a two-dimensional photonic crystal with the slight variation that it has a finite thickness. In a non-absorbing slab, the modes can either be radiating, meaning they have a limited lifetime within the slab, or guided, which are confined to the slab indefinitely [74].

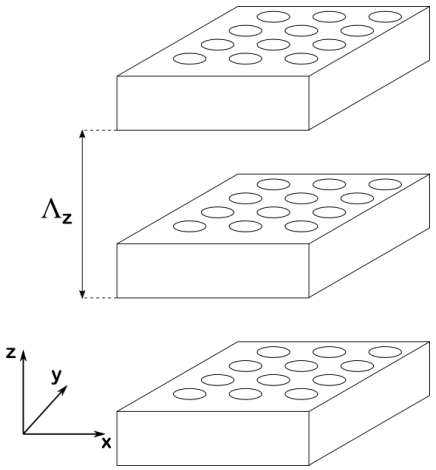

Figure 2.22: Sketch of stacked photonic crystal slabs with period Λ_z in the z-direction.

By only considering the guided modes the derivation presented in subsection 2.5.2 still holds with minor changes and can be justified by the fact that the radiating modes lie above the light line [74]. The change, when compared to what was outlined in subsection 2.5.2, is that the structure is assumed periodic in the z-direction too, i.e., it consists of stacked photonic crystal slabs which are separated by layers of the surrounding medium as sketched in fig. 2.22. Thus the reciprocal lattice vector is modified as

$$\mathbf{G} = m_x G_x\hat{\mathbf{x}} + m_y G_y\hat{\mathbf{y}} \quad\Longrightarrow\quad \mathbf{G} = m_x G_x\hat{\mathbf{x}} + m_y G_y\hat{\mathbf{y}} + m_z G_z\hat{\mathbf{z}},$$

but otherwise the above considerations still hold.

2.5.3.1 Photonic Crystal Slabs in Metallic Parallel Plate Waveguide

In order to model the circumstances under which the transmission measurements in this project are carried out, the model should be able to imitate a photonic crystal slab sandwiched by parallel metal plates, as is sketched in fig. 2.23a. Given that the boundary condition requires the tangential part of the electric field at an interface is preserved, it has to be zero at both metal interfaces, since the electric field inside a perfect electric conductor is zero. Using eq. (2.194) the tangential parts of the electric field is found as

$$E_{\mathbf{k},n,x}(\mathbf{r}) = \frac{-1}{i\omega\varepsilon_0\varepsilon(\mathbf{r})}\sum_{\mathbf{G}} i\Bigg[-\frac{(m_xG_x+k_x)(m_zG_z+k_z)}{|\hat{\mathbf{z}}\times(\mathbf{G}+\mathbf{k})|}h_{\mathbf{G},\mathbf{k},n,1} \\ -\frac{-(m_yG_y+k_y)}{|\hat{\mathbf{z}}\times(\mathbf{G}+\mathbf{k})|}h_{\mathbf{G},\mathbf{k},n,2}\,|\mathbf{G}+\mathbf{k}|\Bigg] e^{i(\mathbf{G}+\mathbf{k})\cdot\mathbf{r}}, \tag{2.197}$$

$$E_{\mathbf{k},n,y}(\mathbf{r}) = \frac{-1}{i\omega\varepsilon_0\varepsilon(\mathbf{r})}\sum_{\mathbf{G}} i\Bigg[-\frac{(m_yG_y+k_y)(m_zG_z+k_z)}{|\hat{\mathbf{z}}\times(\mathbf{G}+\mathbf{k})|}h_{\mathbf{G},\mathbf{k},n,1} \\ -\frac{(m_xG_x+k_x)}{|\hat{\mathbf{z}}\times(\mathbf{G}+\mathbf{k})|}h_{\mathbf{G},\mathbf{k},n,2}\,|\mathbf{G}+\mathbf{k}|\Bigg] e^{i(\mathbf{G}+\mathbf{k})\cdot\mathbf{r}}. \tag{2.198}$$

Both these components have to equal zero at $z=[0,h]$ which is enforced by restructuring the modelled structure by mirroring the photonic crystal through either of the metal interfaces, as seen in fig. 2.23b. Only in-plane propagation will be considered, meaning $k_z=0$. This also means that the above equations have a rather useful symmetry with respect to m_z, which can be exploited to enforce the boundary conditions. An attempt to clarify this symmetry has been made here

$$E_{\mathbf{k},n,x}(\mathbf{r}) = \Gamma_0(\mathbf{r})\sum_{\mathbf{G}} i\left[-\Gamma_1 m_zG_z h_{\mathbf{G},\mathbf{k},n,1} + \Gamma_2\,|\mathbf{G}+\mathbf{k}|\;h_{\mathbf{G},\mathbf{k},n,2}\right] e^{i(\mathbf{G}_\perp+\mathbf{k})\cdot\mathbf{r}_\perp}e^{im_zG_zz}, \tag{2.199}$$

$$E_{\mathbf{k},n,y}(\mathbf{r}) = \Gamma_0(\mathbf{r})\sum_{\mathbf{G}} i\left[-\Gamma_2 m_zG_z h_{\mathbf{G},\mathbf{k},n,1} - \Gamma_1\,|\mathbf{G}+\mathbf{k}|\;h_{\mathbf{G},\mathbf{k},n,2}\right] e^{i(\mathbf{G}_\perp+\mathbf{k})\cdot\mathbf{r}_\perp}e^{im_zG_zz}, \tag{2.200}$$

where the different Γs have been introduced to suppress factors which effects are indifferent for the following arguments. In order for the field components in eqs. (2.199) and (2.200) to obey the boundary condition both terms in the parenthesis have to be odd as this would allow for eqs. (2.199) and (2.200) to be rewritten as

$$\sum_{m_z=1}^{\infty}\Gamma_{m_z}(\mathbf{r})\left[e^{im_zG_zz}-e^{-im_zG_zz}\right] = \sum_{m_z=1}^{\infty}2i\Gamma_{m_z}(\mathbf{r})\sin(m_zG_zz), \tag{2.201}$$

where the $\Gamma_{m_z}(\mathbf{r})$ is used to suppress all non-relevant factors. Here it has been utilised that if the parentheses in eqs. (2.199) and (2.200) are odd the terms arising from $-m_z$ and m_z will be equal except for a sign. Hence it is only necessary to calculate half the sum as shown in eq. (2.201), and as $G_z=\frac{2\pi}{2h}$, this then satisfies the boundary condition $z=[0,h]$. For the parentheses to be odd $h_{\mathbf{G},\mathbf{k},n,1}$ has to be symmetric around $m_z=0$ as m_zG_z is asymmetric, whereas $h_{\mathbf{G},\mathbf{k},n,2}$ has to be asymmetric around $m_z=0$ since $|\mathbf{G}+\mathbf{k}|$ is symmetric.

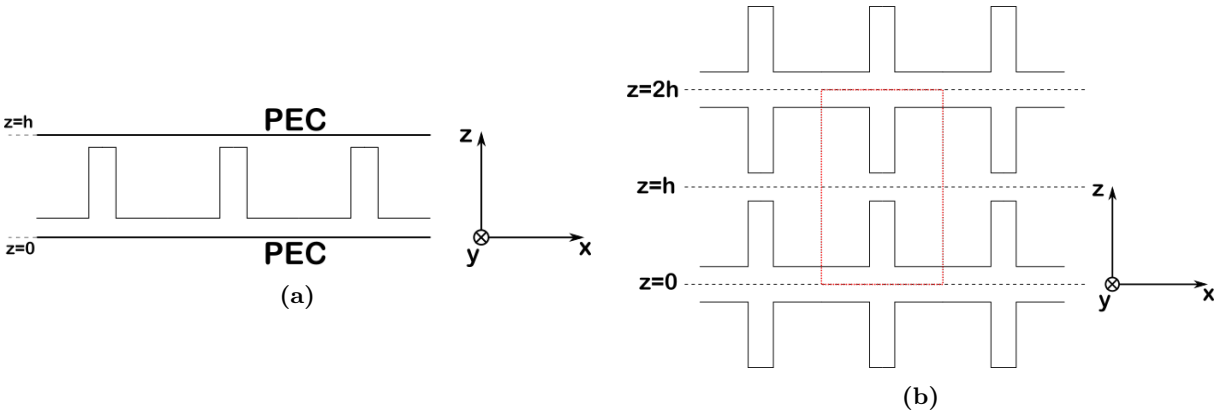

Figure 2.23: **(a)** Sketch of a photonic crystal structure in a parallel metal plate waveguide, where PEC stands for perfect electric conductor. **(b)** A periodic structure in which the situation in **(a)** can be imitated, where the red outline shows the unit cell from the side illustrating the symmetry around $z = h$.

2.5.4 Considerations for the Dielectric Constant

By introducing the third dimension the fields can not be decoupled completely and hence further considerations have to be made on how the dielectric constant is applied, e.g., eq. (2.195). As the field is only calculated in a discrete set of points, care has to be taken around the dielectric boundaries. This is because each point represents the field in the area around said point, and the boundary therefore has to be handled with care, the procedure of which is covered in this section.
Inspecting eq. (2.19) the dielectric constant has to be applied to the curl of the magnetic field which through Ampere's law is related to the displacement field as

$$\nabla \times \mathbf{H}(\mathbf{r}) = -i\omega \mathbf{D}(\mathbf{r}). \tag{2.202}$$

Hence the fields of interest at the boundary are the electric and displacement field, which both have preserved components

$$\mathbf{D}_1^n = \mathbf{D}_2^n, \tag{2.203}$$

$$\mathbf{E}_1^t = \mathbf{E}_2^t, \tag{2.204}$$

where the superscript n denotes the normal component and superscript t denotes the tangential component. These are related through the polarisation, eqs. (2.6) and (2.9), which in turn can be given as

$$\mathbf{P}(\mathbf{r}) = (\varepsilon(\mathbf{r}) - 1)\,\varepsilon_0 \mathbf{E}(\mathbf{r}) = \left(1 - \frac{1}{\varepsilon(\mathbf{r})}\right) \mathbf{D}(\mathbf{r}). \tag{2.205}$$

As can be seen, the polarisation field has a different proportionality to the dielectric function, depending on if it is expressed using the electric or displacement field. Hence if it is the polarisation that is averaged over the cell it can be seen that the projection onto the tangential and normal components of the surface should be treated differently. This can be seen by letting the polarisation be expressed as the sum of a normal and tangential component

$$\mathbf{P}(\mathbf{r}) = \mathbf{P}^n(\mathbf{r}) + \mathbf{P}^t(\mathbf{r}) = \left(1 - \frac{1}{\varepsilon(\mathbf{r})}\right) \mathbf{D}^n(\mathbf{r}) + (\varepsilon(\mathbf{r}) - 1)\,\varepsilon_0 \mathbf{E}^t(\mathbf{r}), \tag{2.206}$$

where this formulation ensures that the field in question for a given component is continuous over an interface. The average polarisation field in a gridpoint is then found as the sum of the average of each component. The average of the normal component can be found by

$$\mathbf{P}^n_{avg} = \frac{1}{V_{g.c.}} \int_{g.c.} \left(1 - \frac{1}{\varepsilon(\mathbf{r})}\right) \mathbf{D}^n(\mathbf{r}) d^3r, \tag{2.207}$$

where *g.c.* stands for gridpoint cell. Assuming that the gridpoint cell is very small makes it possible to enforce eq. (2.203) and approximate the above as

$$\mathbf{P}^n_{avg} \approx \frac{\mathbf{D}^n_{g.c.}}{V_{g.c.}} \int_{g.c.} \left(1 - \frac{1}{\varepsilon(\mathbf{r})}\right) d^3r. \tag{2.208}$$

As the averaging is done by utilising a subgrid in each cell, the integration is converted to a sum over the N_{sub} subgrid points in a gridpoint cell as

$$\begin{aligned} \mathbf{P}^n_{avg} &\approx \frac{\mathbf{D}^n_{g.c.}}{V_{g.c.}} \sum_{j=1}^{N_{sub}} \left(1 - \frac{1}{\varepsilon(\mathbf{r}_j)}\right) V_{s.g.c.} \\ &= \frac{\mathbf{D}^n_{g.c.}}{N_{sub}} \sum_{j=1}^{N_{sub}} \left(1 - \frac{1}{\varepsilon(\mathbf{r}_j)}\right) = \mathbf{D}^n_{g.c.} - \mathbf{D}^n_{g.c.} \frac{1}{N_{sub}} \sum_{j=1}^{N_{sub}} \frac{1}{\varepsilon(\mathbf{r}_j)}, \end{aligned} \tag{2.209}$$

where it has been used that $\frac{V_{s.g.c.}}{V_{g.c.}} = N^{-1}_{sub}$, where *s.g.c* stands for subgridpoint cell. By using eq. (2.204) instead of eq. (2.203) the same procedure can be used for the tangential part which leads to

$$\mathbf{P}^t_{avg} \approx \frac{\varepsilon_0 \mathbf{E}^t_{g.c.}}{N_{sub}} \sum_{j=1}^{N_{sub}} (\varepsilon(\mathbf{r}_j) - 1) = -\varepsilon_0 \mathbf{E}^t_{g.c.} + \varepsilon_0 \mathbf{E}^t_{g.c.} \frac{1}{N_{sub}} \sum_{j=1}^{N_{sub}} \varepsilon(\mathbf{r}_j). \tag{2.210}$$

The averaged dielectric constant that is associated to the tangential part of the field is from eq. (2.210) found as

$$\varepsilon_t = \frac{1}{N_{sub}} \sum_{j=1}^{N_{sub}} \varepsilon(\mathbf{r}_j), \tag{2.211}$$

which is a simple geometric average. However, the one associated to the normal part of the field is a bit more peculiar. Given that the averaging in eq. (2.209) is of the inverse dielectric profile, the inverse of this averaging is taken to obtain the averaged dielectric constant for the normal component of the field as

$$\varepsilon_n = \left[\frac{1}{N_{sub}} \sum_{j=1}^{N_{sub}} \frac{1}{\varepsilon(\mathbf{r}_j)} \right]^{-1}. \tag{2.212}$$

These then have to be applied to the rotation of the magnetic field, eq. (2.195), projected onto the normal vector and the tangential vector, this can be expressed in tensor form as

$$\overleftrightarrow{\boldsymbol{\varepsilon}} = \varepsilon_n |\hat{\mathbf{n}}\rangle\langle\hat{\mathbf{n}}| + \varepsilon_t |\hat{\mathbf{t}}\rangle\langle\hat{\mathbf{t}}| = \varepsilon_n |\hat{\mathbf{n}}\rangle\langle\hat{\mathbf{n}}| + \varepsilon_t \left(\overleftrightarrow{\mathbf{I}} - |\hat{\mathbf{n}}\rangle\langle\hat{\mathbf{n}}| \right) \tag{2.213}$$

and in order to correctly introduce an inverse dielectric component, it should be the inverted tensor component since for the general case

$$\left[\overleftrightarrow{\boldsymbol{\varepsilon}}^{-1}\right]_q \neq \frac{1}{\left[\overleftrightarrow{\boldsymbol{\varepsilon}}\right]_q}, \tag{2.214}$$

where q represents an arbitrary component. So to summarise, the product $\frac{1}{\varepsilon(\mathbf{r})}\mathbf{D}$ should be substituted by $\left[\overleftrightarrow{\boldsymbol{\varepsilon}}(\mathbf{r})\right]^{-1}\mathbf{D}$. The tensor used to model the problems in this project can, in Cartesian coordinates, be given as

$$\overleftrightarrow{\boldsymbol{\varepsilon}} = (\varepsilon_n - \varepsilon_t)\begin{bmatrix} \frac{\varepsilon_t}{\varepsilon_n-\varepsilon_t} + n_x^2 & n_x n_y & 0 \\ n_y n_x & \frac{\varepsilon_t}{\varepsilon_n-\varepsilon_t} + n_y^2 & 0 \\ 0 & 0 & \frac{\varepsilon_t}{\varepsilon_n-\varepsilon_t} \end{bmatrix}. \tag{2.215}$$

The reason for all the contributions that should contain a factor of n_z is zero, is a consequence of the way the gridpoint cells are constructed, as each gridpoint cell is taken to be homogeneous in the z-direction. This means that within a gridpoint cell the normal vector of the interface will be contained in xy-plane, resulting in $n_z = 0$.

3 | Method

The samples fabricated in this project are one- and two-dimensional photonic crystals. The one-dimensional photonic crystals are all-dielectric gratings based on wafers of thickness 100 μm, with etch depths of up to 28 μm. The two-dimensional photonic crystals will be fabricated in two configurations, air holes in silicon and silicon rods standing on a silicon substrate. These will be fabricated on 100 μm and 200 μm wafers respectively. The holes will go through the wafer, while rods of heights up to 150 μm are sought. To this end, the following chapter will introduce the methods used to fabricate and characterise the various samples. For the sake of brevity, the numerous optimisation rounds that came before the final procedure of each method will not be covered in detail, though the insight gained will be touched upon when discussing the final modus operandi. The chapter begins by introducing the various forms of dry etching procedures, with a focus on reactive ion etching (RIE). Following a brief overview of photolithography, the method of laser ablation on two different time scales is introduced, followed by a brief overview of the laser system used in this project. Finally, an introduction to the mechanisms of Terahertz Time-Domain Spectroscopy (THz-TDS) is provided.

3.1 Reactive Ion Etching

This section will cover the principles of one of the main fabrication methods utilised in this project, RIE, which is a subcategory of plasma-assisted dry etching [75]. The method is used to fabricate the Fano structures and the photonic crystal based on "free-standing silicon rods". The rods will not be truly freestanding, instead, a thin silicon base is retained. Dry etching is capable of anisotropic etch, which is its main advantage over wet etching where any exposed surface is etched, though the rate can vary along different crystal planes. This results in smaller undercuts, which allows for smaller features. Dry etching can be divided into three main categories, ion etching, high-pressure chemical plasma etching, and reactive ion etching. All methods use a mask to protect parts of the surface. The characteristic etch profiles are seen in fig. 3.1b.
Ion etching: Also known as sputtering and ion milling, is a method where noble gases or large clusters of atoms are ionised by plasma and afterwards accelerated towards the surface of the sample by an applied voltage. The accelerated ions transfer part of their kinetic energy to the atoms of the sample, knocking them out of the surface. The method is often used for sample preparation, where unwanted adsorbed atoms are removed from the sample surface [76]. This process does not involve any reactions and has low selectivity, close to 1:1 for many combinations of materials. Selectivity refers to the removal rate of different atoms on the surface, which in ion etching is primarily controlled by the binding energy of said atoms. Selectivity is calculated as

the etch rate of the sample divided by the etch rate of the mask. Metals are weakly bound, while salts are strongly bound. The method can provide highly anisotropic etch, however, the non-specificity of the method means that the mask is etched at a similar rate as the sample surface. Combining this with etch rates of a couple nm/min, the method is unsuitable for the needs of this project because the thickness of the mask is limited to a couple hundreds of nanometers, while the desired etch depth is above ten micrometers in the case of the Fano structures, and above 100 micrometers for the photonic crystal. [75, 77, 78]

High-pressure chemical plasma etching: In this method, reactive species, typically halogen radicals in the case of Si, are created. These radicals form gaseous byproducts when they interact with the surface of the sample. These byproducts are pumped away, exposing fresh sample atoms to be etched. Thus, the surface of the sample is removed via chemical reactions. A mask that has a low reaction rate with the radicals is used to protect the underlying substrate. This process therefore requires a suitable combination of etching gas (etchant), substrate, and mask. The problem with only using chemical plasma etching is that the method is isotropic, resulting in undercutting, where the substrate below the mask is etched away at the same rate, hence it is unsuitable for the needs of this project. [75, 77, 78]

Reactive ion etching: Is a combination of the two former categories, and is the method used in this project. A combination of ionised atoms and radicals is used to etch the sample, resulting in etch rates that are greater than the sum of the two methods [79]. When the ions collide with the sample surface, bonds are broken which make the surface atoms more likely to react with the radicals, enhancing etching rates and allowing otherwise inert surfaces to be chemically etched. Because the ions are only accelerated vertically, they do not enhance the lateral etch rate, increasing the anisotropy of the etch compared to high-pressure chemical plasma etching. To achieve high aspect ratios (>5:1), known as deep reactive ion etching (DRIE), the sample either needs to be cooled down to $\sim -110^\circ$ (cryogenic DRIE) or a passivisation layer has to be adsorbed to the sidewalls of the etch, known as the Bosch process. The mechanism of both methods is to make etching impossible without the ion bombardment, which only happens in the vertical direction. The available equipment to this project group only allows for regular RIE, and the undercutting therefore has to be accounted for in the designs. [75, 77, 78]

Both the plasma and the DC bias accelerating the positively charged ions towards the sample surface is commonly created by a capacitively-coupled plasma (CCP) source. Here, a radio frequency (RF) source is used to drive a voltage (100 to 1000V) between two electrodes. [78] The sample is placed on the plate connected to the RF source, while the opposing electrode is grounded, see fig. 3.1a. The frequency is commonly 13.56 MHz, slow enough that the electrons can move to and be absorbed by the conducting plates, yet fast enough that the positively charged atoms can not. The electrons accumulating at the plate connected to the RF source generate a DC bias between it and the positively charged plasma. In a standard CCP, this bias voltage between the sample and the plasma is controlled by the power of the RF source, which has to be relatively high to facilitate adequate plasma density. Therefore, there will be significant ion bombardment with this setup, such that the masking material erodes relatively fast, despite it being inert to the chemical etching. How fast the mask is removed depends on the material and the power of the RF source. Using photoresist as the mask, the sample to mask erosion is below 5:1 [78]. A good mask for reactive ion etching is therefore both inert to the etchant gas, and exhibits minimal erosion from the ion bombardment. This often necessitates the use of hardmasks, such as SiO_2, Al, Cr, and Au. In the case of Si as the sample material and SF_6 as the etchant, both Cr and Al have high selectivity, however, Cr can withstand more energetic ion bombardment than Al and is therefore the used hardmask in the project [80].

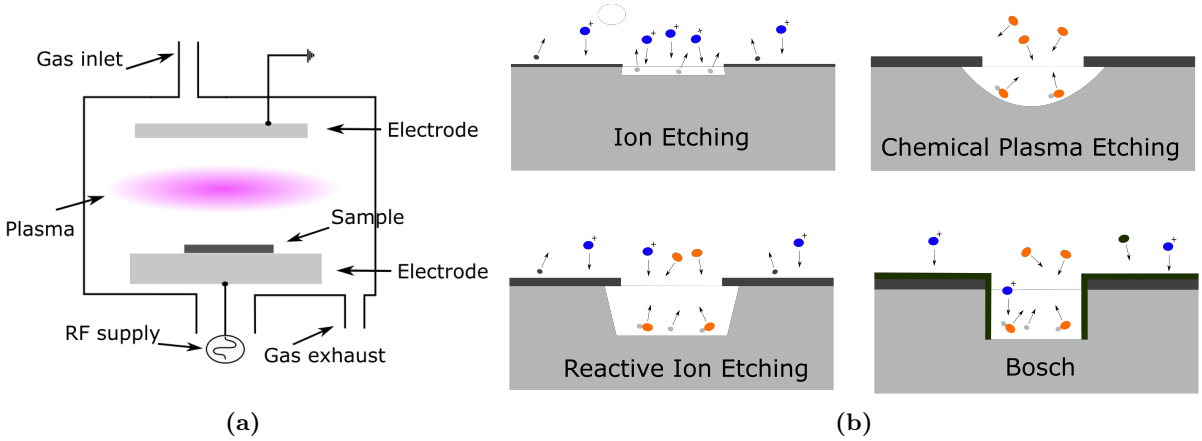

Figure 3.1: **(a)** Sketches the reactive ion etching machine. **(b)** Sketches the expected etching profiles when using the different plasma-assisted dry etching techniques.

The RIE machine used in this project is a Surface Technology Systems 320 PC RIE. The variable parameters that can be directly controlled with this machine are

- Choice of gas: CHF_3, O_2, CF_4, He, C_3F_8, and SF_6. The optimal choice of gas depends on the sample material and further affects which masks can be used. In this project, SF_6 is used to etch Si. Because fluorine radicals can etch silicon without the help of ion bombardment, the anisotropy of the etch is limited when no surface passivisation steps are used [78].
- RF power: Increasing the power increases both the energy and concentration of available electrons creating the ions used for bombardment. It also increases the DC bias between the sample and plasma, increasing the sputtering of both sample and mask. It is therefore expected that increasing the wattage will increase the anisotropy of the etch, but also reduce the maximum etch depth for a given mask layer, which was observed in this project.
- Chamber pressure: Changes the concentration of etchant gas in the chamber. For all relevant combination of pressure and RF power, the ratio between ionised and neutral particles will be much less 0.01. If the sample material can be etched without the assistance of the ion bombardment, an increase in the chamber pressure decreases the anisotropy of the etch because directional etch of the ions becomes less pronounced, but the overall etching rate is also increased [75].
- Gas flow rate: Influences how long the gas remains in the chamber. Increasing the flow rate will increase the etch rate.

The majority of the work thus consists of optimising these various input parameters, with the exception of the choice of gas, until a recipe is found that produces satisfactory samples, which in this project was

- RF power: 100 W
- Chamber pressure: 20 mTorr.

- Gas flow rate: 70 sccm of SF6.
- Hardmask: Up to 200 nm of Cr.
- Etch time: Up to 210 minutes.

3.1.1 RIE Undercutting

As sketched in fig. 3.1b there is significant undercutting when using the RIE process. This happens because the highly reactive species in the etchant gas can etch the wafer material without the help of the ion bombardment, although this happens at a slower rate, allowing the substrate around the edges of the hardmask to be etched.

Undercutting causes two artifacts that must be accounted for. For one, the structures become smaller than the mask designs, and secondly, the sidewall of the etch has a slope of less than 90°. Both of these effects are visible in fig. 3.2(c) and fig. 3.2(d), where it can be seen that the Si rod beneath the Cr layer has had its radius reduced below the initial Cr radius determined by the photolithography mask. In the case of the Fano structures, this is not a significant issue because the etch depths, and therefore the etch times, are relatively short, meaning that the undercutting taking place is not enough to completely remove the structures. However, because it is expected that the free-standing rods need to have heights above 100 micrometers, the etch times are much longer, and undercutting becomes a significant issue. To account for this, tests were performed, measuring the loss of radii as a function of time from spherical patterns with varying starting radii, presented in fig. 3.2(a). The slopes of the fits are between -0.41μm/min and -0.49μm/min. This information, along with the slope of the etch profile, can be used to decide the mask dimensions resulting in a photonic band gap at the frequency of interest. The slope of the samples are determined by analysing SEM images in ImageJ [81]. Based on the measurements, the average slope of the rods are $\sim 60°$. To account for this slope in the PWE model used to design the structures, a geometric averaging is performed, i.e., it is required that the volume of the produced and modelled rods are the same,

$$r^2\pi h = \frac{1}{3}h\pi\left(R_1^2 + R_2^2 + R_1R_2\right), \tag{3.1}$$

with sketches of the two rods seen in fig. 3.2(b). Solving eq. (3.1) for R_1 yields,

$$R_1(r) = \frac{\frac{-h}{\tan(\theta)} + \sqrt{\frac{h^2}{\tan^2(\theta)} - 4\left(-r^2 + \frac{h^2}{3\tan^2(\theta)}\right)}}{2}, \tag{3.2}$$

which relates the radius at the top of the produced rods to the radius of the modelled rods. However, the reduction in radius from the etching process should also be accounted for. As stated, the free-standing rods will be made from wafers of thickness $\sim 200\mu$m, and the aim is to have heights up to 150 μm. The reason that the height must be known is because it determines the etch time, which in turn determines how much of the radius is lost to undercutting. After being etched for 210 minutes, the average height of the rods was 157 micrometers, meaning the etch rate is $\sim 0.75\mu$m/min. It then follows that the radii of the rods on the mask must be increased by $R_{comp} \sim 102\mu$m,

$$R_{mask}(r) = R_1(r) + R_{comp}. \tag{3.3}$$

It is worth noting that these tests were carried out on regular wafers, and not the expensive thin wafers used to fabricate the photonic crystals. The results were later calibrated for thin wafers, where it was found that $R_{comp} \sim 120\mu$m was optimal for the produced samples.

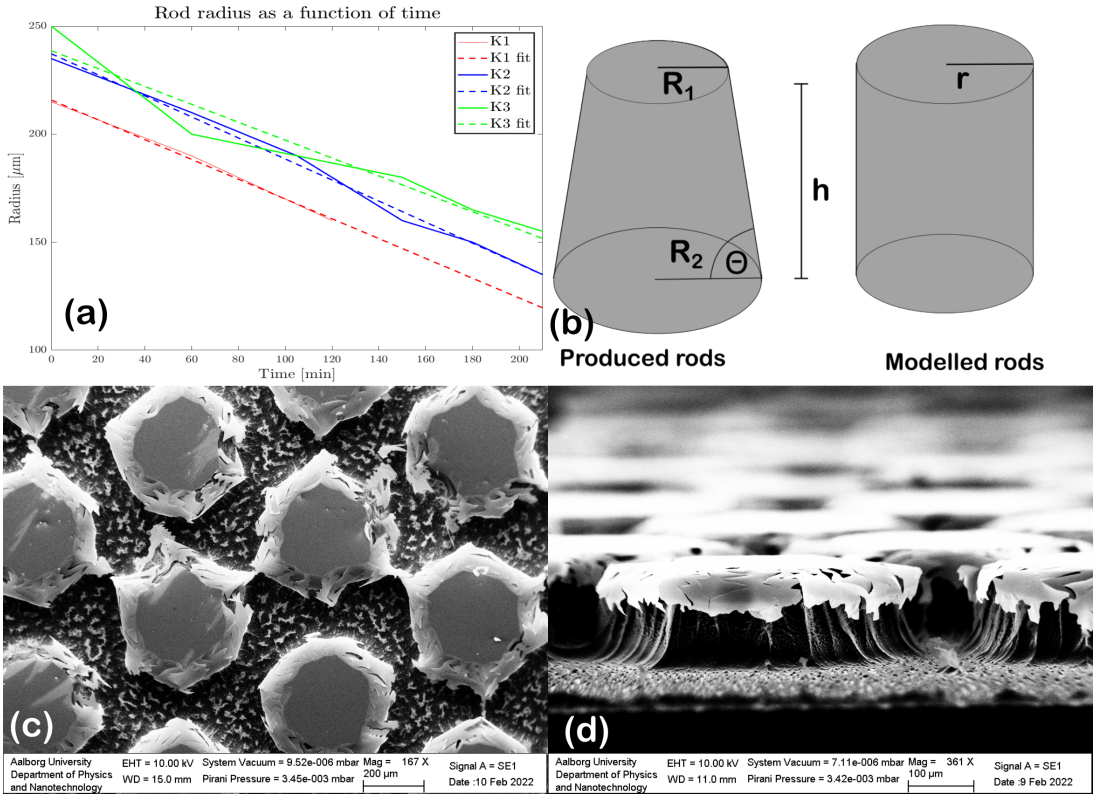

Figure 3.2: **(a)** Change in radius as a function of time. **(b)** Sketches the produced and modelled rods. **(c)** and **(d)** SEM images of sample K2 after 210 and 180 minutes of RIE, respectively.

3.1.2 Photolithography

To transfer the patterns from the photomask to the wafer, photolithography is used, utilising a positive resist. The entire fabrication process is outlined in fig. 3.3.

The wafers are cleaned by being submerged in acetone and placed in an ultrasonic bath for 10 minutes, after which they are rinsed with DI water and isopropanol, and dried using a nitrogen gun. A positive photoresist, *MICROPOSIT^{TM} S1813^{TM} G2*, is used, and the mask is printed by a *RICOH IM C5500* printer in the case of the free-standing rods, whereas a professional mask made by Delta Mask b.v. is used for the Fano structures. The photoresist is spun at 500 rpm for 15 seconds, followed by 4000 rpm for 30 seconds, after which it is placed on a 110 °C hotplate for 60 seconds. The patterns are developed using *mr-Dev 600* from *micro resist technology*. After development, the samples are rinsed with DI water, dried, and loaded in a *Cryofox Explorer 600*, where a sufficient chromium layer is deposited which, depending on the sample, is $30 - 200$ nm. Acetone is used for lift-off, removing the remaining photoresist and the chromium above it. Etch times depend on the sample, with the Fano structures being in the range 5 - 20 minutes, and the free-standing structures being in the range 150 - 210 minutes.

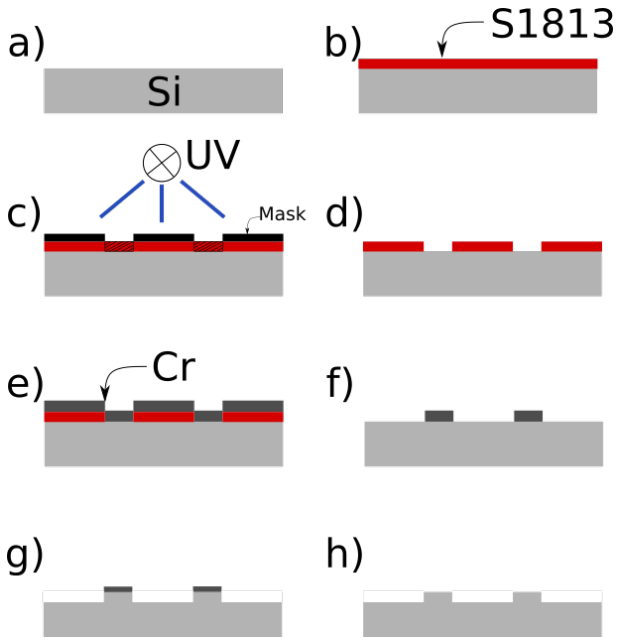

Figure 3.3: Sketches the steps used to fabricate the final structure. **(a)** Clean wafer. **(b)** Apply photoresist. **(c)** Expose photoresist. **(d)** Develop photoresist. **(e)** Deposit chromium. **(f)** Lift-off. **(g)** Reactive ion etching. **(h)** Remove excess chromium.

After the etching procedure, excess chromium is removed using *ALDRICH chromium etchant*, product number 651826.

The Fano structures are characterised using a scanning electron microscope (SEM), a profilometer, and the TeraSmart time-domain terahertz spectrometer from Menlo Systems. Measurements on M1 can be seen in fig. 3.4. The height of the strips, t, is measured using a profilometer, while the period and width, Λ and w_t, are obtained by analysing scanning electron microscope (SEM) images in the software *ImageJ* [81]. The height of the wafers, h, is determined by matching the measured transmittance oscillations with the FMM model for a three-layered structure, air-Si-Air, e.g., in fig. 3.4c the transmittance graph of a wafer is measured, along with the FMM calculated spectra for three different heights. It is clear that a height of 94μm matches the measured data for the entire spectra, and that this method is sufficiently precise, as changes to the height by $\pm 5\mu$m make the model deviate significantly from the measurements. Figure 3.4c also illustrates the absorption from water vapour, when the measurement chamber has not been sufficiently purged. From here on, all TDS measurements on Fano structures will be performed after the chamber has been purged for 5 minutes, which according to the creator of the system [82] is enough to reduce the relative humidity in the chamber from 50% to 5%. All averaged dimensions and their standard deviation can be found in table 4.1.

Having determined all relevant dimensions of the structures, the transmittance spectrum can be calculated and compared with the Fourier transform of the time-domain spectra. The spectra are obtained by averaging 500 measurements, each with a scan range of 420 ps. All measurements are made at normal incidence unless otherwise specified. A schematic of the setup, sample holder, and the cross-section of a sample can be seen in fig. 3.5. As seen in the figure, the sample holder is placed such that the incident light is collimated. The sample holder is made of aluminium and has a 45° tapered circular hole, gradually decreasing the diameter until reaching a minimum

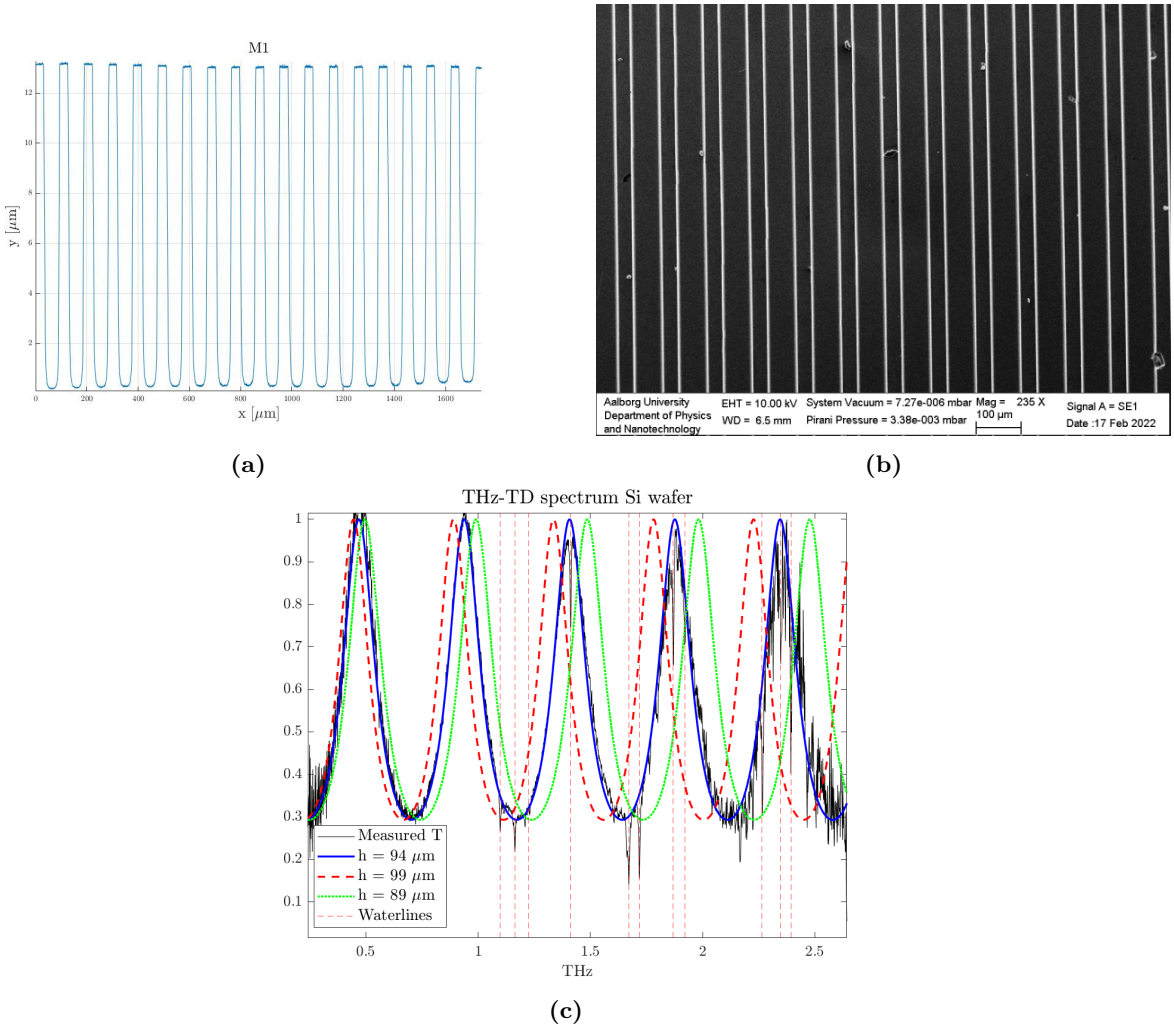

Figure 3.4: **(a)**, **(b)** profilometer and SEM measurement of sample M1. **(b)** TDS measurement and FMM model for Si wafer with $h = 94\mu\text{m} \pm 5\mu\text{m}$

radius of 6.5 mm in the holder. The sample is placed behind this hole. The sample holder is used for angles of incidence between 0° and 10°. The Fourier transform was performed in accordance with the method outlined in *Phase Retrieval in Terahertz Time-Domain Measurements: a "how to" Tutorial* by [83].

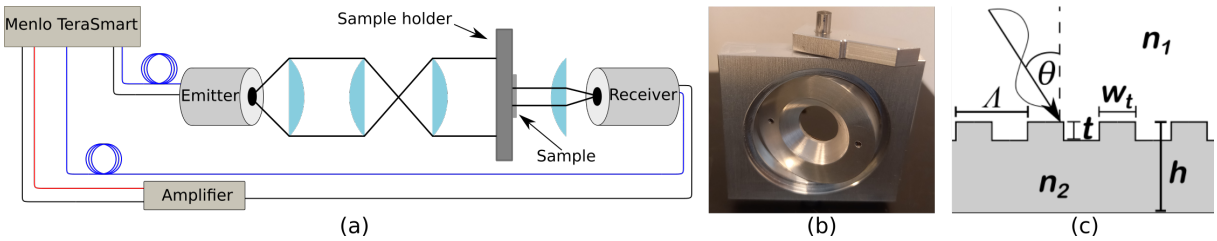

Figure 3.5: **(a)** Schematic of the experimental setup. **(b)** Image of the front side of the sample holder, in which the taper can be seen. **(c)** Sketch of the sample cross-section.

3.2 Laser Ablation

Though the fabrication of photonic crystals can be achieved through many classic clean room techniques [84–86], another technique of interest is laser ablation due to its versatility in handling a large number of materials as well as its high precision [87]. The downsides of laser ablation are that it may result in fabrication artifacts namely redeposition, and heat-affected zones resulting in structural damage [88]. Especially the structural damage is of great concern in the fabrication of photonic crystals based on air holes as it was shown in section 2.3 that the radius of the hole has to be $\frac{r}{\Lambda} > 0.42$ resulting in a very porous structure for which even a small amount of structural damage may result in the collapse of parts of the structure. Hence minimising the structural damage is crucial for the fabrication of photonic crystals based on air holes, exhibiting a high GMG ratio. To understand how this can be achieved it is worth outlining the current theory of laser ablation.

3.2.1 Laser-Matter Interaction

The fundamental principle of laser ablation is the removal of material by supplying energy in the form of photons. For a given material to be removed a sufficient amount of fluence has to be supplied for the material to ablate. This energy threshold is known as the ablation threshold. To surpass the ablation threshold, pulsed lasers are often used as the peak power of such systems is extremely high. Pulsed laser systems are categorised by the pulse length ranging from femto- to microseconds. Each pulse duration exhibits a different interaction mechanism with the material in question, hence it is worth considering the advantages and disadvantages of each pulse type. [88, 89] However, the only systems available to the project are a femto- and a nanosecond laser system, and the following considerations will thus be limited to these systems.

The femtosecond laser pulses, often referred to as ultra-fast pulses, are much faster than the characteristic relaxation times of the electron-to-ion energy transfer time or the electron heat conduction time, which are both on the order of several picoseconds, and the laser pulse is consequently done before the ablation process takes place. On the contrary, in the nanosecond laser system the process of ionisation, sample heating and, vaporization all take place while the pulse is still interacting with the sample [88, 89]. Due to the pulse duration of the femtosecond system being shorter than these characteristic parameters, it can be shown that the ablation process can be considered as a solid-vapor or solid-plasma transition, with heating occurring afterwards. Furthermore, thermal conduction into the sample may be neglected in a first-order approximation, whereas for the nanosecond pulses there is enough time for a thermal wave to propagate into the sample. [89] Because of this, ultra-fast laser ablation generally reduces the thermal damage of the sample and reduces the heat-affected zone [88]. The main mechanism of energy absorption in the two laser systems is different, as for the ultra-short pulses the system is generally best approximated as a system not in equilibrium, as all the energy is transferred to the electrons which can then be viewed as a reservoir with one temperature and the bulk sample is then another reservoir with another temperature [89]. On the other hand, the nanosecond laser system can be viewed as a system in equilibrium hence the absorption process is linear [88].
A concern with the ultra-fast pulses is the high peak intensity resulting in nonlinear effects becoming significant in this regime, with impact ionisation and photoionisation being major processes for free-electron generation during the ultra-short laser ablation [88]. Generally, in

femtosecond laser ablation the removal of material is governed by two distinct steps, the Coulomb explosion, and the thermal vaporisation. The thermal vaporisation results in more damage done to the sample, i.e., a larger heat-affected zone and is hence undesirable. The Coulomb explosion happens as energy exceeding the Fermi level is transferred to the electrons. An electric field is then created between the now free electrons and the ionized atoms at the surface. If the energy of the free electrons is larger than the binding energy of the ions in the lattice they can be removed from the surface resulting in the removal of the first few monolayers of the surface. The ablation resulting from the Coulomb explosion is also called gentle ablation [88]. If the laser power is sufficiently above the ablation threshold the Coulomb explosion is then followed by thermal vaporisation which exhibits an ablation rate that is an order of magnitude faster [88]. Due to the speed of the femtosecond pulse there is not enough time for the electrons to transfer their heat to the lattice and the result is a phase transition from solid to vapour which is then ejected from the material. Due to the heat not being transferred to the lattice the heat affected zone will be lessened when using femtosecond pulses as compared to using nanosecond pulses. [90]
If the laser power greatly exceeds the ablation threshold, the kinetic energy of the electrons may result in ionisation avalanches where the free electrons transfer some of their energy to other electrons and hence creates more free electrons. [90] However, thermal evaporation occurs on a much slower time scale and thus only happens after the Coulomb explosion. Using nanosecond laser pulses the time scale of the pulse results in the electrons being able to continually transfer their energy in the form of phonons, resulting in no Coulomb explosion taking place, and hence thermal vaporisation dominates in this regime, resulting in more heat damage done to the sample. [88, 90] Furthermore, it has been shown [91] that the Coulomb explosion process results in smoother edges and less redeposition, hence this is generally the process that is preferable for micromachining which is why the femtosecond laser system is used instead of the nanosecond laser system. An overview of the ablation process for different time scales is provided in fig. 3.6. A property worth noting is that the complete process takes on the order of 1 ms. This is in accordance with the findings that subsequent pulses may interact with one another if the processes overlap corresponding to a repetition rate above 1000 Hz. For this reason, a repetition rate of 1000 Hz was chosen for this project [92].

3.2.2 Femtosecond Laser System

In fig. 3.7 an overview of the laser setup used can be seen. The principle used is chirped pulse laser amplification (CPA), which is conducted by the Spectra-Physics Spitfire module [93]. The source pulse is supplied by the Spectra-Physics Tsunami [94], which is a Ti:sapphire mode-locked laser, with a folded cavity. The mode-locking is achieved by standard acoustic optical modulation and the system is pumped by a Spectra-Physics Millennia Pro which is a diode-pumped Nd:YAG laser [94, 95]. CPA is the main workhorse in high energy density physics (HEDP) which is the study of physics under extreme conditions. This is due to the high peak intensity of the ultra-short pulses, which when focused can obtain fluence in the range of $10^{18}\,\mathrm{W}\cdot\mathrm{cm}^{-2}$, which is necessary for laser ablation. [88].

Before CPA was invented, it was limited how high a peak intensity that could be obtained. This was due to nonlinear effects in the laser cavity, such as self-focusing, which destroyed the laser cavity as plasma was created in the cavity. CPA works by stretching a source pulse, from the femtosecond to nanosecond range, then amplifying it with a pump laser before compressing it back down. Thus at no point in the pumping step will the peak intensity result in unwanted

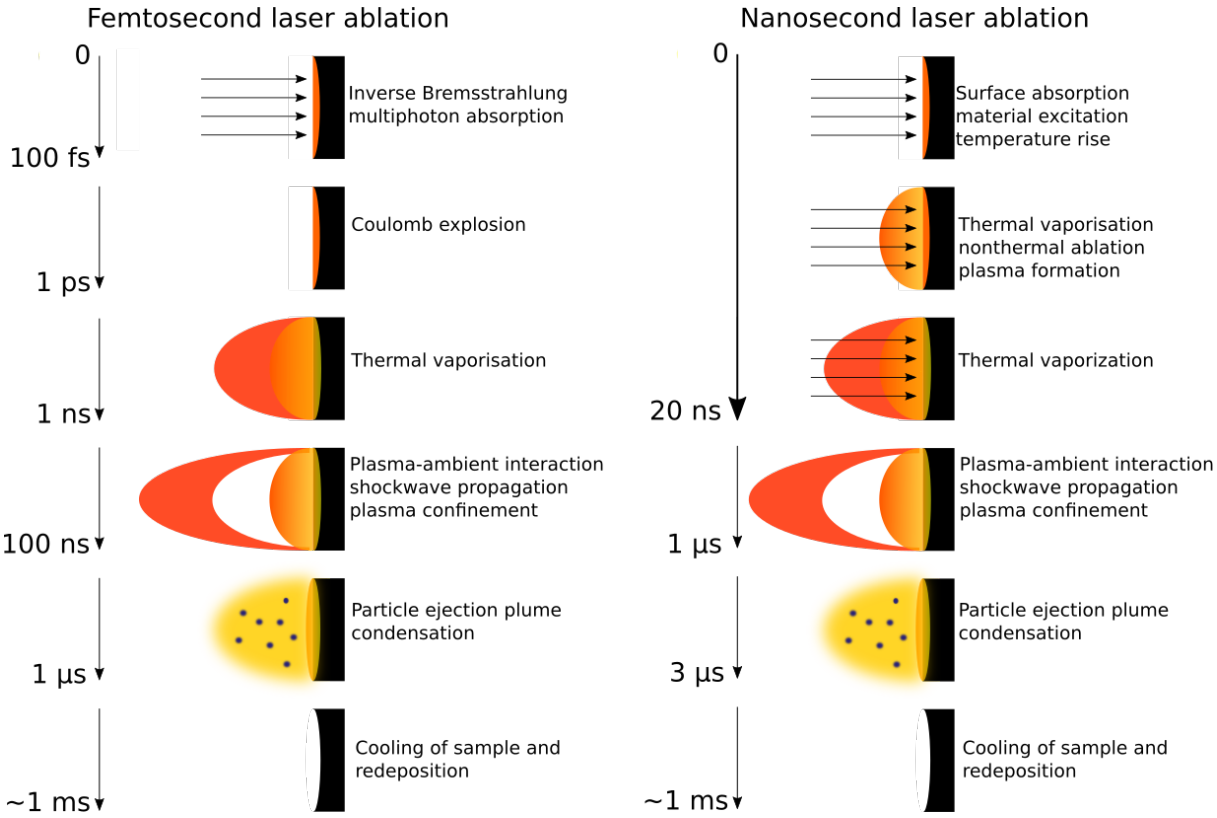

Figure 3.6: Shows the ablation process for both the nano-, and femtosecond laser systems in ambient gas, as can be seen the pulse in the femtosecond system delivers its energy before the plasma is created, while the nanosecond laser ablation system continually delivers energy even while the plasma is created. The figure is inspired by figures in [88, 90]

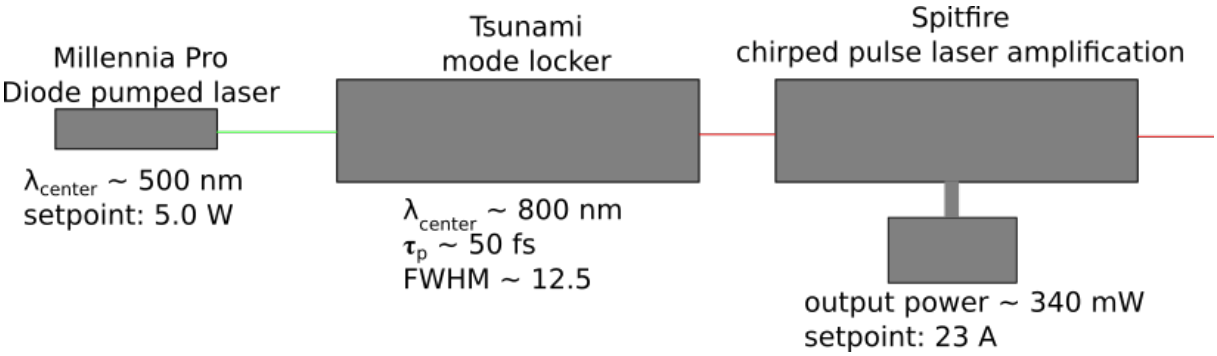

Figure 3.7: Schematic overview of the modules used to generate the femtosecond pulses used for laser ablation.

nonlinear effects and hence a large peak intensity can be obtained. The stretching and compression are both done with optical gratings, which results in differing optical path lengths for each wavelength component, hence the pulse is spatially stretched. It may then be amplified and compressed in the same way, i.e., changing the optical path again, such that the total optical path for each component is the same. [88,93] In the system used for this project the CPA works by Q-switching the optical cavity and the repetition rate of this can be tuned by the user, from 1000 Hz down to 1 Hz allowing for a broad span of output fluence [93].

3.3 Terahertz Time-Domain Spectroscopy

As the goal of this project is to fabricate structures that have some desired response in the THz region it is a necessity to be able to characterise the response in this frequency region. This may be done in a multitude of ways, but in the case of this project, the primary optical characterisation is performed by the TeraSmart time-domain terahertz spectrometer from MenloSystems. [96]. This is a THz-TDS system and for the convenience of the reader a brief overview of the working principles of such a system will be presented here. The THz-TDS system has a multitude of advantages, namely a high bandwidth (> 6THz), quickness of operation, and that it is the direct electric field that is measured which in turn means that the phase change through the sample is retained which opens a multitude of measuring options, e.g., direct measurement of the refractive index [97].

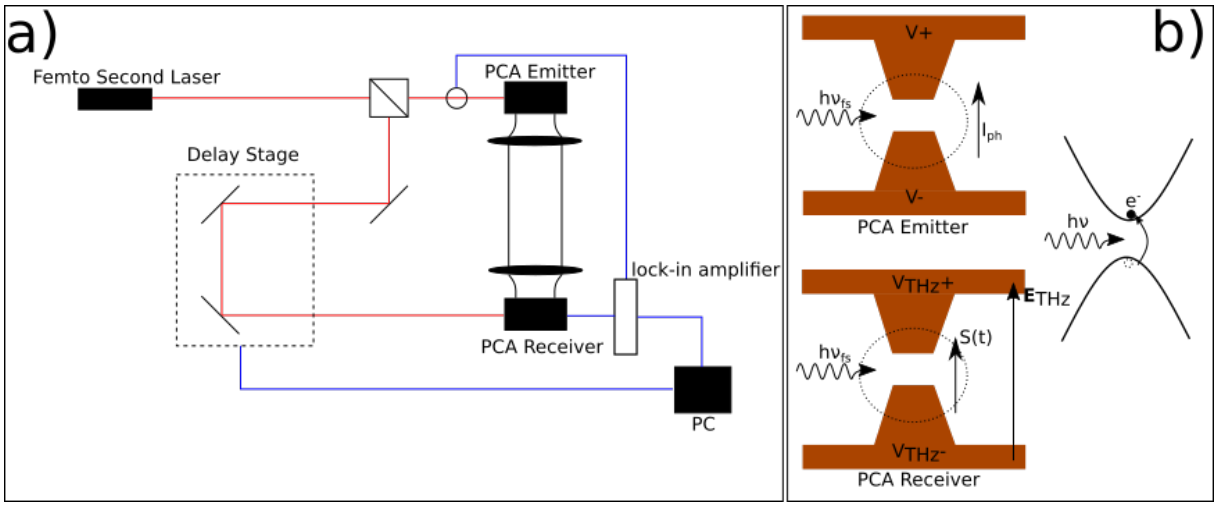

Figure 3.8: **(a)** A sketch of the optical setup of the the THz-TD emitter and receiver. The THz pulse is scanned by a delay stage and is detected utilising lock-in detection. **(b)** The fields and currents at the emitter and detector and a sketch of the band structure of the semiconductor for which electrons are moved to the conduction band such that a photocurrent may be induced.

The Menlo system uses photoconductive antennas (PCA), both as the THz emitter and receiver [96]. The PCA consists of a dipole antenna placed on a photoconductive substrate. The antenna is driven by focusing a femtosecond laser onto the gap between the conductors hence creating charge carriers as the electrons of the valance band are excited over the band gap. A bias is applied across the electrodes, accelerating the free charge carriers. This in turn results in a photocurrent and in turn the antenna creates a THz pulse [97, 98]. It is therefore a given that the creation of the pulse is intrinsically tied to the material properties of the semiconductor in question, such as the carrier lifetime, the mean free path, and the doping level of the semiconductor. The carrier lifetime is directly related to the temporal width of the outgoing THz pulse, generally, a long carrier lifetime is desired as this results in a small temporal width which in turn results in a higher bandwidth [98, 99]. The Menlo system used for this project has a bandwidth of ~ 0.1 - 6 THz. The receiver is also a PCA, however, without the externally applied bias. Instead, the incoming THz-field will bias the antenna, if charge carriers are then created in the gap, a photocurrent will run which will be proportional to the electric field of the THz radiation. The charge carriers in the receiver are generated as in the emitter, that is to say

with a femtosecond laser [97–99]. Hence, the measured signal will be the convolution between the THz signal hitting the detector and the femtosecond pulse, i.e.,

$$S(t') \propto E_{THz}(t') * I_{Femto}(t). \tag{3.4}$$

As the femtosecond pulse is much shorter in time than the THz pulse, about three orders of magnitude, it may be viewed as a delta function hence eq. (3.4) can be rewritten as

$$S(t) \approx E_{THz}(t') * \delta(t) = E_{THz}(t). \tag{3.5}$$

By varying the time of arrival for the optical pulse the temporal change in electric field change can be scanned [98]. The working principle of both the emitter and receiver can be seen in fig. 3.8(b) where the emitter has an external voltage applied (V±) resulting in the photocurrent I_{ph}, while for the receiver the voltage results from the incoming THz radiation, and the signal $S(t)$ may then be measured. To temporally scan the incoming THz pulse the optical path length is varied, as the speed of light in air is about 300 $\frac{\mu m}{ps}$ a path length change of one micrometer will result in a delay of 6.6 fs hence the temporal THz pulses can readily be scanned by changing the optical path length with micrometer precision [97]. The optical setup can be seen in fig. 3.8(a) the femtosecond laser hits a beam-splitter from which the signal is then sent to both the PCA emitter and receiver. The part of the beam going to the receiver is passed through a delay stage which allows for the temporal scan of the THz pulse. The measured signal is amplified using a lock-in amplifier and can be recorded by a PC.
The resulting THz beam can then be guided and focused using suitable optical devices, and hence may be used in either reflection or transmission experiments. For this project, the system was used in transmission, both for the characterisation of Fano resonances as well as the determination of optical properties of photonic crystals.

Part II

Fano Resonances

4 | Results and Discussion

In this chapter, the fabricated one-dimensional photonic crystals and their Fourier transformed THz-TDS spectra are presented along with FMM modelled transmission spectra, for angles of incidence between 0° and 10°. Through the work presented in this chapter the authors have published an article *"All-dielectric one-dimensional gratings exhibiting Fano resonances in the terahertz region"* [1]. Thus the data from the M1 sample, as well as the Propagation constant Matching Model (PMM), have been presented in the article first.

4.1 Results: M-series

In this section, the samples designed to exhibit Fano resonances dubbed the M-series, and their spectra at normal incidence are presented. The optical setup and sample holder can be seen in fig. 3.5. The M-series is based on the same wafer of thickness $100\pm20\mu$m. Wafers of this thickness are not a requirement for the existence of Fano resonances, however, the thicker the sample the smaller the period of the transmittance oscillations demonstrated in fig. 3.4c becomes, which could obscure transmittance dips caused by Fano resonances. Furthermore, the amount of Fano resonances is increased while the width of each peak is reduced, setting higher requirements for both the fabrication and the following measurements. Both of these effects can be seen in fig. 4.1a, where the transmittance spectrum of a structure with the same dimensions as the M1 wafer, except wafer thickness, is plotted. It was therefore decided to use the thinnest wafers available.

In fig. 4.1b the modelled spectra for M1 are plotted using between 1 and 7 Fourier coefficients. It can be seen that using 5 and 7 coefficients gives the same result, and all subsequent graphs are therefore calculated using $N = 7$. Zoomed-out images of the M-series, meant to give a qualitative idea of sample quality, are provided in fig. 4.2. Based on presence, fig. 4.2, and uniformity, table 4.1, of the strips, the best sample is M1, while the worst is M2. M1 is not missing any strips, and has the lowest standard deviation of period and strip width of all the samples, while M2 has many of its strips damaged and the second-highest standard deviation. M3 and M5 are lacking in different areas, M5 having the largest standard deviations, while M3 lack some of its strips. The standard deviations are presented in table 4.1.

When presenting the spectra for the M-series, the frequencies will be limited to $\frac{c}{\Lambda n_{sub}} < \nu < \frac{c}{\Lambda}$. For frequencies above this upper limit, diffraction orders can exist in air which could look like the Fano resonances of interest in the transmittance spectra. This frequency limit was therefore introduced to remove any ambiguity in the presented spectra. For frequencies below the lower

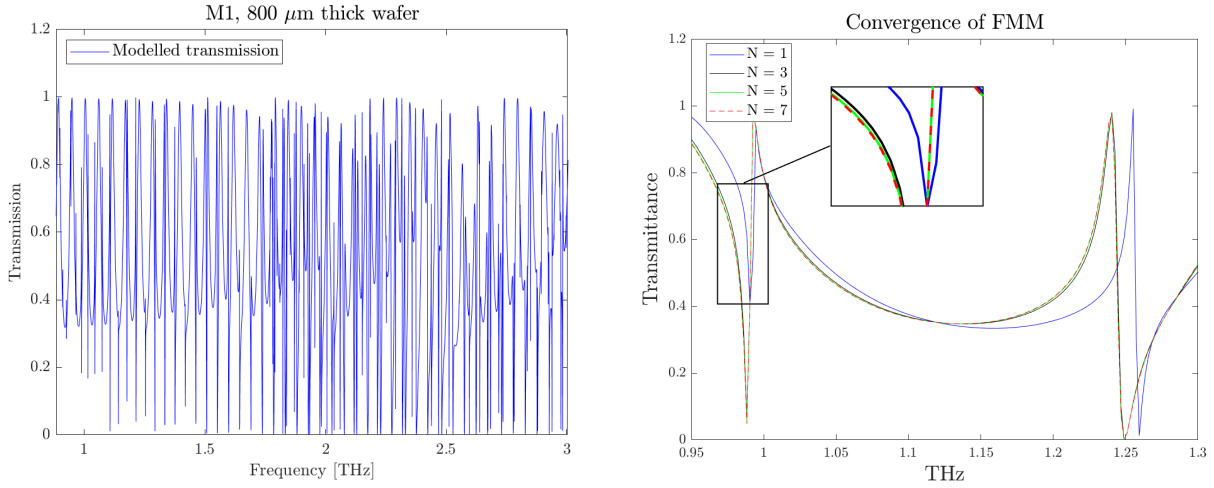

(a) **(b)**

Figure 4.1: **(a)** Modelled transmittance spectra of a sample with the same dimensions as M1, but with a wafer thickness 800 μm **(b)** Convergence of the FMM model using between 1 and 7 Fourier coefficients for a structure with the same dimensions as M1.

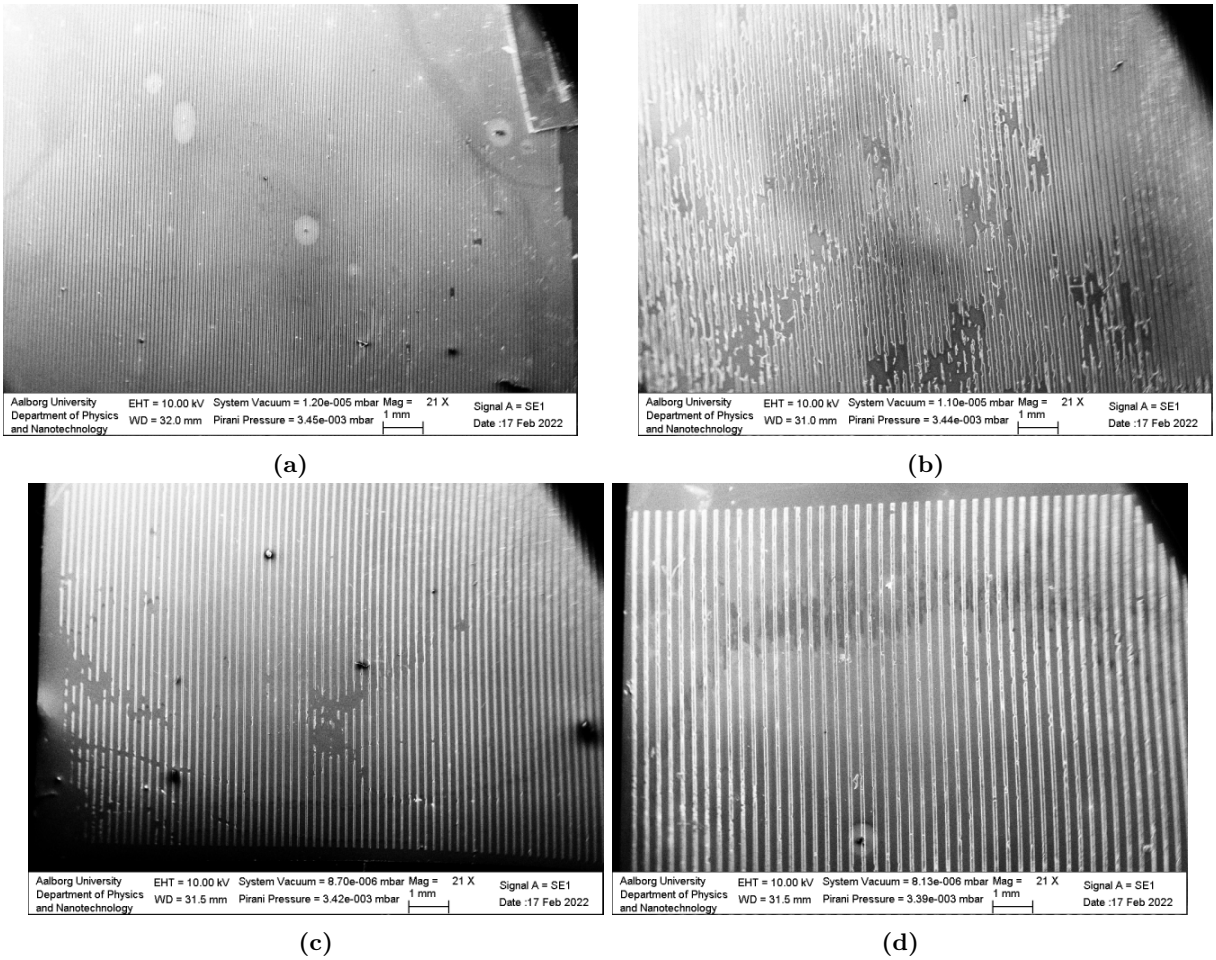

(a) **(b)**

(c) **(d)**

Figure 4.2: SEM images of the four Fano samples. **(a)** M1, **(b)** M2, **(c)** M3, and **(d)** M5.

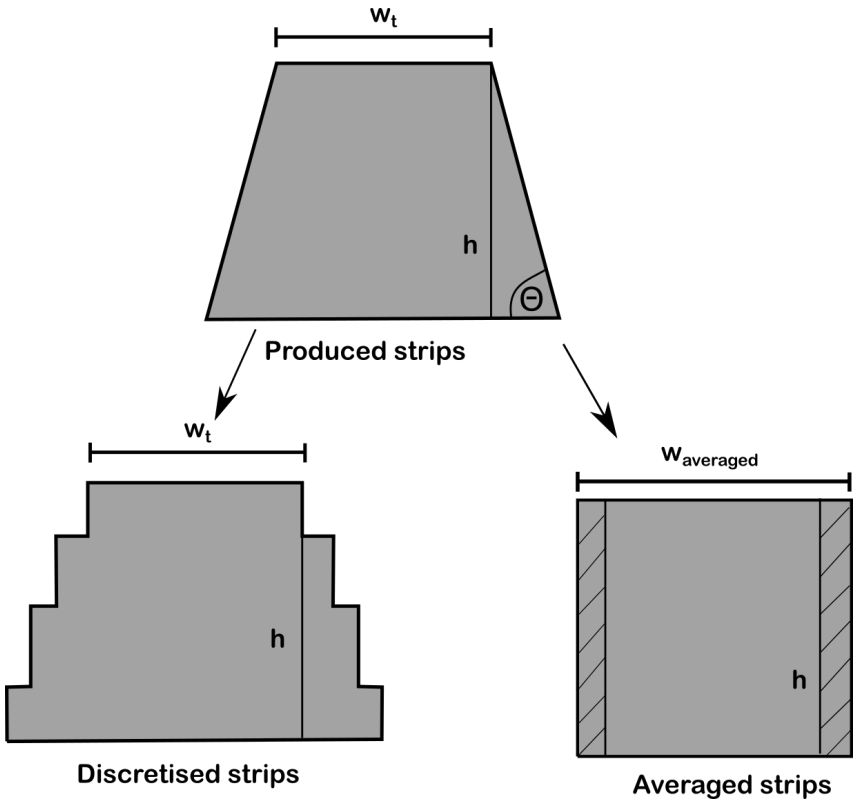

Figure 4.3: Sketches the cross-sections of the produced and modelled strips. The dashed cross-sectional area on the averaged strip is the cross-sectional area that is lacking if w_t is used in the model.

limit no diffraction orders exist in the substrate, which is hypothesised to be a necessity for the existence of Fano resonances. Indeed, no Fano resonances have been observed in the model or the measured spectra on any of the samples for frequencies below this limit. A more thorough explanation and a discussion of the chosen frequency limit will be provided in section 4.2.

Recall that the used etch procedure results in sidewalls with a slope between 50° and 60° as discussed in subsection 3.1.1. As a result, the width that was measured and presented in table 4.1 as w_t is the strip width at the top, which then underestimates the effective width of the strips. There are two ways of accounting for this mismatch, either by averaging the strip-widths, i.e., using a strip width that results in strips with the same cross-sectional area as the produced strips or by introducing more layers to the FMM model, gradually broadening the strip down to its base. Assuming a sidewall slope of 55°, the average strip width can be calculated as

$$w_{t,averaged} = w_t + \frac{h}{\tan(\theta)}. \tag{4.1}$$

The two strip types are sketched in fig. 4.3, and the result of using the various strip types can be seen in fig. 4.4 using the structure parameters of M1. There is a clear difference between the model when using the measured strips, and the model when either an averaging or discretisation has been performed. However, by zooming in it becomes clear that the location of the Fano resonances in the modelled spectra using averaged and discretised strips are also different, and as the location of the resonances are the main criteria on which the model is judged, their location is of crucial importance. The largest frequency differences between Fano resonances

modelled with the averaged strips and strips using five discretisation steps are 2.2 GHz and 2.4 GHz for the S- and P-polarisation, respectively. Although it is a measurable difference, it was not enough to warrant using the discretised strips in the FMM model, as it has a significantly longer computational time.

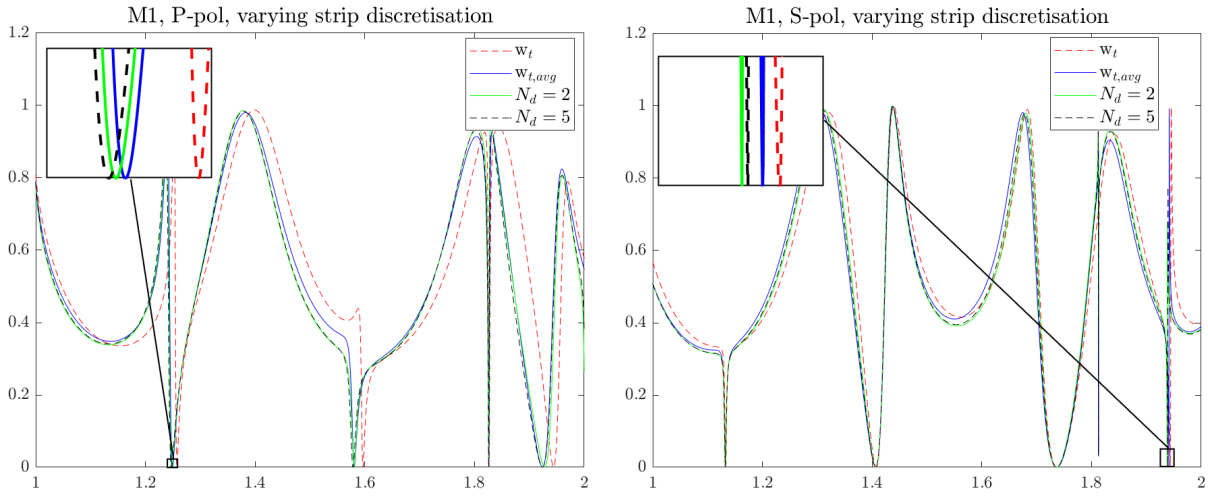

Figure 4.4: Modelled spectra using the measured, averaged, and discretised strips, while the rest of the dimensions are those measured for M1, presented in table 4.1. **(a)** P-polarisation. **(b)** S-polarisation.

The spectra for the M-series are presented in fig. 4.5 and fig. 4.6 along with the FMM model. The model uses both the measured and averaged strip-widths along with the dimensions presented in table 4.1. Using $w_{t,averaged}$ slightly redshifts the model, which more often than not results in a better correspondence between modelled and measured Fano resonances as compared to using the measured strip-widths. There are also examples where it leads to a worse correspondence, e.g., the Fano resonances found for the P-polarisation at ~ 1.92 THz in fig. 4.5a and ~ 0.9 THz in fig. 4.5b. Nevertheless, comparisons from here on out are made between measured spectra and the modelled spectra using $w_{t,avg}$.

The spectra are judged based on two criteria, the correspondence between the positioning of the peaks, i.e., are the modelled transmittance dips located at the same frequencies as the measurements, and the transmittance at the frequencies where the Fano resonances are located. M1 shall be covered first, and with more detail than the remaining three samples as it is by far the most pristine sample.

In general, the correspondence between model and measurement is close. This is especially true for M1, where the difference in measured and modelled frequency is less than 9 GHz for the first three Fano resonances found for both polarisations. Furthermore, all the transmittance dips predicted by the model can be found in the measurement at, or close to, the predicted frequencies, with the exception of the resonance at ~ 1.96 THz in fig. 4.5a for the S-polarisation, which was predicted by the model but nowhere to be found in the measurement. Another example is the shallow resonance seen at ~ 1.83 THz for the P-polarisation. Although the resonance is present, the transmittance at the center frequency is around 60%, much higher than the predicted transmittance of 0%. The common factor for these two examples is that the resonances predicted

by the model are very narrow. In the case of M1, the transmittance at most of the measured Fano resonances are below 10% with some reaching $\sim 0\%$ for the S-polarisation, a feature only seen for M1. The exceptions are the shallow dips found at ~ 0.94 THz for the S-polarisation and ~ 0.99 THz for the P-polarisation. The lacking Fano resonances at some frequencies and high transmittance at other frequencies could be caused by the dimensions of the strips varying slightly, giving a broadening effect. To test this, the uncertainties presented in table 4.1 were included in the FMM model, weighted at 5%. This was done by calculating all 27 combinations of $\{w_{t,avg}, w_{t,avg} \pm \sigma_w, t, t \pm \sigma_t, \Lambda, \Lambda \pm \sigma_\Lambda\}$, where the structure with dimensions $\{w_{t,avg}, \Lambda, t\}$ was weighted by one, and the rest were weighted by 1/20, the result of which can be seen in fig. 4.7a for M1. While including the measured deviations does not produce an exact match, it does alleviate some of the discrepancies between the FMM model and the measurements commented on previously, e.g., by reducing the modelled transmittance at the very narrow resonances, and it is therefore a plausible explanation for the mismatch between model and measurement.

The correspondence between measurement and model for samples M3 and M5 are similar, with the worst discrepancy between modelled and measured resonances being 15 GHz. The M5 sample reaches lower transmittance than M3, close to 0% in some cases. A possible reason for the high transmittance observed for M3 is the areas where M3 has damaged, or entirely lacks, strips, meaning that the THz beam can be transmitted unaffected.
Finally, there is the M2 sample, which only gets below 20% transmittance once. Again, the high transmittance was likely caused by the poor quality of the sample, which is supported by fig. 4.7b where the standard deviation has been included in the model at a weight of 5%, the same as was done for M1 in fig. 4.7a. Including the standard deviations also remove, or tone down, some of the sharper resonances predicted by the model but not observed in the measurements, e.g., at ~ 0.95 and 1.17 THz for the S-polarisation and at 1.4 THz for the P-polarisation.

It has thus been shown that the model based on the FMM method predicts the presence of most Fano resonances, and their location within ~ 15 GHz of the measured spectra for the four samples fabricated in this project when illuminated at normal incidence. Discrepancies between the model and the measurements with respect to the frequency location and transmittance at the Fano resonances were partially accounted for by including the measured uncertainties in the model at a weight of 5%.

Table 4.1: Dimensions and standard deviation of the fabricated samples.

Sample	h [μm]	t [μm]	σ_t [μm]	w$_t$ [μm]	σ_w [μm]	$w_{t,avg}$	Λ [μm]	σ_Λ [μm]
M1	105	12.89	0.10	32.45	0.46	41.50	99.74	0.55
M2	100	14.59	0.14	77.99	1.17	88.25	199.76	3.82
M3	105	17.32	0.23	27.16	0.77	39.93	196.24	1.34
M5	105	28.03	0.18	65.77	2.14	85.47	292.28	4.22

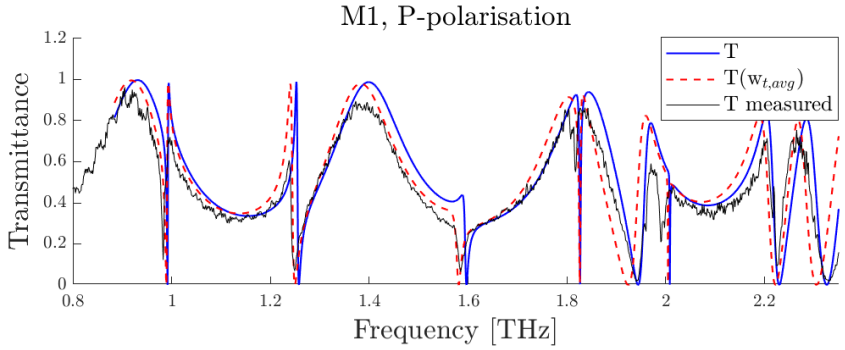

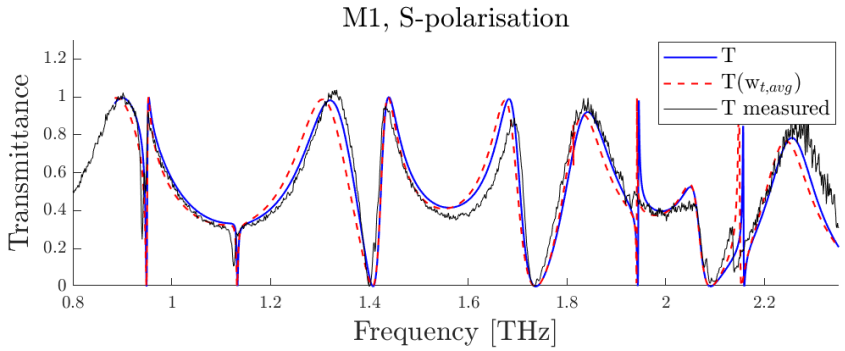

(a)

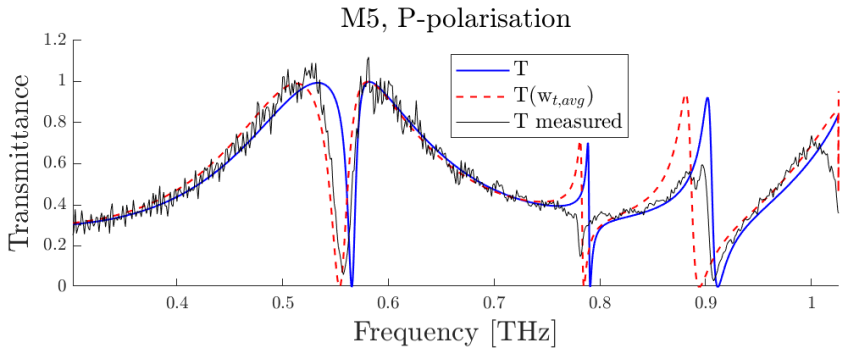

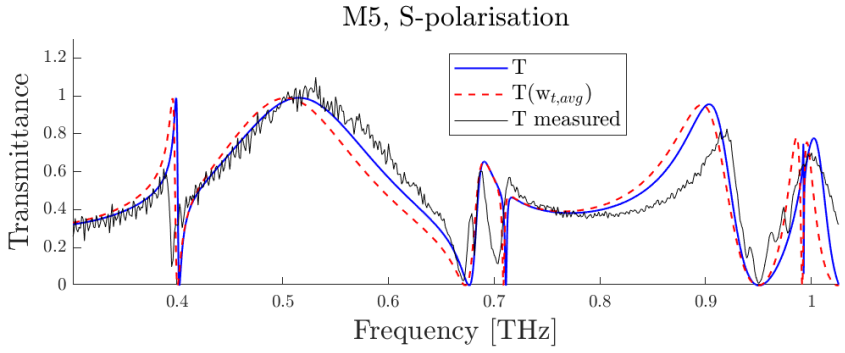

(b)

Figure 4.5: Fourier transformed TD transmittance spectra and the FMM spectra based on the measured and averaged strip width. The data shown in **(a)** was first presented in [1]. **(a)** M1. **(b)** M5.

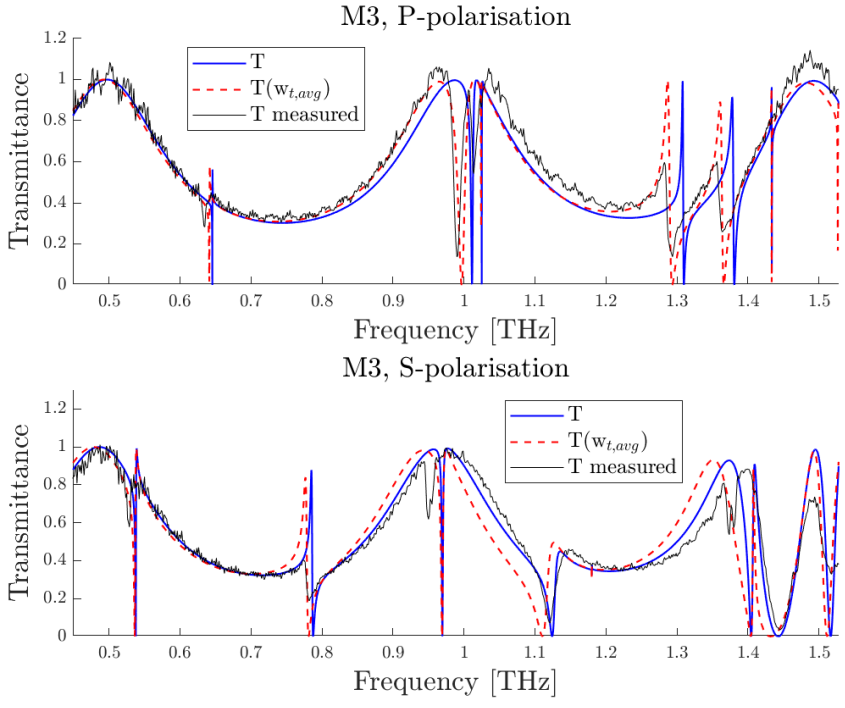

(a)

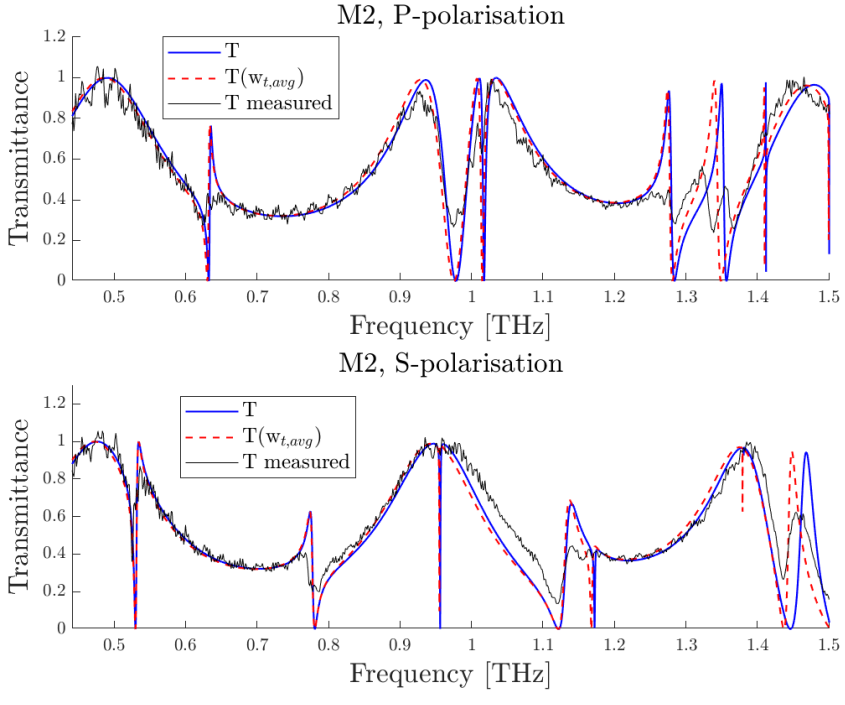

(b)

Figure 4.6: Fourier transformed TD transmittance spectra and the FMM spectra based on the measured and averaged strip width. **(a)** M3. **(b)** M2.

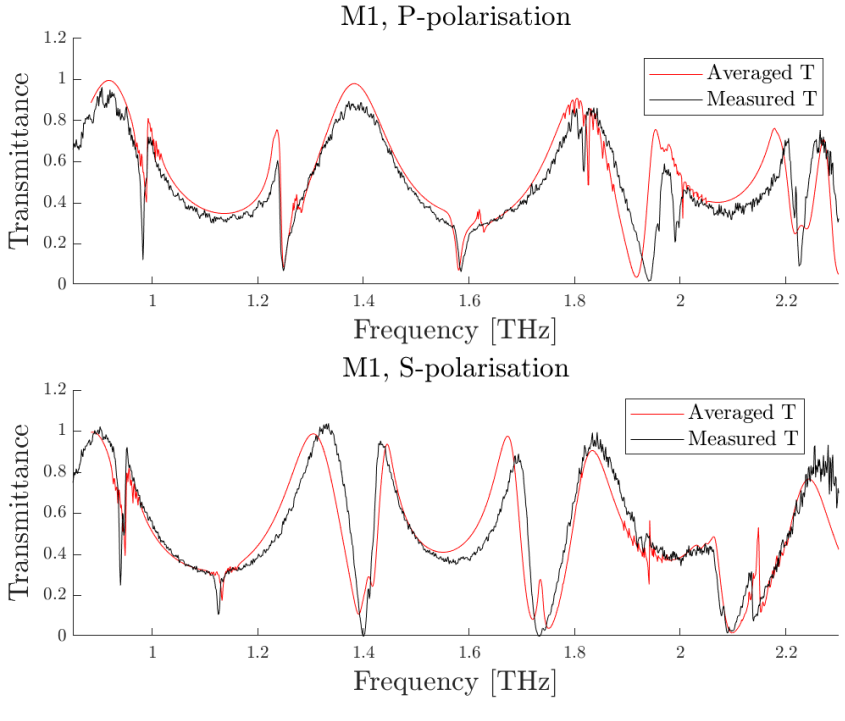

(a)

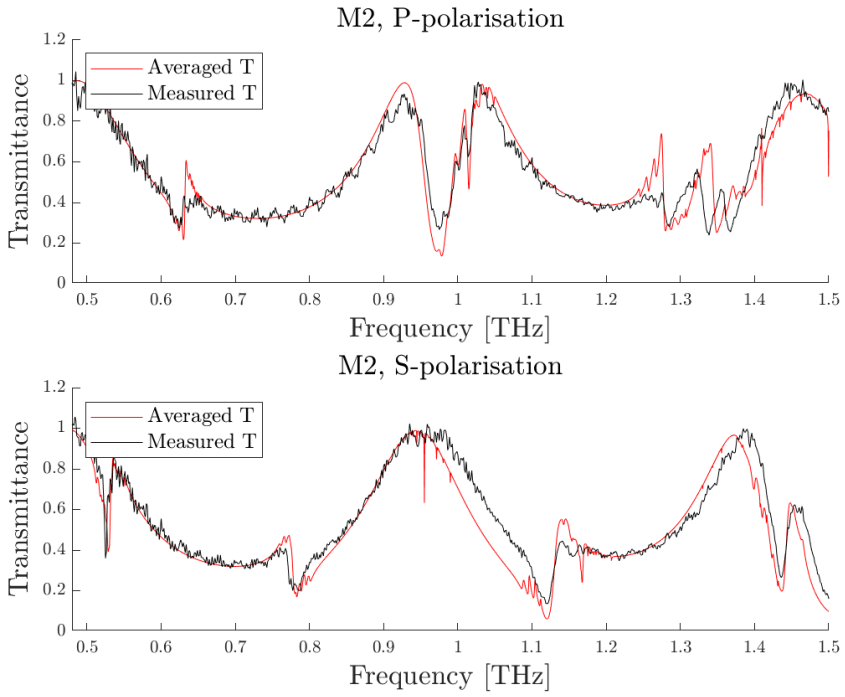

(b)

Figure 4.7: Fourier transformed TD transmittance spectra and the FMM modelled spectra based on the data presented in table 4.1 with the deviations weighted by 5%. The measured data shown in **(a)** was first presented in [1]. **(a)** M1. **(b)** M2.

4.1.1 Varying Angle of Incidence

In the literature, it has been demonstrated that the location of Fano resonances for S-polarised light can be tuned by changing the angle of incidence [100, 101] which will be tested here for both polarisations, by varying the angle of incidence between zero and ten degrees. The angle is sketched in figure fig. 3.5(c), corresponding to a rotation around the y-axis. A rotation about the x-axis does not significantly change the spectra, which was also reported by [101]. The model and measurement are shown for M1 in fig. 4.8 with $\theta = 0°$ and $10°$. As was the case for normal incidence, the model is in excellent agreement with the measurements for $\theta = 10°$, although it is not an exact match.

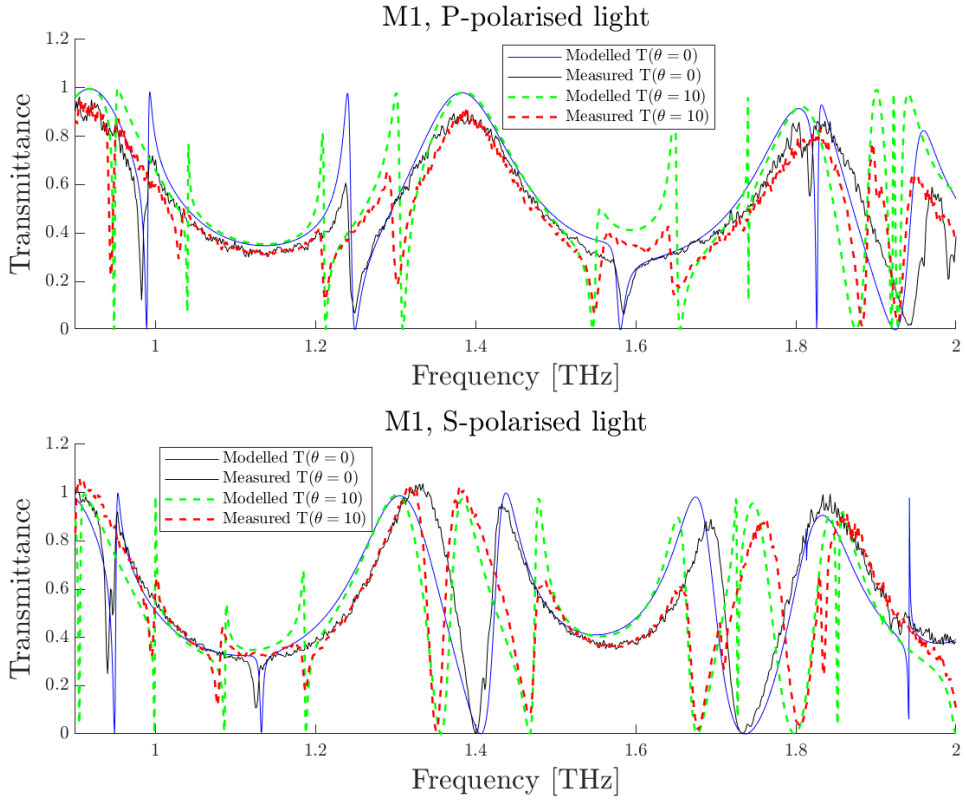

Figure 4.8: Measured and modelled spectra of M1 with angle of incidence equal to 0° and 10°. The angle with respect to the strips can be seen in fig. 3.5(c). The measured data at normal incidence was first presented in [1].

To present the data in a compact form, surface plots presenting transmittance spectra for all angles and frequencies are made, seen for M1 in fig. 4.9, where both the modelled and measured spectra are presented for both polarisations. The remainder of this section will exclusively cover sample M1. The surface plots of M2, M3 and M5 can be found in Appendix C. As can be seen in fig. 4.9 there is a high level of agreement between the measured and modelled spectra for a majority of resonances, both with respect to the width and frequency placement of individual resonances. There are, however, a few resonances that are barely visible in the model that can be difficult to identify in the measurement. As an example, the resonance at ~ 1.95THz for the S-polarisation is only just visible at 0° and 2° but then disappears for higher angles of incidence. Note that this resonance could not be found at normal incidence either.

In fig. 4.9 it is observed that all resonances at $\theta = 0°$ become two resonances, which move towards lower and higher frequencies as the angle of incidence grows. Using five of the most explicit resonances for each polarisation observed for sample M1, the averaged frequency change of Fano resonances observed when going from $\theta = 0°$ to $10°$ is presented in table 4.2. All data points, and their differences, are presented in table 4.3 for the S-polarisation and in table 4.4 for the P-polarisation. From table 4.2 it can be seen that, on average, the location of the Fano resonances can be tuned by ~ 50 GHz simply by changing the angle incidence. The general trend is that Fano resonances at higher frequencies move farther apart when the angle of incidence is increased, which can be seen in table 4.3 and table 4.4. The data presented in table 4.2 also shows that, on average, the measured change in the centre frequency of a resonance is within 8 GHz of the change predicted by the model, the same deviation that was observed between the presented spectra at normal incidence for sample M1.

The discrepancies between the measurements and the FMM model can be ascribed to two factors, which are valid for all the angles of incidence presented here. The first is that the model can calculate the presented spectra with arbitrary spectral resolution, which has the consequence that it is more likely that the center frequency of the resonance is presented in the modelled spectra, as opposed to the measured spectra whose resolution is limited. The second reason is that the angle of incidence of the measured spectra has some uncertainty on the first decimal point, whereas the model has arbitrary precision.

M1	Increase [GHz]	Decrease [GHz]
$\Delta S_{measured}$	63.3	47.3
$\Delta S_{modelled}$	65.2	55.2
$\Delta P_{measured}$	55.5	47.5
$\Delta P_{modelled}$	60.9	51.4

Table 4.2: Average increase and decrease of the center frequency of five Fano resonances found using the FMM model and the Fourier transformed THz-TDS spectra when the angle of incidence is changed from $\theta = 0°$ to $\theta = 10°$.

It has thus been shown that there is a high level of agreement between the rigorous FMM model and the measurements on sample M1 using angles of incidence up to $10°$. Both the modelled and measured spectra show that the frequency location of the resonances depends on the angle of incidence, with the averaged difference of the change of frequency location between model and measurement being less than 8 GHz. The FMM model therefore clearly provides a rigorous tool that can be used to calculate the transmittance spectrum of the structures fabricated in this part of the project. However, it does not provide much intuition as to the mechanism causing the Fano resonances, nor is it an efficient tool for designing structures with resonances at some desired frequencies.
Therefore, an independent model will be established in the following discussion with the intent of giving an intuition behind the Fano resonances, but also to create a less computational intensive model which can be used to search the parameter space for structures exhibiting Fano resonances at some particular frequencies. This model was first shown in [1].

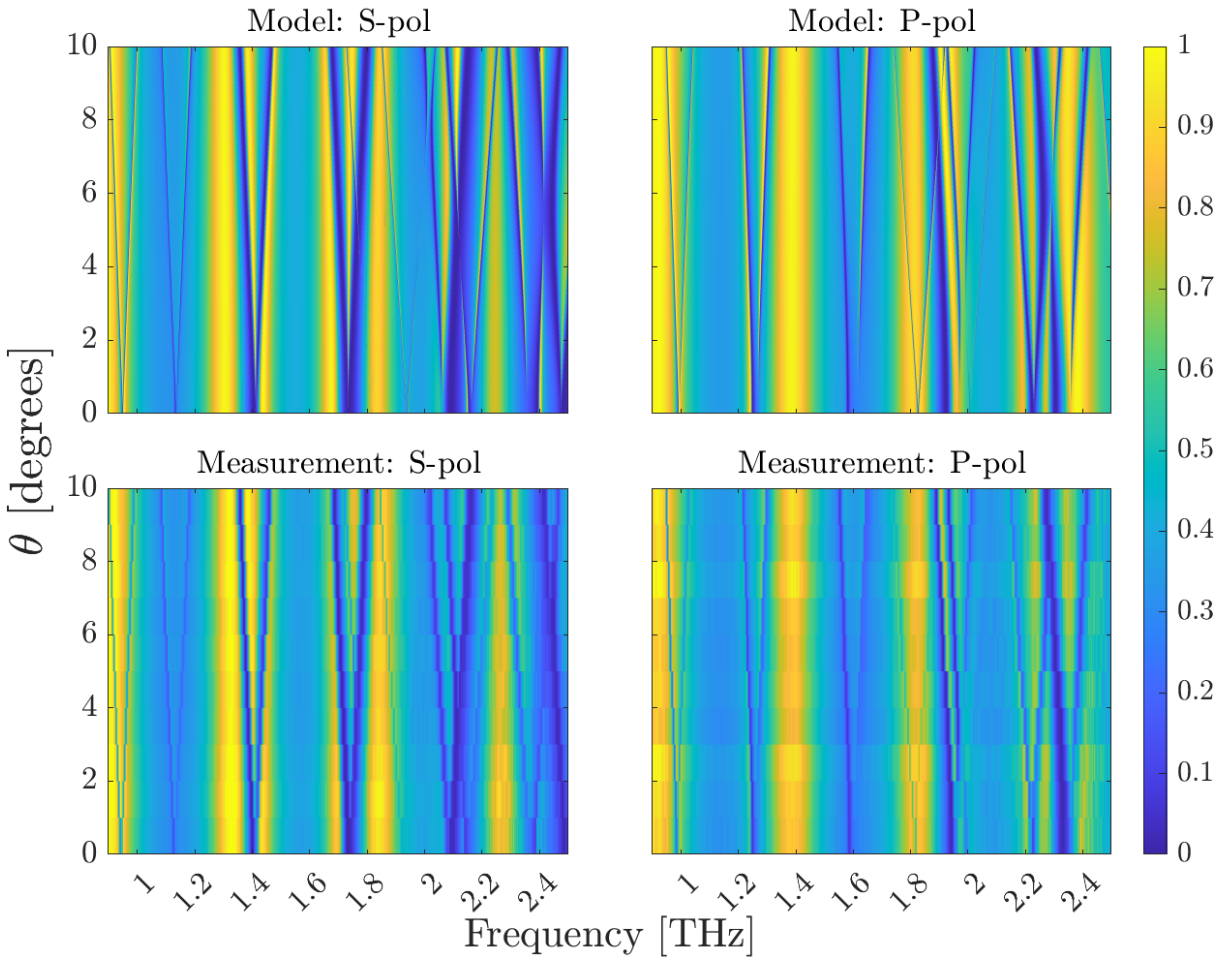

Figure 4.9: Surface plot of the modelled and measured transmittance spectra of the M1 sample for various frequencies and angles of incidence. The data presented in this figure have earlier been published in [1].

M1	$\theta = 0$ [THz]	$\theta = 10$, L [THz]	Δ_L [GHz]	$\theta = 10$, U [THz]	Δ_U [GHz]
$\#1_{S,measured}$	0.941	0.903	38.8	0.986	46.3
$\#1_{S,modelled}$	0.949	0.905	43.442	0.998	49.561
$\#2_{S,measured}$	1.126	1.085	41.25	1.180	53.76
$\#2_{S,modelled}$	1.132	1.087	45.72	1.187	54.68
$\#3_{S,measured}$	1.401	1.358	43.76	1.460	58.75
$\#3_{S,modelled}$	1.407	1.358	48.68	1.468	61.57
$\#4_{S,measured}$	1.734	1.686	47.5	1.798	63.76
$\#4_{S,modelled}$	1.736	1.676	60.0	1.798	61.36
$\#5_{S,measured}$	2.139	2.074	65.01	2.233	93.76
$\#5_{S,modelled}$	2.153	2.075	78.08	2.252	98.72

Table 4.3: List of the center frequencies and the differences of five Fano resonances using S-polarised light for $\theta = 0°$ and $\theta = 10°$ using both the FMM model and the Fourier transformed TD measurements.

M1	$\theta = 0$ [THz]	$\theta = 10$, L [THz]	Δ_L [GHz]	$\theta = 10$, U [THz]	Δ_U [GHz]
$\#1_{P,measured}$	0.984	0.948	36.253	1.026	42.508
$\#1_{P,modelled}$	0.990	0.949	40.800	1.039	49.726
$\#2_{P,measured}$	1.249	1.298	32.500	1.216	48.760
$\#2_{P,modelled}$	1.248	1.213	35.280	1.307	58.440
$\#3_{P,measured}$	1.586	1.553	33.750	1.644	57.510
$\#3_{P,modelled}$	1.581	1.548	33.000	1.655	74.320
$\#4_{P,measured}$	2.333	2.275	57.500	2.415	82.510
$\#4_{P,modelled}$	2.307	2.238	69.330	2.418	110.520
$\#5_{P,measured}$	2.228	2.150	77.510	2.274	46.250
$\#5_{P,modelled}$	2.226	2.147	78.760	2.237	11.600

Table 4.4: Lists the center frequency and the differences of five Fano resonances using P-polarised light for $\theta = 0°$ and $\theta = 10°$ using both the FMM model and the Fourier transformed TD measurements.

4.2 Propagation Constant Matching Model

In the previous section, the FMM was used to model the transmittance spectra of the fabricated samples, which it did with high accuracy. However, because the FMM model is two-dimensional it is computationally expensive and is therefore not a great candidate for designing structures exhibiting Fano resonances at some desired frequency. Another shortcoming of the model based on the FMM is that it does not explain the mechanism behind the resonances. Both of these shortcomings will be remedied in this section, where a one-dimensional model will be derived, which both predicts the frequency location of Fano resonances and gives an intuitive understanding of the mechanism that causes them. This model is dubbed the Propagation constant Matching Model (PMM) as it predicts the Fano resonances by matching the propagation constant of a slab waveguide to the diffraction orders of the periodic layer.

To derive an intuitive and computationally inexpensive model for the prediction of Fano resonances the structure is viewed as a four-layer structure consisting of air, one-dimensional photonic crystal, substrate, and air, shown in fig. 4.10. Consider now an incoming field on the form

$$\mathbf{A} = A_0 e^{-ik_z z} e^{ik_x x} \hat{\mathbf{y}}, \tag{4.2}$$

where $\mathbf{A}$ denotes either a magnetic or electric field based on which polarisation is investigated. In fig. 4.10 the orientation of the fields with respect to the structure is seen. In accordance with the Helmholtz equation, eq. (2.18), the wave vectors in a homogeneous dielectric media have the following relation

$$k_0^2 \varepsilon_i = k_z^2 + k_x^2, \tag{4.3a}$$

$$k_z = \sqrt{k_0^2 \varepsilon_i - k_x^2}. \tag{4.3b}$$

As such, for any propagating mode in the z-direction to exist it is required that $k_0^2 \varepsilon_i > k_x^2$, as all other modes will be evanescent. As discussed thoroughly in section 2.3, because one layer is periodic along the x-axis the wave vector in this direction and layer is given as

$$k_{x,m} = k_x + m\frac{2\pi}{\Lambda}, \qquad m = 0, \pm 1, \pm 2, \pm 3, ..., \tag{4.4}$$

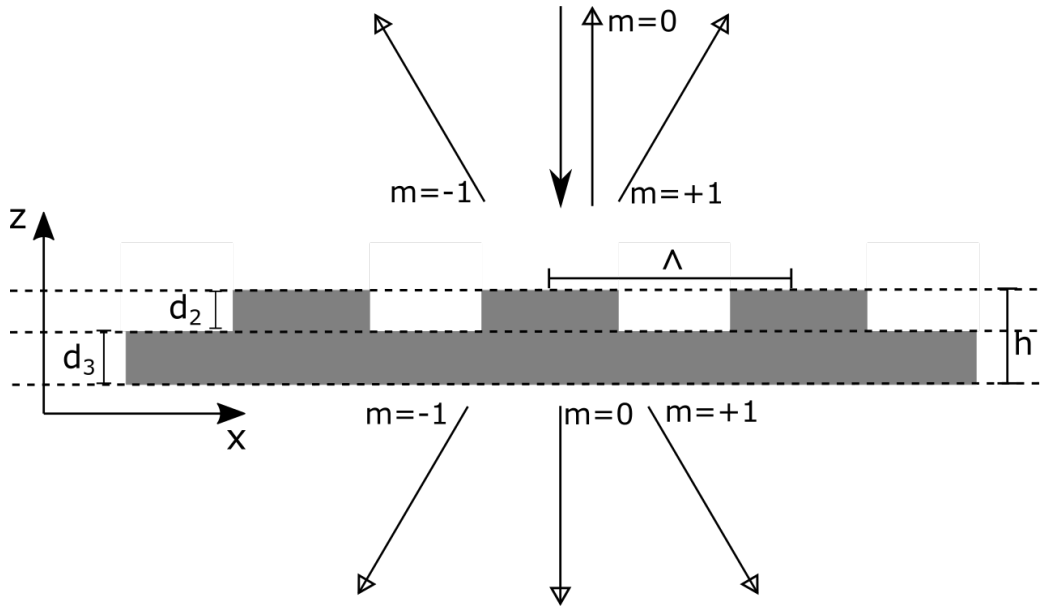

Figure 4.10: Shows the structure in question, the incident field, and the first diffraction orders, both above and below the structure.

with Λ being the period of the structure. It is thus possible for the photonic crystal layer to scatter the light into higher diffraction orders which could then either be bound to the high index structure, be reflected, or transmitted under some angle. For this project, the frequencies of interest are when diffraction orders are accessible inside the structure, but evanescent in air. The considerations will be limited to normal incidence, $k_x = 0$, though the proposed model should work for any angle of incidence. Hence for a mode to propagate inside the structure, the following has to be true

$$k_0\, n_i > m\frac{2\pi}{\Lambda}, \qquad m = 0, 1, 2, 3, ..., \tag{4.5}$$

with n_i being the refractive index of the material. Expanding k_0 as $k_0 = \frac{2\pi}{c}\nu$ the requirement that no diffraction orders are propagating in the air layer can be written as

$$n_i\,\frac{\Lambda\,\nu}{c} < 1, \tag{4.6}$$

i.e., eq. (4.6) is the requirement to only having 0'th order modes propagating along $\hat{\mathbf{z}}$ in the air layer. This is generally not surprising as this corresponds to the classical limit, $\lambda > \Lambda$, expected for gratings. The question then becomes if Fano resonances can be expected for any frequency smaller than $\frac{c}{n_{sub}\Lambda}$, to which the answer is no. This is due to the fact that Fano resonances are the result of coupling between a continuum and a discrete set of modes. The discrete set of modes in this case is the bound modes of the entire high index slab, both the photonic crystal layer and the substrate layer. Thus, it is necessary to be able to excite these bound modes in order to have Fano resonances. As all bound modes will be traveling along the slab in the x-direction it is necessary for some of the diffraction orders to be propagating otherwise the discrete set can not be excited and hence no coupling is possible. As the substrate is a high index material it is possible to have higher-order diffraction modes in this region while still only having the 0'th order mode be propagating outside the structure in accordance with eq. (4.5).

Hence it is straightforward to show that the largest interval both supporting Fano resonances, while disallowing regular grating effects is in the spectral range

$$\frac{c}{\Lambda\, n_{sub}} < \nu < \frac{c}{\Lambda}, \tag{4.7}$$

as if the frequency is outside this range either diffraction effects are present or a discrete set of bound modes are inaccessible.

It then follows that the location of Fano resonances can be predicted if a model for the bound modes in the structure can be established, as the Fano resonances will only occur when the $k_{x,m}$ of a diffraction order matches the propagation constant of a bound mode. The task then becomes to calculate the relation between the free space wavelength and the propagation constant, and then match the latter to the diffraction orders in the structure. For the substrate layer, this is trivial as this corresponds to a slab waveguide for which a multitude of methods exist for calculating this relation [102]. However, it is more nuanced for the periodic layer of the structure, which has to be included in the model because its refractive index on average is larger than air, and it is therefore able to support bound modes.

Two methods for calculating the effective refractive index of the periodic layer, and thereby including the periodic layer in the guiding structure, were tested. An empty lattice approach, and a more rigorous approach based on the work in [103]. Both methods proved sufficient, and the simpler method of the empty lattice approach was therefore utilised when judging the ensuing model for predicting Fano resonances.

Based on the work in [104], an empty lattice approach is used. In this approach, the refractive index will be approximated by a geometric average, which neglects some effects, i.e., the tendency of high-frequency radiation to accumulate in regions of high refractive index [43]. Furthermore, the effect of band gaps in the structure is also ignored. The reader is again referred to [103] for a more thorough approach.

With the necessary assumptions established, the task then becomes to calculate the propagation constant, β_n, of the bound modes of the structure, and matching these to the diffraction orders,

$$\beta_n = \frac{2\pi}{\Lambda} m. \tag{4.8}$$

The propagation constants can be found using various numerical methods. Two models were tested, one based on the FEM, and one based on the finite difference method, with the former being chosen because it exhibited higher stability for small frequencies. The results of this can be seen in fig. 4.11 for a sample with dimensions identical to those of M1. In this figure, it can be seen that only a discrete set of intersections are present in the range of interest, which is the expected result. If the hypothesis holds, it would then be at these intersections that Fano resonances are found, which will be tested shortly.

One interesting feature of this approach is that it immediately reveals that Fano resonances can always be expected for S-polarised light, but not for P-polarised light [105]. This is because when the dielectric profile is asymmetric the P-polarisation does not have a fundamental mode and hence if the total height of the structure becomes small enough only the S-polarised light will exhibit Fano resonances. Furthermore, simultaneous Fano resonances, that is Fano resonances present at the same frequency for both S- and P-polarised light, are exceedingly rare and may not be achieved for any frequency for a given configuration, as it requires an intersection at two

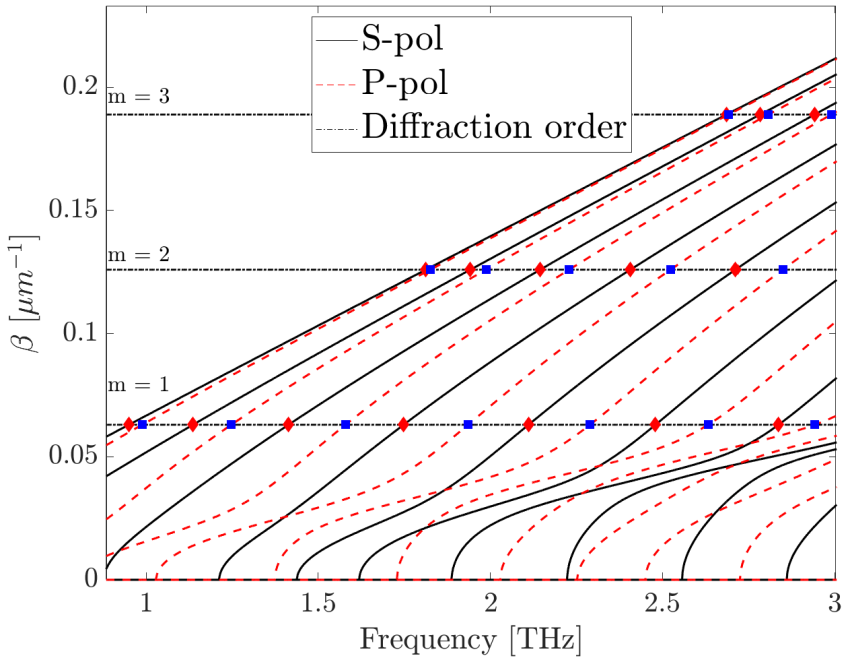

Figure 4.11: The calculated propagation constants for the M1 sample in the range of frequencies of interest along with the first three diffraction orders. Fano resonances are expected at the intersections, with Fano resonances for S-polarised light shown with solid red diamonds while those for P-polarised light are shown with solid blue squares. A figure using the same calculated data was first presented in [1].

different diffraction orders at the same time. Simultaneous Fano resonances are of interest, if the structures are to be used as spectral filters for unpolarised sources.

4.2.1 Evaluation of the Propagation Constant Matching Model

The task is now to quantify to which degree the PMM is able to predict the location of the Fano resonances, as if this new model does not replicate the FMM, which has already been shown to be in great agreement with the measured results, it is of little use in any sense. The comparison of the FMM and PMM using the settings of sample M1 can be seen in fig. 4.12. The frequency location of the Fano resonances predicted with the FMM are found using visual inspection of the transmittance graphs and can be seen as the red filled circles in fig. 4.12 while the predictions made by the PMM are noted as black triangles.

From the graphs on the left in fig. 4.12 it is clear that there is a high level of agreement between the two models. To quantify the result, box plots are presented on the right, with the input being the difference between the two models for each resonance, calculated as

$$\Delta\nu = \nu_{PMM} - \nu_{FMM}. \tag{4.9}$$

A box plot is a way of quantifying the spread of a data set by sorting the data into four quartiles, sorted from the lowest to the highest value. The second and third quartiles are contained inside the blue box and are separated by the red line, indicating the median value of the data set. The first and fourth quartiles are found between the lower and upper horizontal black line and

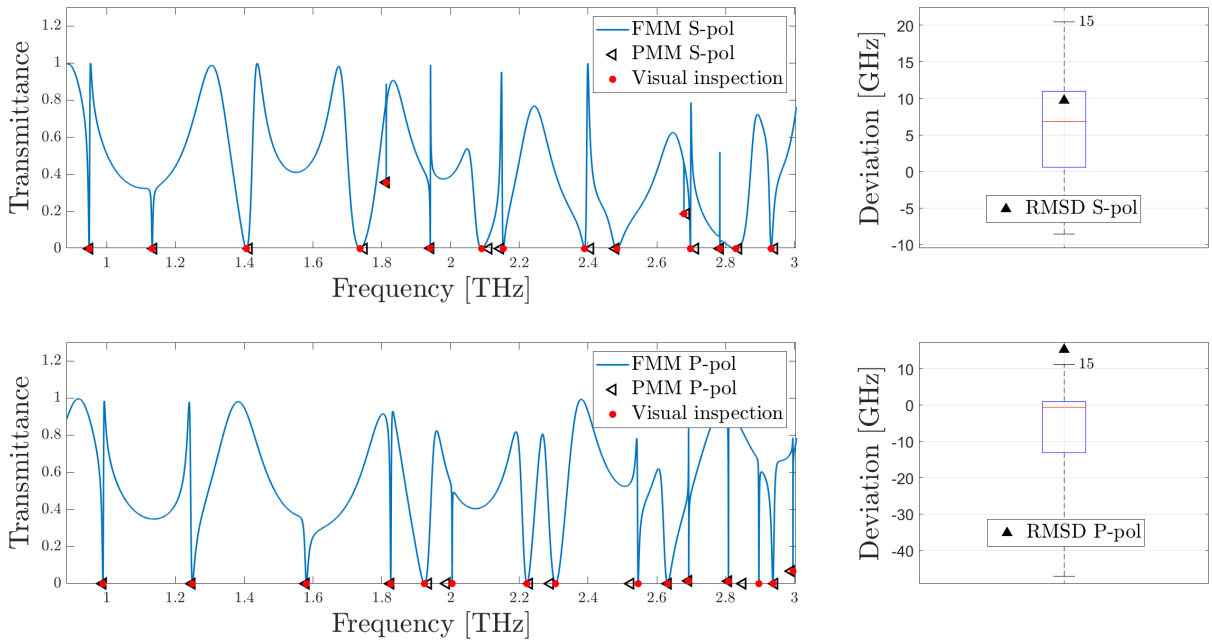

Figure 4.12: Comparison of visual inspection of the FMM spectra and the predictions made by the PMM for a structure with the same parameters as M1, which are presented in table 4.1. The FMM used a spectral resolution of 0.1 GHz. The graphs shown to the left are the spectra calculated with FMM, where the PMM predictions for the center frequencies have been overlayed. On the right, box plots of the difference between the visual inspection and the PMM predictions are shown, as well as the root mean square deviation of the data set. Tilted triangles: PMM predictions of Fano center frequencies. Filled circles: Fano center frequencies found from visual inspection of the spectra. Black filled triangles: Root mean square deviation. This data was first presented in [1].

the blue box, respectively. The root-mean-square-deviation (RMSD) is represented as the filled black triangle, and the amount of Fano resonances is marked with a number, in this case there are 15 resonances. From the box plot, it can be seen that the difference in frequency location of half of the resonances are within $\sim$ 14 GHz, while the entire data set is within $\sim$ 54 GHz. The RMSD are 15.4 and 9.7 GHz for P- and S-polarisation, respectively, very comparable with the difference found between the FMM and measured data. Besides being faster to compute, the PMM also finds the location of the Fano resonances itself, whereas the FMM had to be visually inspected. Additionally, the frequency resolution of the PMM need not be as high as the FMM to find the most narrow Fano resonances, such as the one located at $\sim$ 1.8 THz for the S-polarisation in fig. 4.5a. Hence the PMM has advantages over the FMM besides being faster, while still maintaining high accuracy.

To further test the correspondence between the two models, all the 36 combinations arising from the settings of $h = \{101, 149, 201\}$ μm, $\Lambda = \{100, 125\}$ μm, $\varepsilon = \{3.4^2\}$, $t = \{9, 15, 22\}$ μm, and $w_t = \{21, 54\}$ μm are tested. The spectral resolution of the FMM calculation is 100 MHz, and the Fano resonances found using FMM are again determined by visually inspecting the calculated spectra. For each setting, a box plot is calculated for both polarisations, seen in fig. 4.13.

The average RMSD values of all the box plots are 20.14 and 13.72 GHz for the S- and P-polarisation, respectively. At the extremes, the largest (smallest) RMSD values are 62.42 (7.02) GHz and 31.37 (3.85) GHz, for S- and P-polarisation respectively. The average absolute median deviation is 2.4 GHz and 4.4 GHz for the P- and S-polarisation, respectively.
All these results are very comparable to what was found using the settings of sample M1, presented in fig. 4.12, meaning that the results found there are not an isolated occurrence, but in fact the standard result one can expect. Furthermore, the accuracy of the PMM is excellent compared to the prediction accuracy of other models, e.g., the three-dimensional FEM model which was used in [101], which had a prediction precision of 98 and 59 GHz for P- and S-polarisation, respectively.

In figs. 4.14a and 4.14b the deviation of each Fano resonance is plotted as a function of normalised frequency, i.e., $\frac{\nu}{\nu_\Lambda}$, where the blue, red, and yellow asterisks are Fano resonances accessed by the first, second, and third diffraction order. By plotting against the normalised frequency, an interesting pattern occurs. When a diffraction order opens up, corresponding to the three vertical lines in figs. 4.14a and 4.14b, the deviation between Fano resonances is closest to zero, and then gradually spread out as the frequency is increased. This happens for all the diffraction orders, though it is more pronounced for the first order. This pattern is probably caused by the most significant assumption made in the PMM model, i.e., the empty lattice approximation, which treats the dielectric profile as an effective medium. This is of course a simplification for all frequencies, but it is an especially egregious assumption for high-frequency radiation, as it tends to accumulate in the region of high refractive index [43]. While this is a fitting explanation for Fano resonances utilizing the first diffraction order, marked as blue asterisks in fig. 4.14a and fig. 4.14b, it does not explain why the deviation for resonances using the other diffraction orders lies concentrated around zero deviation when their diffraction order becomes accessible. This can, however, also be explained by the empty lattice approximation. Figure 4.14c sketches the modelled structure as a slab waveguide where the periodic layer has been replaced by a homogeneous material with a lower refractive index than the substrate. The sketch shows that light with a wave vector equal to a diffraction order, e.g., $|\mathbf{k}| = \frac{2\pi m}{\Lambda}$ travels horizontally along

the structure, whereas it travels under an angle, θ, if the wave vector is larger, $|\mathbf{k}| > \frac{2\pi m}{\Lambda}$. Modes that travel using a large angle penetrate deeper into the cladding, meaning that they have a larger fraction of the field in the air and periodic region of the structure [44]. Thus, when a given diffraction order opens up, the radiation will travel almost exclusively along x, and penetrate minimally into the periodic layer. As the frequency increases, more of the radiation can be found in the periodic region, and the empty lattice approximation therefore has an increasing effect on the result, explaining the trend seen in figs. 4.14a and 4.14b.

Although a lot of attention was given to the deviations between the FMM and PMM models, the overall takeaway is that there is a sufficiently high agreement between the two models, and it is therefore concluded that the PMM model is a reliable tool for predicting the amount of Fano resonances and their frequency location. It is particularly strong when it comes to determining the existence of very sharp peaks, which would otherwise require a high spectral resolution when using the FMM. Furthermore, it does so with a significantly lower computational time.

Before proceeding with the last use case of the PMM, some caveats regarding the calculation of the box plots, fig. 4.13, will be covered. As stated, the location of Fano resonances found using FMM was determined by a visual inspection of the calculated spectra. The frequency range of the FMM calculation was limited to the range in eq. (4.7), however, the PMM was allowed to search for Fano resonances 20% past this upper-frequency limit. This was done to ensure Fano resonances found using the FMM near the upper frequency limit could always be partnered with predictions made with the PMM. If multiple peaks were found for frequencies in the extended region, only the resonances closest to the frequency region eq. (4.7) was kept. The total amount of Fano resonances found and presented in the box plots is 1387, however, two additional resonances were found. These two resonances were removed from the data sets because the location of the resonances could not be unambiguously assigned, as the FMM calculated spectra were hard to interpret. With there only being two issues out of 1387 found resonances, it is concluded that the PMM predicts the amount of Fano resonances with very high accuracy.

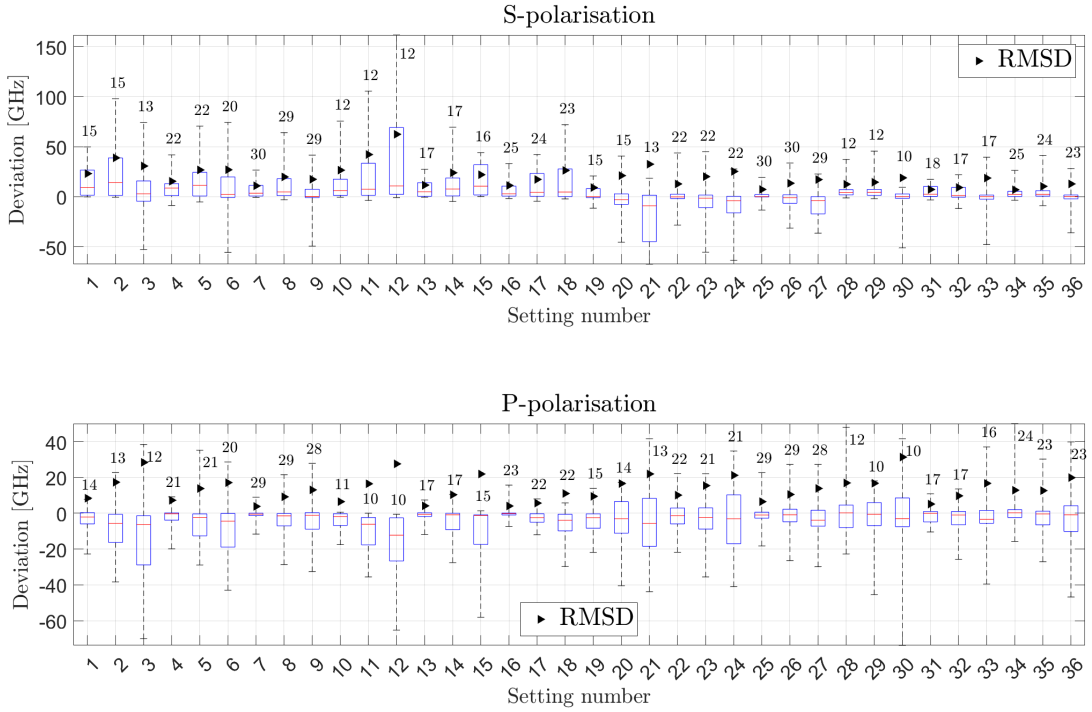

Figure 4.13: Box plots of the deviation between the PMM and FMM for both polarisations.

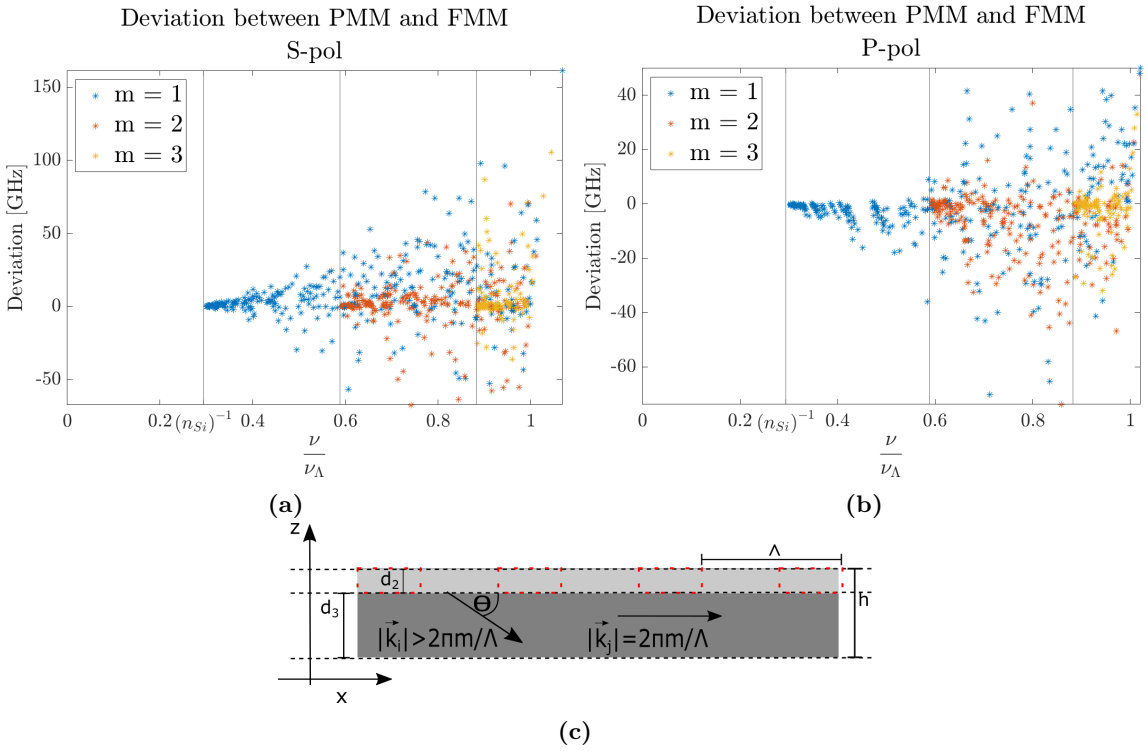

Figure 4.14: Deviation between the PMM and FMM plotted against the normalised frequency for **(a)** S-polarisation and **(b)** P-polarisation. **(c)** Sketch of the structure as a slab waveguide with the periodic part replaced by an effective medium.

4.2.2 PMM Based Design Model

Because the PMM model is one-dimensional it is feasible to search the whole set of configurations, for a given wafer height h, which in turn opens up for constructing a simple model that takes the wafer height and desired frequency as input, and then finds the necessary parameters which have a Fano resonance at the input frequency. As a first primitive model will search the entire set of configurations for a given frequency to find a subset of configurations resulting in resonances at this frequency. Then, as the frequency is kept constant the following parameters can be freely varied

$$[d_2,\, d_3,\, \Lambda,\, w_t],$$

which may be further reduced to two independent parameters. This is done by first fixing the period of the structure such that the desired frequency is inside the range of interest, eq. (4.7). For convenience, the period is chosen such that the frequency of interest is in the middle of the range. This choice is completely arbitrary and any choice of period which results in the frequency of interest being inside the range would be fine. It is therefore fine to limit the choice of period to what can be feasibly fabricated with the tools available. Furthermore, it will be required that the total height of the structure is constant, i.e., $d_2 + d_3 = h$. Thus these parameters are coupled in such a way that only one needs to be varied as the other can be made dependent. In the following algorithm, d_2 was chosen as the varying parameter. The proposed algorithm is then as follows:

1. Choose the frequency of interest: ν_i
2. Calculate the corresponding wavelength: $\lambda_i = \frac{c}{\nu_i}$
3. Calculate the period: $\Lambda = \lambda_i \left(\frac{2}{1+n_{sub}}\right)$
4. Let d_2 be defined in the range $d_2 \in [0, h]$. The range may be changed based on the fabrication specifications.
5. Let w_t be defined in the range $w_t \in [0, 1]\Lambda$. The range may be changed based on the fabrication specifications.
6. For each w_t calculate the effective refractive index.
7. For each set (d_2, w_t) calculate the propagation constants for the set of bound modes for both polarisations.
8. Calculate the contour lines for the first N-diffraction orders, $G_{x,m} = k_x + m\frac{2\pi}{\Lambda}$.
9. Each contour line represents the set of structures that will result in a Fano resonance at the desired frequency.

The implementation of the algorithm can be seen in fig. 4.15, where both d_2 and w_t have been sampled 100 times resulting in 10000 different combinations. As can be seen from fig. 4.15c a wide set exists which allows for the construction of a structure that has a Fano resonance at 1.6 THz. Another feature which can be seen in fig. 4.15c is that for this period no simultaneous resonances exist. If this was a requirement it is necessary to also vary the period to examine if such a configuration is possible.

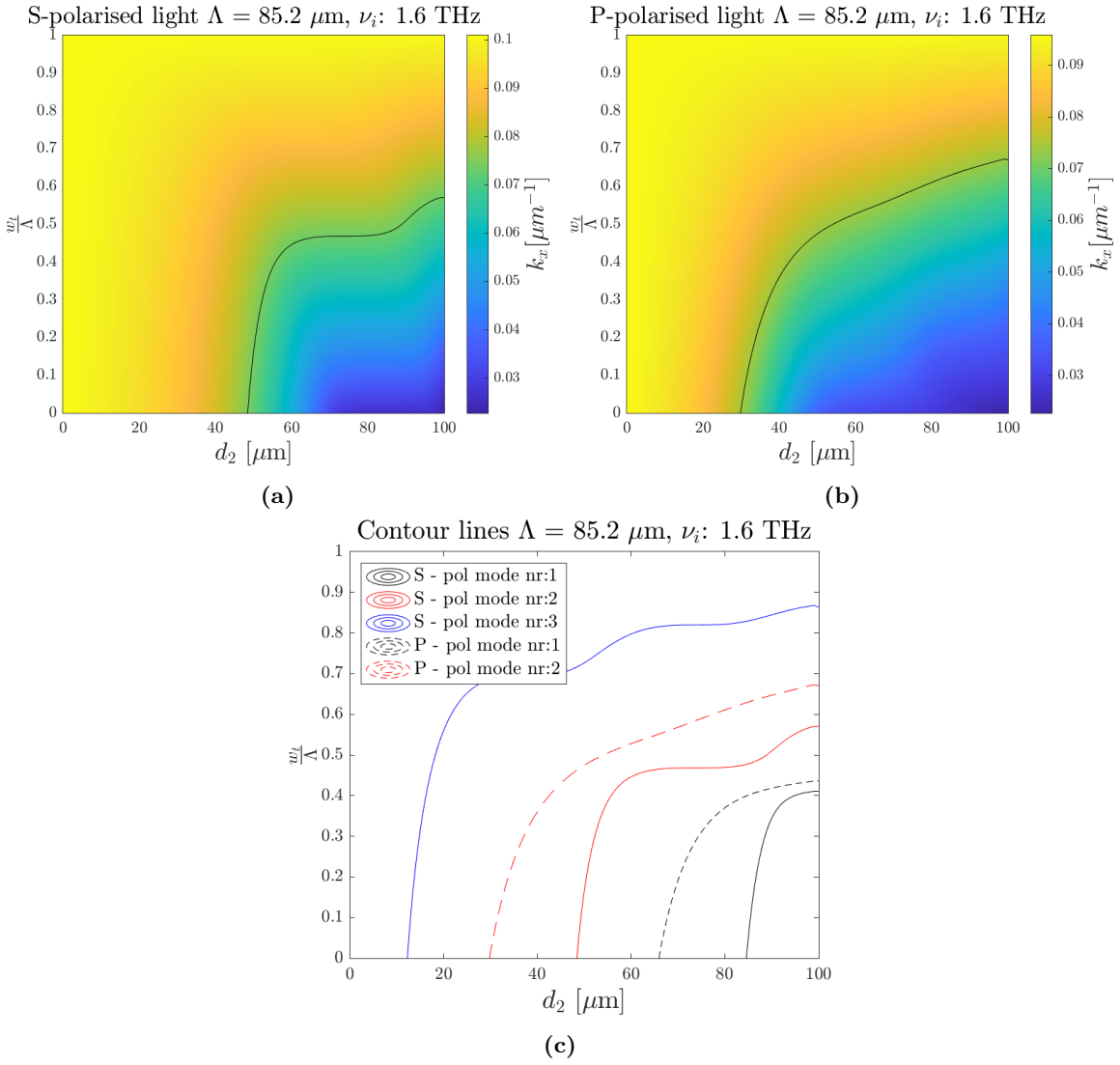

Figure 4.15: **(a)** Shows the map of propagation constants for the second bound mode, for S-polarised light along with the contour line at the first diffraction order. It is along this line that the PMM model predicts Fano resonances at the desired frequency. **(b)** The same as **(a)**, but for P-polarised light. **(c)** Shows the contour lines for each of the modes that result in a Fano resonance at the desired frequency, according to the PMM model.

4.3 Conclusion of Part I

In this part of the project, four samples supporting Fano resonances were presented along with Fourier transformed time-domain transmittance spectra for angles of incidence up to 10°. The physical characteristics of the samples were measured, and the Fourier Modal Method was used to calculate the transmittance spectra of the structures. High agreement between modelled and measured transmittance spectra was shown, with the modelled and measured Fano resonances being found within 15 GHz for all samples at normal incidence, and within 8 GHz for one sample for angles of incidence between 0 and 10°. A one-dimensional model, dubbed the Propagation constant Matching Model, was developed, explaining the cause of the Fano resonances as coupling of discrete and continuous guided modes in the structure. Despite approximations, the one-dimensional model was in excellent agreement with the rigorous two-dimensional model based on the Fourier Modal Method. Finally, a simple algorithm was presented, utilising the inexpensiveness of the one-dimensional model to search parameter space for combinations of etch depth and strip width that result in Fano resonances at some input frequency.

Part III

Photonic Crystals

5 | Results and Discussion

In this part of the project, two-dimensional photonic crystals exhibiting band gaps in the frequency range 0.1-0.4 THz are presented along with their transmittance spectra. Furthermore, samples with line and point defects are also presented. The samples are based on two fabrication procedures, laser ablation, used to fabricate samples consisting of air holes in silicon, and reactive ion etching used to fabricate free-standing silicon rods. The free-standing rods are based on wafers of thickness 200 $\pm 10\mu$m. The photonic crystals based on air holes in silicon use wafers of thickness 100 $\pm 20\mu$m.

The first step to create effective waveguides in the THz region based on photonic crystals is to fabricate structures with band gaps in the regions of interest. As was outlined in subsection 2.3.2 the photonic crystals of interest are silicon rods as well as air holes in silicon. The former exhibits band gaps for S-polarised light using both square and hexagonal lattice with a wide range of r/Λ [43]. The holed structure features a band gap for both polarisations when a hexagonal lattice is used, but it does so in a much narrower range of r/Λ. Hence these are the three configurations that were fabricated and tested. To dimension the structures, the band diagrams calculated using PWE are used (see subsection 2.3.4). Based on these calculations, and the experience attained with the two fabrication methods, the focus was placed on the lower end of the terahertz spectrum because the two fabrication methods lend themselves better to fabricate structures with corresponding dimensions. To target the higher frequencies, rods, and holes of smaller radii would have to be produced, which is a challenge because of the undercutting taking place when using regular RIE, subsection 3.1.1. In the case of holed structures, smaller holes would have to be produced which would significantly increase the fabrication time.

The optical response of the fabricated structures was measured using time domain-spectroscopy. For direct comparison with the measured time-domain spectra, the FMM model presented in subsection 2.4.5.3 was used to model transmittance graphs based on the measured dimensions of the structures. The fabricated structures and their dimensions were introduced at the beginning of the chapter, commenting on the quality of the samples and how the fabrication method resulted in structures that deviate from the ideal versions, for which band structures and GMG ratios were presented in subsection 2.3.4. Transmittance spectra of the fabricated samples were then presented and a thorough analysis of the observed band gaps was made in relation to the transmittance spectra calculated with the two-dimensional FMM model as outlined in subsection 2.4.5.3. Then to bridge the gap between the ideal two-dimensional structures used in the FMM model and the fabricated samples, the three-dimensional FFT model presented in section 2.5 was used, where the effect of introducing a homogeneous dielectric layer between the metal plate of the sample holder and the sample was investigated. The chapter is concluded

by analysing the effect of introducing line defects (waveguides) and point defects (cavities) to photonic crystals.

5.1 Photonic Crystals based on Laser Ablation

The photonic crystals fabricated using laser ablation were all based on hexagonal arrays of holes in high-resistivity silicon wafers. A detailed description of the principles of laser ablation and the system used can be found in section 3.2. In this chapter, only a select set of parameters are commented upon.

The pulsed laser system was operated at a repetition rate of 1 kHz and provides an output effect of $\sim$ 340 mW. The pulses were focused onto the surface of the Si wafer, ablating the surface. Holes were cut using stepper motors such that the sample may be freely moved in a plane perpendicular to the laser beam. The wafer was moved in a circle of radius 200 μm, which takes $\sim$ 0.5 seconds. To cut through the wafer, this motion was repeated between 30 and 160 times for each hole, depending on the wafer thickness and the given day. After the circular motions have been repeated for the set amount of times, a shutter blocks the beam, and the stepper motor moves the wafer to the coordinates of the next circle. Every sample in this project has between 240 and 595 individual holes, making the fabrication time last between 1 and 13 hours.

The various types of ablated photonic crystals can be seen in fig. 5.1, showing both one- and two-dimensional structures. The ablation profile in this project was not vertical, as can be seen in fig. 5.2(a), which is an SEM image of the ablation profile when cutting a line into a wafer with a thickness of 100 μm. The result of this ablation profile was that the radius of the hole on the entry side is larger than it is on the exit side, sketched in fig. 5.2(e). Another thing which can be seen from fig. 5.2(a) is that there is a significant amount of redeposited material on the entry side. Specifically, fig. 5.2(a) has in increased height around the cut on the entry side of $47 \pm 2\mu$m. This is noteworthy because it prevents the metal plates on the sample holder to come into direct contact with the wafer, resulting in an air layer between the photonic crystal and sample holder. The issue of redeposition was eventually solved by using a lens of shorter focal length and wafers of thickness $200 \pm 10\mu$m, e.g., fig. 5.2(b). Originally, a lens with a focal length of 50 cm was used, which did not provide enough fluence to cut through wafers with a thickness of 200 μm. Therefore, focal lengths of 25, 10, and 7.5 cm were tested. It was found that the shorter the focal length, the less material was redeposited and the number of circles needed to cut through a wafer was significantly reduced. The shorter focal length also results in a higher fluence at the laser focus, as written in section 3.2. This in turn means that the ablation process is no longer dominated by the Coulomb explosion, instead, thermal evaporation dominates [88]. It was therefore expected that redeposition would increase, however, the opposite was instead observed. This may be due to the gas phase being ejected at high velocities due to the vapour pressure and the recoil pressure of light [90]. If the vapour phase is removed far enough from the sample, the removed particles will not be redeposited on the wafer during the subsequent solidification, explaining the decrease in redeposited material observed in this project when lenses with shorter focal lengths were used.

However, as will be discussed later, only the samples based on wafers of thickness $100 \pm 20\mu$m have a noteworthy optical signal, why the amount of redeposited material shown in fig. 5.2(a) has to be taken into account, because no wafers remained to create new samples with the 7.5

cm lens. Figure 5.2(c) and fig. 5.2(d) show ablated structures from the entry and exit sides, respectively. It is clear that there is much less redeposited material on the exit side.

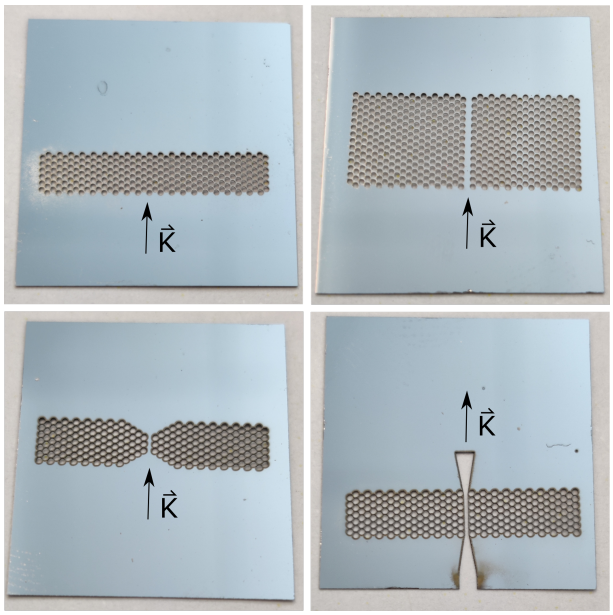

Figure 5.1: Images of the various types of photonic crystals fabricated using laser ablation. All structures based on holes were designed to probe the **K**-direction.

5.2 Photonic Crystals based on RIE

Various types of photonic crystals fabricated using RIE are presented in fig. 5.3, featuring both square and hexagonal arrays of silicon rods standing on a silicon substrate. A description of the principles of RIE can be found in section 3.1. Because the fabrication time of these samples was independent of the amount of placed rods, the hexagonal samples have been made so that both the **K**- and **M**-direction can be probed on a single sample, as the rotation of 90 degrees changes the direction from **M** to **K** or vice versa. The reason this was only done for the rod samples was that for the Hex-hole samples the structured part of the samples, i.e. the surface area where the dielectric function is periodic, was not made large enough in both directions, as can be seen by comparing figs. 5.1 and 5.3.

There are three ways that the rods produced in this project deviate from the ideal rods modelled in subsection 2.3.4. The first and most obvious deviation is that the free-standing rods are not truly free-standing, but instead stand on a substrate layer, e.g., fig. 5.4(c). The effect of this substrate layer and its thickness will be covered later in subsection 5.3.2. The second reason was touched upon when the method of RIE was introduced, subsection 3.1.1, and that is the significant undercutting taking place. Besides making it difficult to design the photolithography masks, it also yields angled rods, which can be seen in fig. 5.4(c). The third way the produced rods deviate is that they are not circular at the top or base, as can be seen in fig. 5.4(a). The reason for the odd shape of the rods can be traced back to the photolithography mask, which was printed by a regular laser printer, a RICOH IM C5500. This results in a photolithography mask that does not consist of perfect circles, and therefore the resulting hardmask does not either,

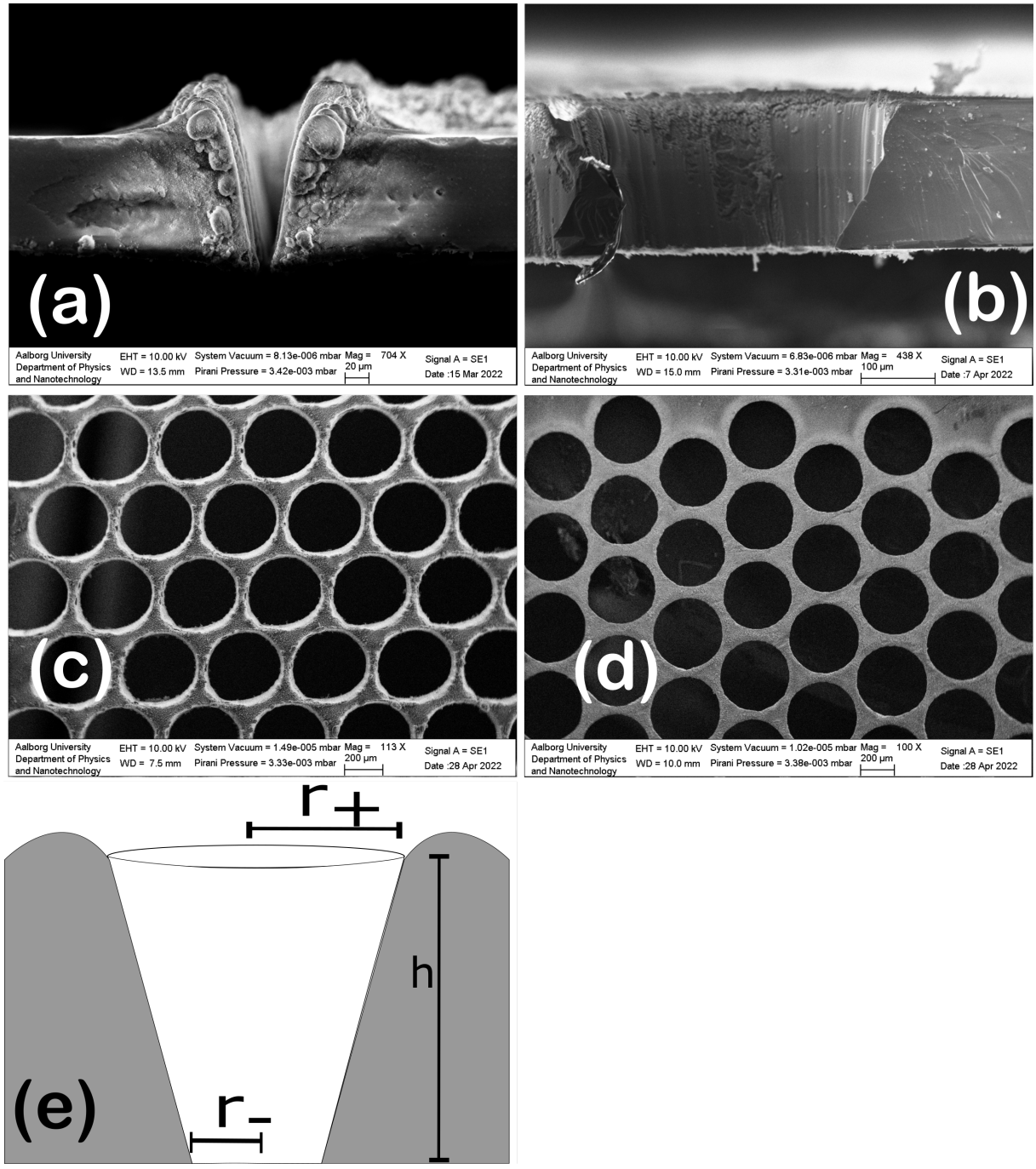

Figure 5.2: **(a)** SEM image of the ablation profile through a wafer with a thickness of 100 μm. A lens with a focal length of 50 cm was used to focus the beam. It is clearly seen that the cut is wider and that the height of the redeposited material is larger on the entry side. **(b)** SEM image of the ablation profile of a wafer with thickness 200 μm. A lens with a focal length of 7.5 cm was used to focus the beam. It is clearly seen that there is much less, if any, redeposited material. **(c)** SEM image of a photonic crystal based on air holes in Si, imaged from the entry side of the pulsed laser. **(d)** SEM image of a photonic crystal based on air holes in Si, imaged from the exit side of the pulsed laser. Both samples **(c)** and **(d)** was cut using a lens with a focal length of 7.5 cm. **(e)** Sketches the hole profile resulting from the varying ablation width through the wafer, not to scale with the actual holes produced in this project.

as seen in fig. 5.4(d). This issue can easily be solved by using a professionally manufactured photolithography mask, resulting in much sharper etch profiles as was the case for the Fano samples, e.g., fig. 3.4b. However, due to the much longer etch times needed for the free-standing rods, etch profiles as sharp as those achieved for the Fano samples are not expected, even with better photolithography masks. For that to succeed, a more sophisticated etch process, like the Bosch process is probably needed.

To account for the structures being angled and the silicon base that the rods are standing on, the three-dimensional FFT model presented in section 2.5 was used instead. In it, the samples were approximated as the structure shown in fig. 5.4(b), and the parameters r_-, r_+, h, and t_w therefore have to be determined. The radius at the top and bottom of the rods, r_- and r_+, respectively, was determined by calculating the radius of a circle of equal area. The area was determined by outlining the top and bottom of the rods, as shown by the red and blue lines in fig. 5.4(a), and using ImageJ to calculate the area [81]. In fig. 5.4(c) both the remaining wafer thickness, t_w, and the height of the rods, h, can be measured directly. This was only possible because the wafer has been fractured down its center. It was not possible to measure t_w or h on whole samples for two reasons. The first is that, by design, the edge of all samples was protected by the hardmask during the etch, providing a surface more resilient where the sample can be picked up by tweezers. As shown in fig. 5.4(f), this edge prohibits the samples from being imaged from the side, and the height of the rods can therefore not be measured. The profilometer used for the measurements of Fano samples proved imprecise for structures with heights around $\sim 100\mu$m, and was therefore not used. The second reason is that just like the etch process undercuts the protective Cr layer, the etchant gas also diffuses underneath the wafer, providing a slight etch to the edges on the bottom side of the wafers. Therefore, t_w and h were generally estimated from etching times, though a few samples have been broken from which the etch rates have been determined.

In fig. 5.5(a)-(d), SEM images of some of the samples from the first series of free-standing rods are presented. The samples were designed to have heights of 150 μm, and volumes equivalent to a cylinder with a radius of 100 μm and a ratio $r/\Lambda \sim 0.175$, which would produce a band gap around 0.2 THz, according to the graphs in subsection 2.3.4. Six samples were prepared, having hardmask radii in the range 165 - 215 μm in accordance with the considerations in subsection 3.1.1. The etch times varied between 155 and 210 minutes. The sample presented in fig. 5.5(a) had hardmask radii of $\sim$ 150 μm, and was etched for 210 minutes. The sample was fractured, and the height was measured to 149 μm. Although the sample reached the intended height, the shape of the top of the rods was too poor for the procedure to be deemed a success. It is worth noting, that even with rods as misshapen as those presented in fig. 5.5(a), a photonic band gap at 0.21-0.23 THz when illuminated along the **M**-direction was clearly detectable, fig. D.7. The sample in fig. 5.5(b) also had an etch time of 210 minutes, but the initial hardmask radii was $\sim$ 185 μm. Although the top of the rods is still far from circular, it is a vast improvement from the rods presented in fig. 5.5(a). Figure 5.5(c) and fig. 5.5(d) are from the same sample which also had a hardmask radii of 185 μm, but this sample was only etched for 155 minutes. It is clearly seen that the shape of the rods in this sample is superior to those presented in fig. 5.5(a) and fig. 5.5(b), though the height of the rods is smaller due to the shorter etching time. Based on this initial series of samples, a compromise had to be made between rod height and shape. To do this, all samples from this series were measured using THz-TDS and based on the quality of the transmittance spectra, all subsequent samples used the same fabrication parameters as the sample presented in fig. 5.5(c) and fig. 5.5(d). That is,

even when $\sim$ 50% of the wafer remains as a substrate material, band gaps and point defects were still detectable.
All relevant information about the samples for which optical spectra are presented has been gathered in table 5.1 for both rods and holes.

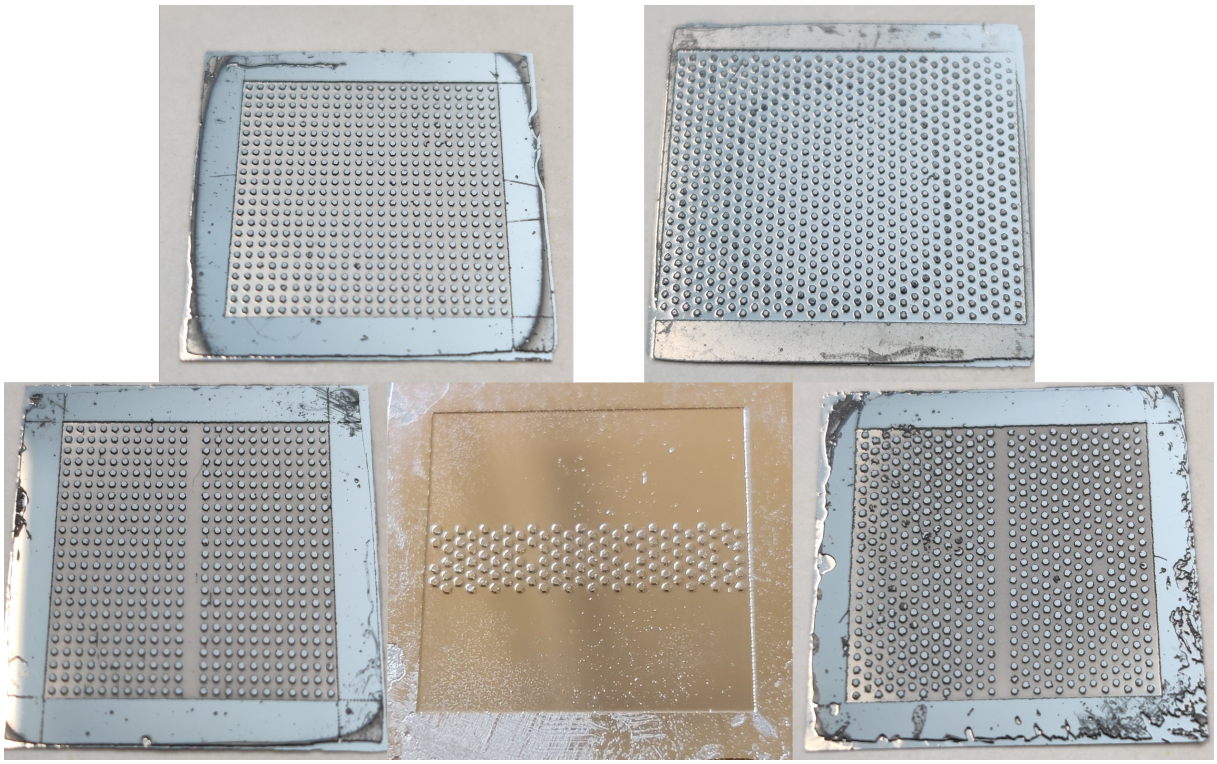

Figure 5.3: Images of the various types of photonic crystals fabricated using reactive ion etching. From left to right in descending order: Square array, hexagonal array, waveguide in square array, cavities in hexagonal array and waveguide in hexagonal array.

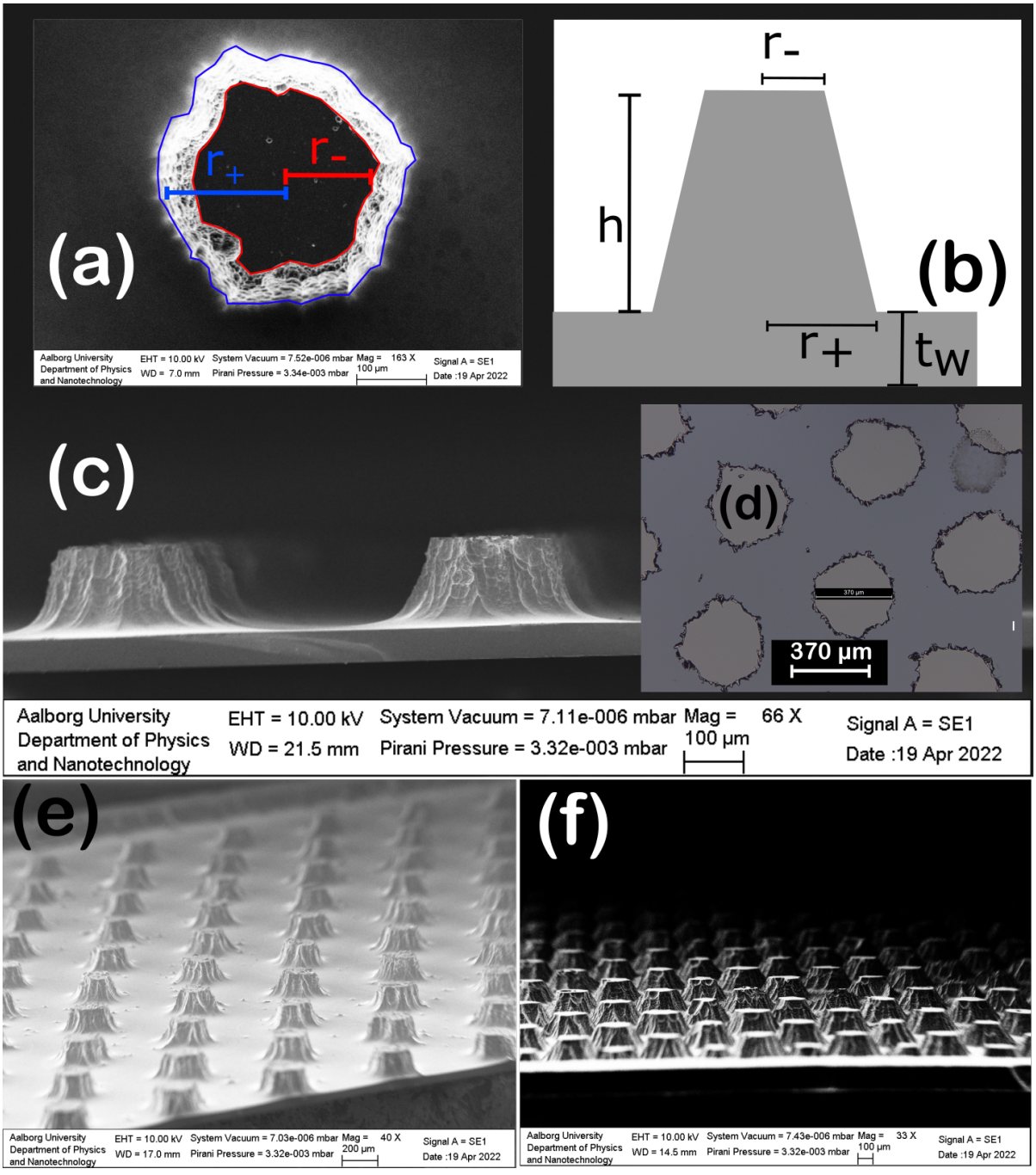

Figure 5.4: **(a)** Close-up SEM image of a rod viewed from the top. The radius at the top and bottom of the rod is illustrated with red and blue, respectively. The red and blue outlines illustrate how the area at the top and bottom was measured, from which the radius of an equivalent circle was calculated. It was in this manner that the radii used in the various models were determined. **(b)** Sketches all relevant structural parameters used in the models of the photonic crystals based on free-standing rods. **(c)** Side view of the Hex-rod-4 sample. **(d)** Light microscope image of the hardmask before any etching has taken place. It can be seen that the hardmask does not have the intended circular shape. **(e)** SEM image of a photonic crystal sample fractured down by its centre. Using this sample, the wafer and rod height can be directly measured. **(f)** SEM image of a photonic crystal sample that has not been fractured, illustrating how the protective edges prohibit direct measurement of the rods.

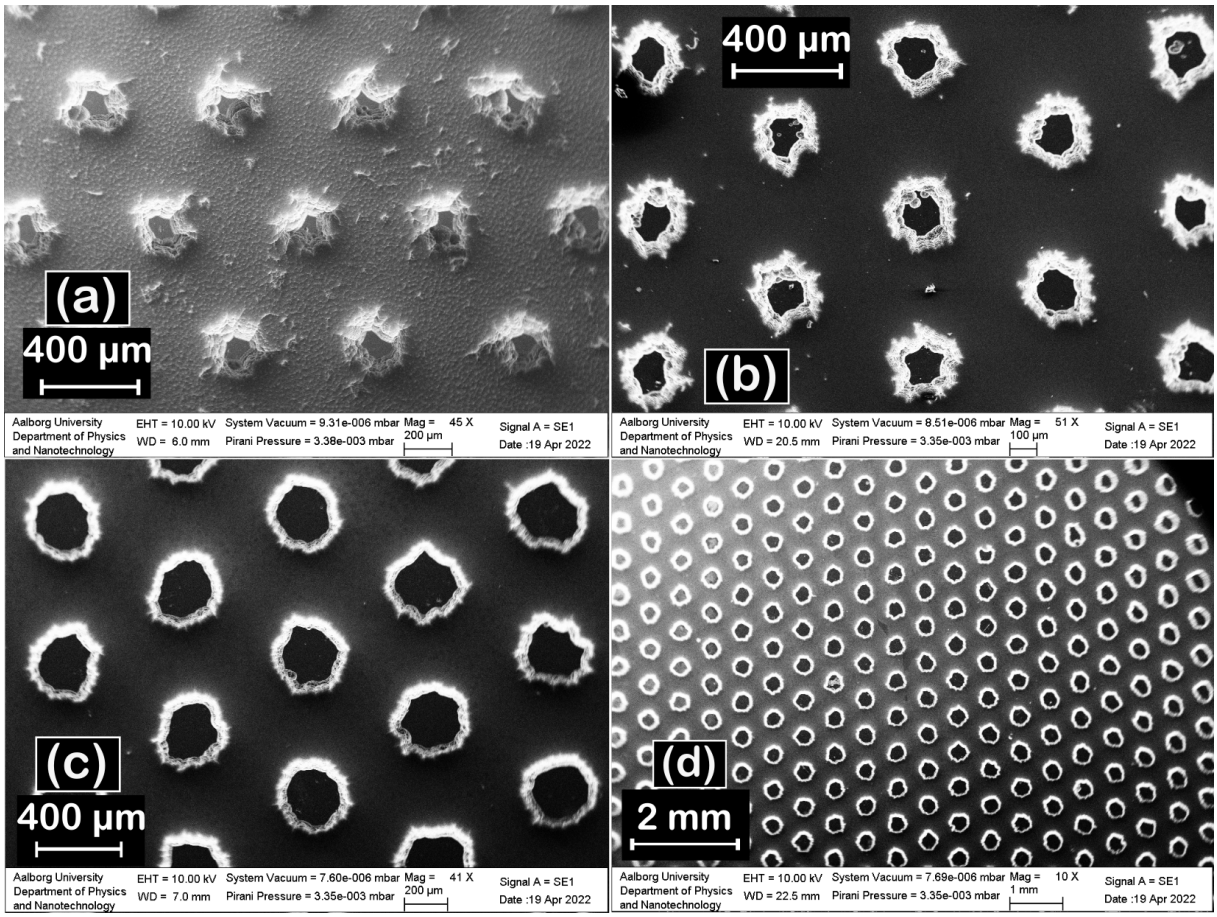

Figure 5.5: SEM images of the first series of photonic crystals based on free-standing rods. The different images had differing hardmask radii and etch times. **(a)** 150 μm, 210 minutes. **(b)** 185 μm, 210 minutes. (c), (d) 185 μm, 155 minutes.

	$\Lambda[\mu m]$	$r_-[\mu m]$	$r_+[\mu m]$	$t_w[\mu m]$	$h[\mu m]$	Orientation	Rows
Hex-hole-2	494.73	201.74	210.877	-	100 $\pm$20	K	13
Hex-hole-WG-1	434.63	202.23	222.33	-	100 $\pm$20	K	28
Hex-hole-WG-2	495.04	200.80	206.02	-	100 $\pm$20	K	13
Hex-hole-WG-3	491.00	201.00	210.60	-	100 $\pm$20	K	13
Hex-rod-3	616.35	76.26	124.96	92.11	98.74	M/K	36/51
Hex-rod-4	721.99	85.41	108.64	59.16	142.15	M/K	31/45
Square-rod-1	659.10	148.01	191.97	-	99.78†	X	23
Square-rod-WG-1	668.55	167.17	197.97	-	99.78†	X	23
Hex-rod-WG-1	660.00	152.99	202.03	-	99.78†	K	22
Hex-rod-cavity-2	638.16	161.14	161.14	-	99.78†	K	10

Table 5.1: Presents the dimensions relevant to modelling the fabricated samples. The naming convention for holes and rods is visualised in fig. 5.2(e) and fig. 5.4(b), respectively. †: calculated from etch time. In table D.1 the dimensions relevant for modelling all the fabricated samples can be found.

5.3 Optical Characterisation of Two-Dimensional Photonic Crystals

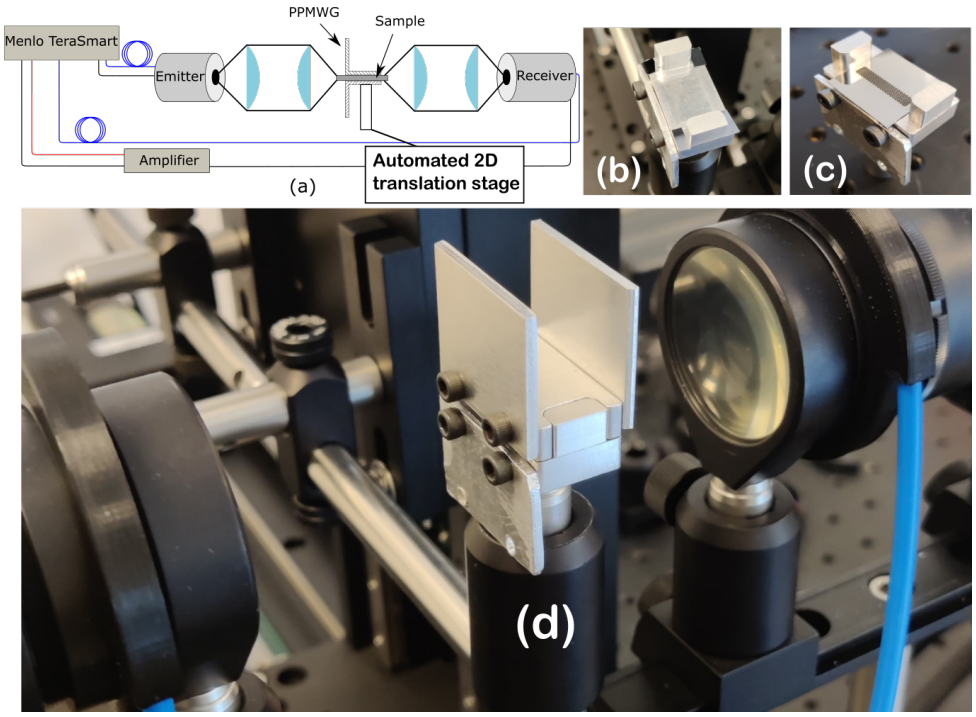

Figure 5.6: **(a)** Schematic of the experimental setup. **(b)** Image of the sample holder without the top metal plate. Parts of a broken wafer were placed at each corner, such that an air channel of 100 - 200 μm (depending on the pieces) was created. This was how the reference spectra were obtained for the two-dimensional photonic crystals. **(c)** Image of the sample holder with a photonic crystal placed inside it. **(d)** Image of the experimental setup.

To measure the optical response of the samples the Menlo THz-TDS system was used, the principles of which were outlined in section 3.3. The setup has been changed from what was used to measure Fano resonances, i.e., a parallel-plate metal waveguide (PPMWG) was used, and the edge of the sample was placed at the focus of the first lens, rather than at the collimated part of the beam. A scanning stage has been implemented, used for scanning the opening of the waveguides and the location of the point defects. The setup can be seen in fig. 5.6. All the measured spectra can be viewed in Appendix D.

5.3.1 FMM Transmittance Spectra

In this subsection, the focus will be on four samples designed to exhibit band gaps, to tell a more concise story. The four samples are Hex-hole-2, Square-rod-1, Hex-rod-3, and Hex-rod-4. These represent all the different configurations of both dielectric profile and lattice type. The measured results, FMM calculated transmittance spectra, and the band edges found using the three-dimensional FFT model can be seen in figs. 5.9 to 5.12. The FMM calculated spectra use the average of r_- and r_+, while the band edges found using the three-dimensional FFT model uses the dimensions presented in table 2.1. Before analysing the modelled and measured

spectra, it is noted that the measured transmittance reaches well above 1 for many frequencies below 0.3 THz. There are a variety of possible reasons for this, one being that the Menlo system used is particularly noisy for frequencies below 0.3 THz. Furthermore, the reference was measured by keeping the PPMWG open using small pieces of either 100 or 200 μm thick wafer pieces, such that it was essentially an air channel of corresponding thickness. This removes the significant reflection loss expected when transitioning from air to silicon, and it would therefore be expected that more radiation was transmitted through the reference, yet this, as mentioned, was not the case. It was hypothesised that this might be due to a better field overlap with the silicon-filled PPMWG-mode and hence a higher incoupling of power resulting in a higher signal for the sample, although this has not been investigated. Additionally, the sample protrudes a couple of mm outside the sample holder. Therefore, if the focus of the Menlo system lies a couple of mm in front of the opening of the sample holder, it is expected that more signal can be transmitted when a sample, rather than the reference, is measured.

The spectra in figs. 5.9 to 5.12 clearly show band gaps in the expected frequency region, where in particular the **K**-direction of Hex-rod-4 shows excellent agreement between the FMM modelled spectra and measurements. Generally, the Hex-rod samples exhibit acceptable agreement for the lower band gap edge (LBGE) for both directions, whereas the upper band gap edge (UBGE) is only well predicted for the **K**-direction, when compared to the FMM spectra. The Hex-hole-2 sample on the other hand shows a large blueshift of the band gap in relation to the FMM modelled spectrum with a lower band gap change of 77.64% and an upper band gap edge change of 42.65%. All percent deviations in this chapter were calculated as the absolute deviation, i.e.,

$$\text{percent deviation} = \frac{\text{measured value} - \text{modelled value}}{\text{modelled value}} \cdot 100. \tag{5.1}$$

The Square-rod-1 sample also shows a shift of the band edges. However, in this case the upper edge has moved to lower frequencies while the lower edge has moved to higher frequencies resulting in a band gap that is situated in the right frequency region but is too small when compared to the FMM modelled spectra. In table 5.2 the band gap shift in % of the four samples presented here are shown along with the percentage of the wafer thickness which is structured and calculated as

$$\text{percentage} = \frac{d_{PC}}{D} \cdot 100, \tag{5.2}$$

where d_{PC} is the thickness of the photonic crystal, and D is the distance between the metal plates. The distance D and d_{PC} vary because of redeposited material and the remaining wafer, for air holes in silicon and free-standing rods, illustrated in fig. 5.7(a) and (b), respectively.

Band gap shift:	LBGE **M**	UBGE **M**	LBGE **K**	UBGE **K**	LBGE **X**	UBGE **X**	% PC
Hex-hole-2	-	-	77.64%	42.65 %	-	-	NaN
Square-rod-1	-	-	-	-	16.22 %	-17.18 %	50%
Hex-rod-3	-1.05 %	-27.37 %	7.80 %	-13.01 %	-	-	59 %
Hex-rod-4	-2.30 %	-21.57 %	3.31 %	-8.54 %	-	-	70 %

Table 5.2: Presents the deviation in % of the upper and lower band gap edges of the measured data with respect to the spectra modelled with the FMM, calculated as eq. (5.1). The last column denotes the percent of the wafer thickness which is a photonic crystal.

The discrepancy between the measured and FMM modelled spectra is quite pronounced for all samples. A shift of band gaps has been reported earlier by *Zhongping Jian et al 2005* [70].

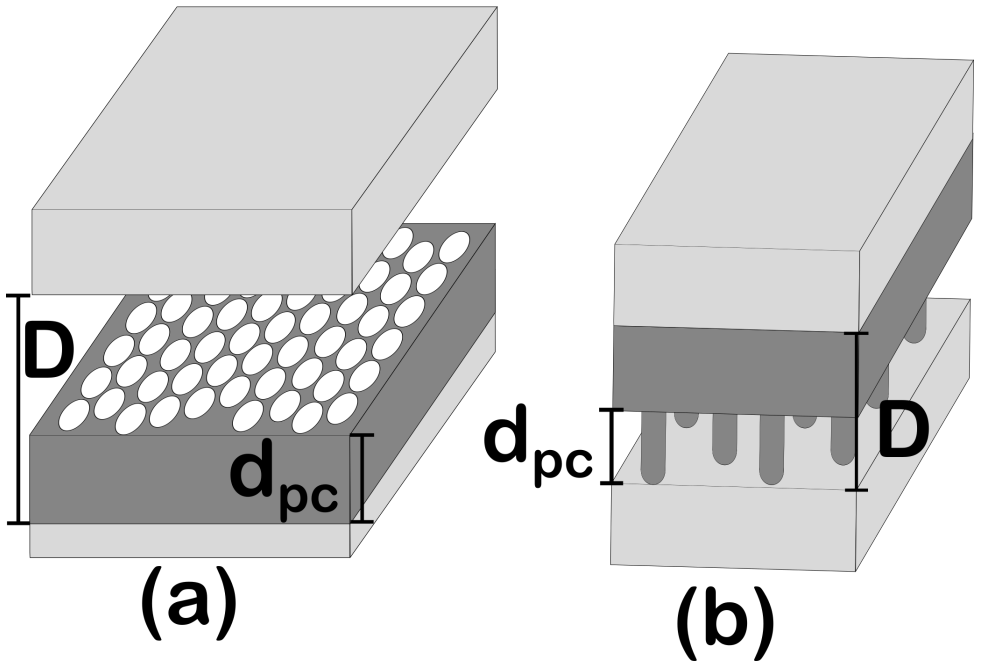

Figure 5.7: Schematic illustrating how the structured part of the photonic crystals does not extend through the entire height of the sample holder. **(a)** Air holes in silicon, and **(b)** Silicon rods.

Here, a systematic blueshift was observed for the band gaps in a photonic crystal consisting of a hexagonal array of air holes in a silicon wafer of thickness 300 μm. In their paper, they attributed this shift to the finite thickness of the wafer, in accordance with the theory outlined in *Two-dimensional terahertz photonic crystals fabricated by deep reactive ion etching in Si* [106]. This theory outlines how the overall in-plane refractive index in the metal waveguide is lowered as multiple modes are allowed within the guide. This in turn would result in the band gap moving to higher frequencies [43]. For this to be a valid explanation for the blueshift observed in Hex-hole-2, multiple modes have to exist inside the sample holder.
To investigate the number of possible modes, the cutoff frequency for a homogeneous medium between two perfect electric conductors was derived (Appendix E) with the result being

$$\nu > \frac{m\,c}{2\,D\,n_i}. \tag{5.3}$$

If $m = 1$ for the 200 μm wafer i.e., for one additional mode to exist other than the fundamental mode, in the region between the PPMWG, the frequency has to be above $\nu > 0.22$ THz if the space is filled with silicon, or $\nu > 0.75$ THz for an air-filled waveguide. Hence this could only affect the upper band gap edge for Hex-hole-1, Hex-rod-3, and Hex-rod-4 samples. This would be the case if the metal waveguide was filled with silicon, in reality most of the structured space would be air, bringing the effective refractive index closer to that of air, and thus none of the photonic crystals fabricated in this project would support multiple PPMWG modes for the frequencies of interest, and therefore the explanation provided in [106] is not a valid explanation for the deviations presented in table 5.2. Instead, a solution to this problem is presented in subsection 5.3.2 using the three-dimensional FFT model. Before proceeding with that explanation, the size of the measured band gaps will be commented on.

As outlined in subsection 2.3.1 a measure of the size of the band gap is the GMG ratio. In

table 5.3 the measured GMG ratios and those modelled with the FMM and PWE have been tabulated. It can be seen that the measured GMG ratios for the samples are in the range $\sim [19-34]\%$, the GMG ratios calculated with PWE being between $\sim [32-37]\%$ for the rod samples and $\sim 2\%$ for the hole samples. The measured GMG ratios are good considering the fabrication limitations when compared with the GMG ratios expected in table 2.1 on page 30. However, these are all inferior to the GMG ratios predicted by the FMM model presented in table 2.1. This has a simple explanation, namely that the FMM model has all its radiation propagating along one specific direction, and it therefore probes a single transition in the band structure, either **M**, **K**, or **X**, whereas the GMG ratios found with the PWE method were for indirect band gap transitions, and are consequently lower. Between these two extremes are the measurements, which probe some, but not all of the transitions in the band structure, because the incident radiation was not collimated, as the lens has diameter of 38 mm and focal length of 50 mm, corresponding to an angle-space of $\sim 21^\circ$ at the focus. For reference, a rotation of 30° is equivalent to changing from the **K** to **M** direction, or vice versa.
Consequently, the measured GMG ratios are significantly reduced from their FMM calculated counterpart, yet, some of them are still above the expected values for the indirect gap, especially pronounced for the Hex-hole-2 band gap, despite the fact that the measured band gap has been blueshifted upwards of 77 % as shown in table 5.2. In general, most of the measured GMG ratios are reduced to about half of those modelled by the FMM. Furthermore, as will be shown in fig. 5.13 for the holed sample, the fabrication limitations result in the band gap naturally shrinking as it is blueshifted and hence both effects will result in a reduction of the GMG ratio. For the rod samples, the expected shift is instead a redshift which would in turn result in a higher GMG ratio, however, the band gap still shrinks, and it was furthermore speculated that aperiodic effects can further reduce the band gap, further reducing GMG ratios [107].

GMG:	**M**	**M** FMM	**K**	**K** FMM	**X**	**X** FMM	PWE
Hex-hole-2	-	-	19.33%	40.75 %	-	-	~ 2 %
Square-rod-1	-	-	-	-	18.93 %	51.66 %	32 %
Hex-rod-3	22.82 %	52.59 %	31.21 %	51.72 %	-	-	36.5 %
Hex-rod-4	25.68 %	46.9 %	34.36 %	46.05 %	-	-	36.5 %

Table 5.3: Measured GMG ratios of the samples along with the ones found using the FMM and PWE model. The FMM entries give the value of either the **M** or **K** transition, while the PWE gives the value of the indirect gap based on the findings in subsection 2.3.4 using the r/Λ ratios from table 5.1.

5.3.2 Three-Dimensional FFT Analysis

In this section, the cause of the shifted and shrunken measured band gaps, as compared to those predicted by the FMM, see figs. 5.9 to 5.12, will be investigated by performing a three-dimensional analysis of the structures using the FFT method outlined in section 2.5. The three-dimensional treatment of the problem allows for the incorporation of some of the deviations between the fabricated and idealised structures discussed in section 5.1 and section 5.2, i.e., the silicon layer that the rods necessarily has to stand on, that all structures are angled, and the existence of redeposited material on the ablated structures. In the case of the rods, incorporating the silicon layer increases the effective refractive index in the metal waveguide and hence would redshift the bands in accordance with the previously mentioned paper [106]. The opposite is expected for the ablated structures. The sample Hex-hole-1 was fabricated with the same setup that resulted in fig. 5.2(a) and it is therefore expected that a large amount of redeposited material is present, around 47 μm. This would then result in an air layer being present between the wafer and the metal plate, reducing the effective refractive index and thereby blueshifting the band gap [106].

To determine to what extent these regions of homogeneous dielectric media might explain the shifts observed in the measurements, the band structure was calculated for a two-layered system, a photonic crystal layer, and a layer of homogeneous dielectric material, placed between two metal plates. If the photonic crystal was based on silicon rods, then the distance between the metal plates, D, was fixed, and for each calculation, the thickness of the dielectric material was increased, while the photonic crystal layer, d_{pc}, was correspondingly decreased. If the photonic crystal is based on air holes, then the thickness of the photonic crystal, d_{pc}, was held constant, and the dielectric layer material, and the distance between the metal plates, D, were increased for each calculation. Refer to fig. 5.7 for annotations. The result of these calculations along with the measured shift of the band gaps with respect to the FMM model is presented in fig. 5.13. The dotted lines are from the FFT calculations, while the triangles are from the measured spectra.

As mentioned, the exact height of redeposited material on the Hex-hole-1 sample was not able to be measured without breaking the sample, and this height is therefore not known. Instead, lines corresponding to the shift of the band edges have been drawn, seen as the horizontal blue and red lines in fig. 5.13. It can be seen that there is great agreement between the measurement of Hex-Hole-2 and the modelled band edges if the redeposited material constitutes about 37% of the height within the metal waveguide. This would correspond to having redeposited 58.7μm for a wafer of 100 μm thickness and 52.8 μm for a 90 μm wafer. This is between 10% and 20% more redeposited material than was observed in fig. 5.2(a), which is not unrealistic although higher than expected. The vertical red lines in fig. 5.9 is the result of shifting the LBGE and UBGE of the FMM modelled spectra by the percent deviation corresponding to 40% air, found in fig. 5.13(**a**). This produces a significantly better agreement between modelled and measured band gap, though the measured LBGE and UBGE are found at slightly lower frequencies than their modelled counterparts.

In the case of silicon rods, the effect on the position of the LBGE and UBGE when introducing a silicon layer in the three-dimensional FFT model, and the measured deviations with respect to the FMM spectra can be seen in fig. 5.13(b)-(d). It is clearly observed that the FFT model predicts that both band gap edges move to lower frequencies when the silicon layer is increased. However, because the shift is much larger for the UBGE the band gap shrinks with respect to

the band gap predicted by the FMM, an effect observed for all the rod-based samples presented in this chapter. The band edges predicted by the FFT model for the rod-based samples are seen in figs. 5.10 to 5.12 as the vertical red bars. While the measured band gaps for the rod-based samples were always found within the frequency range predicted by the FMM model, the size of the band gap predicted by the FFT model is in much better correspondence with the measurements, though a general tendency, with the exception being Hex-rod-4 **K**, is that the FFT band edges are slightly red-shifted with respect to the measured band edges for rod-based samples.

Further inspection of fig. 5.13 reveals that the photonic crystals based on air holes are more sensitive to the dielectric layer, seeing as the LBGE and UBGE have changed by $\sim 30\%$ and $\sim 42\%$ after introducing a dielectric layer of 10%, far exceeding the modest changes of a couple percent observed for the photonic crystals based on silicon rods when a dielectric layer of 10% is introduced. The reason for this difference between the two sample types may be understood by considering a simple one-dimensional configuration as shown in fig. 5.8, where the geometric effective dielectric constant may be found as

$$\frac{1}{\varepsilon_{eff}} = \frac{d/H}{\varepsilon_{\mathrm{Si}}} + \frac{1 - d/H}{1}. \tag{5.4}$$

The reason for the effective dielectric constant being calculated as $\frac{1}{\varepsilon_{eff}}$ is that only the S-polarisation can exist for the waveguides in question, as argued in Appendix E. For the samples produced in this project the factor d/H in eq. (5.4) will be rather small and it will further be divided by $\varepsilon_{\mathrm{si}}$ which in comparison is large. Therefore, when the equation is inverted to calculate ε_{eff} it will be the second term that dominates and thus the value will be very close to the dielectric constant of air. Hence increasing the silicon layer that the rods stand on will not significantly increase the effective refractive index for this region, and the bands will not shift by much. On the other hand, for the hole configuration the enumerators of the two terms will be switched as

$$\frac{1}{\varepsilon_{eff}} = \frac{1 - d/H}{\varepsilon_{\mathrm{Si}}} + \frac{d/H}{1}. \tag{5.5}$$

For the same reason as outlined above, this will then result in the effective dielectric constant in eq. (5.5) being somewhat close to that of air when it should be close to silicon. The dielectric difference would, therefore, be smaller and this would shift the band gaps up. This simple model thus offers a suggestion as to why the two configurations show differing sensibilities regarding the thickness of the dielectric layer.

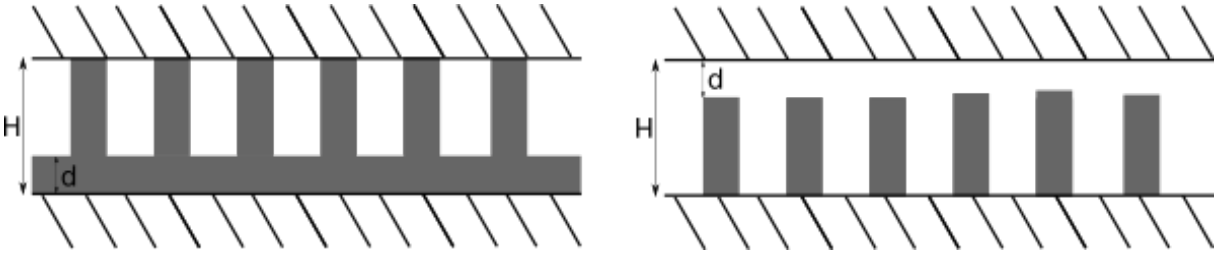

Figure 5.8: A sketch of the two configurations of photonic crystals used to explain the difference in effective dielectric constant.

There are other significant effects that influence the location of the LBGE and UBGE, i.e., the FMM model assumes that the sample is only probed along a specific direction, e.g., the

M-direction, while the measured spectra probe an angle space of $\sim 21°$. Another reason for the smaller band gaps could be due to aperiodicity in the photonic crystals, which can result in localised modes near the band edge [107]. In the case of a finite crystal, some of these modes could be transmitted through the crystal, resulting in smaller band gaps.

It has thus been shown that two-dimensional photonic crystals exhibiting wide band gaps in the low THz region can be created and characterised with the methods outlined in this project. Furthermore, it has been shown that by utilising the PPMWG configuration it is possible to create band gaps for dielectric rod structures which do not exhibit band gaps for P-polarised light. It has also been shown that the band gaps persist even though the structured part of the sample was contained to only half of the total wafer thickness, and despite defects such as angled structures. The question then becomes if these photonic crystal structures can be utilised to guide THz radiation and if cavity modes can be excited.

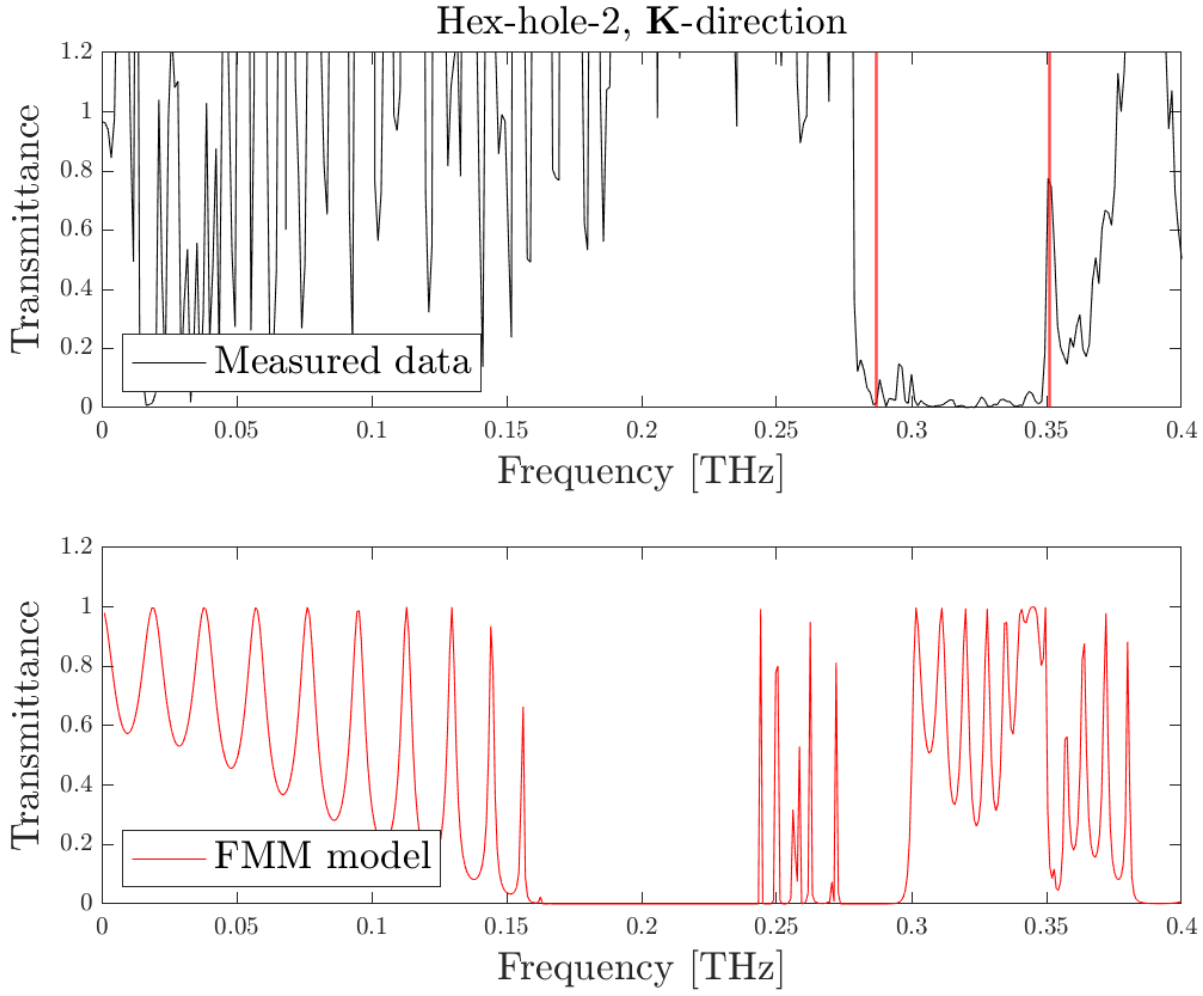

Figure 5.9: The measured and modelled transmittance spectra of the Hex-hole-2 sample, oriented such that the light propagates along the **K**-direction. The measured band gap was determined to be between 0.29 and 0.35 THz while the calculated band gap lies between 0.16 and 0.24 THz. The red vertical lines show the location of the band gap using a fully three-dimensional FFT method with an air layer corresponding to 40 % of the height in the PPMWG, or equivalently 67 μm.

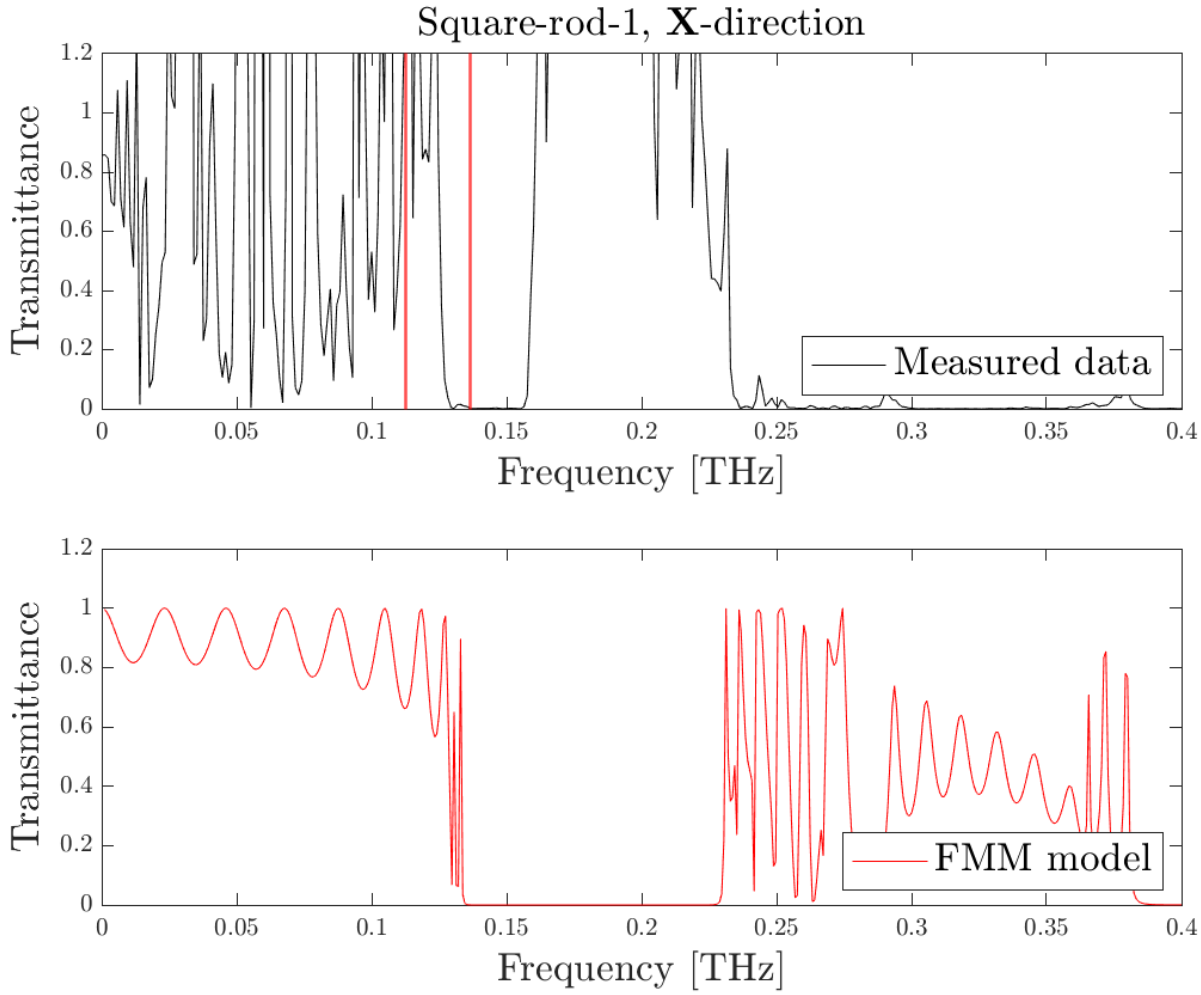

Figure 5.10: The measured and modelled transmittance spectra of the Square-rod-1 sample oriented such that the light propagates along the **X**-direction. The measured band gap was determined to be between 0.13 and 0.16 THz while the calculated band gap lies between 0.11 and 0.19 THz. The red vertical lines show the location of the band gap using a fully three-dimensional FFT method with a Si-layer making up 50% of the space between the metal plates.

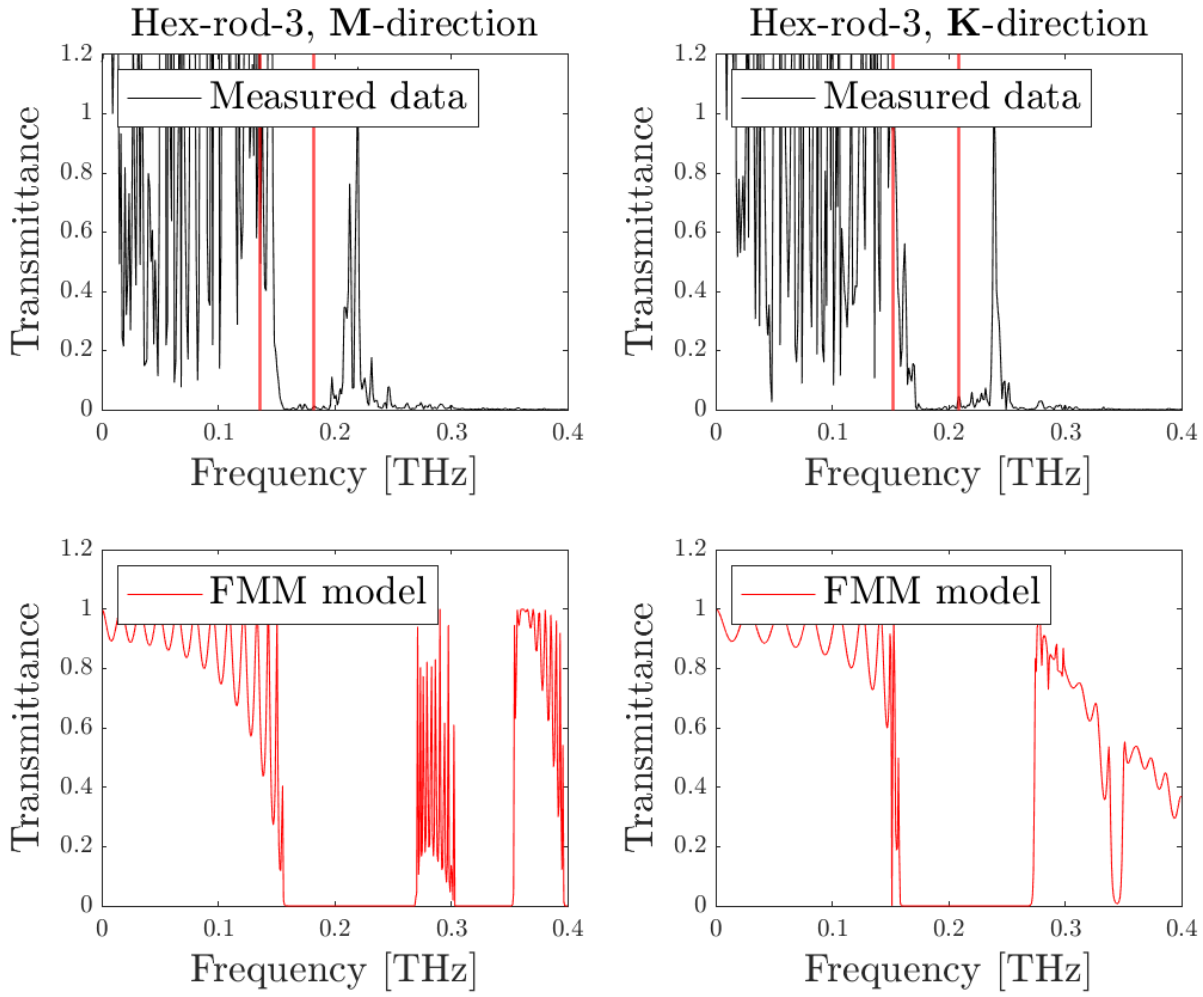

Figure 5.11: The measured and modelled transmittance spectra of the Hex-rod-3 sample for light propagating along both the **M**- and **K**-direction. The measured band gap for the **M**-direction was determined to be between 0.16 and 0.20 THz, for the **K**-direction it was determined to lie between 0.17 and 0.24 THz. The calculated band gap lies between 0.16 and 0.27 THz for the **M**-direction, and between 0.16 and 0.27 THz for the **K**-direction. The red vertical lines show the location of the band gap using a fully three-dimensional FFT method with a Si-layer making up 40% of the space between the metal plates.

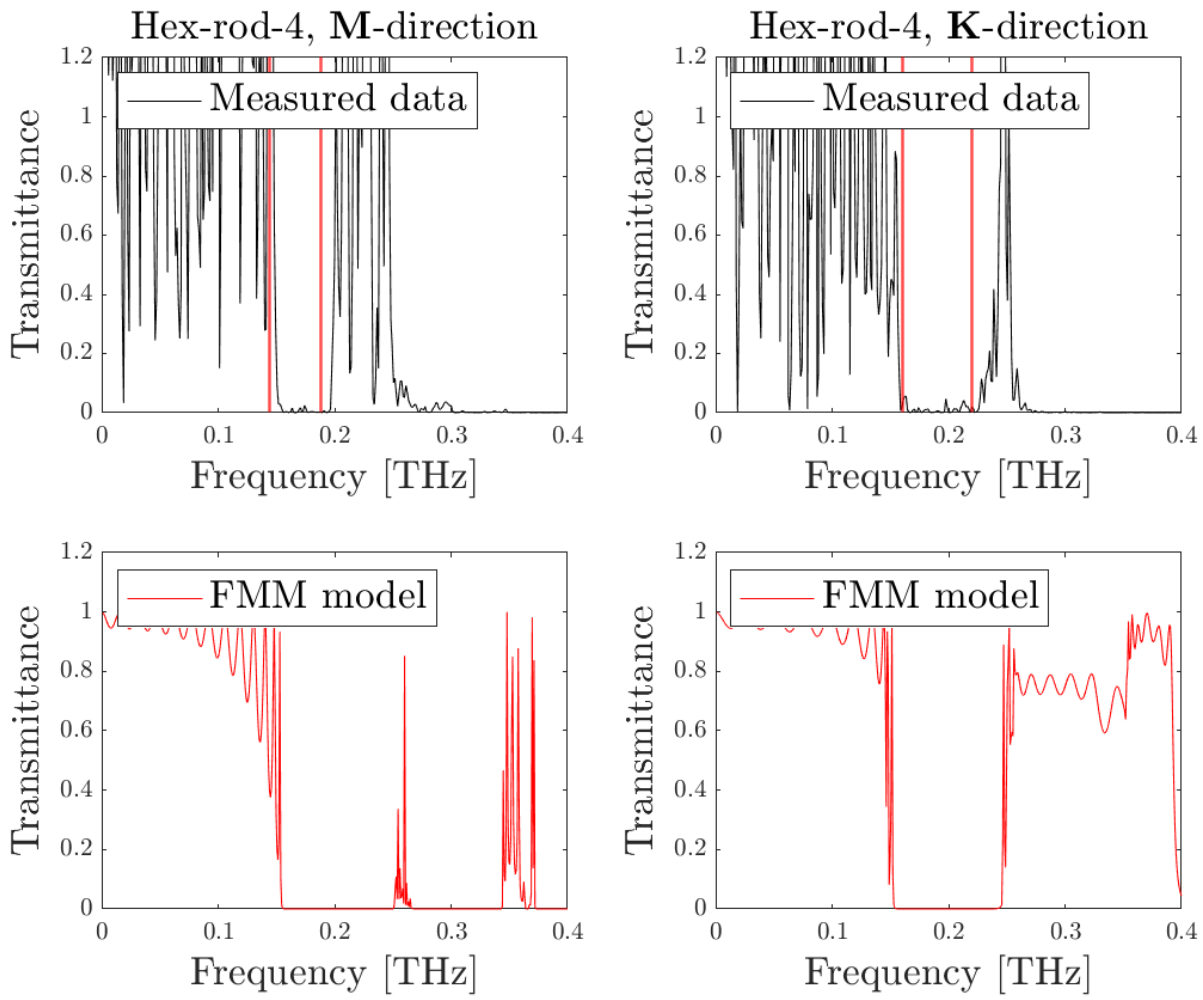

Figure 5.12: The measured and modelled transmittance spectra of the Hex-rod-4 for light propagating along both the **M**- and **K**-direction. The measured band gap for the **M**-direction was determined to be between 0.15 and 0.20 THz, for the **K**-direction it was determined to lie between 0.16 and 0.22 THz. The calculated band gap lies between 0.16 and 0.25 THz for the **M**-direction, and 0.15 and 0.25 THz for the **K**-direction. The red vertical lines show the location of the band gap using a fully three-dimensional FFT method with a Si-layer making up 30% of the space between the metal plates.

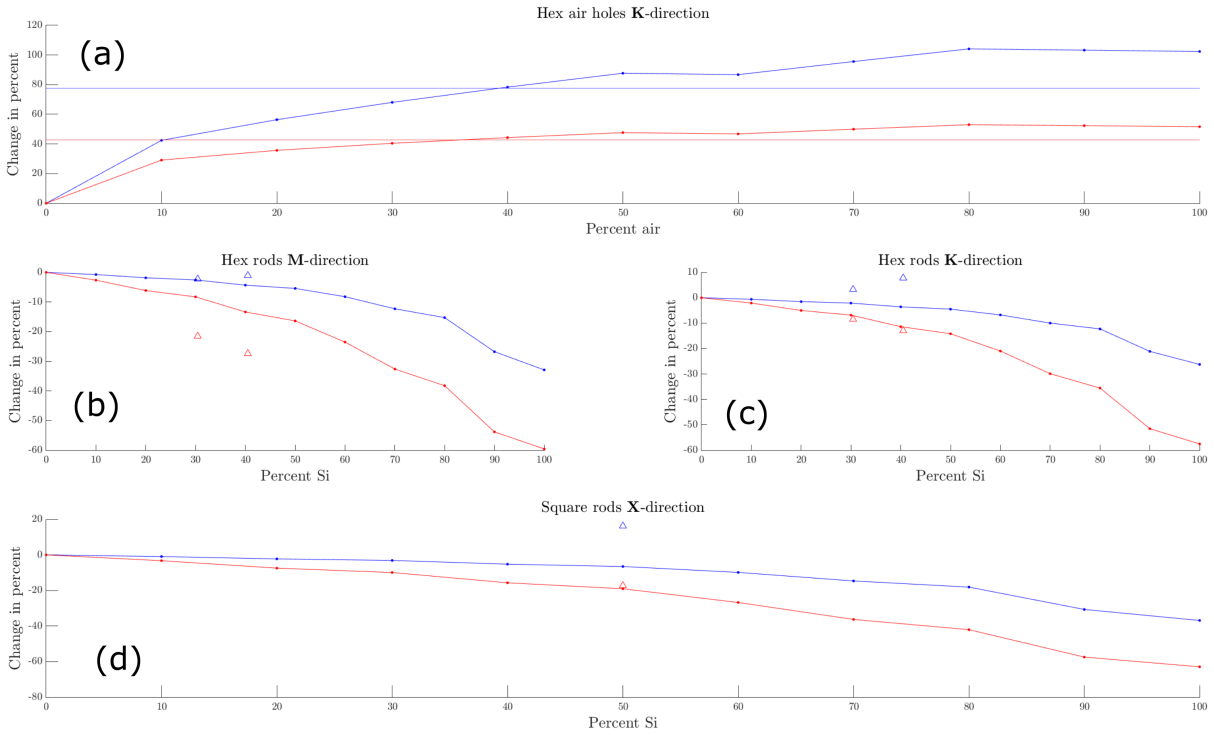

Figure 5.13: The change in band edges in relation to the addition of a homogeneous layers. The lower band edge is shown in blue while the upper band edge is shown in red. The triangles in **(b)**-**(d)** denote the fabricated samples and their respective shift of band edges, while the horizontal blue and red lines in **(a)** are the measured change of the LBGE and UBGE for sample Hex-hole-2, respectively. The addition of the homogeneous layer for the rod samples amounts to fixing the height between the metal plates and then letting a higher percent of this distance be taken up by the homogeneous silicon layer. For the samples based on air holes in silicon the addition amounts to moving the upper metal plate by some distance, keeping the thickness of the structured part constant.

5.4 Waveguides

Having shown that band gaps can be produced in the lower THz region it is now of interest to examine the possibility of creating waveguides based on these band gaps. This would make it possible to guide the radiation, which opens up for the creation of a multitude of components such as phased arrays, multiplexers or just to collect power from multiple sources [6, 29]. The waveguides use the same photonic crystals as those presented in the previous sections, i.e. Hex-hole, Hex-rod, and Square-rod. To characterise the samples the Menlo THz-TDS system was used, fig. 5.6, where the scan stage was used to scan the entrance of the waveguide. In this section the results of the ablated and the etched samples will be presented separately, starting with the samples based on air holes in silicon.

5.4.1 Air Holes

All the waveguides created in the hole configuration were made to guide the radiation along the **K**-direction and can be seen in fig. 5.1. Three waveguides were created, two of which have a high-refractive-index silicon core, while one has an air core, thereby both hollow- and solid-core configurations were tested. Theoretical calculations of the band structures were made based on the two-dimensional FFT method outlined in section 2.5, and for all calculations, the waveguide core was surrounded by 6 unit cells on either side resulting in a supercell with $|\mathbf{a}_1| = 13\Lambda$ and $|\mathbf{a}_2| = \Lambda$ which may be seen in the inserts. The calculations use 40 bands with 50 **k**-points along the **K**-direction. The calculations were made for both core types and can be seen in figs. 5.14 and 5.15. Here the colored regions constitute continua, which in the case of infinitely many unit cells on either side would be completely filled with allowed modes. Hence the bands outside these continua are the waveguiding bands. It can readily be seen in fig. 5.14, which is the spectra for a solid-core waveguide, that the otherwise forbidden region has a multitude of bands, which extend throughout the entire forbidden region. The multiple bands correspond to multiple modes of propagation in the waveguide which would result in a waveguide with high modal dispersion. However, for detecting waveguide modes this is an advantage as it is expected that the signal can readily be transmitted at every frequency in the otherwise disallowed region.

In fig. 5.15 the band structure for a hollow-core photonic crystal waveguide based on a hexagonal array of air holes in silicon can be seen. It is clearly observed that there are almost no bands penetrating into the forbidden region. Only one of these bands narrowly penetrates into the omnidirectional band gap, marked with a red triangle and the number 2. This means that this mode would appear as a reduction in the band gap, which as discussed in the previous section is already an observed effect in the structure due to fabrication limitations. Hence, concluding that guided modes are present for this sample is likely going to be troublesome.

Starting with the high index core samples, a scan was conducted over the opening of the Hex-hole-WG-1 sample, the scan range was $x \in [259, 269]$mm and $y \in [174, 174.3]$mm, with 37 and 2 steps, respectively. This scan can be seen in fig. 5.16, where the spectrum is also plotted for three positions, two on either side of the waveguide and the last in the waveguide. The band gap can clearly be seen for the positions outside the waveguide. Furthermore, this band gap also corresponds nicely with the band gap that was shown for the Hex-hole-2 sample. The difference amounts to the LBGE being off by -0.66% and UBGE being off by 1.5%. For the spectrum

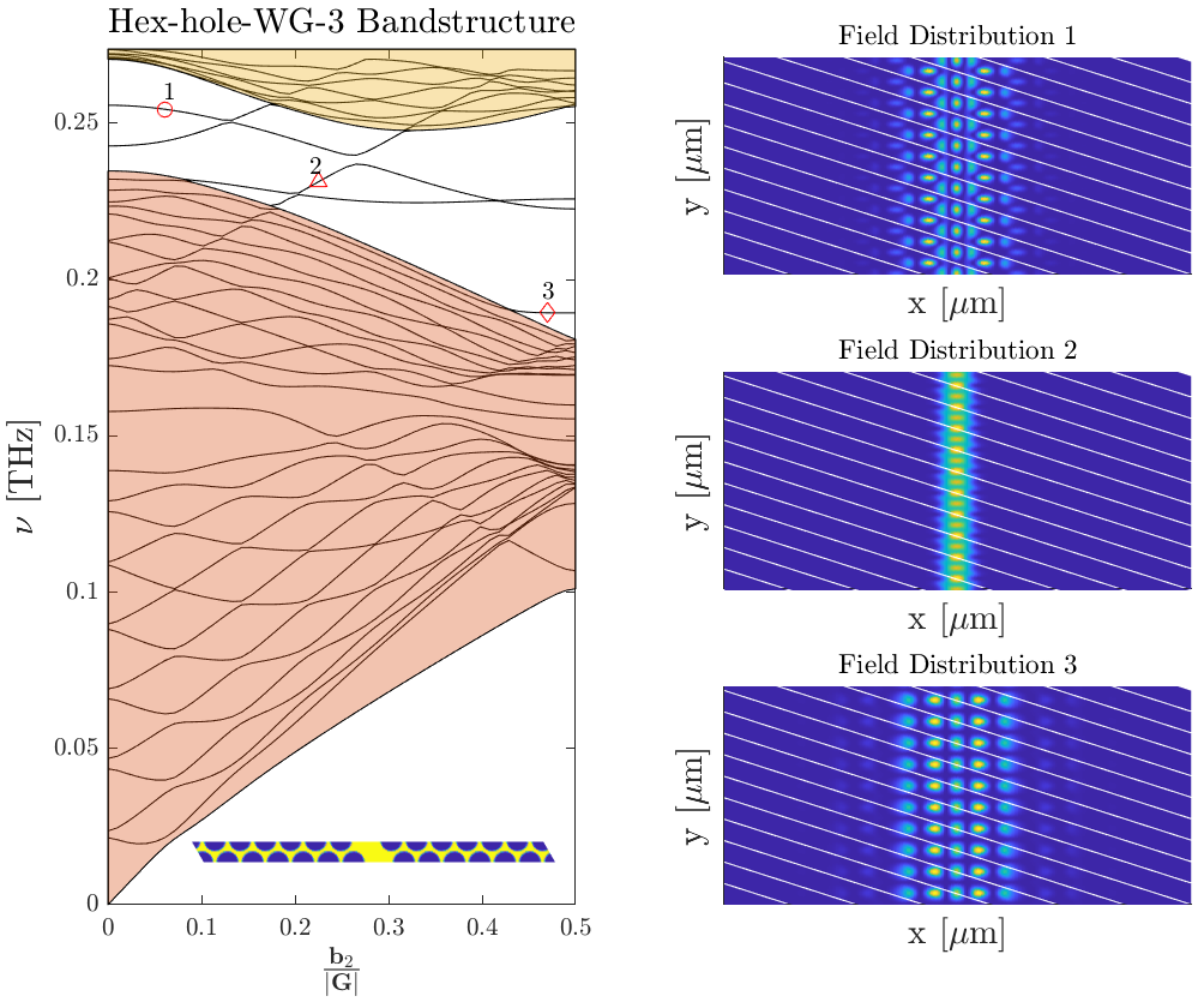

Figure 5.14: The band structure of a waveguide configuration with a high refractive index core inside a hexagonal array of air holes. Multiple bands penetrate into the otherwise forbidden region and constitute bound modes. The field distributions of three bands inside the forbidden region are also shown.

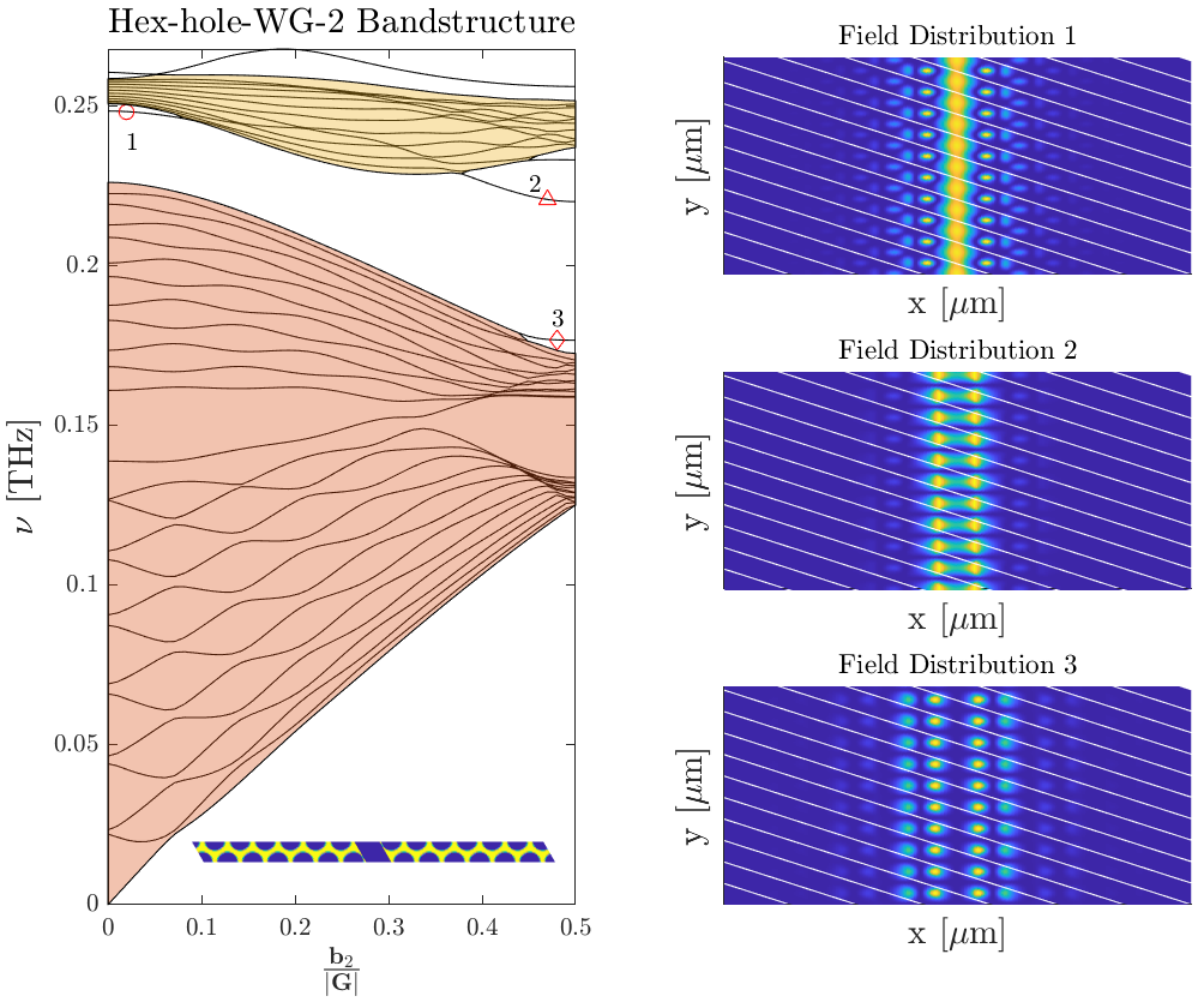

Figure 5.15: The band structure of a waveguide configuration with a low refractive index core inside a hexagonal array of air holes. Multiple bands penetrate into the otherwise forbidden region and constitute bound modes. The field distributions of three bands inside the forbidden region are also shown.

within the waveguide it can be seen that the overall transmittance is not significantly different from that of the frequencies outside the band gap. This was also what was expected from the band structure calculations shown in fig. 5.14, because waveguide bands extended all through the entire band gap region and consequently it is expected that there is a transmitted signal inside the band gap similar to the signal outside the band gap, just as observed. The same effect is seen for Hex-hole-WG-3, which can be observed in fig. 5.17. This is also expected as the two samples are almost identical with the main difference being the number of rows and that a taper was made to better couple in the radiation, as can be seen in fig. 5.1. However, it can be seen that the taper does not significantly increase the width of the sample which may be hit and subsequently have light coupled into the waveguide, as both Hex-hole-WG-1 and Hex-hole-WG-3 has an incoupling length of about 2 mm, from [264-266] mm in the case of Hex-hole-WG-1 and [263-265] mm for Hex-hole-WG-3.

The transmittance scan for the hollow-core waveguide is shown in fig. 5.18. It is immediately clear that no significant signal can be found inside of the band gap region for the expected positions. The highest transmittance within the band gap is 0.15. This was achieved at $x = 266$ mm, which is a shift of 2 mm with respect to the location of the waveguide. By inspection of the measured spectral spectrum, the graphs on the right in fig. 5.18, it can be seen that the high transmittance is due to the band edge creeping into the band gap. It was noted from fig. 5.15 that a waveguiding band would be present here. However, it is well below the continuum of allowed modes and hence it is impossible to confidently conclude from the measurement that this small increase in transmittance is caused by a waveguided mode. As was commented upon previously, the band structure for this sample predicts much worse conditions for guided modes, and it is therefore not surprising that such a mode could not be convincingly measured.

It has thus been shown that waveguides constructed using the Hex-hole configuration were achieved successfully by using a high-refractive-index silicon core. In this configuration, the entire forbidden region gets filled with waveguiding bands, and it was observed that when coupling into the waveguide the radiation was transmitted throughout the otherwise forbidden frequency region. The incoupling length of the waveguides were 2 mm. It was not possible to fabricate a working hollow-core waveguide in this configuration. However, this was also expected from two-dimensional FFT calculations showing very few bands in the forbidden region.

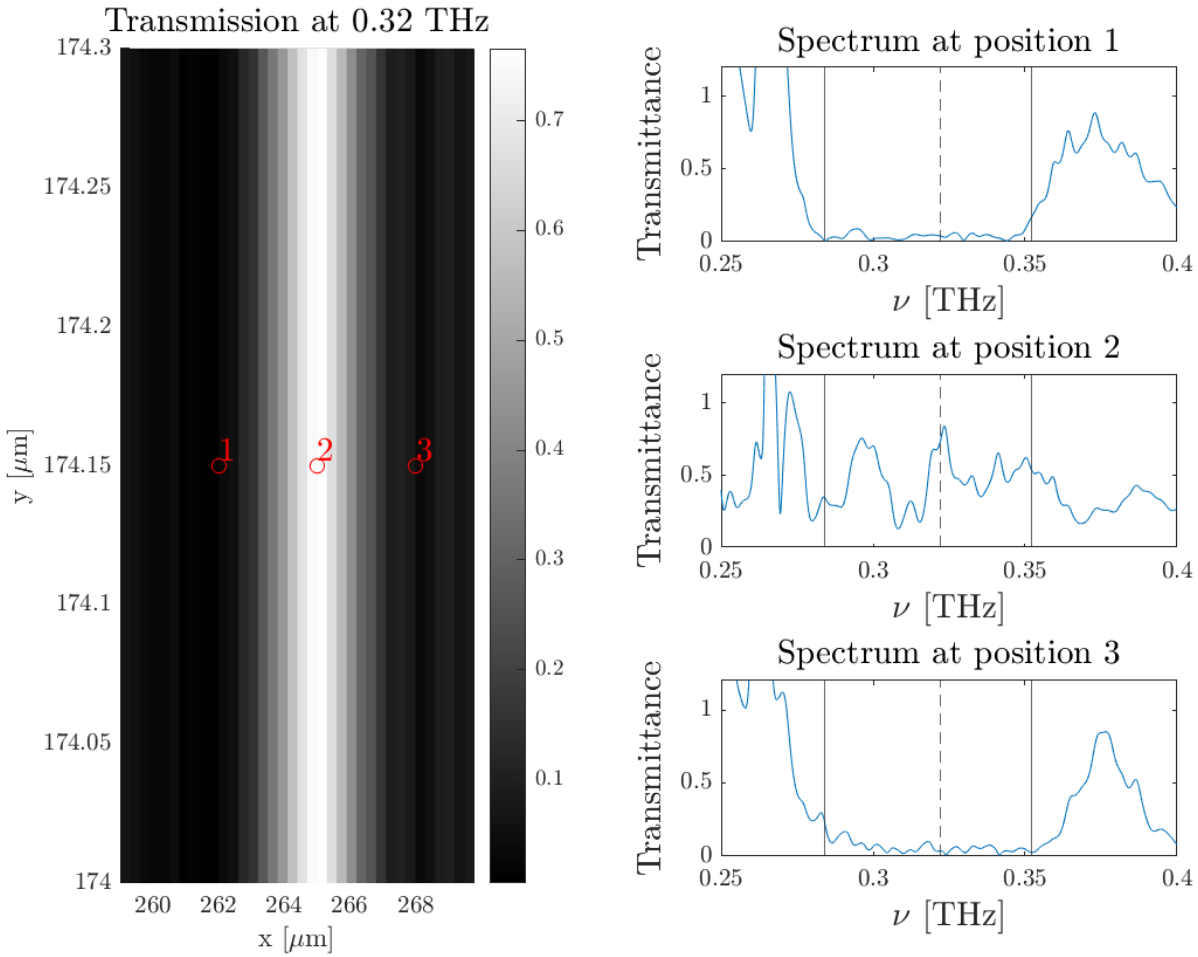

Figure 5.16: Left: The transmittance value at 0.32 THz for a scan over the opening of the Hex-hole-WG-1. Right: Three transmittance spectra, taken at three points of the scan namely at [262, 265, 268]mm.

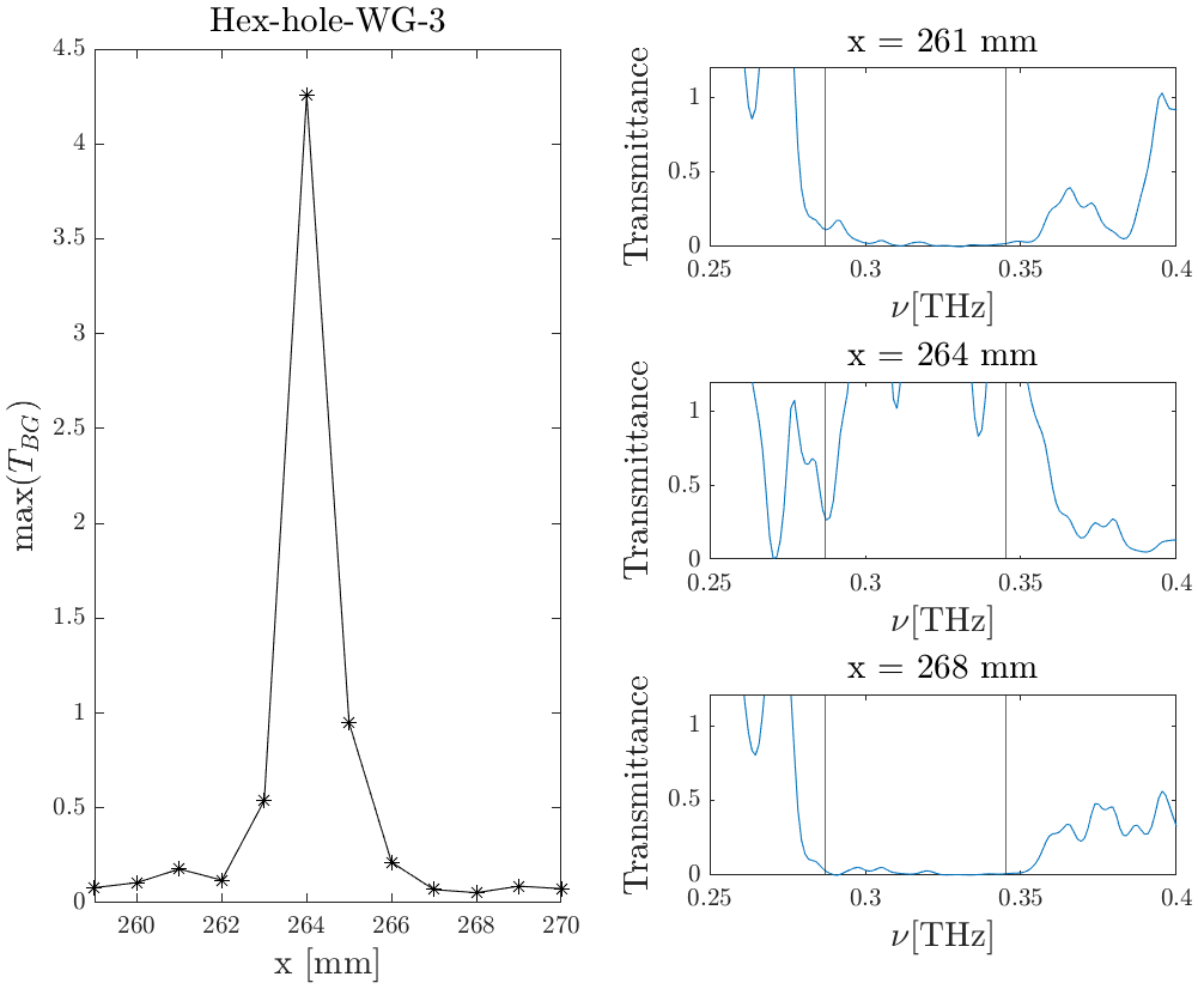

Figure 5.17: Left: The maximum transmittance value found in the band gap determined as BG $\in$ [0.28; 0.34]THz. Right: Three transmittance spectra, taken at three points of the scan namely at [261, 264, 268]mm.

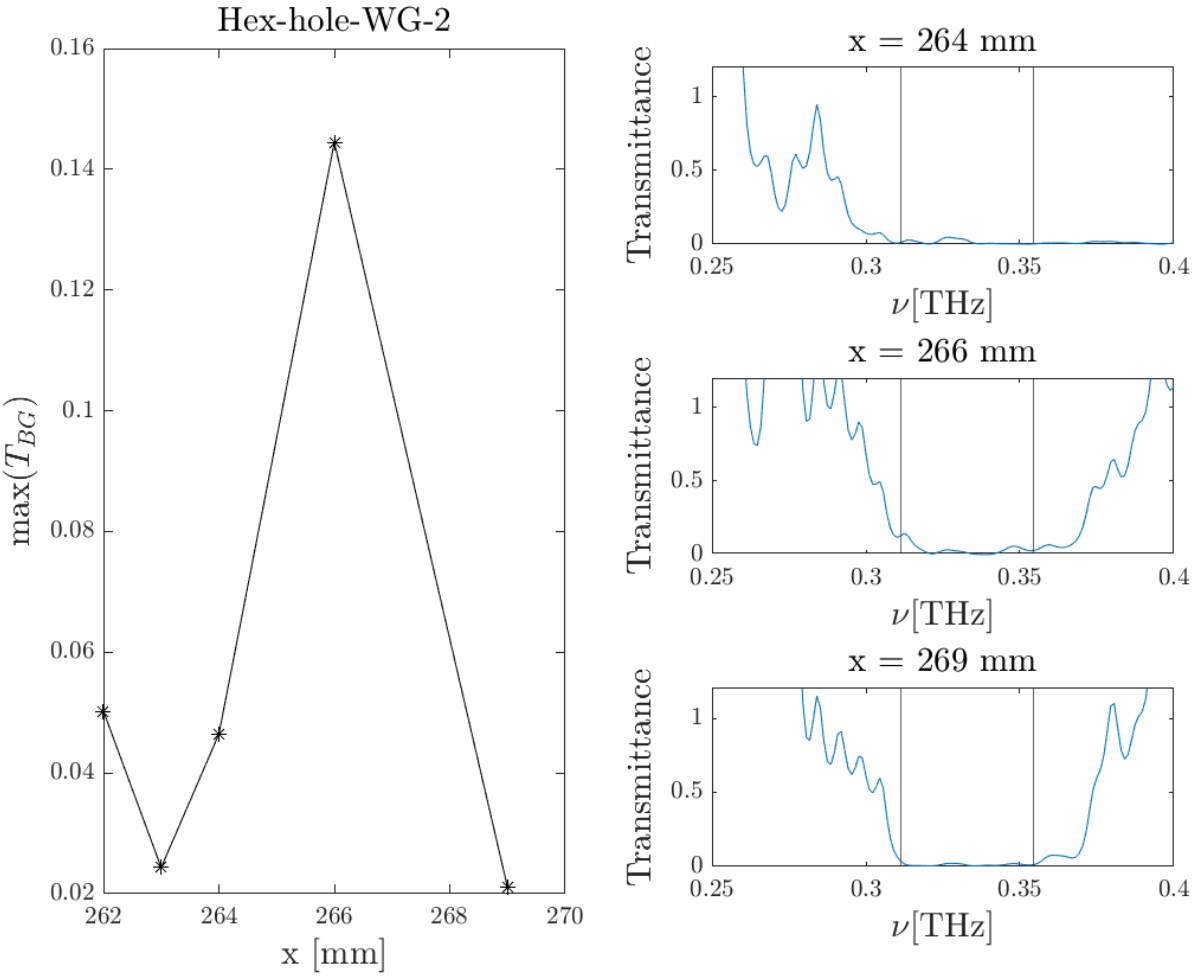

Figure 5.18: Left: The maximum transmittance value found in the band gap determined as BG $\in$ [0.31; 0.35]THz. Right: Three transmittance spectra, taken at three points of the scan namely at [264, 266, 269]mm.

5.4.2 Si Rods

For the samples based on silicon rods, all the waveguides were created as hollow-core waveguides. The FFT band structures can be seen in figs. 5.19 and 5.20, where it is observed that only one band extends into the forbidden region. Yet, the configuration still shows more promise than the hollow-core waveguide created with the Hex-hole configuration, as the waveguiding band extends halfway into the forbidden region, and hence detecting a signal is more probable. However, because the waveguiding band does not extends throughout the entire forbidden region, there consequently will not be a signal in the entire forbidden region.

This waveguide configuration does present significant advantages over all the other waveguide band structures that were presented in the previous subsection because it only has one waveguiding band and it is therefore not expected to be dispersive in the same manner as is expected for multi mode Hex-hole waveguide shown in the previous section.

Two waveguide configurations were created, a square and a hexagonal lattice, and the measurements can be seen in figs. 5.21 and 5.22, neither of which show any guiding modes. For the Hex-rod-WG-1 sample, the band gap is very clear at all positions and the maximum value for the transmittance within the band gap never reaches above 0.08. As discussed previously, subsection 5.3.2, the remaining silicon that the rods are standing on causes the UBGE to move towards lower frequencies. If this effect is sufficiently pronounced, the continuum of states would overlap with the guiding mode, and hence make it impossible to detect a guiding mode.

To the right in fig. 5.22 the spectral spectra of Square-rod-WG-1 can be seen. At first glance, it does seem like there is a tendency for a higher transmitted signal in the middle of the scan range. However, by inspecting the spectrum for $x = 264.6$mm, approximate position of the waveguide, it can be seen that this is due to creeping of the lower band edge and that no distinct change happen within the band gap. There is however a peak within the band gap around 0.136 THz that was not observed in the Square-rod-1 sample. This peak is placed at the correct frequency but is also present in all three of the shown spectra, which covers a much wider area than the opening of the waveguide. It could be hypothesised that light could be scattered into the waveguide when missing the waveguide opening, but as this was not observed for the Hex-hole waveguides, it was instead concluded that this is in fact not a waveguiding mode.

As none of the Si-rod samples exhibit any waveguiding modes a cavity sample was created, namely Hex-rod-cavity-2. As can be seen in fig. 5.3 this sample had cavities spaced $\sim$ 4mm apart resulting in 4 cavities total. Due to the spacing of the cavities on the fabricated sample, it was possible to choose the modeling parameters such that the distance between two cavities was the same in the model. This corresponds to making a supercell out of 8×8 standard unit cells, the $\Gamma - \mathrm{M} - \mathrm{K} - \Gamma$ route was then divided into 60 $\mathbf{k}$-points and the calculation was done for 80 bands. An insert of the dielectric profile along with the band structure and a field distribution plot can be seen in fig. 5.23. A single cavity mode is found within the forbidden region, which is located at 0.156 THz, hence it is expected that if the light is focused onto the photonic crystal where one of these cavities is located the crystal will work as a resonator, and hence a large transmission is expected. Therefore, high transmittance around 0.156 THz spaced $\sim$ 4mm apart is expected when the sample is scanned. This is also what is observed as can be seen in fig. 5.24. Here the three spectral spectra seen to the right were taken at $x = [265, 266.8, 268.9]$ mm respectively. A clear peak inside the band gap at 0.1524 THz is visible in the spectra at

265 and 268.9 mm while it is not present in the measurement at 266.8 mm which would then be exactly between the two cavities. Furthermore, in the two-dimensional scan it can be seen that there is another, albeit smaller peak, at $x = 261.4$, which would fit with there being another cavity at this location. The measured resonance is only shifted by -2.3 % from the modelled spectra in fig. 5.23, with the downwards shift being expected from having the rods placed on a silicon base. These are all strong indicators that there is indeed a resonator transmission line detected at this frequency.
The band gap of this sample is not very well defined as was otherwise observed for the rod-based samples. One difference is the number of rows in this sample which is significantly reduced from the other rod samples, as can be seen in table 2.1, likely contributing to a less defined band gap. However, it is still clear that the signal is in a transmission valley around these frequencies as is expected for a band gap. Hence it is concluded that it was possible to fabricate a structure in the hex-rod configuration which exhibited a resonator mode.

For the two-dimensional photonic crystals based on silicon-rods hollow-core waveguides were fabricated based on quadratic and hexagonal lattices, but it was not possible to detect waveguide modes. This was attributed to the fact that the guiding modes extended from the UBGE into the forbidden region, thus if the upper band gap was shifted down into the forbidden region it might not be distinguishable from the upper continuum of modes. It is likely the case that a solid-core waveguide based on a quadratic and hexagonal array of silicon rods would perform better, a structure that can readily be fabricated using the same procedures with a slightly altered photolithography mask. It was however possible to fabricate and detect a resonator-mode created using a hexagonal array of silicon rods. As this band is exceedingly flat this does show promise that using this fabrication technique it is possible to realise waveguiding modes.

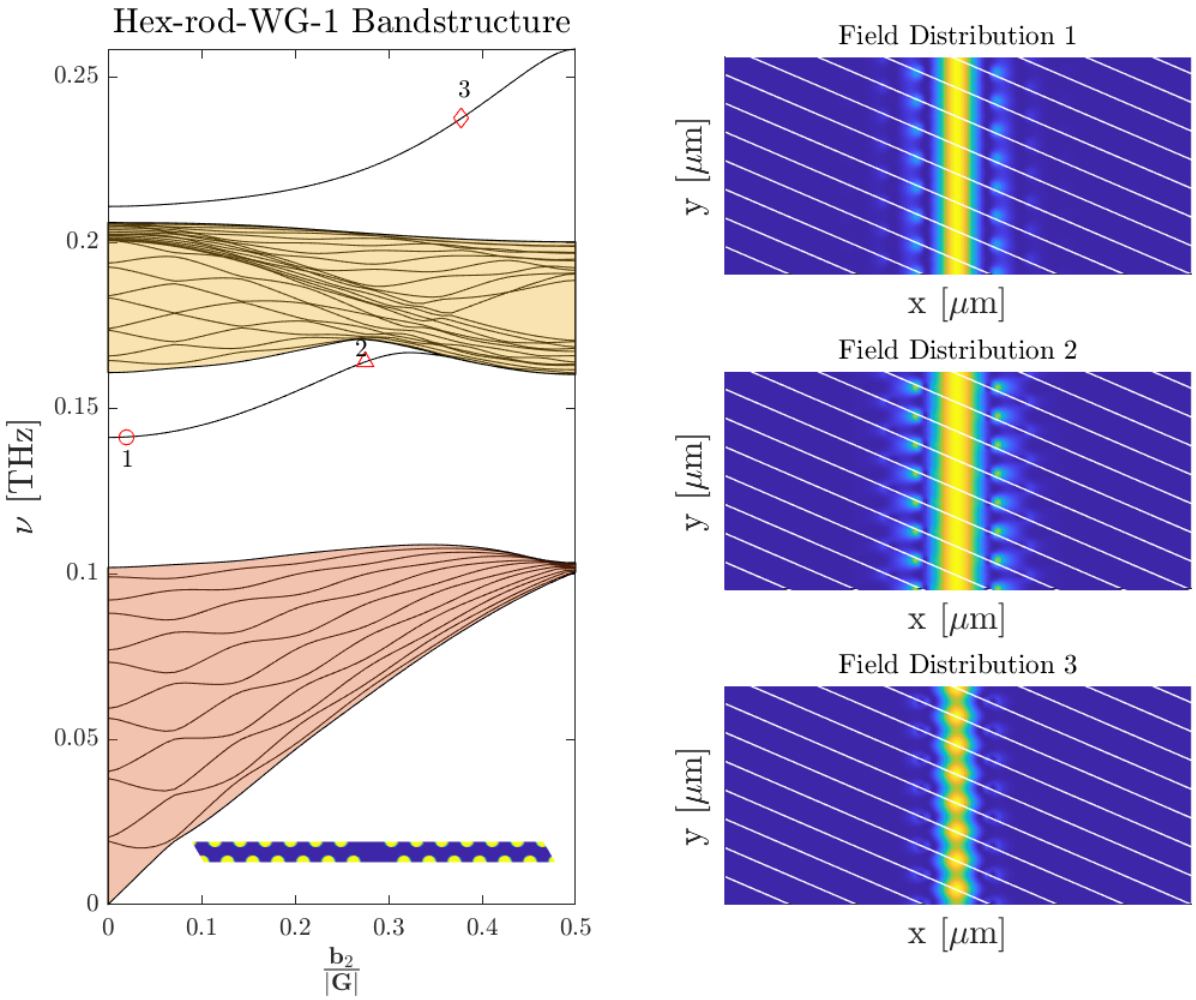

Figure 5.19: The band structure of a waveguide configuration with a hollow-core inside a hexagonal array of Si-rods. A single band penetrates into the otherwise forbidden region and constitute a bound mode. The field distributions of three **k**-points inside the forbidden region are also shown.

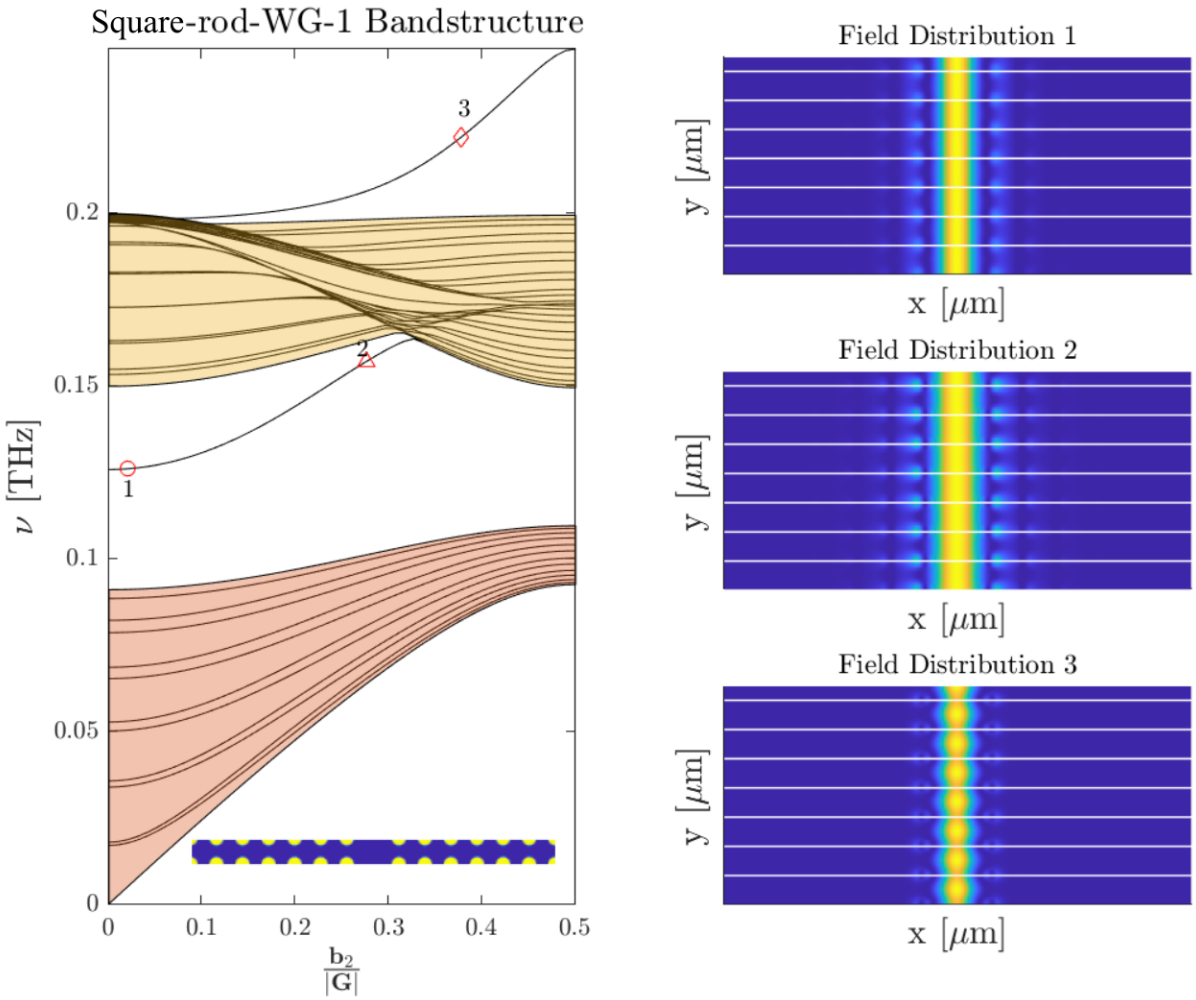

Figure 5.20: The band structure of a waveguide configuration with a hollow-core inside a square array of Si-rods. A single band penetrates into the otherwise forbidden region and constitute a bound mode. The field distribution of three **k**-points inside the forbidden region is also shown.

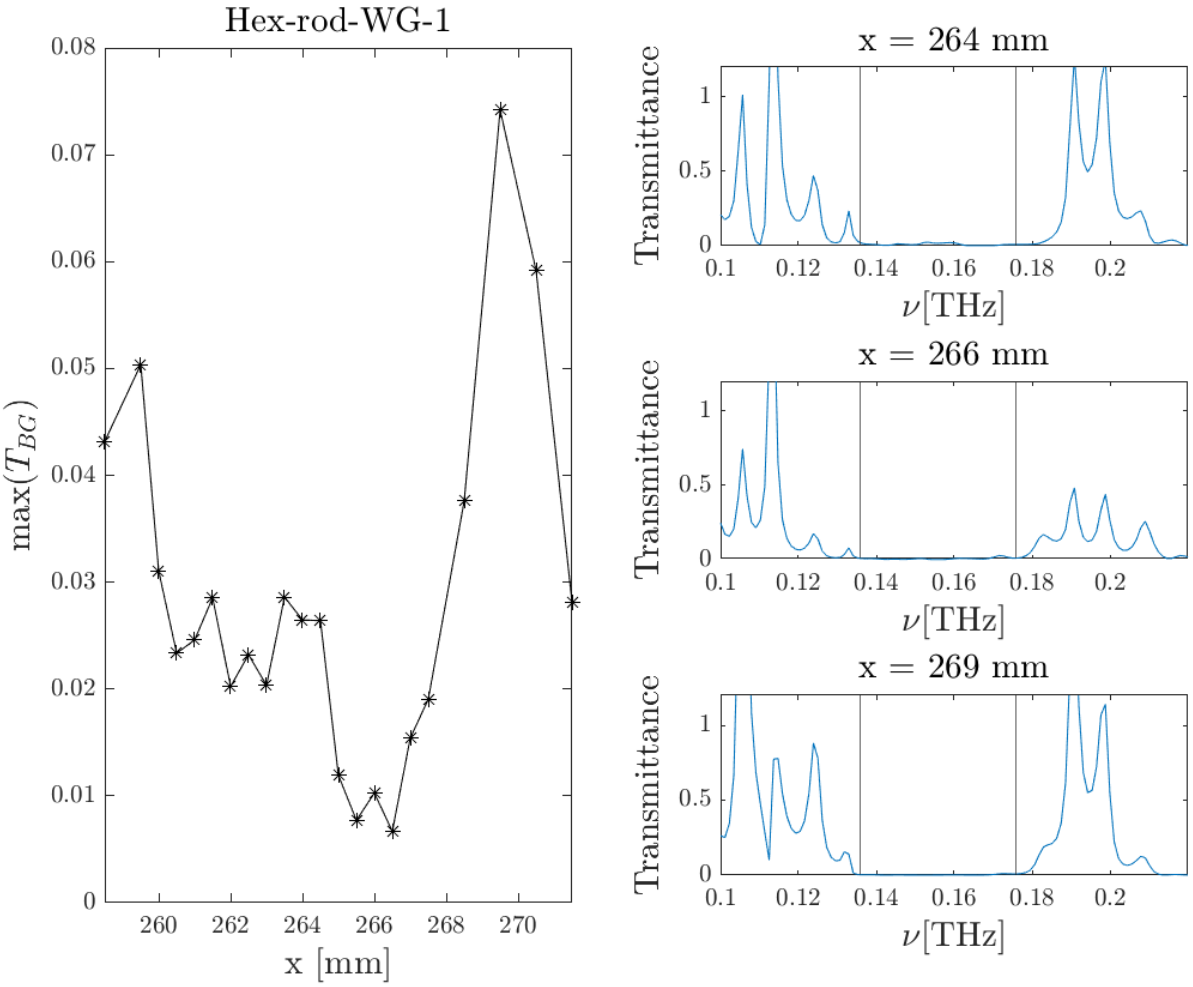

Figure 5.21: Left: The maximum transmittance value found in the band gap determined as BG $\in$ [0.136; 0.176]THz. Right: Three transmittance, spectra taken at three points of the scan namely at [264, 266, 269]mm

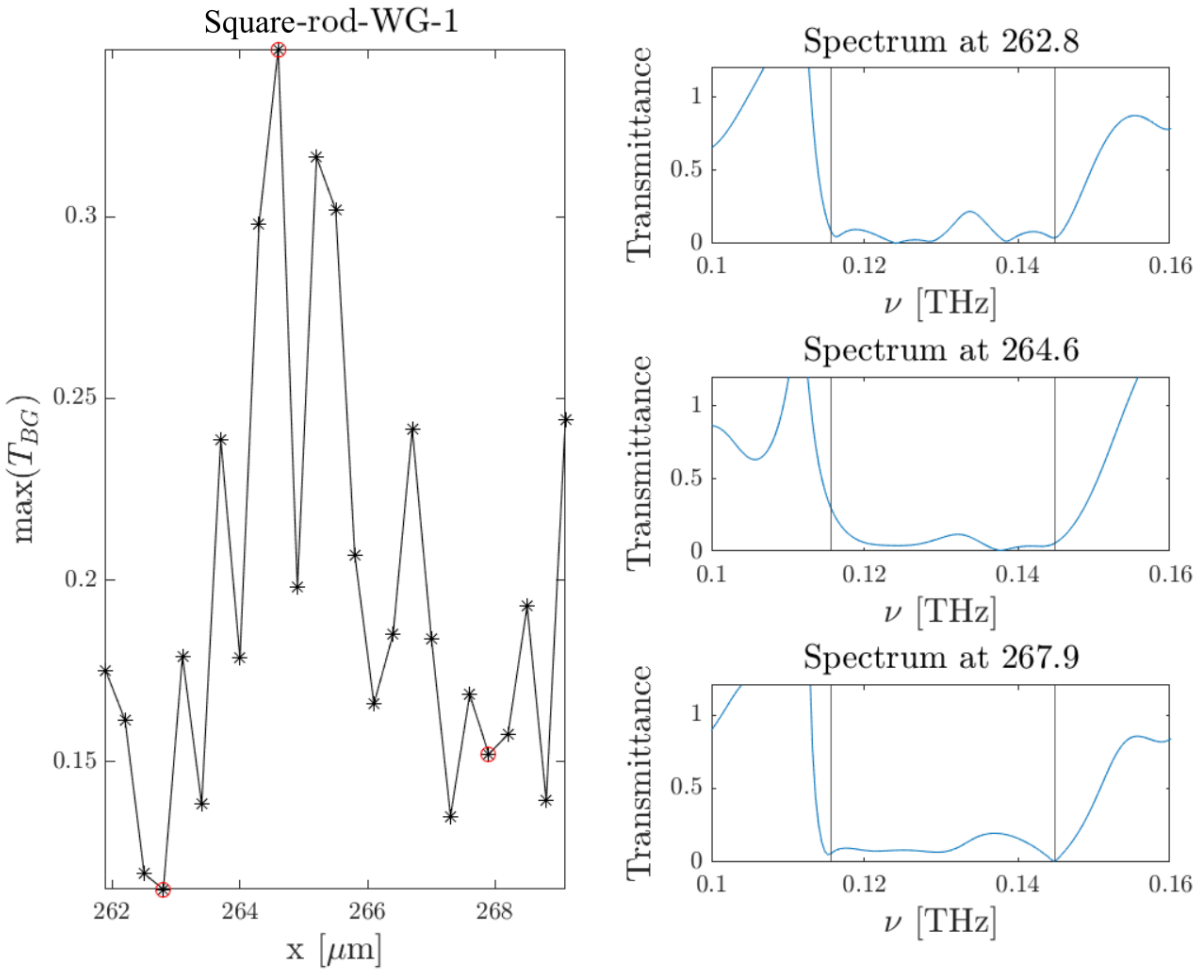

Figure 5.22: Left: The maximum transmittance value found in the band gap determined as BG $\in$ [0.11; 0.15]THz. Right: Three transmittance, spectra taken at three points of the scan namely at [262.8, 264.6, 267.9]mm

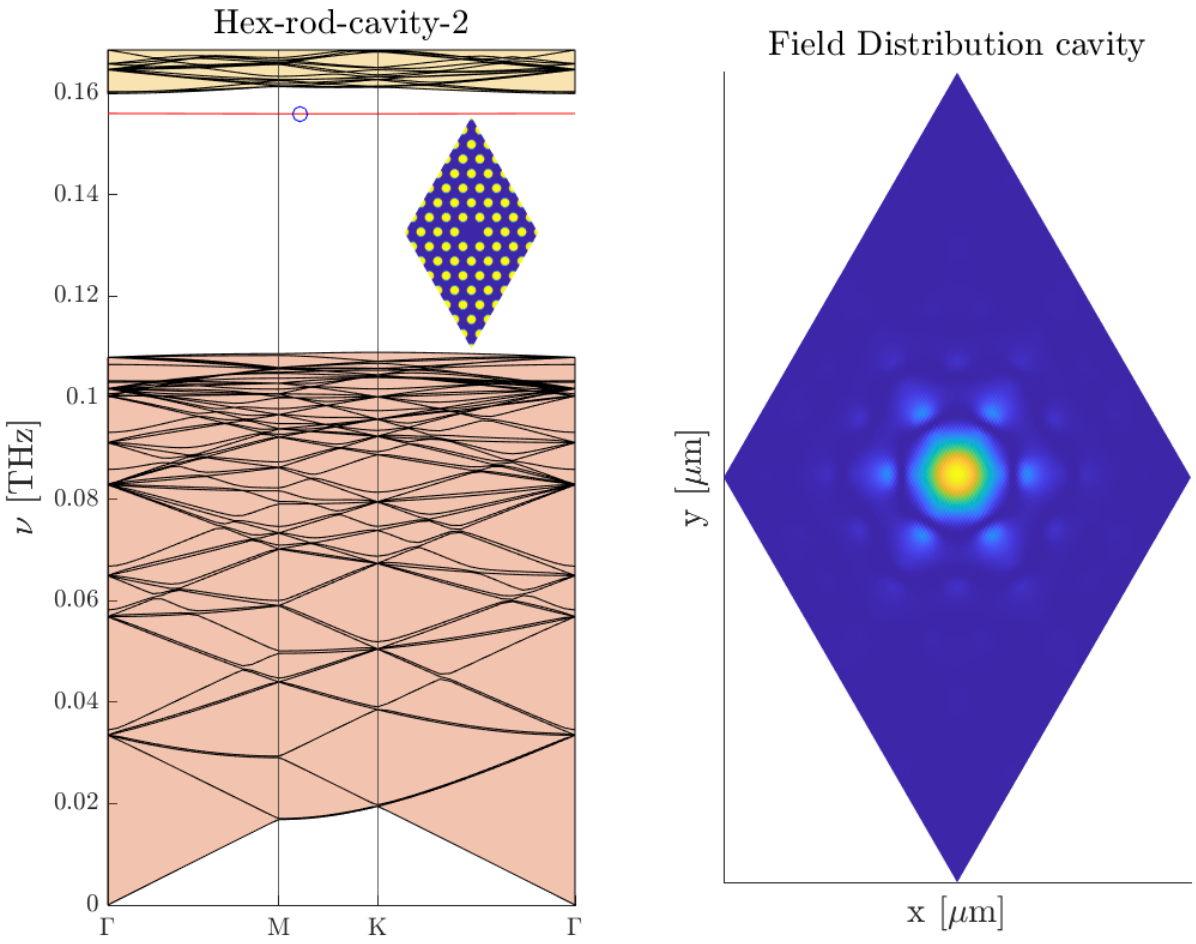

Figure 5.23: The band structure of a cavity configuration with a hollow-core inside a hexagonal array of silicon rods. A single band penetrate into the otherwise forbidden region and constitute a bound mode. The field distribution of the cavity mode inside the forbidden region is also shown.

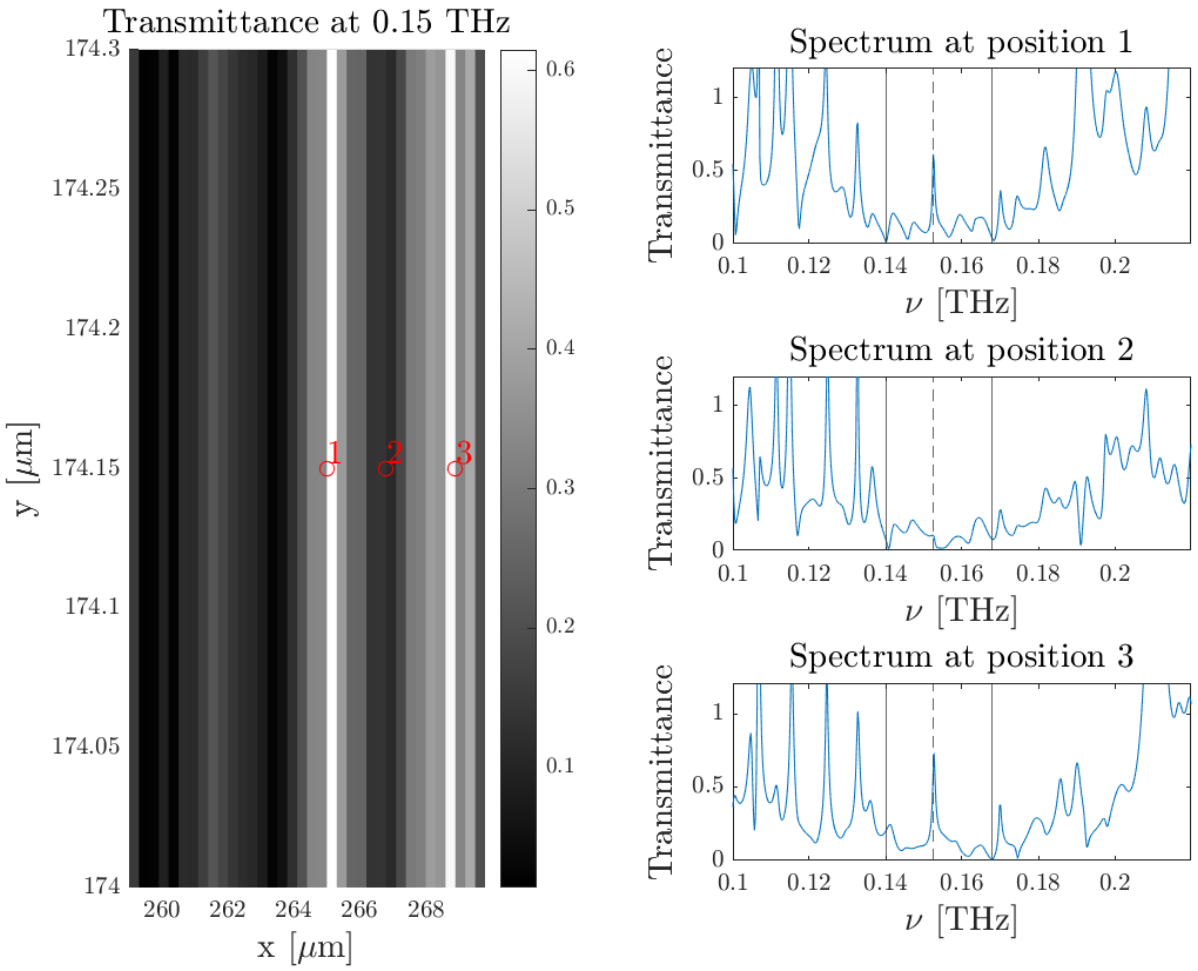

Figure 5.24: Left: The transmittance value at 0.15 THz for a scan over the opening of the Hex-rod-cavity-2. Right: Three transmittance spectra, taken at three points of the scan namely at [265, 266.8, 268.9]mm

6 | Summary and Conclusion

This project is sectioned into three parts. In the first part, theories that served as the basis for the numerical programs used in this work were introduced and the two fabrication methods were introduced. The method of Plane Wave Expansion was used to find the optimal design for wide band gap photonic crystals, and also illuminated the need for a metal sample holder. The Fourier Modal Method was extensively used to design one-dimensional sub-wavelength gratings and was further used in the discussion of the band gaps of the two-dimensional photonic crystals. An iterative Fast Fourier Transform model was introduced, used to bridge the figurative gap between the idealised structures modelled with the Plane Wave Expansion method, and those fabricated in this project. The method was also used to calculate the band structures of photonic crystals where line- and point defects had been introduced. The first part concludes by introducing the methods used to fabricate and characterise the photonic crystals.

In the second part of the project, the sub-wavelength all-dielectric gratings and their Fourier transformed time-domain spectra were introduced. Four samples were fabricated using capacitively-coupled reactive ion etching on high-resistivity silicon wafers with measured thicknesses of $100 - 105\mu$m. The gratings had periods between $99.7 - 292.3\mu$m, and etch depths of $12.9 - 28.0\mu$m and averaged strip widths in the range $39.9 - 85.5\mu$m, and exhibited Fano resonances between 0.3 and 3.0 THz. The measurements were performed using collimated, linearly polarised light with angles of incidence between 0° and 10°. The frequency location of measured Fano resonances were found within 15 GHz of the Fourier Modal Method for all four samples, with the best having a deviation of only 8 GHz or less. Continuing with the best sample, the angle of incidence was varied in steps of 1° and it was shown that the center location of the Fano resonances could be tuned by ~ 50 GHz, while the deviation between measurement and the Fourier Modal Method remained within 8 GHz. To explain the underlying cause of Fano resonances, and develop a model which could be used to design structures exhibiting Fano resonances at selected frequencies, the Propagation constant Matching Model was developed. The ability of this model to predict the amount of Fano resonances and their frequency location was tested against the Fourier Modal Method for 36 different sub-wavelength dielectric gratings, showing deviations of resonance-frequency location comparable to those found between the measured spectra and the Fourier Modal Method. The Propagation constant Matching Model is therefore sufficiently capable of predicting Fano resonances and their frequency location, and the explanation that these resonances are caused by coupling between a discrete set of diffraction orders and a continuum of guided modes in the structure is therefore sound. The Propagation constant Matching Model showed the lowest level of precision for the higher frequencies, which was explained by the simplistic assumption of the empty lattice approach, used to approximate the photonic crystal layer, in combination with higher frequencies propagating by higher-order

modes and consequently being more localised in the grating-region of the structure. Finally, the Propagation constant Matching Model was used as the basis for a simple algorithm that searches parameter space for the combination of grating dimensions that result in a Fano resonance at some input frequency. The idea being to have a model that could inexpensively find the grating dimensions for a desired reflector, the spectra of which could then be calculated using the Fourier Modal Method.

In the third and final part of this project, the two-dimensional photonic crystals were introduced. Three varieties were fabricated, quadratic and hexagonal arrays of silicon rods standing on a thin silicon substrate, and hexagonal arrays of air holes in a silicon wafer. All samples used high-resistivity silicon wafers, where the wafers used for the rods and air holes had thicknesses of 200 ± 10 and $100 \pm 20\mu$m, respectively. The rods were fabricated using capacitively-coupled reactive ion etching while the air holes used femtosecond laser ablation. Using the Plane Wave Expansion method the samples were designed to exhibit band gaps in the frequency range 0.1-0.4 THz. Samples were successfully fabricated for all three variations which exhibited band gaps for frequencies between 0.15-0.35 THz. The measured transmittance spectra were obtained using Fourier transformed time-domain spectroscopy. The samples were placed at the focus of a 50 mm lens and used a parallel-plate metal waveguide sample holder, removing the P-polarisation and thereby allowing the structures based on silicon rods to exhibit band gaps. Obtained spectra were compared directly to modelled transmittance spectra based on the Fourier Modal Method. The correspondence between the measured and modelled band gaps was only satisfactory for one sample. The general poor correspondence between modelled spectra and measurements were explained by the measurements having multiple angles of incidence, and the fact that the fabricated structures varied significantly from the idealised versions used in the Plane Wave Expansion and Fourier Modal Method. To bridge this gap, the method of iterative Fast Fourier Transform was used to include the effects of a homogeneous dielectric layer and the structures being angled. This new model in conjunction with the limitations of the measurement setup was used to explain the shift and reduction in the observed band gaps. To exploit these band gaps in optical devices, it was tested if line and point defects would result in waveguides and cavities, respectively. Band structures of photonic crystals with defects were obtained using the two-dimensional Fast Fourier Transform.
The samples using a hexagonal array of air holes in silicon were fabricated both as solid- and hollow-core waveguides. In accordance with the modelled band structure, the measurements on the solid-core waveguide revealed waveguiding modes all throughout the photonic band gap. No waveguiding modes were detected for the hollow-core waveguide. The band structure of the hollow-core waveguide in a hexagonal array of air holes showed only a few waveguiding bands, which did not extend far out from the continuum of states. Combining this with the general tendency of narrower band gaps in the fabricated photonic crystals, caused by the homogeneous dielectric layer, the lack of waveguided radiation was no surprise.
Hollow-core waveguides were fabricated by using both hexagonal and quadratic arrays of silicon rods. Although the band structure of both samples had waveguiding bands extending significantly longer into the forbidden region, as compared to the structure based on air holes, no significant signal was detected. The lack of transmitted radiation was probably caused by the upper band gap edge being shifted down due to the homogeneous dielectric layer. The final sample presented in this project was a hexagonal array of silicon rods where four defects in the form of missing rods were introduced. A scan across this sample clearly showed sharp transmittance resonances at a frequency within 2.3% of the frequency predicted by the model.

The methods used in this project to fabricate samples were reactive ion etching and laser ablation. Although the methods were not used to create identical samples, their strengths and weaknesses observed in this project can still be identified. The method of reactive ion etching had more steps, and therefore opportunities for failure than laser ablation. From design phase to produced sample, reactive ion etching was also far more laborious, however, the method scales much better, because multiple samples can be etched simultaneously. It is therefore a great method for "mass-producing" the finalised sample but slow during the initial iteration of the sample design. On the other hand, the method of laser ablation can in the span of a few hours go from design to finalised sample, but only one sample can be fabricated at one time. Additionally, if structures with deep features are of interest, e.g., holes in silicon wafers, laser ablation was found to be a better tool as the slope of the walls was much steeper than what could be produced using reactive ion etching.

Conclusion

This project aimed to design, fabricate, and characterise passive optical devices able to manipulate terahertz radiation. To this end, one- and two-dimensional all-dielectric photonic crystals have been modelled, fabricated, and characterised using readily accessible methods. The modelled and measured optical spectra were in excellent agreement with the one-dimensional structures exhibiting Fano resonances. The two-dimensional photonic crystals exhibited the calculated band gaps, though the models had to be extended from two to three dimensions to achieve a better agreement with the measured spectra. Optical components exploiting photonic crystals, such as spectral-specific reflectors, waveguides, and cavities, were fabricated and their intended effect was shown.

Future Work

Although this project group achieved what it set out to do, many questions have been left unanswered, and there is consequently room for more work, before the samples presented can be integrated in optical devices.
Solid-core waveguides were successfully fabricated, but if they are to be used to, e.g., collect the signal of multiple sources, it is necessary to introduce bends to the waveguides, which was not attempted in this project.
Although never tested, the models predict that the rod-based photonic crystals only exhibit band gap effects because P-polarised light was removed by a metal sample holder. At its thinnest, this sample holder was multiple centimeters thick, which inhibits the design of compact optical devices. It is therefore of interest to design structures, where a metal layer is deposited directly onto the sample. This can easily be done for the backside of the wafer, i.e., the solid silicon substrate that the rods are standing on. On the top side, it could be conceived that a sufficiently thin metal plate could be glued on. The question of how thick the metal should be to suppress P-polarised light is also an open question.
No hollow-core waveguides were successfully fabricated in this project, likely due to a relatively thick layer of redeposited silicon during the laser ablation, or the remaining silicon substrate that the rods are standing on. The issue of redeposited material has been solved by using lenses with

shorter focal lengths, yet no wafers were left to fabricate new photonic crystals. It can therefore easily be tested if hollow-core waveguides based on air holes can be successfully fabricated when the redeposited material is significantly reduced. To reduce the substrate layer that the silicon rods are standing on is more tricky, the issue being that the samples are prone to break when the substrate gets sufficiently thin. A possible method could be to glue the previously mentioned metal layer to the backside of the wafer, before the etching procedure is started, allowing more of the substrate to be etched without the sample becoming too fragile.
Discrepancies were found between the measured and modelled photonic band gaps, which were explained by a variety of factors, one being that the non-collimated light was used to measure the sample. It is therefore of interest to investigate the samples using collimated light. All this, and much more, are ideas that this project group did not explore. We leave the rest to the coming generations at Aalborg University.

Sincerely,
Anders, Jesper, and Karl

Acknowledgements

A special thanks to Mathias Hedegaard Kristensen who supplied a MATLAB program capable of performing the calculations for the Fourier transforms of the data obtained from THz-TDS measurements. Likewise, a heartfelt thanks goes out to Thomas Møller Søndergaard for supervising us throughout most of the last four years, and for supplying the MATLAB program capable of performing the modelling with the three-dimensional iterative Fast Fourier Transform. Lastly we would like to thank Søren Erik Bruun and Klaus Kjær, for producing the numerous sample holders we have requested throughout the project, and in that regard, for always putting up with our not-up-to-standard technical drawings for said sample holders.

Bibliography

[1] A. M. Westerkam, J. L. W. Sonne, K. G. Danielsen, E. Skovsen, and T. M. Søndergaard, "All-dielectric one-dimensional gratings exhibiting Fano resonances in the terahertz region," J. Opt. Soc. Am. B (Posted 20 May 2022).

[2] B. Li, K. Hu, and Y. Shen, "A scientometric analysis of global terahertz research by web of science data," *IEEE Access*, vol. 8, pp. 56092–56112, 2020.

[3] D. M. Mittleman, "Perspective: Terahertz science and technology," *Journal of Applied Physics*, vol. 122, no. 23, p. 230901, 2017.

[4] R. Gill, S. Punia, and H. K. Malik, "Terahertz radiation for medical application," *EPL (Europhysics Letters)*, vol. 123, p. 65003, Oct 2018.

[5] Y. Wang, S. Jia, and J. Qin, "Tunable fano resonance and enhanced sensing in terahertz metamaterial," *Frontiers in Physics*, vol. 8, 2021.

[6] J. Dong, A. Tomasino, G. Balistreri, P. You, A. Vorobiov, É. Charette, B. Le Drogoff, M. Chaker, A. Yurtsever, S. Stivala, M. A. Vincenti, C. De Angelis, D. Kip, J. Azaña, and R. Morandotti, "Versatile metal-wire waveguides for broadband terahertz signal processing and multiplexing," *Nature Communications*, vol. 13, p. 741, Feb 2022.

[7] V. Fedotov, "Phase control of terahertz waves moves on chip," *Nature Photonics*, vol. 15, pp. 715–716, Oct 2021.

[8] B. Ferguson and X.-C. Zhang, "Materials for terahertz science and technology," *Nature Materials*, vol. 1, pp. 26–33, Sep 2002.

[9] P. Smith, D. Auston, and M. Nuss, "Subpicosecond photoconducting dipole antennas," *IEEE Journal of Quantum Electronics*, vol. 24, no. 2, pp. 255–260, 1988.

[10] R. A. Lewis, "A review of terahertz sources," *Journal of Physics D: Applied Physics*, vol. 47, p. 374001, Aug 2014.

[11] R. A. Lewis, "A review of terahertz detectors," *Journal of Physics D: Applied Physics*, vol. 52, p. 433001, Aug 2019.

[12] N. T. Yardimci and M. Jarrahi, "High-performance terahertz detectors based on plasmonic nano-antennas," in *2016 41st International Conference on Infrared, Millimeter, and Terahertz waves (IRMMW-THz)*, pp. 1–2, 2016.

[13] A. Singh, H. Surdi, V. V. Nikesh, S. S. Prabhu, and G. H. Döhler, "Improved efficiency of photoconductive thz emitters by increasing the effective contact length of electrodes," *AIP Advances*, vol. 3, no. 12, p. 122106, 2013.

[14] C. Sirtori, "Terahertz race heats up," *Nature Photonics*, vol. 15, pp. 1–2, Jan 2021.

[15] S. S. Dhillon, M. S. Vitiello, E. H. Linfield, A. G. Davies, M. C. Hoffmann, J. Booske, C. Paoloni, M. Gensch, P. Weightman, G. P. Williams, E. Castro-Camus, D. R. S. Cumming, F. Simoens, I. Escorcia-Carranza, J. Grant, S. Lucyszyn, M. Kuwata-Gonokami, K. Konishi, M. Koch, C. A. Schmuttenmaer, T. L. Cocker, R. Huber, A. G. Markelz, Z. D. Taylor, V. P. Wallace, J. A. Zeitler, J. Sibik, T. M. Korter, B. Ellison, S. Rea, P. Goldsmith, K. B. Cooper, R. Appleby, D. Pardo, P. G. Huggard, V. Krozer, H. Shams, M. Fice, C. Renaud, A. Seeds, A. Stöhr, M. Naftaly, N. Ridler, R. Clarke, J. E. Cunningham, and M. B. Johnston, "The 2017 terahertz science and technology roadmap," *Journal of Physics D: Applied Physics*, vol. 50, p. 043001, Jan 2017.

[16] A. G. Davies, A. D. Burnett, W. Fan, E. H. Linfield, and J. E. Cunningham, "Terahertz spectroscopy of explosives and drugs," *Materials Today*, vol. 11, no. 3, pp. 18–26, 2008.

[17] J. F. Federici, B. Schulkin, F. Huang, D. Gary, R. Barat, F. Oliveira, and D. Zimdars, "THz imaging and sensing for security applications—explosives, weapons and drugs," *Semiconductor Science and Technology*, vol. 20, pp. S266–S280, Jun 2005.

[18] G. G. Hernandez-Cardoso, L. F. Amador-Medina, G. Gutierrez-Torres, E. S. Reyes-Reyes, C. A. Benavides Martínez, C. Cardona Espinoza, J. Arce Cruz, I. Salas-Gutierrez, B. O. Murillo-Ortíz, and E. Castro-Camus, "Terahertz imaging demonstrates its diagnostic potential and reveals a relationship between cutaneous dehydration and neuropathy for diabetic foot syndrome patients," *Scientific Reports*, vol. 12, p. 3110, Feb 2022.

[19] L. Yu, L. Hao, T. Meiqiong, H. Jiaoqi, L. Wei, D. Jinying, C. Xueping, F. Weiling, and Z. Yang, "The medical application of terahertz technology in non-invasive detection of cells and tissues: opportunities and challenges," *RSC Adv.*, vol. 9, pp. 9354–9363, 2019.

[20] W.-C. Kan, W.-S. Lee, W.-H. Cheung, V. P. Wallace, and E. Pickwell-MacPherson, "Terahertz pulsed imaging of knee cartilage," *Biomed. Opt. Express*, vol. 1, pp. 967–974, Oct 2010.

[21] S. Wietzke, C. Jansen, N. Krumbholz, O. Peters, N. Vieweg, C. Jördens, M. Scheller, D. Romeike, T. Jung, M. Reuter, S. Chatterjee, M. Koch, F. Physik, B. Baudrit, T. Zentgraf, T. Hochrein, and M. Bastian, "Terahertz spectroscopy: A powerful tool for the characterization of plastic materials," in *2010 10th IEEE International Conference on Solid Dielectrics*, pp. 1–4, 2010.

[22] C. Jansen, S. Wietzke, O. Peters, M. Scheller, N. Vieweg, M. Salhi, N. Krumbholz, C. Jördens, T. Hochrein, and M. Koch, "Terahertz imaging: applications and perspectives," *Appl. Opt.*, vol. 49, pp. E48–E57, Jul 2010.

[23] A. Gowen, C. O'Sullivan, and C. O'Donnell, "Terahertz time domain spectroscopy and imaging: Emerging techniques for food process monitoring and quality control," *Trends in Food Science & Technology*, vol. 25, no. 1, pp. 40–46, 2012.

[24] H. Viswanathan and P. E. Mogensen, "Communications in the 6g era," *IEEE Access*, vol. 8, pp. 57063–57074, 2020.

[25] S. Dang, O. Amin, B. Shihada, and M.-S. Alouini, "What should 6g be?," *Nature Electronics*, vol. 3, pp. 20–29, Jan 2020.

[26] C. Xu, Z. Ren, J. Wei, and C. Lee, "Reconfigurable terahertz metamaterials: From fundamental principles to advanced 6g applications," *iScience*, vol. 25, no. 2, p. 103799, 2022.

[27] M. Hangyo, "Development and future prospects of terahertz technology," *Japanese Journal of Applied Physics*, vol. 54, p. 120101, Nov 2015.

[28] J. Xie, W. Ye, L. Zhou, X. Guo, X. Zang, L. Chen, and Y. Zhu, "A review on terahertz technologies accelerated by silicon photonics," *Nanomaterials*, vol. 11, no. 7, 2021.

[29] X. Fu, F. Yang, C. Liu, X. Wu, and T. J. Cui, "Terahertz beam steering technologies: From phased arrays to field-programmable metasurfaces," *Advanced Optical Materials*, vol. 8, no. 3, p. 1900628, 2020.

[30] G. Valušis, A. Lisauskas, H. Yuan, W. Knap, and H. G. Roskos, "Roadmap of terahertz imaging 2021," *Sensors*, vol. 21, no. 12, 2021.

[31] M. F. Limonov, M. V. Rybin, A. N. Poddubny, and Y. S. Kivshar, "Fano resonances in photonics," *Nature Photonics*, vol. 11, pp. 543–554, Sep 2017.

[32] U. Fano, "Effects of configuration interaction on intensities and phase shifts," *Phys. Rev.*, vol. 124, pp. 1866–1878, Dec 1961.

[33] A. A. Darki, A. Parthenopoulos, J. V. Nygaard, and A. Dantan, "Profilometry and stress analysis of suspended nanostructured thin films," *Journal of Applied Physics*, vol. 129, no. 6, p. 065302, 2021.

[34] W. Zhou, D. Zhao, Y.-C. Shuai, H. Yang, S. Chuwongin, A. Chadha, J.-H. Seo, K. X. Wang, V. Liu, Z. Ma, and S. Fan, "Progress in 2d photonic crystal fano resonance photonics," *Progress in Quantum Electronics*, vol. 38, no. 1, pp. 1–74, 2014.

[35] X. Romain, R. Degl'Innocenti, F. I. Baida, and P. Boyer, "Tunable polarization-induced fano resonances in stacked wire-grid metasurfaces," *Communications Physics*, vol. 4, p. 115, Jun 2021.

[36] C. Wu, N. Arju, G. Kelp, J. A. Fan, J. Dominguez, E. Gonzales, E. Tutuc, I. Brener, and G. Shvets, "Spectrally selective chiral silicon metasurfaces based on infrared fano resonances," *Nature Communications*, vol. 5, p. 3892, May 2014.

[37] Q. Xie, G.-X. Dong, B.-X. Wang, and W.-Q. Huang, "High-q fano resonance in terahertz frequency based on an asymmetric metamaterial resonator," *Nanoscale Research Letters*, vol. 13, p. 294, Sep 2018.

[38] R. Singh, I. A. I. Al-Naib, M. Koch, and W. Zhang, "Sharp fano resonances in thz metamaterials," *Opt. Express*, vol. 19, pp. 6312–6319, Mar 2011.

[39] Y. P. Cao, Y. Y. Wang, Z. X. Geng, J. Liu, Y. P. Yang, and H. D. Chen, "Tuning of fano resonances in terahertz metamaterials," *Journal of Applied Physics*, vol. 117, no. 6, p. 063107, 2015.

[40] Z. Liu, Z. Liu, J. Li, W. Li, J. Li, C. Gu, and Z.-Y. Li, "3d conductive coupling for efficient generation of prominent fano resonances in metamaterials," *Scientific Reports*, vol. 6, p. 27817, Jun 2016.

[41] L. R. S. R.S., "Xxvi. on the remarkable phenomenon of crystalline reflexion described by prof. stokes," *The London, Edinburgh, and Dublin Philosophical Magazine and Journal of Science*, vol. 26, no. 160, pp. 256–265, 1888.

[42] E. Yablonovitch, "Photonic crystals: What's in a name?," *Optics & Photonics News*, vol. 18, pp. 12–13, Mar 2007.

[43] J. D. Joannopoulos, S. G. Johnson, J. N. Winn, and R. D. Meade, *Photonic Crystals: Molding the Flow of Light*. Princeton University Press, 2nd ed., 2008.

[44] S. O. Kasap, *Optoelectronics and Photonics*. Pearson Education, 2nd ed., 2013.

[45] R. H. Lipson and C. Lu, "Photonic crystals: a unique partnership between light and matter," *European Journal of Physics*, vol. 30, pp. S33–S48, Jul 2009.

[46] S. John, "Strong localization of photons in certain disordered dielectric superlattices," *Phys. Rev. Lett.*, vol. 58, pp. 2486–2489, Jun 1987.

[47] E. Yablonovitch, "Inhibited spontaneous emission in solid-state physics and electronics," *Phys. Rev. Lett.*, vol. 58, pp. 2059–2062, May 1987.

[48] E. M. Purcell, "Spontaneous Emission Probabilities at Radio Frequencies," *Physical Review*, vol. 69, p. 681, 1946.

[49] E. Yablonovitch, T. J. Gmitter, and K. M. Leung, "Photonic band structure: The face-centered-cubic case employing nonspherical atoms," *Phys. Rev. Lett.*, vol. 67, pp. 2295–2298, Oct 1991.

[50] T. Krauss, R. De La Rue, and S. Brand, "Two-dimensional photonic-bandgap structures operating at near-infrared wavelengths," *Nature*, vol. 383, Oct 1996.

[51] D. Norris and Y. Vlasov, "Chemical approaches to three-dimensional semiconductor photonic crystals," *Advanced Materials*, vol. 13, pp. 371 – 376, Mar 2001.

[52] H. Sözüer and J. P. Dowling, "Photonic band calculations for woodpile structures," *Journal of Modern Optics*, vol. 41, no. 2, pp. 231–239, 1994.

[53] K. M. Ho, C. T. Chan, C. M. Soukoulis, R. Biswas, and M. Sigalas, "Photonic band gaps in three dimensions: New layer-by-layer periodic structures," *Solid state communications*, vol. 89, no. 5, pp. 413–416, 1994.

[54] P. Russell, "Photonic crystal fibers," *Science (American Association for the Advancement of Science)*, vol. 299, no. 5605, pp. 358–362, 2003.

[55] M. Michieletto, *Hollow core fibers for high power laser applications*. PhD thesis, Technical University of Denmark, 2016.

[56] D. J. Griffiths, *Introduction to Electrodynamics*. Cambridge University Press, 4th ed., 2017.

[57] P. N. Butcher and D. Cotter, *The Elements of Nonlinear Optics*. Cambridge Studies in Modern Optics, Cambridge University Press, 1990.

[58] C. Kittel, *Introduction to Solid State Physics*. Wiley, 8th ed., 2004.

[59] D. J. Sandiford, F. Mandel, and A. C. Phillips, *Introduction to Quantum Mechanics*. John Wiley & Sons Ltd, 2003.

[60] J. Dahl, *Introduction to the quantum world of atoms and molecules*. Singapore: World Scientific, 2001.

[61] L. Li, "Use of fourier series in the analysis of discontinuous periodic structures," *J. Opt. Soc. Am. A*, vol. 13, pp. 1870–1876, Sep 1996.

[62] J. Dai, J. Zhang, W. Zhang, and D. Grischkowsky, "Terahertz time-domain spectroscopy characterization of the far-infrared absorption and index of refraction of high-resistivity, float-zone silicon," *J. Opt. Soc. Am. B*, vol. 21, pp. 1379–1386, Jul 2004.

[63] D. Armand, S. Koya, and Y. Kadoya, "Photonic crystal sandwiched in parallel plates as thz waveguide," in *2013 38th International Conference on Infrared, Millimeter, and Terahertz Waves (IRMMW-THz)*, pp. 1–2, 2013.

[64] A. Zygmund and R. Fefferman, "Classes of functions and fourier series," in *Trigonometric Series*, Cambridge Mathematical Library, ch. 4, p. 127–181, Cambridge University Press, 3th ed., 2003.

[65] E. Popov, M. Nevière, and N. Bonod, "Factorization of products of discontinuous functions applied to fourier–bessel basis," *J. Opt. Soc. Am. A*, vol. 21, pp. 46–52, Jan 2004.

[66] P. Lalanne and G. M. Morris, "Highly improved convergence of the coupled-wave method for tm polarization," *J. Opt. Soc. Am. A*, vol. 13, pp. 779–784, Apr 1996.

[67] G. Granet and B. Guizal, "Efficient implementation of the coupled-wave method for metallic lamellar gratings in tm polarization," *J. Opt. Soc. Am. A*, vol. 13, pp. 1019–1023, May 1996.

[68] A. V. Lavrinenko, J. Lægsgaard, N. Gregersen, F. Schmidt, and T. Søndergaard, *Numerical Methods in Photonics*. Optical Sciences and Applications of Light, CRC Press, 1st ed., 2017.

[69] T. M. Søndergaard, *Green's Function Integral Equation Methods in Nano-Optics*. CRC Press, 1st ed., 2019.

[70] Z. Jian, J. Pearce, and D. M. Mittleman, "Two-dimensional photonic crystal slabs in parallel-plate metal waveguides studied with terahertz time-domain spectroscopy," *Semiconductor Science and Technology*, vol. 20, 2005.

[71] W. M. Robertson, G. Arjavalingam, R. D. Meade, K. D. Brommer, A. M. Rappe, and J. D. Joannopoulos, "Measurement of photonic band structure in a two-dimensional periodic dielectric array," *Phys. Rev. Lett.*, vol. 68, pp. 2023–2026, Mar 1992.

[72] S. Jin, S. Wu, G. Zhou, Y. Li, L. Li, B. Li, and X. Wang, "A query-based quantum eigensolver," *Quantum Engineering*, vol. 2, no. 3, p. e49, 2020.

[73] M. P. Teter, M. C. Payne, and D. C. Allan, "Solution of schrödinger's equation for large systems," *Phys. Rev. B*, vol. 40, pp. 12255–12263, Dec 1989.

[74] S. G. Johnson, *Photonic crystals: from theory to practice.* PhD thesis, Massachusetts Institute of Technology, 2001.

[75] B. Bhushan, *Springer Handbook of Nanotechnology.* Springer Handbook of Nanotechnology, Springer Berlin Heidelberg, 2010.

[76] H. Lüth, *Solid Surfaces, Interfaces and Thin Films.* Graduate Texts in Physics, Berlin, Heidelberg: Springer-Verlag Berlin Heidelberg, 2010.

[77] M. Shearn, X. Sun, M. D. Henry, A. Yariv, and A. Scherer, "Advanced plasma processing: Etching, deposition, and wafer bonding techniques for semiconductor applications," in *Semiconductor Technologies* (J. Grym, ed.), ch. 5, Rijeka: IntechOpen, 2010.

[78] M. Tilli, M. Paulasto-Krockel, M. Petzold, H. Theuss, T. Motooka, and V. Lindroos, *Handbook of silicon based MEMS materials and technologies.* Elsevier, 2020.

[79] H. F. Winters and J. Coburn, "Surface science aspects of etching reactions," *Surface Science Reports*, vol. 14, no. 4, pp. 162–269, 1992.

[80] H. Jansen, H. Gardeniers, M. de Boer, M. Elwenspoek, and J. Fluitman, "A survey on the reactive ion etching of silicon in microtechnology," *Journal of micromechanics and microengineering*, vol. 6, pp. 14–28, Mar 1996.

[81] C. T. Rueden, J. Schindelin, M. C. Hiner, B. E. DeZonia, A. E. Walter, E. T. Arena, and K. W. Eliceiri, "Imagej2: Imagej for the next generation of scientific image data," *BMC bioinformatics*, vol. 18, no. 1, pp. 529–529, 2017.

[82] P. P. Cielecki and E. Skovsen, "A Compact, 3D printable Purge System for Terahertz Spectroscopy." Zenodo. Sept. 2021. https://doi.org/10.5281/zenodo.5358096.

[83] P. U. Jepsen, "Phase retrieval in terahertz time-domain measurements: a "how to" tutorial," *Journal of Infrared, Millimeter, and Terahertz Waves*, vol. 40, no. 4, pp. 395–411, 2019.

[84] K. Debnath, M. Clementi, T. D. Bucio, A. Z. Khokhar, M. Sotto, K. M. Grabska, D. Bajoni, M. Galli, S. Saito, and F. Y. Gardes, "Ultrahigh-q photonic crystal cavities in silicon rich nitride," *Opt. Express*, vol. 25, pp. 27334–27340, Oct 2017.

[85] W. Bogaerts, P. Dumon, J. Van Campenhout, V. Wiaux, J. Wouters, S. Beckx, D. Taillaert, B. Luyssaert, D. Van Thourhout, and R. Baets, "Deep UV lithography for planar photonic crystal structures," in *2003 IEEE LEOS ANNUAL MEETING CONFERENCE PROCEEDINGS, VOLS 1 AND 2*, pp. 754–755, I E E E, 2003.

[86] C. Shemelya, D. DeMeo, and T. Vandervelde, "Two dimensional metallic photonic crystals for light trapping and anti-reflective coatings in thermophotovoltaic applications," *Applied Physics Letters*, vol. 104, pp. 021115–021115, Jan 2014.

[87] J. Hong, M. Kim, and C. Cha, "17 - multimodal carbon dots as biosensors," in *Theranostic Bionanomaterials* (W. Cui and X. Zhao, eds.), Micro and Nano Technologies, pp. 377–400, Elsevier, 2019.

[88] S. S. Harilal, J. R. Freeman, P. K. Diwakar, and A. Hassanein, *Femtosecond Laser Ablation: Fundamentals and Applications*, pp. 143–166. Berlin, Heidelberg: Springer Berlin Heidelberg, 2014.

[89] B. Chichkov, C. Momma, S. Nolte, F. Von Alvensleben, and A. Tünnermann, "Femtosecond, picosecond and nanosecond laser ablation of solids," *Applied physics. A, Materials science & processing*, vol. 63, no. 2, pp. 109–115, 1996.

[90] A. H. Hamad, "Effects of different laser pulse regimes (nanosecond, picosecond and femtosecond) on the ablation of materials for production of nanoparticles in liquid solution," in *High Energy and Short Pulse Lasers* (R. Viskup, ed.), ch. 12, Rijeka: IntechOpen, 2016.

[91] R. Stoian, D. Ashkenasi, A. Rosenfeld, and E. E. B. Campbell, "Coulomb explosion in ultrashort pulsed laser ablation of Al_2O_3," *Phys. Rev. B*, vol. 62, pp. 13167–13173, Nov 2000.

[92] J. Bonse, S. Baudach, J. Krüger, W. Kautek, and M. Lenzner, "Femtosecond laser ablation of silicon–modification thresholds and morphology," *Applied physics. A, Materials science & processing*, vol. 74, no. 1, pp. 19–25, 2002.

[93] Spectra-physics, *Spitfire, Ti:Sapphire Regenerative Amplifier Systems, Spitfire F, Spitfire USF, Spitfire 50FS, Spitfire P, Spitfire PM, User's Manual.* Spectra-physics, Mountain View, CA, 2004.

[94] Spectra-physics, *Tsunami, Mode-locked Ti:sapphire Laser, User's Manual.* Spectra-physics, Mountain View, CA, 2002.

[95] Spectra-physics, *Millennia Pro s-Series, Diode-Pumped, CW Visible Laser Systems, User's Manual.* Spectra-physics, Mountain View, CA, 2005.

[96] Menlosystems, "Terasmart compact industry-proven thz-tds system." Data sheet, Mar 2021.

[97] J. Neu and C. A. Schmuttenmaer, "Tutorial: An introduction to terahertz time domain spectroscopy (thz-tds)," *Journal of Applied Physics*, vol. 124, no. 23, p. 231101, 2018.

[98] N. M. Burford and M. O. El-Shenawee, "Review of terahertz photoconductive antenna technology," *Optical Engineering*, vol. 56, 2017.

[99] P. U. Jepsen, R. H. Jacobsen, and S. R. Keiding, "Generation and detection of terahertz pulses from biased semiconductor antennas," *J. Opt. Soc. Am. B*, vol. 13, pp. 2424–2436, Nov 1996.

[100] A. Parthenopoulos, A. A. Darki, B. R. Jeppesen, and A. Dantan, "Optical spatial differentiation with suspended subwavelength gratings," *Opt. Express*, vol. 29, pp. 6481–6494, Mar 2021.

[101] Y. Yang, B. Cui, Z. Geng, and S. Feng, "Terahertz magnetic and electric mie resonances of an all-dielectric one-dimensional grating," *Applied Physics Letters*, vol. 106, no. 11, p. 111106, 2015.

[102] S. V. Gaponenko, *Introduction to Nanophotonics*. Cambridge University Press, 2010.

[103] M. Centini, C. Sibilia, M. Scalora, G. D'Aguanno, M. Bertolotti, M. J. Bloemer, C. M. Bowden, and I. Nefedov, "Dispersive properties of finite, one-dimensional photonic band gap structures: Applications to nonlinear quadratic interactions," *Phys. Rev. E*, vol. 60, pp. 4891–4898, Oct 1999.

[104] S. G. Tikhodeev, A. L. Yablonskii, E. A. Muljarov, N. A. Gippius, and T. Ishihara, "Quasiguided modes and optical properties of photonic crystal slabs," *Phys. Rev. B*, vol. 66, p. 045102, Jul 2002.

[105] K. Tsakmakidis, B. Weiss, and O. Hess, "Full-wave electromagnetic modelling of an inp/ingaas travelling-wave heterojunction phototransistor," *Journal of Physics D: Applied Physics*, vol. 39, p. 1805, 04 2006.

[106] N. Jukam and M. S. Sherwin, "Two-dimensional terahertz photonic crystals fabricated by deep reactive ion etching in si," *Applied Physics Letters*, vol. 83, no. 1, pp. 21–23, 2003.

[107] Y. A. Vlasov, M. A. Kaliteevski, and V. V. Nikolaev, "Different regimes of light localization in a disordered photonic crystal," *Phys. Rev. B*, vol. 60, pp. 1555–1562, Jul 1999.

[108] A. Zygmund and R. Fefferman, *FOURIER COEFFICIENTS. ELEMENTARY THEOREMS ON THE CONVERGENCE OF S[f] AND S[f]*, ch. 2, p. 35–73. Cambridge Mathematical Library, Cambridge University Press, 3th ed., 2003.

A | Change of Index on Fourier Series

This appendix gives the reason for keeping the same summation limits on the Fourier series under an index change. It is related to the possibility of writing the product of two periodic functions as

$$v(t)w(t) = \sum_{q=-\infty}^{\infty} v_{\{q\}} e^{iqt} \sum_{n=-\infty}^{\infty} w_{\{n\}} e^{int} = \sum_{n=-\infty}^{\infty} w_{\{n\}} \left(v(t) e^{int} \right). \tag{A.1}$$

Here the Fourier coefficients for the parenthesis, by comparison with, e.g., eq. (2.75), can be found as [108]

$$\frac{1}{2\pi} \int_0^{2\pi} v(t) e^{int} e^{-imt} dt = \frac{1}{2\pi} \int_0^{2\pi} v(t) e^{-i(m-n)t} dt = v_{\{m-n\}}, \tag{A.2}$$

which then leads to [108]

$$v(t)w(t) = \sum_{n=-\infty}^{\infty} w_{\{n\}} \left(\sum_{m=-\infty}^{\infty} v_{\{m-n\}} e^{imt} \right) = \sum_{m=-\infty}^{\infty} e^{imt} \sum_{n=-\infty}^{\infty} v_{\{m-n\}} w_{\{n\}}, \tag{A.3}$$

thus resulting in the same result as the otherwise rather simple and dubious substitution $m = n + q$ that would lead to $q = m - n$.

B | Photonic Crystal FMM Figures

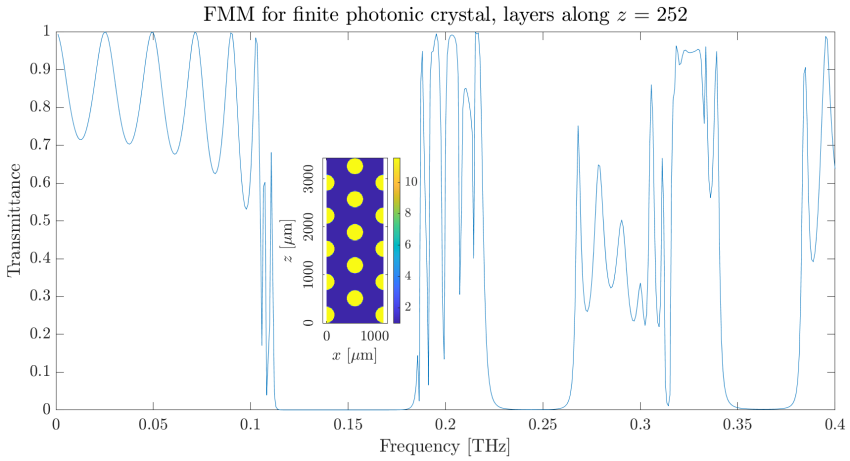

(a)

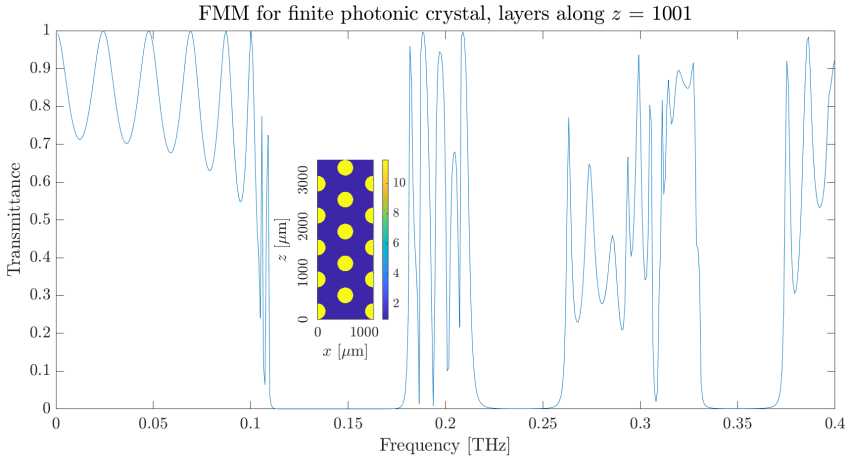

(b)

Figure B.1: (a)-(b) Shows the transmittance of S-polarised light parallel with the **K**-direction in the first Brillouin zone radiation through a photonic crystal that is composed of 10 lines of rods along z. The insert in each figure shows the relative permittivity profile, where $\varepsilon_{rods} = 3.4^2$ and $\varepsilon_{surroundings} = 1^2$. The intermediate values arises from a geometric averaging of the relative permittivity for the points around the interface between the rods and the surrounding medium. The radii of the rods are $r_{rods} = 168.6$ μm and the period between the rods along one of the crystal axes is $\Lambda = 687.6$ μm.

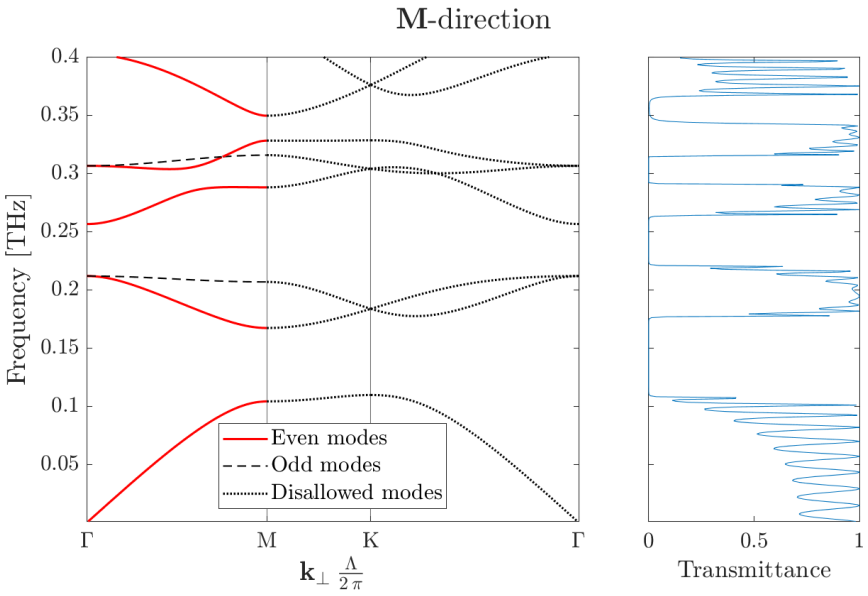

(a)

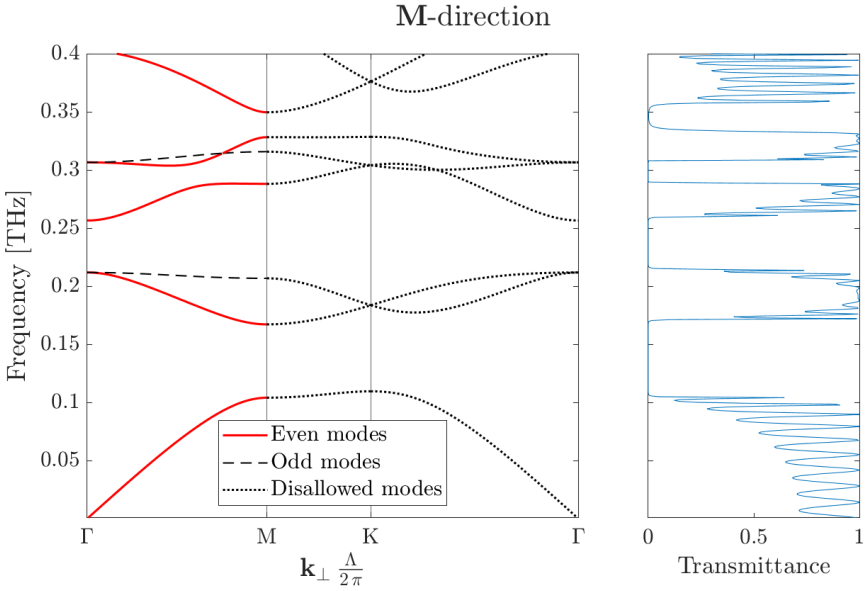

(b)

Figure B.2: A comparison between the band diagram calculated with PWE for an infinite photonic crystal seen on the left and the transmittance calculated with FMM seen on the right, both only for S-polarisation. Only the even modes can be excited, since the odd modes does not match the symmetry of the input field [70, 71] and the disallowed modes is not covered for the given propagation direction. The number of layers along z used for the FMM is 481 for **(a)** and 959 for **(b)**. Again the photonic crystal for the FMM is composed of 10 lines of rods along z, which is parallel with the **M**-direction in the first Brillouin zone, and $\varepsilon_{rods} = 3.4^2$, $\varepsilon_{surroundings} = 1^2$, $r_{rods} = 168.6$ μm, $\Lambda = 687.6$ μm. Contrary to the result presented in fig. 2.20, comparing the graphs in **(a)** and **(b)** it is seen using ~ 500 layers in the z-direction for these settings does not really suffice for all band gaps. However, the placement of the first band gap, which is the one of interest, is sufficiently precise. As such a division similar to that seen in **(a)** will be used to compare the model with the experimental results.

C | Angled Spectra: M2, M3 and M5

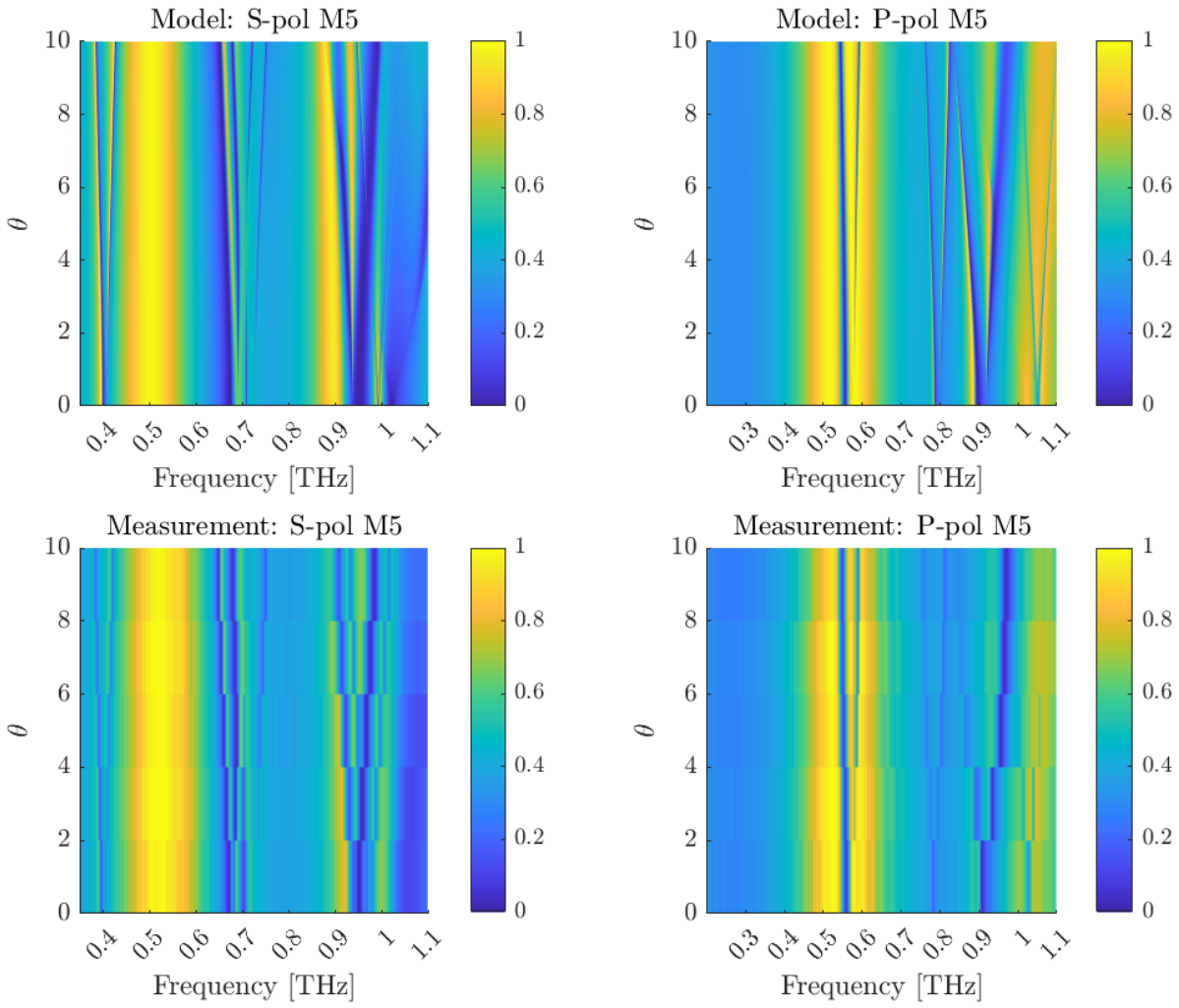

Figure C.1: Surface plot of the modelled and measured transmittance spectra of the M5 sample for various frequencies and angle of incidence.

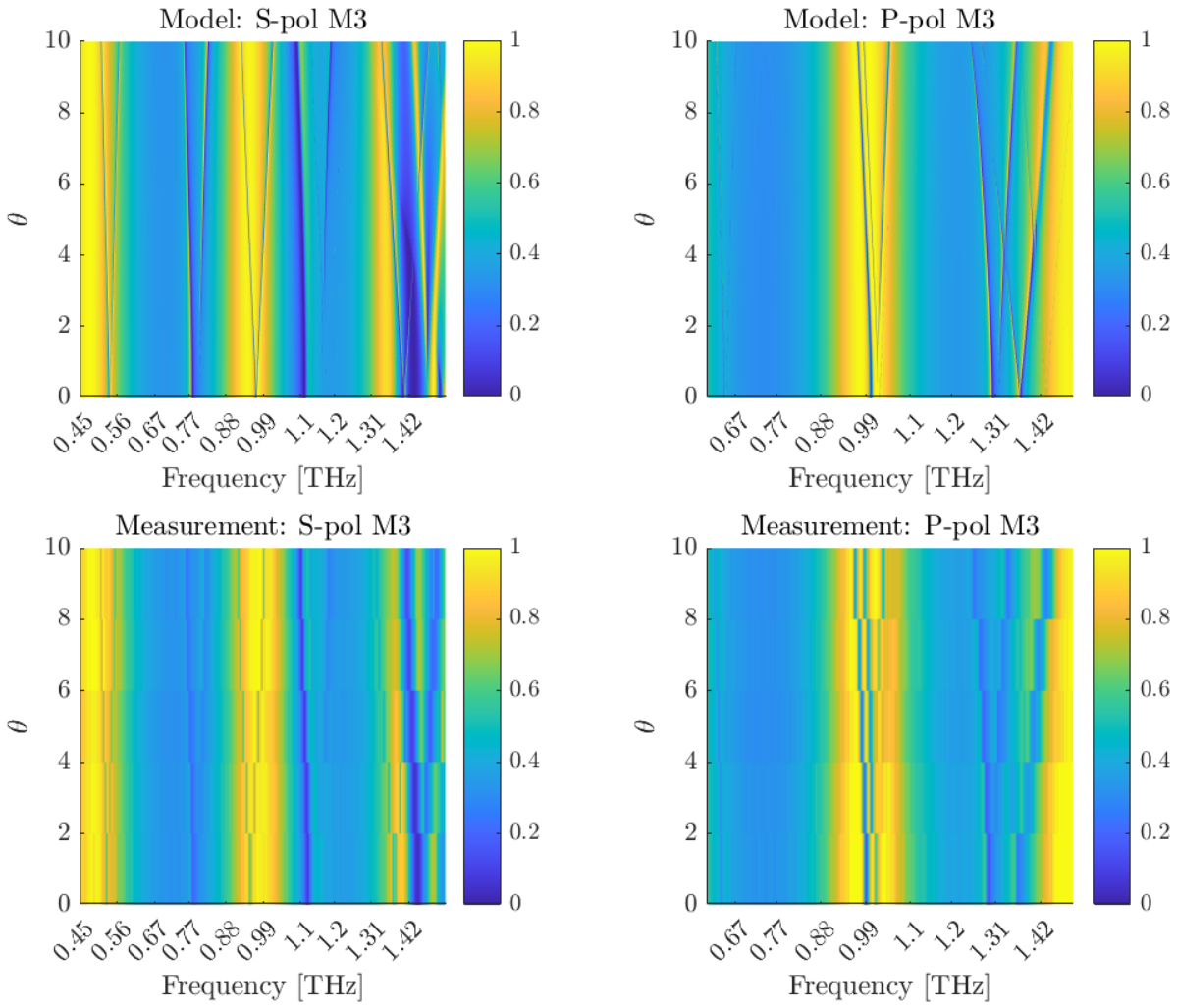

Figure C.2: Surface plot of the modelled and measured transmittance spectra of the M3 sample for various frequencies and angle of incidence.

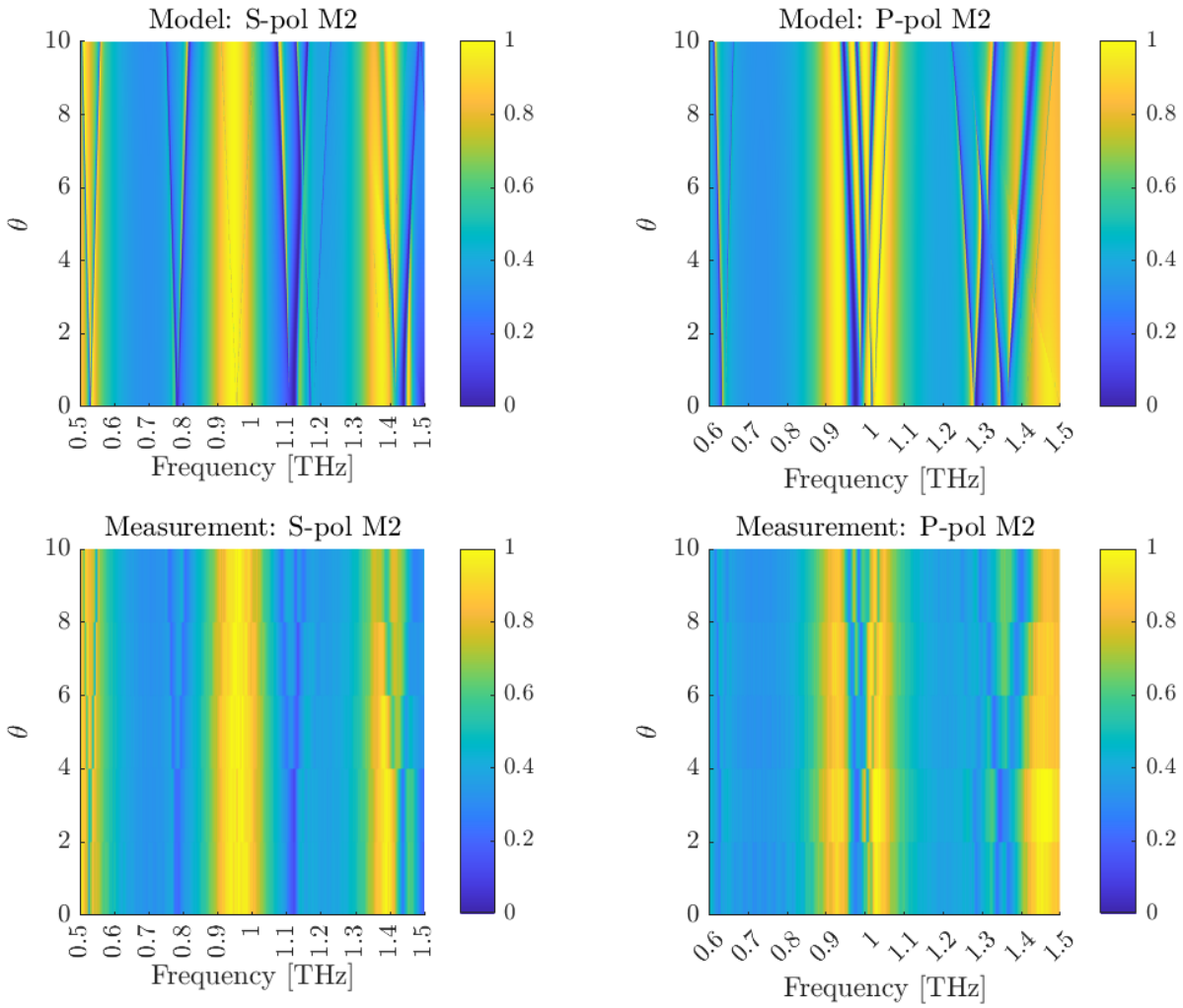

Figure C.3: Surface plot of the modelled and measured transmittance spectra of the M2 sample for various frequencies and angle of incidence.

D | THz-TDS Spectra

	$\Lambda[\mu m]$	$r_-[\mu m]$	$r_+[\mu m]$	$t_w[\mu m]$	$h[\mu m]$	Orientation	Rows
Hex-hole-1	495.59	213.85	218.10	-	100 $\pm$20	M	17
Hex-hole-2	494.73	201.74	210.877	-	100 $\pm$20	K	13
Hex-hole-WG-1	434.63	202.23	222.33	-	100 $\pm$20	K	28
Hex-hole-WG-2	495.04	200.80	206.02	-	100 $\pm$20	K	13
Hex-hole-WG-3	491.00	201.00	210.60	-	100 $\pm$20	K	13
Hex-rod-1	615.74	71.81	171.79	-	-	M/K	36/51
Hex-rod-2	590.97	48.32	117.87	36.06	148.88	M/K	36/51
Hex-rod-3	616.35	76.26	124.96	92.11	98.74	M/K	36/51
Hex-rod-4	721.99	85.41	108.64	59.16	142.15	M/K	31/45
Hex-rod-5	662.84	121.48	164.70	-	-	M/K	32/45
Square-rod-1	659.10	148.01	191.97	-	99.78†	X	23
Square-rod-WG-1	668.55	167.17	197.97	-	99.78†	X	23
Hex-rod-WG-1	660.00	152.99	202.03	-	99.78†	K	22
Hex-rod-cavity-1	630.22	124.95	124.95	-	99.78†	K	10
Hex-rod-cavity-2	638.16	161.14	161.14	-	99.78†	K	10

Table D.1: Presents the dimensions relevant to model the fabricated samples. The naming convention for holes and rods are visualised in fig. 5.2(e) and fig. 5.4(b), respectively. †: calculated from etch time.

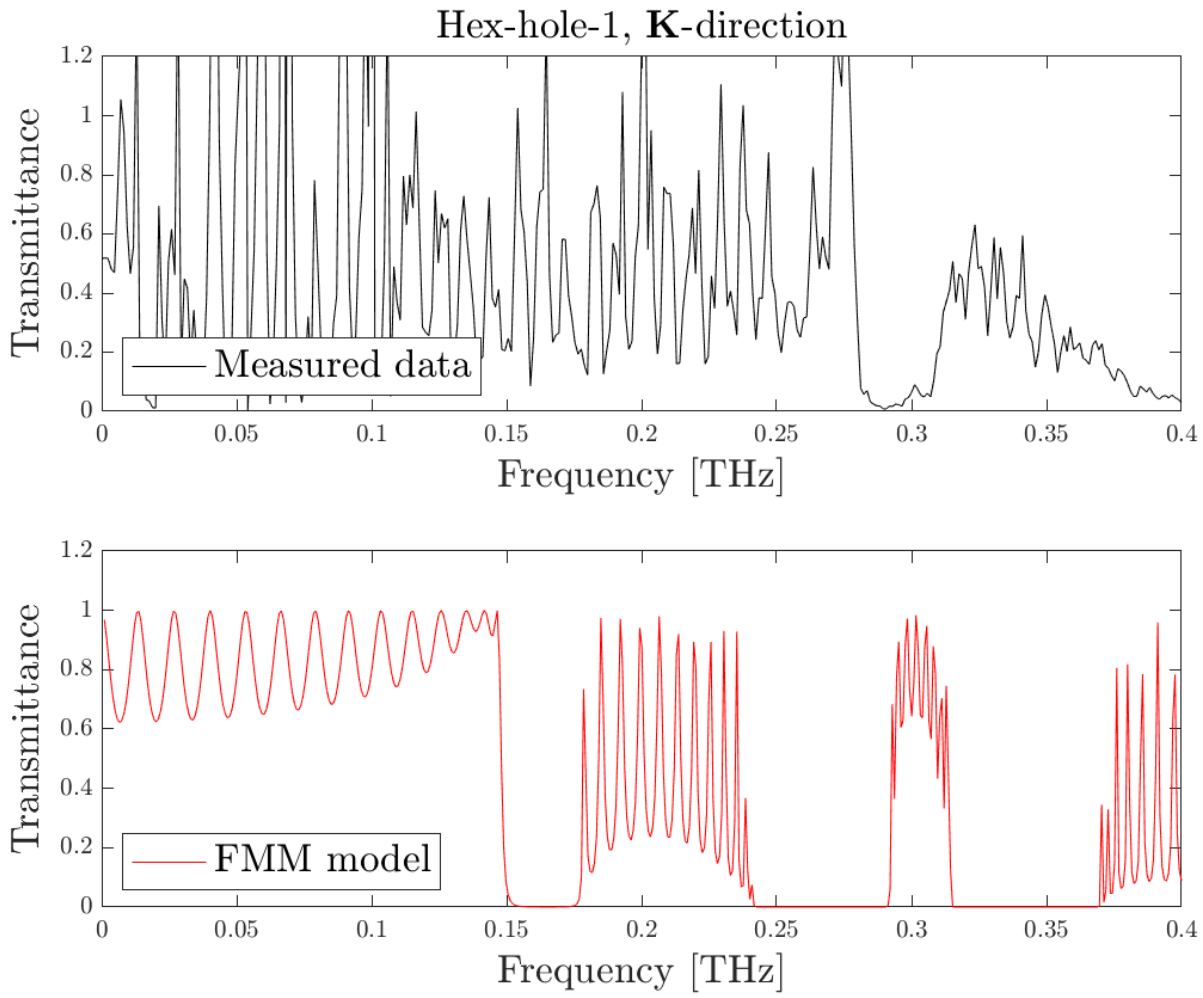

Figure D.1: The measured and modelled transmittance spectra of the Hex-hole-1 sample oriented such that the light propagates along the **K**-direction. The measured band gap was determined to be between 0.28 and 0.30 THz while the calculated band gap lies between 0.15 and 0.18 THz.

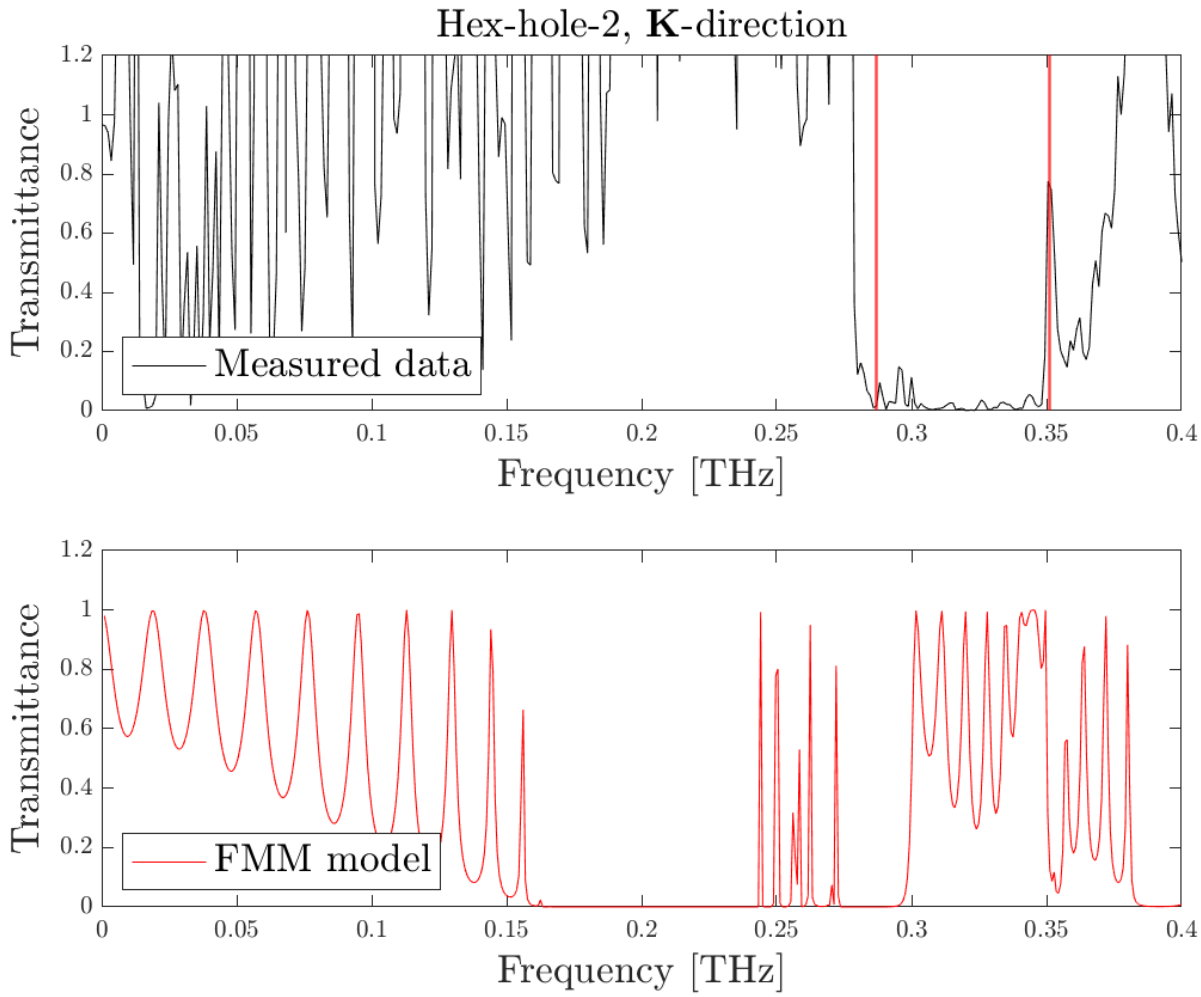

Figure D.2: The measured and modelled transmittance spectra of the Hex-hole-2 sample, oriented such that the light propagates along the **K**-direction. The measured band gap was determined to be between 0.29 and 0.35 THz while the calculated band gap lies between 0.16 and 0.24 THz. The red vertical lines show the location of the band gap using a fully three-dimensional FFT method with an air layer corresponding to 40 % of the height in the PPMWG, or equivalently 67 μm.

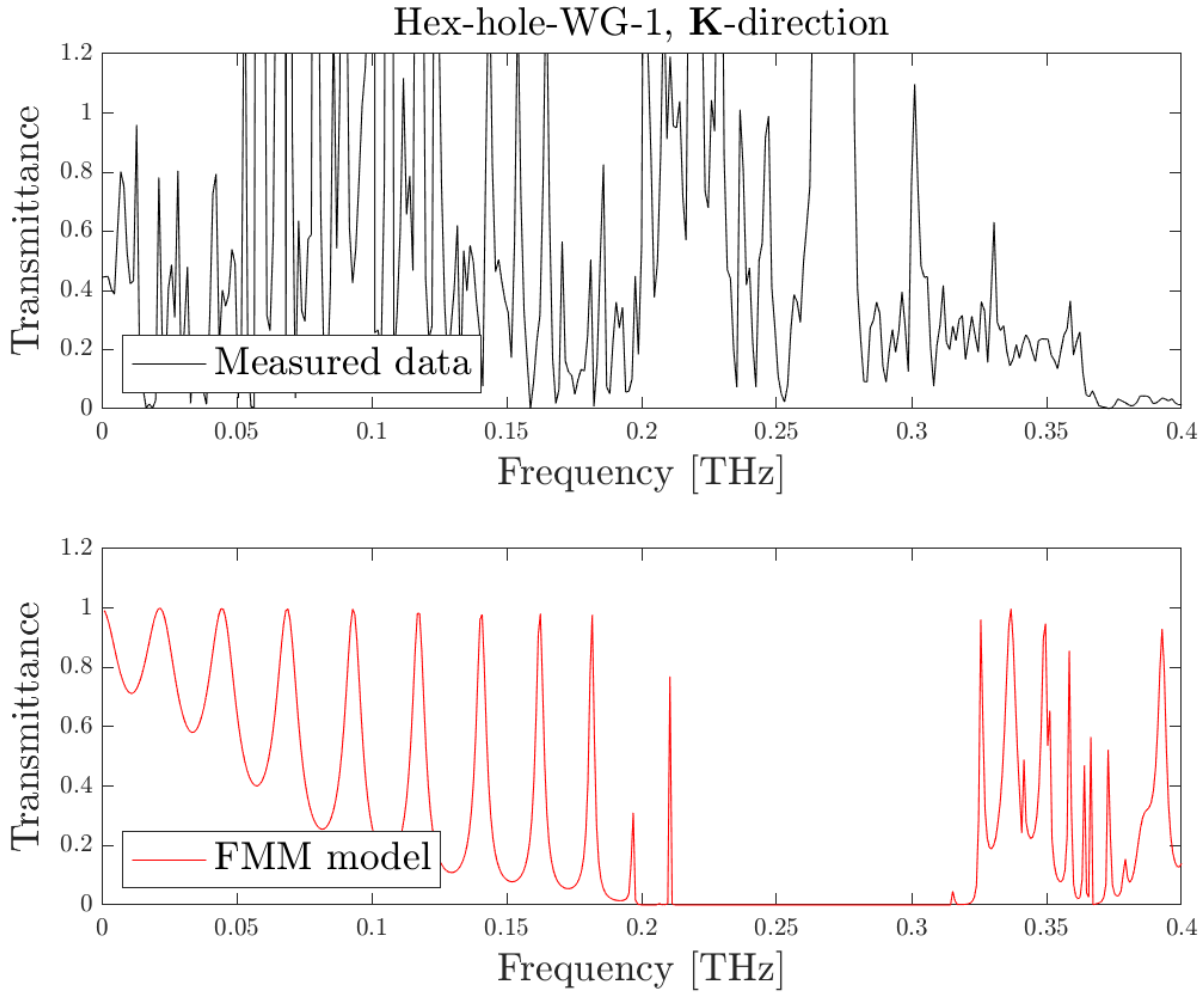

Figure D.3: The measured and modelled transmittance spectra of the Hex-hole-WG-1 sample oriented such that the light propagates along the **K**-direction. The measured band gap could not be determined while the calculated band gap lies between 0.21 and 0.32 THz.

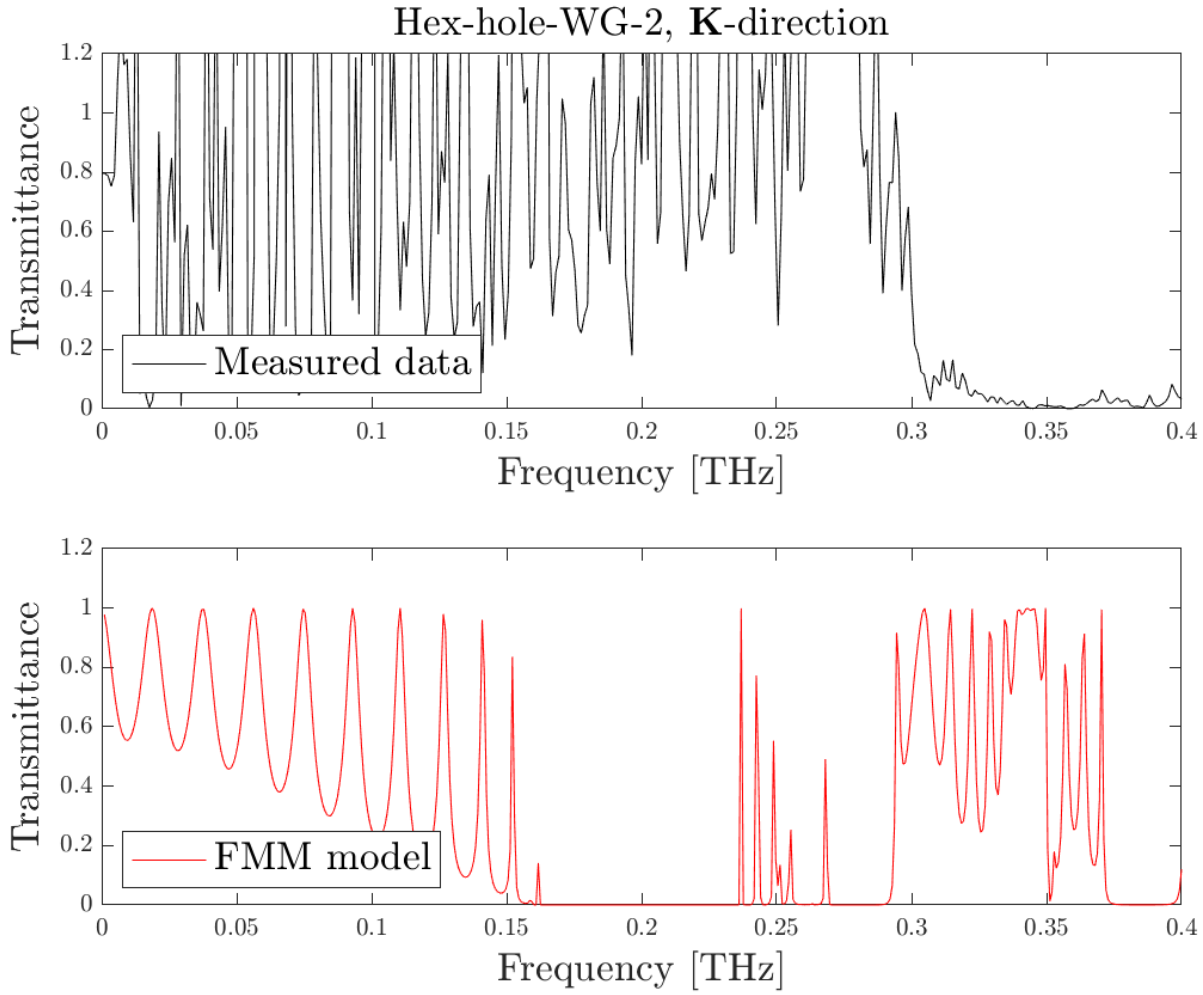

Figure D.4: The measured and modelled transmittance spectra of the Hex-hole-WG-2 sample oriented such that the light propagates along the **K**-direction. The measured band gap could not be determined while the calculated band gap lies between 0.17 and 0.26 THz.

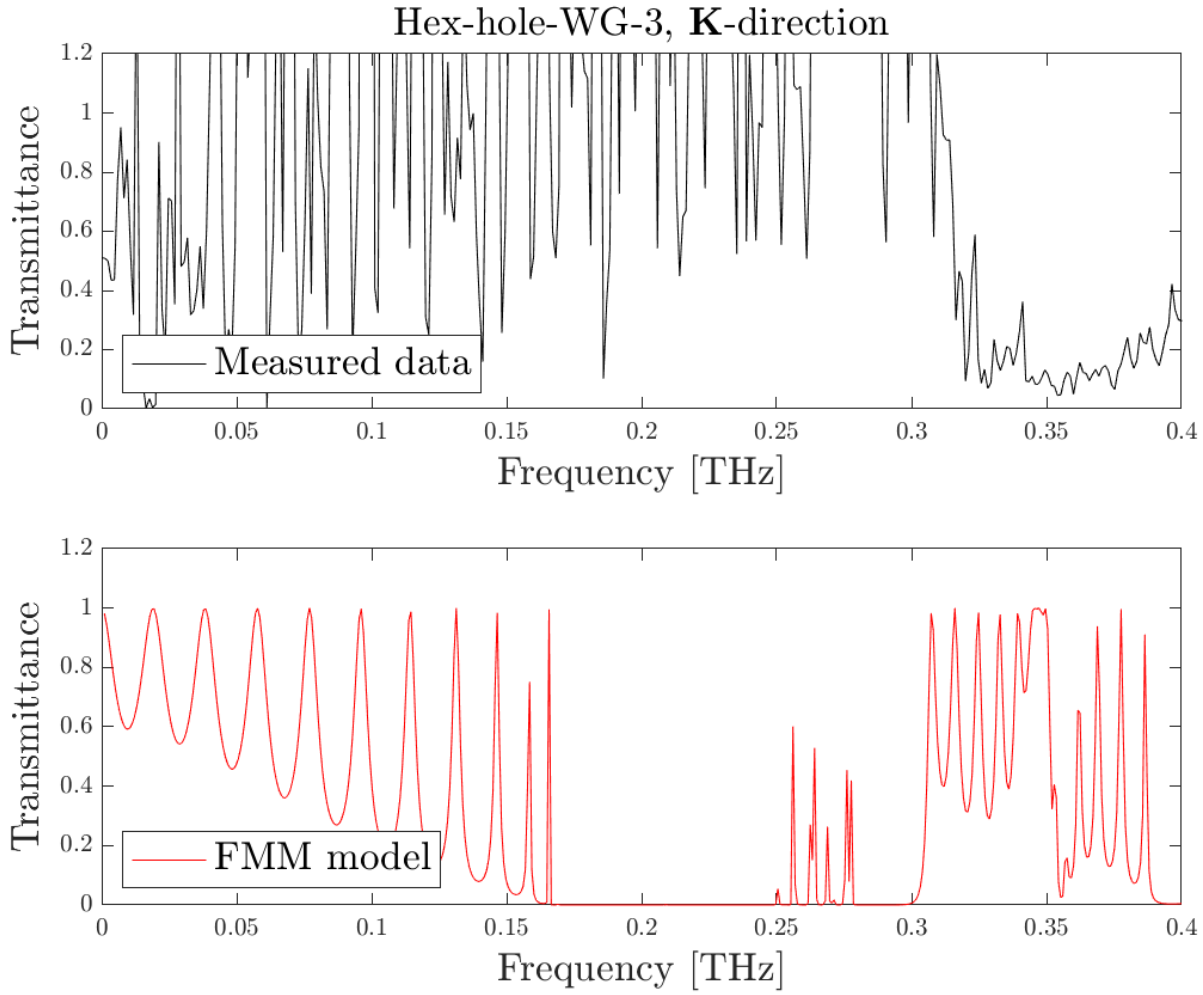

Figure D.5: The measured and modelled transmittance spectra of the Hex-hole-WG-3 sample oriented such that the light propagates along the **K**-direction. The measured band gap could not be determined while the calculated band gap lies between 0.16 and 0.24 THz.

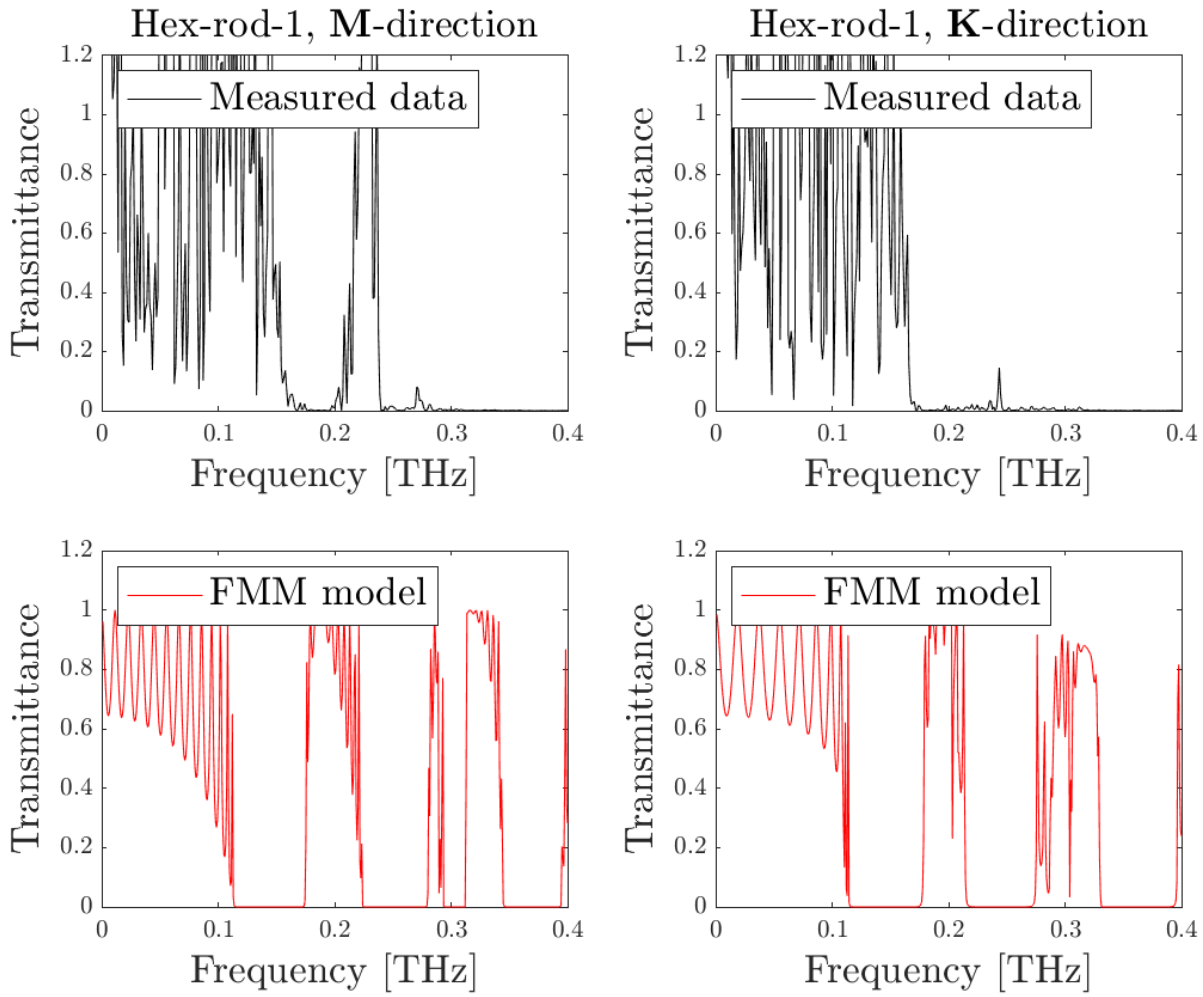

Figure D.6: The measured and modelled transmittance spectra of the Hex-rod-1 sample for light propagating along both the **M**- and **K**-direction. The measured band gap for the **M**-direction was determined to be between 0.17 and 0.21 THz, for the **K**-direction it was determined to lie between 0.17 and 0.24 THz. The calculated band gap lies between 0.11 and 0.17 THz for the **M**-direction, and between 0.11 and 0.18 THz for the **K**-direction.

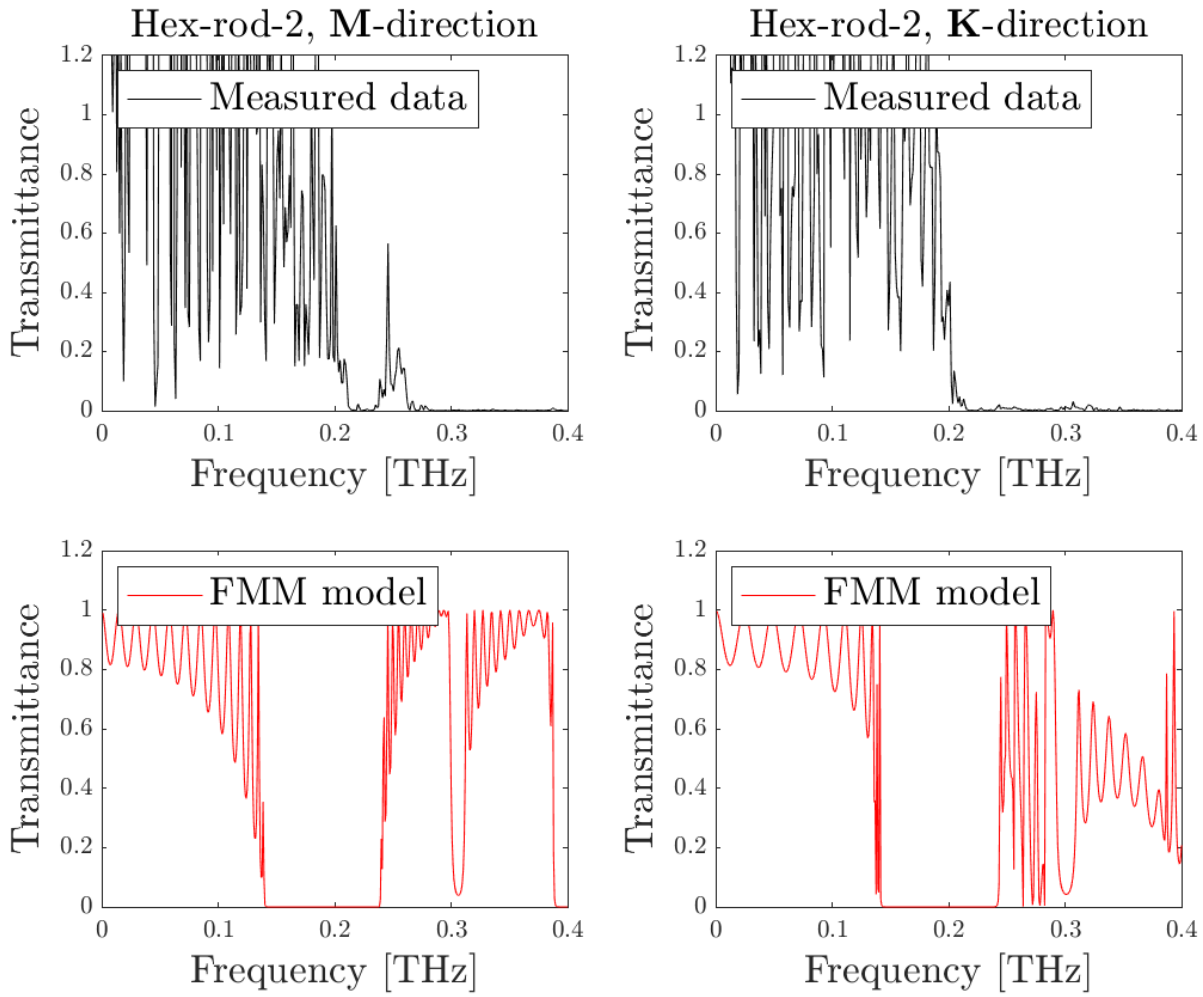

Figure D.7: The measured and modelled transmittance spectra of the Hex-rod-2 sample for light propagating along both the **M**- and **K**-direction. The measured band gap for the **M**-direction was determined to be between 0.21 and 0.24 THz, for the **K**-direction it could not be determined. The calculated band gap lies between 0.14 and 0.24 THz for the **M**-direction, and between 0.14 and 0.24 THz for the **K**-direction.

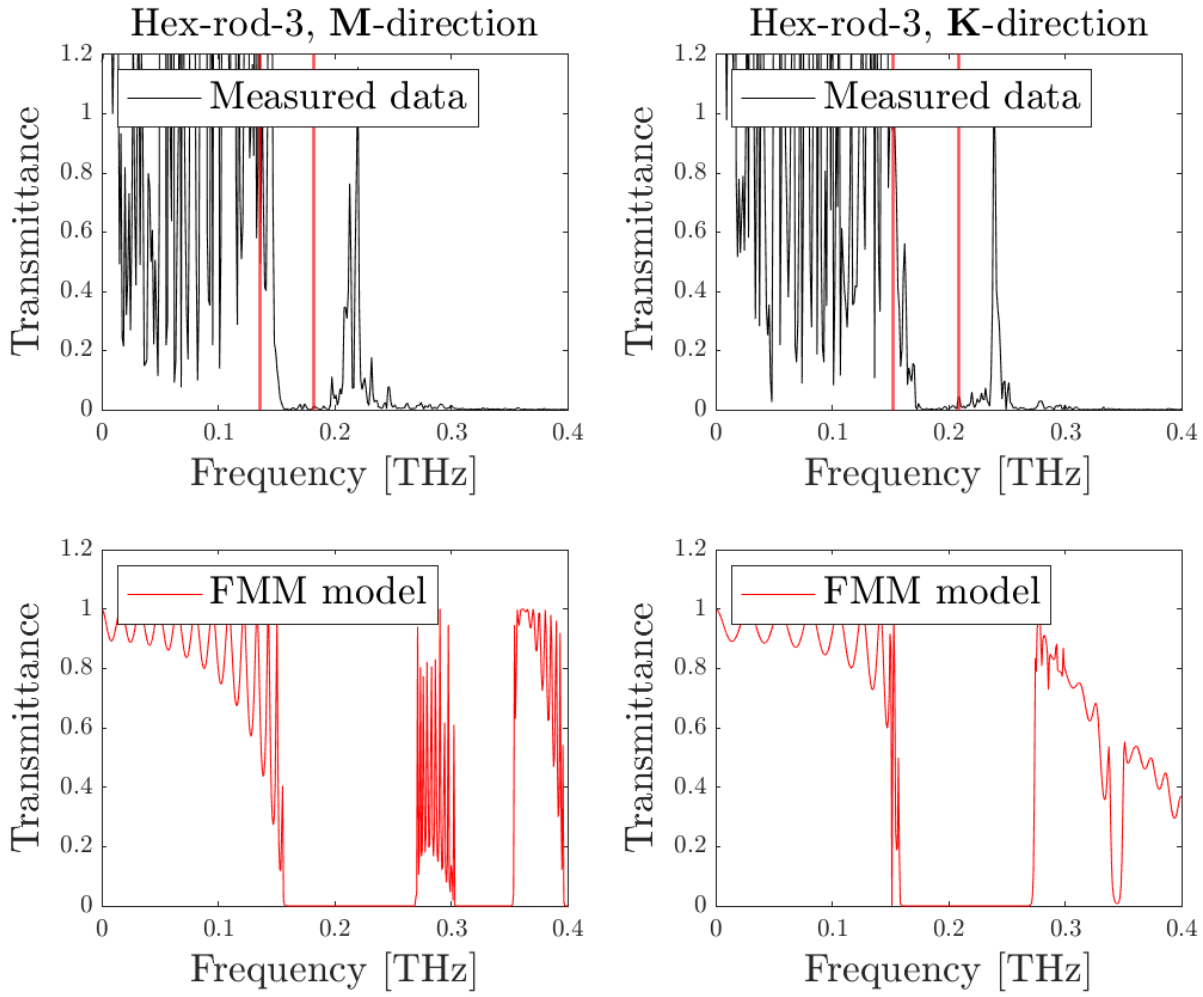

Figure D.8: The measured and modelled transmittance spectra of the Hex-rod-3 sample for light propagating along both the **M**- and **K**-direction. The measured band gap for the **M**-direction was determined to be between 0.16 and 0.20 THz, for the **K**-direction it was determined to lie between 0.17 and 0.24 THz. The calculated band gap lies between 0.16 and 0.27 THz for the **M**-direction, and between 0.16 and 0.27 THz for the **K**-direction. The red vertical lines show the location of the band gap using a fully three-dimensional FFT method with a Si-layer making up 40% of the space between the metal plates.

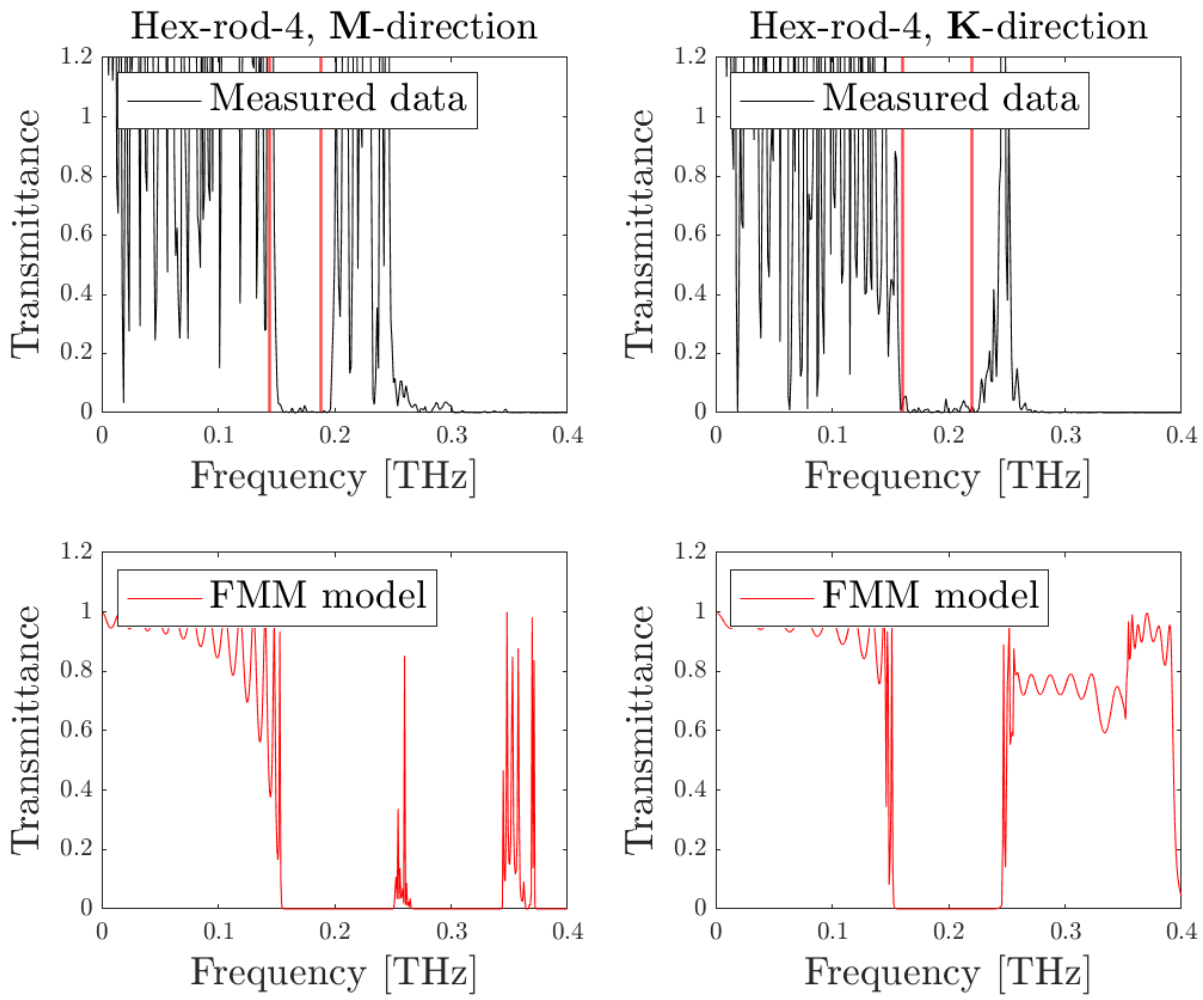

Figure D.9: The measured and modelled transmittance spectra of the Hex-rod-4 for light propagating along both the **M**- and **K**-direction. The measured band gap for the **M**-direction was determined to be between 0.15 and 0.20 THz, for the **K**-direction it was determined to lie between 0.16 and 0.22 THz. The calculated band gap lies between 0.16 and 0.25 THz for the **M**-direction, and 0.15 and 0.25 THz for the **K**-direction. The red vertical lines show the location of the band gap using a fully three-dimensional FFT method with a Si-layer making up 30% of the space between the metal plates.

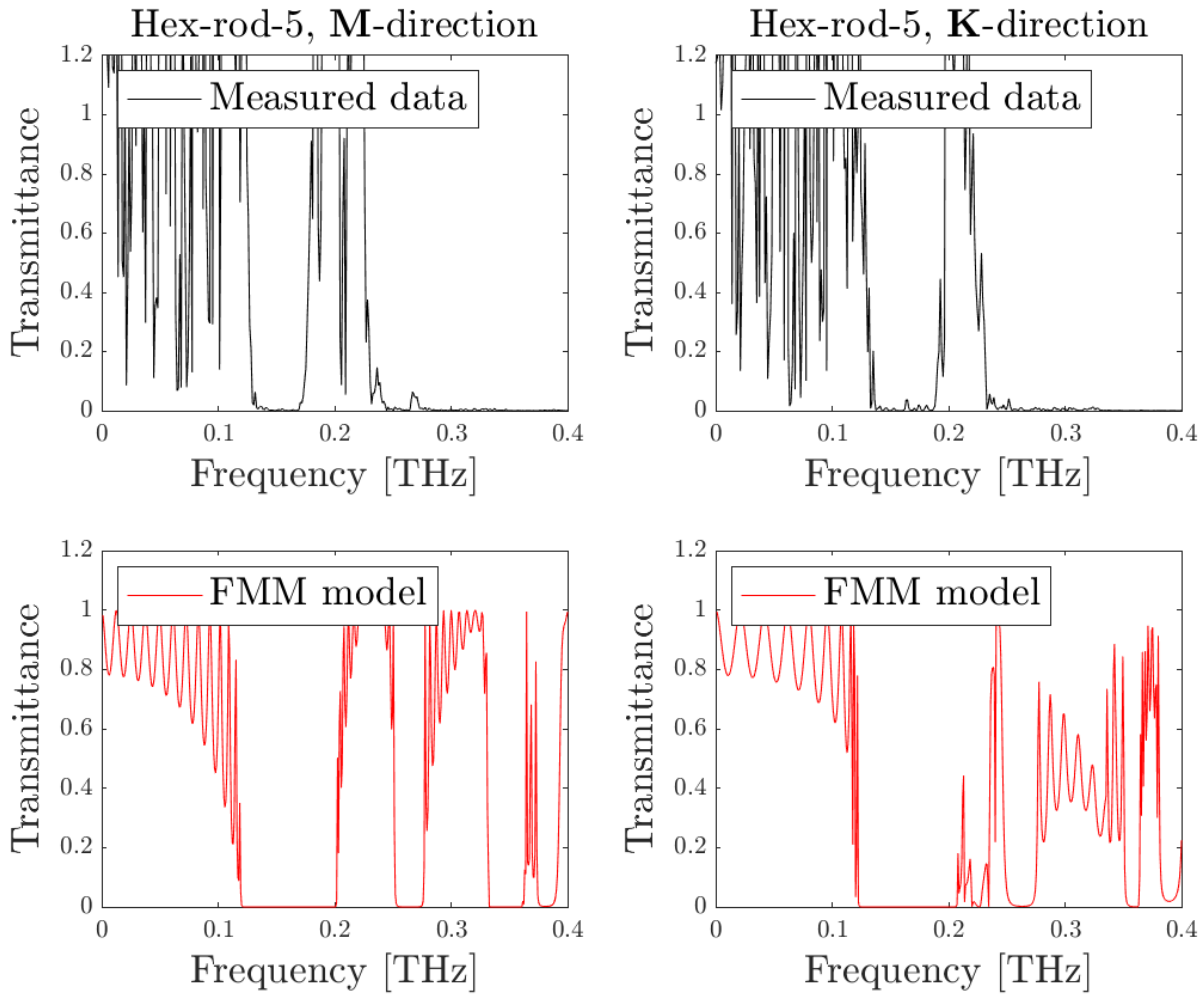

Figure D.10: The measured and modelled transmittance spectra of the Hex-rod-5 sample for light propagating along both the **M**- and **K**-direction. The measured band gap for the **M**-direction was determined to be between 0.13 and 0.17 THz, for the **K**-direction it was determined to lie between 0.14 and 0.19 THz. The calculated band gap lies between 0.12 and 0.20 THz for the **M**-direction, and between 0.12 and 0.21 THz for the **K**-direction.

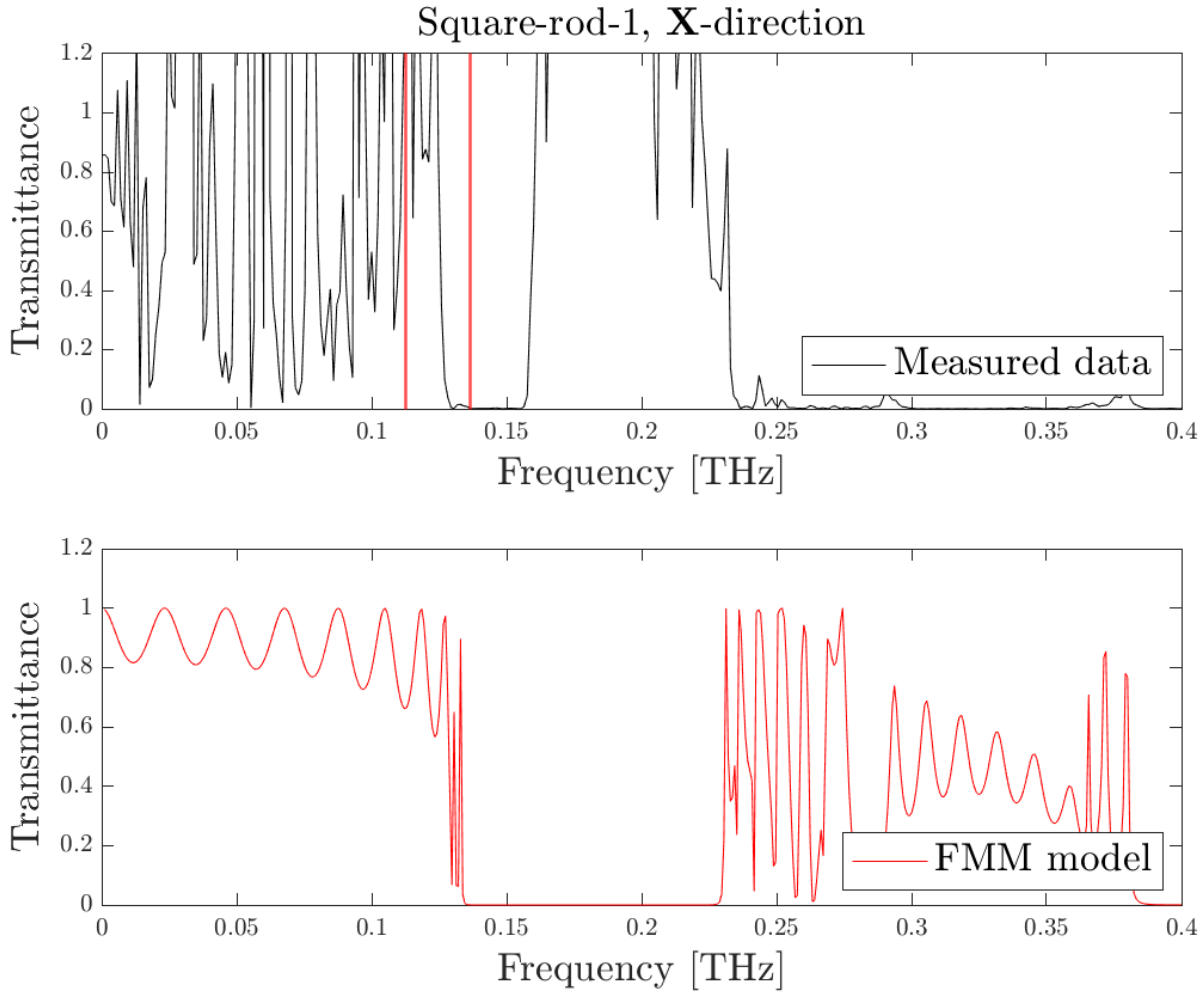

Figure D.11: The measured and modelled transmittance spectra of the Square-rod-1 sample oriented such that the light propagates along the **X**-direction. The measured band gap was determined to be between 0.13 and 0.16 THz while the calculated band gap lies between 0.11 and 0.19 THz. The red vertical lines show the location of the band gap using a fully three-dimensional FFT method with a Si-layer making up 50% of the space between the metal plates.

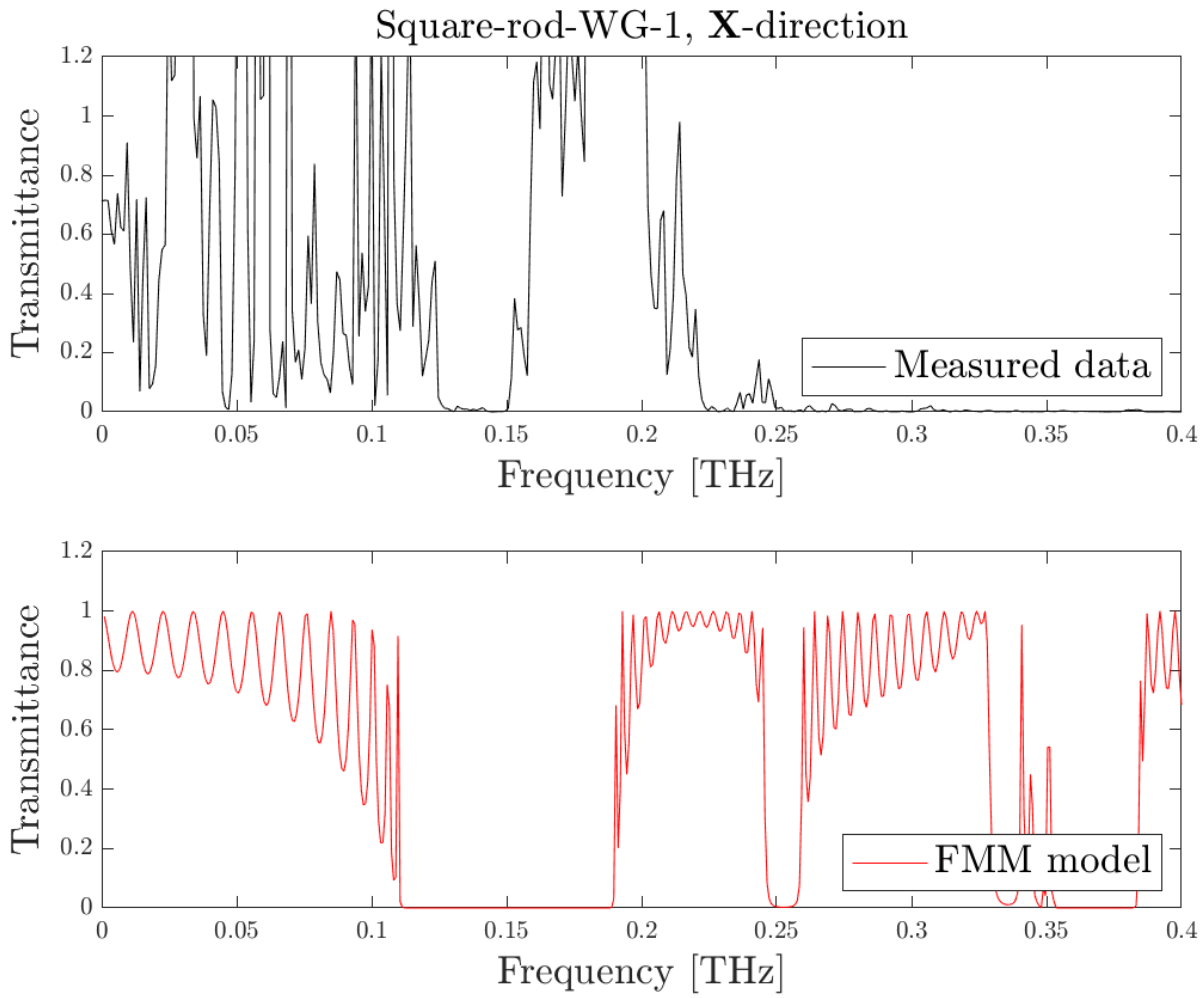

Figure D.12: The measured and modelled transmittance spectra of the Square-rod-WG-1 sample oriented such that the light propagates along the **X**-direction. The measured band gap was determined to be between 0.13 and 0.15 THz while the calculated band gap lies between 0.11 and 0.19 THz.

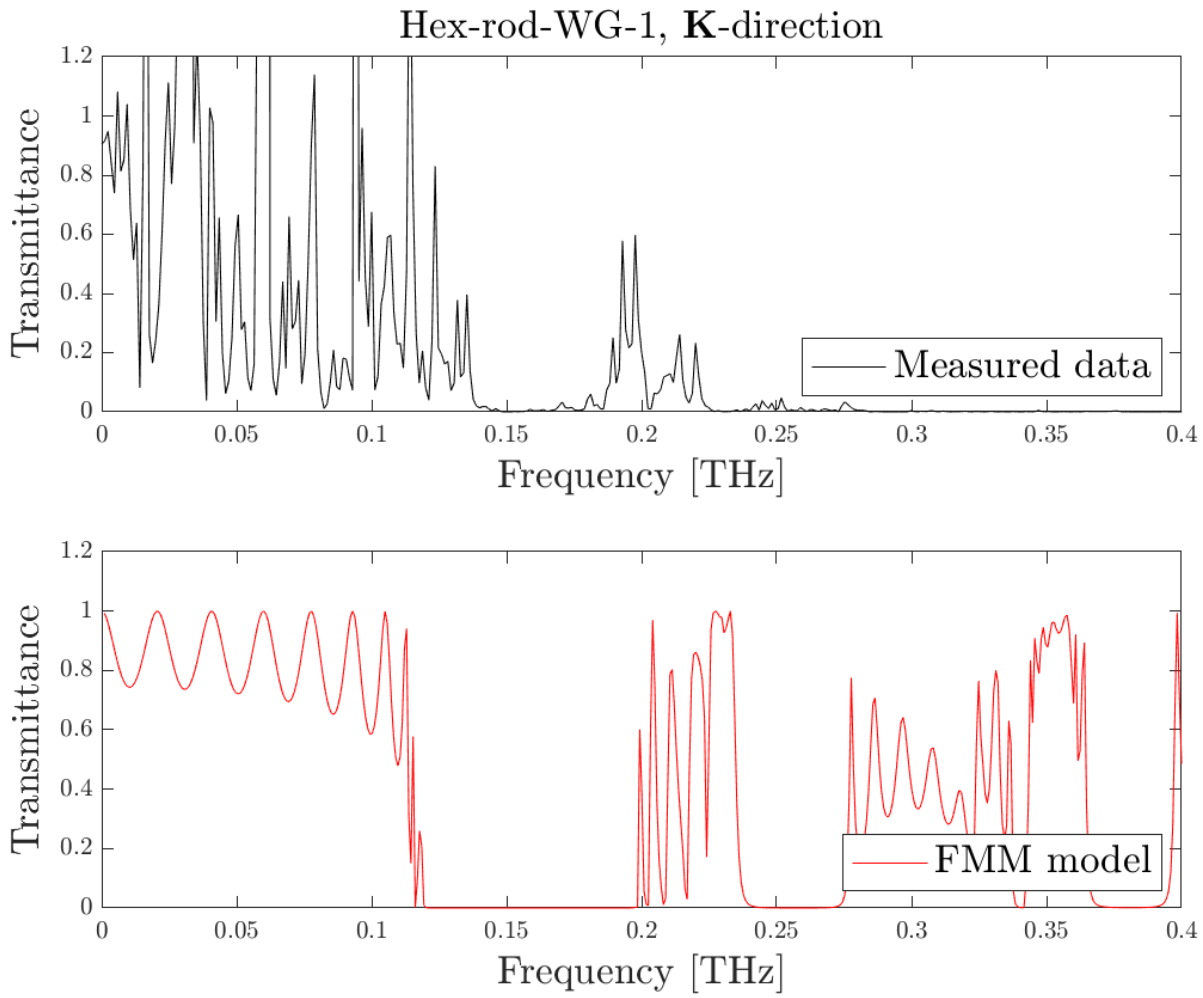

Figure D.13: The measured and modelled transmittance spectra of the Hex-rod-WG-1 sample oriented such that the light propagates along the **K**-direction. The measured band gap was determined to be between 0.14 and 0.19 THz while the calculated band gap lies between 0.12 and 0.20 THz.

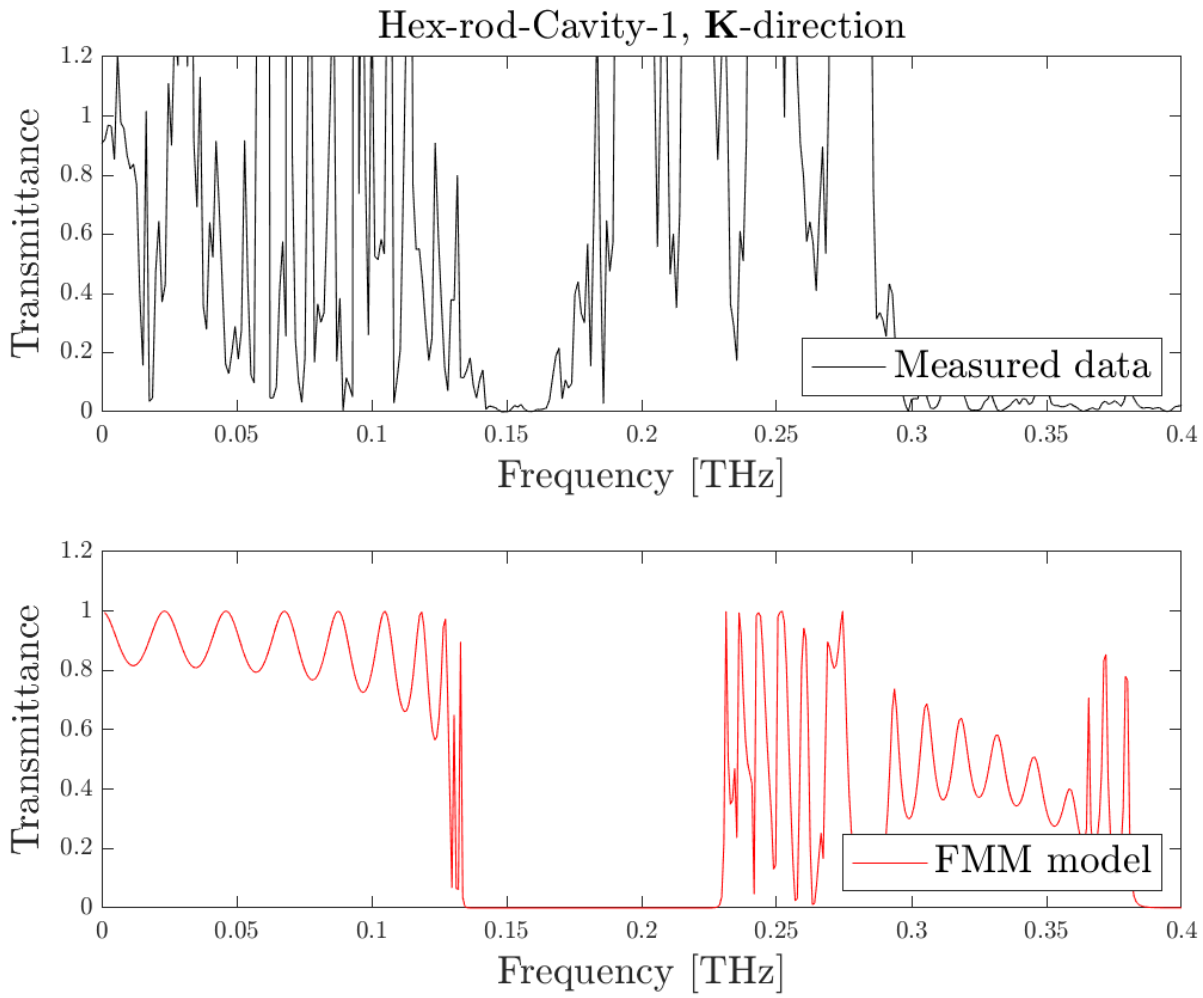

Figure D.14: The measured and modelled transmittance spectra of the Hex-rod-cavity-1 sample oriented such that the light propagates along the **K**-direction. The measured band gap was determined to be between 0.14 and 0.16 THz while the calculated band gap lies between 0.13 and 0.23 THz.

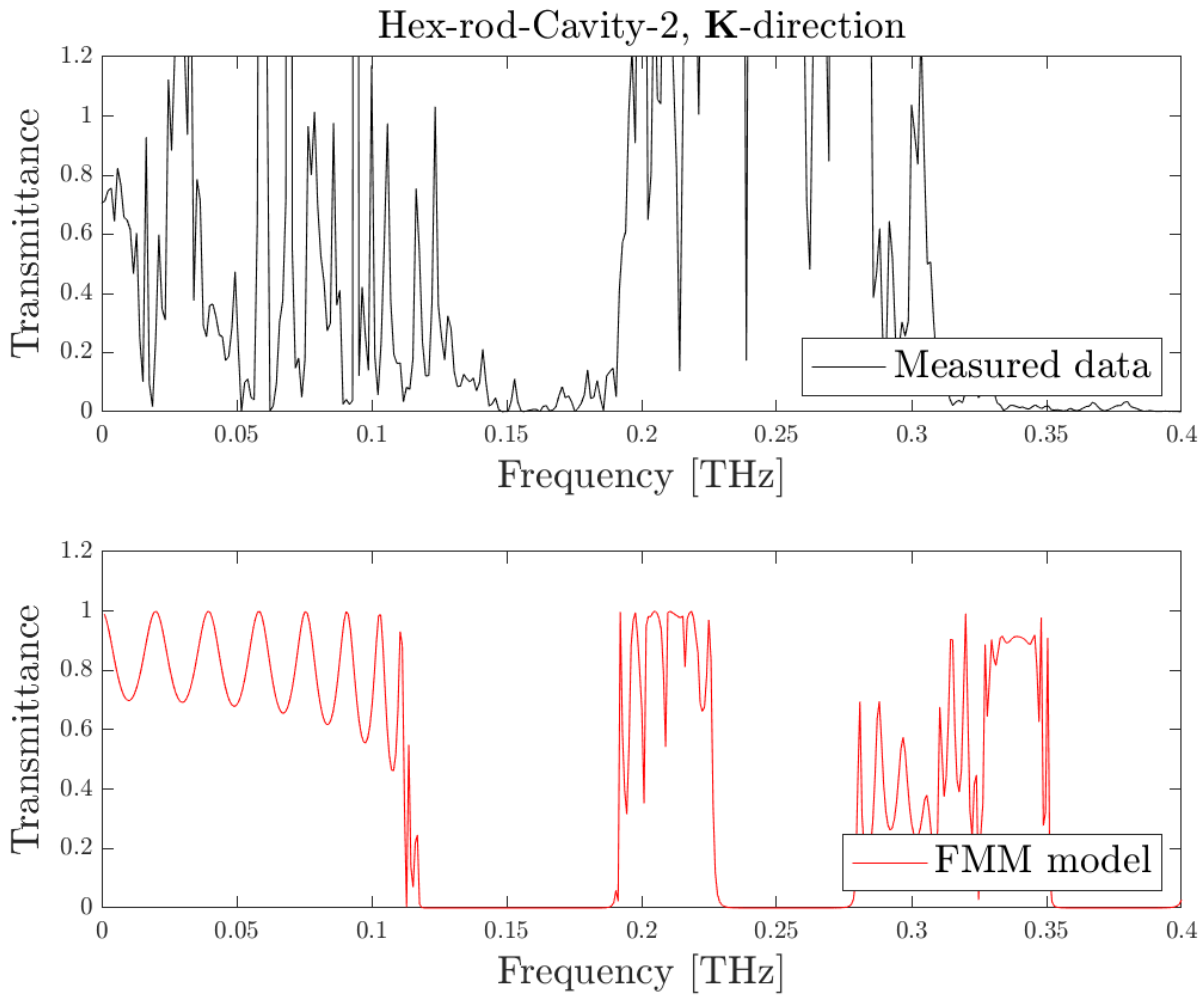

Figure D.15: The measured and modelled transmittance spectra of the Hex-rod-cavity-1 sample oriented such that the light propagates along the **K**-direction. The measured band gap was determined to be between 0.15 and 0.19 THz while the calculated band gap lies between 0.134 and 0.23 THz.

E | One-Dimensional Parallel Plate Metal Waveguide

This appendix outlines the criteria for multiple modes to exist in a region homogeneous dielectric medium between two perfect electric conductors for S-polarised light. The two parallel plates are separated by a distance D along the y-axis, and extend infinitely in the xz-plane. As the region is homogeneous the magnetic field has to satisfy the Helmholtz equation as

$$\left(\nabla^2 + k_0^2 \varepsilon_i\right) \mathbf{H}(\mathbf{r}) = 0, \tag{E.1}$$

with solutions on the form

$$\mathbf{H}(\mathbf{r}) = \hat{\mathbf{z}} H(y) e^{ik_x x}. \tag{E.2}$$

inserting eq. (E.2) into eq. (E.1) then yields

$$\left(\frac{\partial^2}{\partial y^2} - k_x^2 + k_0^2 \varepsilon_i\right) H(y) = 0, \tag{E.3}$$

denoting $\gamma^2 = k_0^2 \varepsilon_i - k_x^2$ and rearranging yields the following second order differential equation

$$\frac{\partial^2}{\partial y^2} H(y) = -\gamma^2 H(y), \tag{E.4}$$

which has the following real solution

$$H(y) = A\, cos(\gamma y) + B\ sin(\gamma y). \tag{E.5}$$

Using the boundary condition for perfect electric conductors, i.e.,

$$E^{||}(0) = E^{||}(D) = 0 \tag{E.6}$$

which can be related to the magnetic field by ampere's law in the frequency domain

$$\nabla \times \mathbf{H} = -i\omega \varepsilon_0 \varepsilon_i \mathbf{E}. \tag{E.7}$$

As $\mathbf{E}(0, D) \cdot \hat{\mathbf{x}} = 0$ this results in the following boundary conditions for the magnetic field

$$\frac{\partial}{\partial y} H(y)\Big|_{y=0} = \frac{\partial}{\partial y} H(y)\Big|_{y=D} = 0. \tag{E.8}$$

By inspection of eq. (E.5) it is clear then that $B = 0$, furthermore the following must be true for γ

$$\gamma = \frac{\pi}{D} m, \qquad m = 0, 1, 2, 3... \tag{E.9}$$

Based on this solution the following relation for k_x emerges

$$k_x = \sqrt{k_0^2 \varepsilon_i - \left(\frac{\pi}{D} m\right)^2} \tag{E.10}$$

hence for propagating solutions to exist in the waveguide the following must be satisfied

$$k_0 \, n_i > \frac{\pi}{D} m, \tag{E.11}$$

then using $k_0 = \frac{2\pi\nu}{c}$ and isolating for ν results in the following requirement for the frequency

$$\nu > \frac{m \, c}{2 \, D \, n_i} \tag{E.12}$$

hence the fundamental mode will always exist but then a cutoff will emerge for the following modes in the waveguide.